

---

# Real-time lattice simulations of classical Yang-Mills theory and fermion effects

---

Dissertation  
zur Erlangung des Doktorgrades  
der Naturwissenschaften

vorgelegt beim Fachbereich Physik  
der Johann Wolfgang Goethe-Universität  
in Frankfurt am Main

von  
Björn Fröhlich Wagenbach  
aus Bad Soden am Taunus

Frankfurt am Main 2018  
D30

vom Fachbereich Physik der  
Johann Wolfgang Goethe-Universität als Dissertation angenommen.

Dekan: Prof. Dr. Owe Philipsen

Gutachter: Prof. Dr. Owe Philipsen  
Prof. Dr. Dirk H. Rischke

Datum der Disputation: 12.10.2018

# Contents

<b>German summary</b>	<b>V</b>
<b>Acknowledgements</b>	<b>XI</b>
<b>1 Introduction</b>	<b>1</b>
<b>2 Theoretical framework</b>	<b>5</b>
2.1 Quantum chromodynamics (QCD)	5
2.1.1 Yang-Mills theory	6
2.1.2 Symmetries of QCD	7
2.2 Hamiltonian field theory	9
2.2.1 Minkowski spacetime	10
2.2.2 Comoving coordinates	11
2.3 From Heisenberg's to Hamilton's equations of motion	13
2.4 Classical aspects of quantum field theory out of equilibrium	15
2.4.1 Schwinger-Keldysh formalism	15
2.4.2 Classiciality condition	17
<b>3 Semiclassical lattice gauge theory</b>	<b>21</b>
3.1 Euclidean path integrals	21
3.2 Fermions on a Minkowski lattice	22
3.3 Stochastic fermion implementation	27
3.4 Gluonic lattice Hamiltonian density	31
3.4.1 The static box scenario	32
3.4.2 Formulation in an expanding system	33
3.5 Lattice equations of motion	34
3.5.1 Static box	34
3.5.2 Expanding system	36
3.5.3 Summary of the field's time evolution on the lattice	37
3.6 Gauss's law	38
3.6.1 Restoring algorithm	40
3.6.2 Gauss's law in the expanding formulation	40
3.7 Real-time static potential	42
3.8 Computation of classical-statistical observables	44

<b>4</b>	<b>The color glass condensate (CGC)</b>	<b>45</b>
4.1	Introduction to the CGC framework and the MV model . . . . .	45
4.2	Initial conditions for the gauge link variables . . . . .	48
4.2.1	Solving Poisson's equation on the lattice . . . . .	53
4.3	Initial conditions for the chromo-electric fields . . . . .	54
4.3.1	Rapidity fluctuations . . . . .	54
4.3.2	Translation to the static box . . . . .	56
<b>5</b>	<b>Technical aspects</b>	<b>57</b>
5.1	Lattice parameters . . . . .	57
5.2	Introducing a physical scale . . . . .	59
5.2.1	Towards non-central collisions . . . . .	60
5.3	UV cutoff . . . . .	61
5.4	Courant-Friedrichs-Lewy condition . . . . .	62
<b>6</b>	<b>Observables</b>	<b>65</b>
6.1	Pressure and energy densities . . . . .	65
6.1.1	Static box . . . . .	66
6.1.2	Expanding system . . . . .	69
6.2	Occupation number . . . . .	71
<b>7</b>	<b>Pure Yang-Mills simulations</b>	<b>73</b>
7.1	SU(2) versus SU(3) . . . . .	74
7.2	Lattice artifacts . . . . .	75
7.2.1	Discretization effects . . . . .	76
7.2.2	Boundary effects . . . . .	76
7.3	Investigating the CGC parameter space . . . . .	77
7.3.1	Number of longitudinal sheets . . . . .	78
7.3.2	Infrared cutoff . . . . .	79
7.3.3	Ultraviolet cutoff . . . . .	80
7.4	Occupation numbers . . . . .	82
7.5	Towards isotropization . . . . .	84
7.5.1	The effect of the fluctuation amplitude . . . . .	85
7.5.2	Variation of the longitudinal box size . . . . .	86
7.5.3	Cutoff dependence of the isotropization times . . . . .	87
7.5.4	Isotropization studies at constant energy density . . . . .	88
7.6	Chromo-Weibel instability . . . . .	88
<b>8</b>	<b>Fermionic impact on the CGC system</b>	<b>93</b>
8.1	Total energy density . . . . .	94
8.2	Isotropization times . . . . .	95

<b>9</b>	<b>Conclusion</b>	<b>97</b>
9.1	Summary and key findings . . . . .	97
9.2	Research perspectives . . . . .	99
<b>Appendices</b>		<b>101</b>
<b>A</b>	<b>Conventions and definitions</b>	<b>103</b>
A.1	Natural units . . . . .	103
A.2	Comments on notation . . . . .	104
A.3	Poisson bracket . . . . .	104
A.4	Generators and structure constants . . . . .	104
A.5	Gamma matrices . . . . .	105
<b>B</b>	<b>Lattice relations</b>	<b>107</b>
B.1	Discretized derivatives . . . . .	107
B.2	Fourier transformation . . . . .	108
B.3	Euclidian formulation . . . . .	109
B.4	From lattice output to physical quantities . . . . .	110
<b>C</b>	<b>Lattice equations of motion</b>	<b>111</b>
C.1	Static box . . . . .	111
C.2	Expanding system . . . . .	115
<b>D</b>	<b>Miscellaneous</b>	<b>119</b>
D.1	Euler-Lagrange equations . . . . .	119
D.2	Operator commutation relations . . . . .	119
D.3	Stochastic low-cost fermions . . . . .	120
D.4	Initial time problem in the 3D expanding system . . . . .	122
D.5	Chromo-Weibel instability: additional figures . . . . .	123
D.6	Pressure ratio including fermions: additional figure . . . . .	127
<b>Bibliography</b>		<b>129</b>
<b>Curriculum vitae</b>		<b>139</b>



# German summary

---

Das *Standardmodell der Elementarteilchenphysik* beschreibt die elektromagnetische, die schwache und die starke Wechselwirkung und beinhaltet somit drei der vier fundamentalen Wechselwirkungen. Es wurde in der zweiten Hälfte des 20. Jahrhunderts entwickelt und kann aufgrund einer Vielzahl experimenteller Nachweise als eine gültige Beschreibung der Natur bis Energieskalen im Bereich von TeV angesehen werden. Hier ist insbesondere die Entdeckung des Higgs-Bosons zu erwähnen, welches im Jahr 2012 experimentell nachgewiesen wurde und bereits in 1960er Jahren durch das Standardmodell vorhergesagt wurde.

Der Erfolg des Standardmodells trotz der fehlenden vierten fundamentalen Wechselwirkung, der Gravitation, mag zunächst verwunderlich erscheinen, kann aber dadurch erklärt werden, dass die relative Stärke der fehlenden Gravitationskraft um ein Vielfaches ( $\approx 10^{-26}$ ) kleiner ist als die der schwachen Wechselwirkung. Nichtsdestotrotz gibt es einige Phänomene, die sich nicht im Rahmen des Standardmodells beschreiben lassen, wie z. B. die Existenz von dunkler Materie und Energie, nicht-verschwindende Neutrinomassen oder die Baryonenasymmetrie, worunter man die Dominanz von Materie gegenüber Antimaterie im Universum versteht. Auf dem Weg zu einer sogenannten *großen vereinheitlichten Theorie* sind also noch viele Probleme zu lösen. Speziell mit Hinblick auf die starke Wechselwirkung, welche im Standardmodell durch die *Quantenchromodynamik (QCD)* beschrieben wird, gibt es noch immer viele Aspekte, deren theoretische Beschreibung unzureichend erscheint oder erst gar nicht existiert.

Experimentelle Beiträge hinsichtlich eines fundierteren Verständnisses der QCD stammen unter anderem auch von (ultra-)relativistischen *Schwerionenkollisionen*. Diese wurden größtenteils am Large Hadron Collider (LHC), der sich unter der französisch-schweizerischen Grenze nahe Genf befindet, und am Relativistic Heavy Ion Collider (RHIC), welcher zum Brookhavens National Laboratory in Upton im US-Bundesstaat New York gehört, durchgeführt. Der geplante Ausbau des GSI Helmholtzzentrums für Schwerionenforschung zu einem internationalen Beschleunigerzentrum für die Forschung mit Ionen- und Antiprotonenstrahlen (FAIR, von Facility for Antiproton and Ion Research) ist aktuell im Gange und soll in Zukunft weitere Erkenntnisse von experimenteller Seite liefern.

Aus theoretischer Sicht handelt es sich bei der QCD um eine nicht-abelsche Quantenfeldtheorie mit  $SU(N_c = 3)$ -Eichsymmetrie.  $N_c$  gibt dabei die Anzahl der verschiede-

nen Farbladungen an, welche für das Wort “Chromo“ in der Namensgebung der Theorie verantwortlich sind. Die QCD beschreibt die Wechselwirkung zwischen Quarks und Gluonen, welche die kleinsten und somit fundamentalen Bausteine von *Hadronen* sind. Letztere sind von der starken Wechselwirkung zusammengehaltene Teilchen und lassen sich wiederum anhand ihres Spins in zwei Gruppen unterteilen: in *Mesonen*, welche aus einem Quark und einem Antiquark bestehen und damit bosonisch sind, also einen ganzzahligen Spin besitzen, und in *Baryonen*, welche entweder aus drei Quarks oder aus drei Antiquarks aufgebaut sind und somit Fermionen, also Teilchen mit halbzahligen Spin, sind. Bekannte Beispiele für Hadronen sind das  $\pi$ - und K-Meson und auf baryonischer Seite das Proton und Neutron.

Die QCD zeichnet sich vor allem durch zwei Besonderheiten aus: einerseits durch das *Confinement* und andererseits durch die *asymptotische Freiheit*. Dabei bezeichnet Confinement das Phänomen, dass Quarks und Gluonen unter normalen Bedingungen aufgrund ihrer Farbladung nicht isoliert vorkommen, sondern lediglich in gebundenen hadronischen Zuständen. Die asymptotische Freiheit beschreibt den Effekt, dass die Stärke der starken Wechselwirkung bzw. die Kopplungsstärke der Quarks mit steigenden Energien abnimmt. Letztere Eigenschaft ermöglicht es insbesondere, den hochenergetischen Bereich der QCD mithilfe von Störungstheorien zu beschreiben. Auf der anderen Seite bedeutet das aber auch, dass eine nicht-perturbative Formulierung der niederenergetischen Region erforderlich ist, was prinzipiell ein Lösen von unendlich-dimensionalen Pfadintegralen beinhaltet.

Eine Reihe verschiedener Techniken wurde diesbezüglich entwickelt. Neben etlichen *effektiven Theorien*, die sehr gute Ergebnisse in den entsprechenden Grenzbereichen liefern, ist die Beschreibung der QCD im Rahmen der *Gittertheorie* (*Gitter-QCD*) die am meisten etablierte. Sie kommt insbesondere ohne zusätzliche Annahmen aus und kann somit – theoretisch – Ergebnisse mit beliebiger Genauigkeit liefern. In der Praxis ist dies natürlich nicht der Fall, da die Rechenkapazitäten beschränkt sind. Daraus können sogenannte *Gitter-Artefakte* resultieren, deren unphysikalischer Einfluss auf die jeweiligen Berechnungen berücksichtigt und untersucht werden muss.

Die Grundidee der Gitter-QCD besteht darin, die Raumzeit zu diskretisieren und somit die Anzahl der auszuwertenden Pfadintegrale auf eine endliche Anzahl zu reduzieren. Das allein reicht jedoch im Allgemeinen noch nicht aus, da immer noch zu viele Pfade ausgewertet werden müssen. Die gängigste Behandlung dieses Problems beinhaltet eine sogenannte *Wick-Rotation* von der gewöhnlichen Minkowski-Raumzeit zur euklidischen Raumzeit. Dies ermöglicht ein Auswerten der hochdimensionalen Pfadintegrale mithilfe des *Importance Samplings*, einer Stichprobenentnahme nach Wichtigkeit. Kombiniert mit sogenannten *Monte-Carlo-Methoden*, also stochastischen Simulationen, können Lösungen dann näherungsweise bestimmt werden.

Der Übergang zur euklidischen Raumzeit hat jedoch auch einen großen Nachteil: Die komplexwertige euklidische Zeit ist offensichtlich nicht mehr mit der physikalischen



---

Zeit zu identifizieren, wodurch nur noch statische Observablen zugänglich sind. Das lässt zwar immer noch viele interessante Studien zu, ist aber für unsere Zwecke eine vernichtende Einschränkung, da wir gerade die Zeitentwicklung des unmittelbar nach einer Schwerionenkollision entstandenen Mediums untersuchen wollen. Wir sehen daher von der Wick-Rotation und dem damit verbundenen Übergang zur euklidischen Raumzeit ab und verfolgen einen anderen Ansatz, den sogenannten *Hamilton-Ansatz* nach Kogut und Susskind. Dabei konstruieren wir die Hamilton-Dichte im Rahmen der *Yang-Mills-Theorie* und lösen die zugehörigen klassischen Bewegungsgleichungen mit den uns vertrauten Methoden der Gitter-QCD. Das beinhaltet die sogenannte *klassische Approximation* der Quantentheorie, welche einen zentralen Bestandteil dieser Arbeit bildet.

Das Zusammenspiel aus Gitter-QCD und der klassischen Approximation liefert eine vielversprechende Umgebung, um das frühe Stadium von Schwerionenkollisionen zu studieren. Einerseits ist die klassische Formulierung nicht nur im Gleichgewicht, sondern auch im *Nicht-Gleichgewicht* gültig, und andererseits steigt die Verlässlichkeit der klassischen Näherung, wenn die Besetzungszahlen der einzelnen Moden hoch sind – wovon bei Schwerionenkollisionen ausgegangen wird. Darüber hinaus leiden Gitterrechnungen unter einem *UV-Cutoff*, welcher proportional zum inversen Gitterabstand  $a$  ist. Gerade das ist hier jedoch von Vorteil, da die klassische Näherung einen UV-Regulator benötigt, was daran liegt, dass sich nur der Infrarotbereich einer Quantentheorie klassisch verhält, nicht aber der Ultraviolettbereich, welcher von Quanteneffekten dominiert ist. Der sogenannte *naive Kontinuumslimit*, bei dem der Gitterabstand gegen Null geschickt wird,  $a \rightarrow 0$ , ist jetzt jedoch problematisch, denn je kleiner  $a$  wird, desto mehr UV-Moden werden bevölkert. Dieses scheinbare Dilemma kann jedoch mithilfe eines *zusätzlichen UV-Cutoffs* umgangen werden, birgt aber den Nachteil eines neuen und unbestimmten Modellparameters. Ausführliche Untersuchungen hinsichtlich dieses zusätzlichen UV-Cutoffs sowie eine Methode, um seine vermeintliche Unbestimmtheit einzuschränken, werden in dieser Arbeit präsentiert.

Die benötigten Anfangsbedingungen, in unserem Fall die Anfangskonfigurationen der Gitter-Eichfelder und der chromo-elektrischen Felder, basieren auf der effektiven Theorie des *Farb-Glas-Kondensats* (CGC, aus dem Englischen: “Color Glass Condensate“). Diese liefert Informationen über die Feldkonfigurationen unmittelbar nach der Kollision zweier ultra-relativistischer Atomkerne mit großer Massenzahl und eignet sich somit hervorragend für die Beschreibung von Schwerionenkollisionen. Im Speziellen wenden wir das sogenannte *McLerran-Venugopalan-Modell* (MV-Modell) an, das eine klassische Approximation in niedrigster Ordnung, also auf *tree-level-Ebene*, darstellt. Dabei werden nur die rein gluonischen Felder berücksichtigt, was damit erklärt wird, dass – wie eingangs erwähnt – bei Schwerionenkollisionen von sehr stark bevölkerten Feldern ausgegangen wird und somit der Beitrag der fermionischen Felder, deren Besetzungszahlen aufgrund des Pauli-Prinzips beschränkt sind, vernachlässigt werden kann. Auch wenn diese An-

nahme plausibel erscheint, wollen wir in dieser Arbeit einen numerischen Beleg dafür bringen und erweitern daher das ursprüngliche MV-Modell durch eine Kopplung an den fermionischen Sektor. Wir verwenden dabei sogenannte *stochastische Fermionen*, die einen verhältnismäßig niedrigen Rechenaufwand benötigen, welcher jedoch immer noch immens im Vergleich zum gluonischen Anteil ist. Da sich Fermionen nicht klassisch beschreiben lassen, das verwendete MV-Modell jedoch im Rahmen der klassischen Yang-Mills-Theorie formuliert ist, spricht man hier von einem *semi-klassischen Ansatz* oder einer *semi-klassischen Approximation*.

Eines der Hauptziele dieser Arbeit liegt darin, den *Isotropisierungsprozess*, der bislang noch viele Fragen aufwirft, aber unter anderem Voraussetzung für das Anwenden von hydrodynamischen Modellen ist, zu studieren. Wir legen dabei einen besonderen Fokus auf die systematische Untersuchung der verschiedenen Parameter, die durch die CGC-Anfangsbedingungen in unsere Beschreibung einfließen, und deren Auswirkungen auf etwa die Gesamtenergiedichte des Systems oder die zugehörigen Isotropisierungszeiten. Währenddessen überprüfen wir zusätzlich den Einfluss der angesprochenen unphysikalischen Gitter-Artefakte und präsentieren eine eichinvariante Methode zur Analyse der Güte unserer klassischen Näherung. Die Zeitentwicklung des Systems betrachten wir dabei sowohl in einer *statischen Box* als auch in einem *expandierenden Medium*, wobei Letzteres durch sogenannte *comoving* Koordinaten beschrieben wird. Zudem liefern wir einen Vergleich von der realistischen SU(3)-Eichgruppe und der rechentechnisch ökonomischeren SU(2)-Eichgruppe.

Mit unseren numerischen Ergebnissen zeigen wir, dass das System hochempfindlich auf die verschiedenen Modellparameter reagiert, was das Treffen quantitativer Aussagen in dieser Formulierung deutlich erschwert, insbesondere da einige dieser Parameter rein technischer Natur sind und somit keine zugehörigen physikalisch motivierten Größen vorhanden sind, die den Definitionsbereich einschränken könnten. Es ist jedoch möglich, die Anzahl der freien Parameter zu reduzieren, indem man ihren Einfluss auf die Gesamtenergie des Systems analysiert und sich diesen zunutze macht. Dadurch gelingt es uns, mithilfe von Konturdiagrammen einige Abhängigkeiten zu definieren und somit die Unbestimmtheit des Systems einzuschränken. Des Weiteren finden wir dynamisch generierte *Filamentierungen* in der Ortsdarstellung der Energiedichte, die ein starkes Indiz für die Präsenz von sogenannten *chromo-Weibel-Instabilitäten* sind. Unsere Studie des fermionischen Einflusses auf den Isotropisierungsprozess des CGC-Systems weist auf, dass dieser bei kleiner Kopplung vernachlässigbar ist. Bei hinreichend großen Werten für die Kopplungskonstante sehen wir allerdings einen starken Effekt hinsichtlich der Isotropisierungszeiten, was bemerkenswertes Resultat ist.

Im Folgenden wollen wir die Struktur der vorliegenden Dissertation erläutern. Nach einem einleitenden Kapitel werden die grundlegenden Konzepte und Theorien, die für das Verständnis dieser Arbeit relevant sind, vorgestellt. Darunter fallen eine Zusammenfassung der Kernaspekte der QCD sowie der hamiltonschen Feldtheorie und die Einfüh-

---

rung der zwei verwendeten Systembeschreibungen (statische Box und expandierendes Medium). Zudem wird darin auch die klassische Näherung motiviert und ein zugehöriges Kriterium ihrer Gültigkeit beschrieben. Das dritte Kapitel widmet sich einzig und allein der Gitter-QCD und liefert dabei eine sehr detaillierte Einführung in die Gitterbeschreibung des vorliegenden Problems. Darin enthalten sind die Formulierung der stochastischen Fermionen, die Herleitung der (Gitter-)Bewegungsgleichungen und erste numerische Tests, die eine korrekte Computerimplementierung bestätigen. Im anschließenden vierten Kapitel geben wir eine kurze Einführung in die Grundlagen der effektiven Theorie des CGC sowie in die des MV-Modells und leiten die daraus resultierenden und für unsere numerischen Simulationen relevanten Anfangsbedingungen auf dem Gitter her. Einige wichtige technische Aspekte, die insbesondere die Gitterimplementierung betreffen, werden im darauffolgenden Kapitel fünf diskutiert. Anschließend, in Kapitel sechs, werden die zu untersuchenden Observablen erst im Kontinuierlichen und dann auf dem Gitter definiert. Die beiden nachfolgenden Kapitel enthalten den Hauptteil der numerischen Ergebnisse unserer Gittersimulationen. Dabei liegt in Kapitel sieben der Fokus auf Rechnungen in reiner Eichtheorie und die damit verbundene Untersuchung der Modellparameter des CGC. Kapitel acht beinhaltet dann unsere ersten semi-klassischen Resultate, also jene, die zusätzlich den fermionischen Sektor miteinbeziehen. Eine Zusammenfassung und ein Fazit sowie ein Ausblick auf mögliche weiterführende Studien werden schließlich in Kapitel neun gegeben. Abgeschlossen wird die Arbeit mit einem umfangreichen Anhang, der relevante Definitionen und Konventionen sowie zusätzliche Abbildungen und ausführliche Rechnungen enthält.



# Acknowledgements

---

First and foremost, I would like to thank my supervisor Owe Philipsen for his advise and help, for his continued interest in my work yielding very instructive discussions and for his financial support during the closing stages of my PhD. I also really appreciated the fruitful conversations during the biannual PhD committee meetings together with him and Dirk Rischke, whom I would thus also like to thank, particularly for being my second supervisor and referee of this work. In addition, I want to thank him for being an excellent teacher throughout my undergraduate studies, which substantially contributed to my interest in theoretical physics.

I would also like to thank Marc Wagner for his support while writing my bachelor and master thesis, where my main knowledge of lattice gauge theory originates from, as well as for being an always friendly and tolerant office neighbor.

Additionally, I would like to thank Alessandro Sciarra and Jonas Glesaaen for all their assistance regarding C++,  $\text{\LaTeX}$  and compiler issues. Furthermore, I would like to thank Moritz Greif, Hendrik von Hees and Sören Schlichting for inspiring conversations.

I had the great pleasure for almost my entire PhD to collaborate with Savvas Zafeiropoulos, who has always supported me and who I could ask for advice at any time.

My special thanks go to my friend and colleague Jonas Scheunert, who patiently answered all my questions and with whom it was a great joy to share the office.

Moreover, I would like to thank Mathias Stockhofe for plenty of welcome distractions and for enduring me as a room mate, which probably was a little exhausting in the final stage of this work.

However, my biggest hugs and thanks I have to give to my family, particularly to my wonderful girlfriend Karolina as well as to my beloved parents and brother – Marianne, Micha and Lars.

Last but not least, I would like to thank HGS-HiRe for financial assistance in form of a scholarship and for providing many interesting lectures and courses.



# Chapter 1

## Introduction

---

The *Standard Model* of particle physics was developed within the second half of the 20th century and describes electromagnetic, weak and strong interactions and thus includes three of the four fundamental forces in the universe. A vast amount of experimental observations confirms the validity of the Standard Model as a description of nature for energy scales up to TeV. However, a complete theory of fundamental interactions obviously has to include the fourth fundamental force, the gravitational force, as well. Moreover, it is well-known that the Standard Model leaves some phenomena unexplained, as for instance the existence of dark matter and energy, neutrino masses or the baryon asymmetry problem [1,2]. In particular, many aspects of the strong interaction, which is described in the Standard Model by the theory of *quantum chromodynamics (QCD)*, still lack a theoretical understanding.

Some of the experimental contributions towards a better understanding of QCD have been carried out at (ultra-)relativistic heavy-ion collisions performed at the Large Hadron Collider (LHC) beneath the France-Switzerland border near Geneva and at the Relativistic Heavy Ion Collider (RHIC) of Brookhavens National Laboratory in Upton, New York. Additionally, the Facility for Antiprotons and Ion Research (FAIR), which is still under construction and will be an expansion of the GSI Helmholtz Centre for Heavy Ion Research in Darmstadt, is expected to yield further insights.

From a theoretical point of view, QCD is a non-abelian quantum field theory with  $SU(N_c = 3)$  gauge symmetry. It describes the interactions between quarks and gluons, which are the fundamental particles hadrons consist of. QCD exhibits two central properties: firstly, the *color confinement*, often simply called *confinement*, which states that color charged particles cannot be isolated and hence cannot be observed under normal conditions, and, secondly, the *asymptotic freedom*, which describes the continuous reduction in the strength of the interactions between quarks and gluons when increasing the energy scale. The latter property allows for a description of the high energy regime

of QCD within the framework of *perturbation theory*, which has resulted in very accurate tests of QCD. Nevertheless, the low energy sector requires a non-perturbative formulation, which entails the problem of solving infinite-dimensional path integrals.

For this purpose, various techniques have been developed, where – besides several *effective theories*, which also yield promising results in the corresponding limits – the most well established one is *lattice QCD*. It is a first principle description of QCD without any assumptions and thus theoretically allows for solutions up to any level of accuracy that is desired. However, in practice, the computation power is limited and one is left with so-called *lattice artifacts*, which are unphysical remnants of the lattice description that have to be monitored.

The idea of lattice QCD is to reduce the analytically intractable infinite-dimensional path integrals by discretizing the four-dimensional spacetime allowing for a numerical evaluation with the help of supercomputers. To this end, a Wick rotation from Minkowski to Euclidean space is performed, which enables an evaluation of the path integrals via *Monte-Carlo methods* based on *importance sampling*. However, the downside of this approach – besides the occurrence of the so-called *sign problem* [3] – is the loss of the possibility of studying observable evolutions in *real-time*, which is the intention of this work. We will therefore refrain from the Wick rotation and use a different approach, the so-called *Hamiltonian approach* [4], where we construct the system’s Hamiltonian within the scope of *Yang-Mills theory* and solve the corresponding classical field equations. The latter involves a *classical approximation* of the quantum theory, which is of central importance for this work.

The interplay of lattice QCD and the classical approximation provides a very promising environment for studying the early stages of heavy-ion collision. On the one hand, the classical formulation does not lose its validity in systems far from equilibrium [5] and on the other hand, the reliability of the classical approximation increases with the number of field quanta in each mode, which fits to the high occupancies present at heavy-ion collisions [6, 7]. Moreover, every lattice formulation entails an ultraviolet (UV) cutoff proportional to the inverse of the lattice spacing  $a$ , which serves as an intrinsic UV regulator for the classical approximation as it is well-known that the infrared (IR) regime of a quantum theory behaves classical, whereas the UV sector is of quantum nature [8]. In this case, taking the naive continuum limit of the lattice description,  $a \rightarrow 0$ , is now problematic since more and more non-classical hard modes enter the description, which is illustrated in Figure 1.1. However, we will propose a method that allows for a “continuous” lattice description without affecting the validity of the classical approximation in the course of this work.

We will employ initial conditions based on the *color glass condensate (CGC)* effective theory, which supplies information about the field properties immediately after the collision. More precisely, our initial field configurations are based on the *McLerran-Venugopalan (MV) model* [9–11], which is a (classical) tree-level description of the CGC.



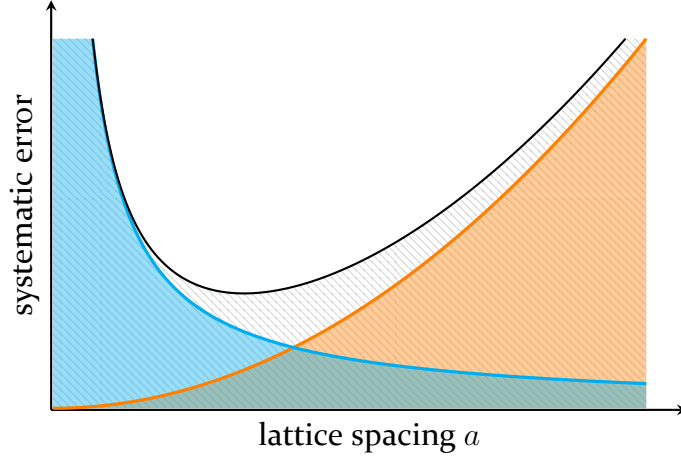


**Figure 1.1:** Sketch of the interplay between the systematic error owed to the classical approximation (cyan) and the discretization error coming from the lattice formulation (orange). The combined total systematic error is the shaded area.

The underlying concept involves a pure gauge formulation which is premised on the mentioned high mode occupations present at heavy-ion collisions. Due to the Pauli exclusion principle the fermionic occupation numbers are limited and it is thus expected that their influence on the system's dynamics is very small. However, a quantitative result which substantiates this statement is still missing.

To this end, we will extend the classical Yang-Mills formulation by adding fermionic degrees of freedom, which are coupled to the gauge sector by the system's evolution equations. Since fermions cannot be treated classically, this is usually referred to as a *semiclassical approach* or a *semiclassical approximation*. Simulations including fermions require significantly larger amounts of computational resources, which is why we will follow the approach presented in [12], where a low-cost implementation of fermions based on stochastic integration is given.

The main purpose of this work is study the isotropization process and thereby present a systematic investigation of the dependence on the variety of parameters entering through the CGC initial condition, as well as the systematics of the classical evolution itself. We will investigate the system's evolution both in a static box and in an expanding medium. Moreover, we perform a comparison between the realistic  $SU(3)$  gauge group and the more economical  $SU(2)$  gauge group, monitor the field occupancies to address the validity of the classical approximation, and quantify the dependence of our results on the various CGC parameters.

We will see that the system is highly sensitive to the model parameters and suggest a method to reduce the number of free parameters by keeping the system's physical energy density fixed. We also present depictions of the filamentation of the energy density in position space, which results from initial quantum fluctuations and indicates the oc-

currence of *chromo-Weibel instabilities* [13–18]. Furthermore, we will obtain that the isotropization process of the CGC system stays virtually unaffected by the fermionic degrees of freedom as long as the gauge coupling is small. For sufficiently large values of the coupling constant, however, the tide turns and we will observe a significant change in the isotropization times.

We would like to mention, that some very early stages of this work were published as a conference proceeding [19], whereas the majority of the findings that we are presenting in this work will appear in [20].

The content of this thesis is organized as follows. The theoretical basics that form the foundation of this work are introduced in Chapter 2. It includes a summary of the key aspects of QCD as well as of the Hamiltonian field theory, and introduces the two different formulations (static box and expanding system) that are dealt with throughout this work. Moreover, it motivates the classical description and quantifies its validity ultimately ending in a classicality condition. Chapter 3 is dedicated to the lattice description and provides a detailed introduction to the employed framework containing the stochastic fermion implementation, the derivation of the lattice equations of motion, and first numerical cross-checks. This is followed by Chapter 4, in which give a brief introduction to the CGC effective theory and the MV model yielding the initial conditions for our lattice simulations. Some important technical aspects including a definition of the various lattice and model parameters are discussed in Chapter 5, and the different observables we want to investigate are summarized in Chapter 6. The two subsequent chapters provide the largest part of the numerical results, where Chapter 7 focuses on pure gauge simulations as well as the involved investigation of the CGC parameter space, and Chapter 8 examines the impact of the fermionic degrees of freedom on these results. Concluding remarks and possible research perspectives are then given in Chapter 9. Finally, at the end of the thesis, extensive appendices containing relevant conventions and definitions as well as additional figures and rather technical calculations can be found.

# Chapter 2

## Theoretical framework

---

### Contents

2.1	Quantum chromodynamics (QCD) . . . . .	5
2.2	Hamiltonian field theory . . . . .	9
2.3	From Heisenberg's to Hamilton's equations of motion . . . . .	13
2.4	Classical aspects of quantum field theory out of equilibrium . . . . .	15

---

### 2.1 Quantum chromodynamics

Quantum chromodynamics (QCD) is a non-abelian gauge theory in Minkowski space-time which is coupled to fermions. Its symmetry group is the *special unitary group*  $SU(N_c)$ , where  $N_c$  is the number of colors.<sup>1</sup> QCD can be separated into a pure gluonic gauge part, the Yang-Mills sector, which is reflected in Section 2.1.1, and a fermionic part including massive fermions described by Dirac 4-spinors  $\psi_f \equiv \psi_f^{\alpha,c}$ , with (Dirac) spinor index  $\alpha \in \{1, \dots, 4\}$ , color index  $c \in \{1, \dots, N_c\}$  and the flavor index  $f \in \{1, \dots, N_f\}$ .

The Standard Model of particle physics counts  $N_f = 6$  flavors and  $f \in \{u, d, c, s, t, b\}$  indicates the different quark species defining the corresponding electric and electroweak charges as well as the quark masses.

The fermionic fields  $\psi_f$  interact among each other via the coupling to the gauge field  $A_\mu \equiv A_\mu^a T^a$ , which is an element of the underlying *Lie algebra*  $su(N_c)$ . In the *fundamental representation*, the generators of the algebra  $T^a$ ,  $a \in \{1, \dots, N_g := N_c^2 - 1\}$ , can be chosen as traceless hermitian  $N_c \times N_c$  matrices, which are normalized by

$$\text{Tr} [T^a T^b] = \frac{1}{2} \delta^{ab} \quad (2.1)$$

---

<sup>1</sup>The formulation of QCD is based on  $N_c = 3$  colors, however, as will be explained later, we will also consider  $N_c = 2$ .

and satisfy the (anti)commutation relations

$$\{T^a, T^b\} = \frac{1}{N_c} \delta^{ab} + d^{abc} T^c, \quad (2.2a)$$

$$[T^a, T^b] = i f^{abc} T^c. \quad (2.2b)$$

In the *adjoint representation*, the generators are represented by  $N_g \times N_g$  matrices, whose elements are defined by

$$(T^a)^{bc} = -i f^{abc}. \quad (2.3)$$

For  $N_c = 2$  flavors, the three generators of  $\text{su}(2)$  are related to the *Pauli matrices*  $\sigma^a$  by  $T^a = \sigma^a / 2$ , and in the case of  $N_c = 3$  flavors, the generators are given by  $T^a = \lambda^a / 2$ , with the eight *Gell-Mann matrices*  $\lambda^a$ . A definition of the Pauli and Gell-Mann matrices as well as the values for the structure constants  $d^{abc}$  and  $f^{abc}$  can be found in Appendix A.4.

As we will carry out in Section 2.2, the *Lagrangian density*  $\mathcal{L}$  is a fundamental quantity which determines the system's dynamics. The fermionic part of the Lagrangian density of QCD is bilinear in the fields  $\psi_f$  and their Dirac adjoint fields  $\bar{\psi}_f \equiv \psi_f^\dagger \gamma_0$  and reads in Minkowski spacetime

$$\mathcal{L}_F = \sum_f \bar{\psi}_f \mathbf{D} \psi_f. \quad (2.4)$$

We defined the so-called *Dirac operator*,

$$\mathbf{D} = i\gamma^\mu D_\mu - m_f, \quad (2.5)$$

together with the *covariant derivative*,

$$D_\mu = \partial_\mu + igA_\mu. \quad (2.6)$$

The latter renders  $\mathcal{L}_F$  invariant under local  $\text{SU}(N_c)$  gauge transformations,

$$\psi(x) \rightarrow \psi'(x) = \Omega(x)\psi(x) \Rightarrow \bar{\psi}(x) \rightarrow \bar{\psi}'(x) = \bar{\psi}(x)\Omega^\dagger(x), \quad (2.7a)$$

$$A_\mu(x) \rightarrow A'_\mu(x) = \Omega(x)A_\mu(x)\Omega^\dagger(x) + ig(\partial_\mu\Omega(x))\Omega^\dagger(x), \quad (2.7b)$$

with  $\Omega \in \text{SU}(N_c)$ , and will lead us to the gluonic part of the Lagrangian density  $\mathcal{L}_G$ , which is discussed in the following subsection.

### 2.1.1 Yang-Mills theory

The initial phase present immediately after a heavy-ion collision is expected to be characterized by the gluonic degrees of freedom. While the fermionic occupation numbers are limited by the Pauli exclusion principle, the gluonic ones are typically large and thus dominate the dynamics [6, 7]. For this reason, and since lattice simulations including

fermions are significantly more expensive in terms of computational effort, we will mostly focus on pure Yang-Mills theory.

After the introduction of the fermionic part of the Lagrangian density of QCD, we will now construct the gluonic part, which is also referred to as the (pure) Yang-Mills part. Starting point is the covariant derivative (2.6), which defines the (*gluon*) *field strength tensor* of QCD as

$$F_{\mu\nu} = \frac{i}{g} [D_\mu, D_\nu] = \partial_\mu A_\nu - \partial_\nu A_\mu + ig [A_\mu, A_\nu]. \quad (2.8)$$

It is equivalent to the one of *quantum electrodynamics* (QED), where the commutator vanishes since QED is an *abelian* gauge theory. Based on the gauge part of the Lagrangian density of QED and the requested invariance under local  $SU(N_c)$  gauge transformations,

$$\text{Tr} [F_{\mu\nu} F^{\mu\nu}] \equiv \text{Tr} [F_{\mu\nu} g^{\mu\alpha} g^{\nu\beta} F_{\alpha\beta}], \quad (2.9)$$

with a proper normalization is a convenient candidate for a gluonic Lagrangian density  $\mathcal{L}_G$ . In fact, the Yang-Mills action in general coordinates is given by

$$S = \int d^4x \mathcal{L}_G = -\frac{1}{2} \int d^4x \sqrt{-\det[(g_{\mu\nu})]} \text{Tr} [F_{\mu\nu} F^{\mu\nu}]. \quad (2.10)$$

We will consider two different metrics  $g^{\mu\nu}$ , which are introduced and discussed in Section 2.2. Together with (2.4) we can then define the full Lagrangian density of QCD,

$$\mathcal{L} = \mathcal{L}_F + \mathcal{L}_G. \quad (2.11)$$

### 2.1.2 Symmetries of QCD

The formulation of relativistic quantum field theories is based on an invariance under *Poincaré transformations*. It includes *spacetime translations* and *Lorentz transformations*, where the latter consist of rotations in space and (Lorentz) boosts. By construction, the QCD Lagrangian (2.11) is invariant under local  $SU(N_c)$  *color* gauge transformations introduced in (2.7).

However, especially in appropriate limits, there are numerous other symmetries. One of these is the so-called *flavor symmetry*, which is particularly relevant for our lattice implementation. Hence, we will briefly summarize its main aspects in this subsection.

First of all, we note that global  $U(1)$  transformations of the fermionic fields  $\psi$ ,

$$\psi(x) \rightarrow \psi'(x) = e^{i\theta} \psi(x), \quad \theta \in \mathbb{R}, \quad (2.12)$$

obviously leave (2.4) invariant and hence lead to a global  $U(1)$  symmetry of the QCD Lagrangian density. The associated conserved charge is the *baryon number*.

By decomposing the fermionic fields into *right-handed* and *left-handed* fields,

$$\psi_R = \frac{1}{2}(1 + \gamma^5)\psi, \quad \psi_L = \frac{1}{2}(1 - \gamma^5)\psi, \quad (2.13)$$

we can rewrite the fermionic Lagrangian (2.4) for a single flavor  $f$ ,

$$\mathcal{L}_F = i\left(\bar{\psi}_L \gamma^\mu D_\mu \psi_L + \bar{\psi}_R i\gamma^\mu D_\mu \psi_R\right) - m\left(\bar{\psi}_L \psi_R + \bar{\psi}_R \psi_L\right). \quad (2.14)$$

Under (2.12), the right-handed and left-handed components of  $\psi$  rotate with an equal phase, which is why this symmetry is called a *vector symmetry*,  $U(1)_V$ .

Although the vector symmetry  $U(1)_V$  is the only exact flavor symmetry, there are further ones in the case of vanishing quark masses, which is usually referred to as the *chiral limit*. This is a good approximation for  $N_f = 2$ , with  $f \in \{u, d\}$  (and in some cases also for  $N_f = 3$ , with  $f \in \{u, d, s\}$ ), due to the low masses of the relevant quarks.

If we now consider *degenerate* quark masses, i.e.  $m_f \equiv m$ , we also observe an  $SU(N_f)$  symmetry. Especially for  $N_f = 2$ , where  $m_u/m_d = 0.48(10)$  [21], this is a good approximation and usually referred to as *isospin symmetry*,

$$\psi(x) \rightarrow \psi'(x) = e^{i\alpha_a T^a} \psi(x), \quad \alpha_a \in \mathbb{R}. \quad (2.15)$$

For  $m = 0$ , the masses are trivially degenerate and hence the  $SU(N_f)$  isospin symmetry is exact, but, moreover, there is no mixing of right-handed and left-handed fields, yielding

$$SU(N_f) \xrightarrow{m=0} SU(N_f)_R \times SU(N_f)_L. \quad (2.16)$$

Furthermore, for vanishing quark masses the Lagrangian density (2.14) is invariant under so-called *chiral transformations*,

$$\psi(x) \rightarrow \psi'(x) = e^{i\theta\gamma^5} \psi(x), \quad \theta \in \mathbb{R}, \quad (2.17)$$

which is referred to as *axial symmetry*  $U(1)_A$ .

Putting these findings together, the flavor symmetry group in the chiral limit, commonly designated as the *chiral symmetry*, reads

$$SU(N_f)_R \times SU(N_f)_L \times U(1)_V \times U(1)_A. \quad (2.18)$$

We want to stress that all of these are symmetries of the massless QCD Lagrangian, but not necessarily symmetries of the related partition function. In particular, the measure of the partition function is not invariant under axial  $U(1)$  symmetry transformations leading to the so-called *axial anomaly* also known as the *Adler-Bell-Jackiw anomaly* [22, 23].

The chiral symmetry (2.18) is not only explicitly broken by (re)introducing a mass term, but also *spontaneously* broken by the QCD vacuum due to a non-vanishing quark condensate  $\langle \psi\bar{\psi} \rangle$ , in this context usually referred to as *chiral condensate*, leading to

$$SU(N_f)_R \times SU(N_f)_L \longrightarrow SU(N_f)_V. \quad (2.19)$$

According to *Goldstone's theorem*, for every spontaneously broken continuous symmetry, the theory must contain a massless particle, which is called a (*Nambu-*)*Goldstone boson*

[24, 25]. If the symmetry is also (slightly) explicitly broken, i.e. the symmetry is not exact, the Goldstone bosons are not massless but have relatively light masses and are therefore called *pseudo-(Nambu)-Goldstone bosons*. The latter scenario is present for the spontaneous chiral symmetry breaking and the corresponding pseudo-Goldstone bosons are the pions, whose masses are one order of magnitude smaller than the nucleon mass.

## 2.2 Hamiltonian field theory

In this section we will introduce the basic concepts of Hamiltonian field theory, which is the field-theoretical analogue of the Hamiltonian formalism of classical mechanics. The *Hamiltonian density*  $\mathcal{H}$  is defined via the Lagrangian density  $\mathcal{L}$  [26],

$$\mathcal{H}[\phi_i, \partial_j \phi_i, \pi_i] = \pi_i \partial_0 \phi_i - \mathcal{L}, \quad (2.20)$$

where the *conjugate momentum density*  $\pi_i$  of the field quantity  $\phi_i$  is given by

$$\pi_i = \frac{\partial \mathcal{L}}{\partial(\partial_0 \phi_i)}. \quad (2.21)$$

The time evolution of the system is then obtained from the *Hamiltonian equations of motion*,

$$\partial_0 \phi_i = \frac{\delta \mathcal{H}}{\delta \pi_i}, \quad \partial_0 \pi_i = -\frac{\delta \mathcal{H}}{\delta \phi_i}, \quad (2.22)$$

where the functional derivative is defined as [26, 27]

$$\frac{\delta}{\delta \psi} \equiv \frac{\partial}{\partial \psi} - \partial_\mu \frac{\partial}{\partial(\partial_\mu \psi)}. \quad (2.23)$$

Regarding the dependencies of the Hamiltonian density (2.20), the Hamiltonian equations of motion reduce to

$$\partial_0 \phi_i = \frac{\partial \mathcal{H}}{\partial \pi_i}, \quad (2.24a)$$

$$\partial_0 \pi_i = -\frac{\partial \mathcal{H}}{\partial \phi_i} + \partial_j \left( \frac{\partial \mathcal{H}}{\partial(\partial_j \phi)} \right). \quad (2.24b)$$

In this work we will mostly apply the so-called *temporal gauge*,

$$A_0 = 0, \quad (2.25)$$

which, in particular, transforms the 0th component of the covariant derivative,  $D_0$ , into an ordinary derivative,  $\partial_0$ . Consequently, for the fermionic Lagrangian density (2.4), with  $\phi \equiv \psi_f$ , we get the conjugate momenta

$$\pi_f = \frac{\partial \mathcal{L}_F}{\partial(\partial_0 \psi_f)} = \frac{\partial}{\partial(\partial_0 \psi_f)} \sum_g \mathbf{i} \bar{\psi}_g \gamma^0 (\partial_0 \psi_g) = \mathbf{i} \bar{\psi}_f \gamma^0 \equiv \mathbf{i} \psi_f^\dagger, \quad (2.26)$$

yielding the fermionic Hamiltonian density

$$\mathcal{H}_F = \sum_f \left( m_f \bar{\psi}_f \psi_f - i \bar{\psi}_f \gamma^i D_i \psi_f \right). \quad (2.27)$$

The Hamilton equations of motion (2.24) are then leading to the following partial differential equation, which determines the time evolution of the fermionic degrees of freedom,

$$\partial_t \psi_f = -i \frac{\partial \mathcal{H}}{\partial \psi_f^\dagger}. \quad (2.28)$$

In the following two subsections we will construct the gluonic Hamiltonian density belonging to the Yang-Mills Lagrangian density (2.10) both in Minkowski spacetime and in comoving coordinates.

### 2.2.1 Minkowski spacetime

We identify the  $z$ -direction as our beam direction and use

$$x = (x^0, x^1, x^2, x^3) \equiv (t, x^1, x^2, z) \quad (2.29)$$

for the 4-dimensional spacetime vector. We will work with the *time favored* Minkowski metric,

$$(g^{\mu\nu}) \equiv (\eta^{\mu\nu}) = \text{diag}(1, -1, -1, -1), \quad (2.30a)$$

$$\det[(\eta_{\mu\nu})] = \det[(\eta^{\mu\nu})] = -1, \quad (2.30b)$$

which, together with (2.10), leads to

$$S = -\frac{1}{2} \int d^4x \text{Tr} [F_{\mu\nu} F^{\mu\nu}] = -\frac{1}{4} \int d^4x F_{\mu\nu}^a F^{\mu\nu,a}, \quad (2.31)$$

where we can read off the Lagrangian density,

$$\mathcal{L} = -\frac{1}{2} \text{Tr} [F_{\mu\nu} F^{\mu\nu}] = \text{Tr} [F_{0i}^2 - \sum_{i<j} F_{ij}^2]. \quad (2.32)$$

In the last step we used the following expression:

$$\begin{aligned} F_{\mu\nu} F^{\mu\nu} &= F_{\mu\nu} g^{\mu\alpha} g^{\nu\beta} F_{\alpha\beta} \\ &= -2 \left[ F_{01}^2 + F_{02}^2 + F_{03}^2 - F_{12}^2 - F_{13}^2 - F_{23}^2 \right] \\ &= -2 \left[ F_{0i}^2 - \sum_{i<j} F_{ij}^2 \right]. \end{aligned} \quad (2.33)$$

To derive the Hamiltonian density we have to construct the conjugate momenta,

$$\begin{aligned} E_i^a &= \frac{\partial \mathcal{L}}{\partial (\partial_t A_i^a)} = \frac{\partial}{\partial (\partial_t A_i^a)} \text{Tr} [(\partial_t A_j^b) T^b (\partial_t A_j^c) T^c] \\ &= \frac{\partial}{\partial (\partial_t A_i^a)} \frac{1}{2} (\partial_t A_j^b)^2 = \partial_t A_i^a = F_{0i}^a, \end{aligned} \quad (2.34)$$



where we used the temporal gauge (2.25) to obtain the last equality.

In classical electrodynamics the expression for the electric field  $\vec{E}$  in terms of the magnetic vector potential  $\vec{A}$  and the electric potential  $\Phi$  is given by

$$\vec{E} = -\nabla\Phi - \partial_t\vec{A}. \quad (2.35)$$

In temporal gauge, this reduces to

$$A_t = 0 \Rightarrow \Phi = 0 \Rightarrow \vec{E} = -\partial_t\vec{A} \Rightarrow E^i = -\partial_t A^i, \quad (2.36)$$

which at first glance is inconsistent with (2.34) due to the additional minus sign. However, in a covariant formulation the index “ $i$ ” of the vector potential  $A$  is a *Lorentz* index while the index “ $i$ ” of the electric field  $E$  is just the ordinary three-dimensional *component* index, i.e.,

$$E^i \equiv E_i, \quad A^i = -A_i \quad (2.37)$$

$$\Rightarrow E_i = \partial_t A_i, \quad (2.38)$$

which is in accordance with (2.34).

Using (2.34), we can now rewrite the Lagrangian density in terms of the conjugate momenta  $E_i^a$  and construct the Hamiltonian density,

$$\begin{aligned} \mathcal{H} &= E_i^a \partial_t A_i^a - \mathcal{L} \\ &= 2 \operatorname{Tr} [E_i^2] - \operatorname{Tr} \left[ E_i^2 - \sum_{i<j} F_{ij}^2 \right] \\ &= \operatorname{Tr} \left[ E_i^2 + \sum_{i<j} F_{ij}^2 \right]. \end{aligned} \quad (2.39)$$

The Hamiltonian equations of motion (2.22) then lead to the time evolution of the field quantities,

$$\partial_t E_i(x) = -D_j F^{ji}(x), \quad (2.40a)$$

$$\partial_t A_i(x) = E_i(x). \quad (2.40b)$$

These are directly related to the well-known *Ampère’s circuital law* and *Faraday’s law of induction* with the identification of the magnetic field

$$B_i = -\frac{1}{2} \epsilon_{ijk} F^{jk}, \quad (2.41)$$

where  $\epsilon_{ijk}$  is 3-dimensional *Levi-Civita symbol* (cf. (A.9) of Appendix A.4).

### 2.2.2 Comoving coordinates

The comoving coordinates,

$$x = (\tau, x^1, x^2, \eta), \quad (2.42)$$

use the longitudinal rapidity coordinate  $\eta$  as well as the longitudinal proper time  $\tau$ , which are defined as

$$\tau = \sqrt{t^2 - z^2}, \quad \eta = \operatorname{atanh}\left(\frac{z}{t}\right). \quad (2.43)$$

Hence, the metric takes the following form:

$$g_{\mu\nu} = \frac{\partial x'^{\alpha}}{\partial x^{\mu}} \eta_{\alpha\beta} \frac{\partial x'^{\beta}}{\partial x^{\nu}} \Rightarrow (g_{\mu\nu}) = \operatorname{diag}(1, -1, -1, -\tau^2), \quad (2.44a)$$

$$g^{\mu\alpha} g_{\alpha\nu} = \delta_{\nu}^{\mu} \Rightarrow (g^{\mu\nu}) = \operatorname{diag}(1, -1, -1, -\tau^{-2}), \quad (2.44b)$$

$$\det[(g_{\mu\nu})] = \det[(g^{\mu\nu})]^{-1} = -\tau^2. \quad (2.44c)$$

Whenever we work in comoving coordinates, we will use a different index notation than we use when working in Minkowski spacetime.<sup>2</sup> This means, e.g., for an object  $\Omega$ , with components  $\Omega_{\mu}$  ( $\mu = 0, 1, 2, 3$ ) we will use:

$$\begin{aligned} \Omega_0 &\rightarrow \Omega_{\tau} \\ \left. \begin{array}{l} \Omega_1 \\ \Omega_2 \end{array} \right\} &\rightarrow \Omega_i, \text{ with } i = 1, 2 \\ \Omega_3 &\rightarrow \Omega_{\eta} \end{aligned} \quad (2.45)$$

Hence, Latin indices do only represent the transverse plane and do never include the  $\eta$ -component. Greek indices ( $\tau$  and  $\eta$  excluded) still designate all four spacetime components.

In order to construct the Hamiltonian density, we start again with the general definition of the action (2.10) and insert (2.44). We obtain

$$S = \int d\tau dx_{\perp} d\eta \tau \operatorname{Tr} \left[ F_{\tau i}^2 + \frac{F_{\tau\eta}^2}{\tau^2} - F_{12}^2 - \frac{F_{i\eta}^2}{\tau^2} \right] \equiv \int d\tau dx_{\perp} d\eta \mathcal{L}, \quad (2.46)$$

with the Lagrangian density being

$$\mathcal{L} = \operatorname{Tr} \left[ \tau F_{\tau i}^2 + \frac{F_{\tau\eta}^2}{\tau} - \tau F_{12}^2 - \frac{F_{i\eta}^2}{\tau} \right]. \quad (2.47)$$

In (2.46) we used

$$\begin{aligned} F_{\mu\nu} F^{\mu\nu} &= F_{\mu\nu} g^{\mu\alpha} g^{\nu\beta} F_{\alpha\beta} = 2 \left[ F_{\tau 1} g^{\tau\tau} g^{11} F_{\tau 1} + F_{\tau 2} g^{\tau\tau} g^{22} F_{\tau 2} + F_{\tau\eta} g^{\tau\tau} g^{\eta\eta} F_{\tau\eta} \right. \\ &\quad \left. + F_{12} g^{11} g^{22} F_{12} + F_{1\eta} g^{11} g^{\eta\eta} F_{1\eta} + F_{2\eta} g^{22} g^{\eta\eta} F_{2\eta} \right] \\ &= -2 \left[ F_{\tau 1}^2 + F_{\tau 2}^2 + \frac{F_{\tau\eta}^2}{\tau^2} - F_{12}^2 - \frac{F_{1\eta}^2}{\tau^2} - \frac{F_{2\eta}^2}{\tau^2} \right] \\ &= -2 \left[ F_{\tau i}^2 + \frac{F_{\tau\eta}^2}{\tau^2} - F_{12}^2 - \frac{F_{i\eta}^2}{\tau^2} \right]. \end{aligned} \quad (2.48)$$

<sup>2</sup>In Minkowski spacetime, Greek indices represent all indices of a 4-vector and run from 0 to 3, while Latin indices indicate the spacial part and hence run from 1 to 3.

Note that we included the  $\tau$  factor into the Lagrangian density (2.47), which is coming from the square root of the negative determinant of  $(g_{\mu\nu})$ . As a consequence, the Lagrangian density as well as the Hamiltonian density, which usually have energy dimension 4, will now have the energy dimension 3.

However, this is a convenient choice, since a variation of the action should lead to the same equations of motion as obtained within the Hamiltonian formalism and in the former case one would obviously have to consider the additional  $\tau$  factor.

The conjugate momenta are then given by

$$\begin{aligned} E_i^a &= \frac{\partial \mathcal{L}}{\partial(\partial_\tau A_i^a)} = \frac{\partial}{\partial(\partial_\tau A_i^a)} \tau \text{Tr} [(\partial_\tau A_j^b) T^b (\partial_\tau A_j^c) T^c] \\ &= \frac{\partial}{\partial(\partial_\tau A_j^a)} \frac{\tau}{2} (\partial_\tau A_i^b)^2 = \tau \partial_\tau A_i^a = \tau F_{\tau i}^a, \end{aligned} \quad (2.49a)$$

$$\begin{aligned} E_\eta^a &= \frac{\partial \mathcal{L}}{\partial(\partial_\tau A_\eta^a)} = \frac{\partial}{\partial(\partial_\tau A_\eta^a)} \frac{1}{\tau} \text{Tr} [(\partial_\tau A_\eta^b) T^b (\partial_\tau A_\eta^c) T^c] \\ &= \frac{\partial}{\partial(\partial_\tau A_\eta^a)} \frac{1}{2\tau} (\partial_\tau A_\eta^b)^2 = \frac{1}{\tau} \partial_\tau A_\eta^a = \frac{1}{\tau} F_{\tau\eta}^a. \end{aligned} \quad (2.49b)$$

To get the respective last equalities, we used the temporal gauge (2.25) in comoving coordinates,  $A_\tau = 0$ , which is sometimes referred to as *Fock-Schwinger gauge*.

With the Lagrangian density (2.47) and the conjugate momenta (2.49), we are able to construct the Hamiltonian density in comoving coordinates,

$$\begin{aligned} \mathcal{H} &= E_i^a \partial_\tau A_i^a + E_\eta^b \partial_\tau A_\eta^b - \mathcal{L} \\ &= 2 \text{Tr} \left[ \frac{E_i^2}{\tau} + \tau E_\eta^2 \right] - \text{Tr} \left[ \frac{E_i^2}{\tau} + \tau E_\eta^2 - \tau F_{12}^2 - \frac{F_{i\eta}^2}{\tau} \right] \\ &= \text{Tr} \left[ \frac{E_i^2}{\tau} + \tau E_\eta^2 + \tau F_{12}^2 + \frac{F_{i\eta}^2}{\tau} \right]. \end{aligned} \quad (2.50)$$

Applying the Hamiltonian equations of motion (2.22) finally leads to the counterparts of (2.40) [28],

$$\partial_\tau E_i = \tau D_j F^{ji} + \frac{1}{\tau} D_\eta F^{\eta i}, \quad \partial_\tau E_\eta = \tau D_j F^{j\eta}, \quad (2.51a)$$

$$\partial_\tau A_i = \frac{1}{\tau} E_i, \quad \partial_\tau A_\eta = \tau E_\eta. \quad (2.51b)$$

## 2.3 From Heisenberg's to Hamilton's equations of motion

This section is meant to motivate the classical description of quantum theories by deriving the equivalence of *Heisenberg's equations of motions* and the classical Hamiltonian equations of motion (2.22) on an operator level.

In the Heisenberg picture of a bosonic quantum field theory the field operators  $\{\hat{\phi}_i(x)\}$  and their conjugate momentum operators  $\{\hat{\pi}_i(x)\}$ ,  $i \in \{1, \dots, n\}$ , satisfy the commutation

relation

$$[\hat{\phi}_i(x), \hat{\pi}_j(x)] = i\delta_{ij}\delta(x-y). \quad (2.52)$$

The corresponding Hamilton operator can be expressed in terms of  $\hat{\phi}$  and  $\hat{\pi}$  as

$$\hat{H} = \sum_{n,m} a_{nm} \hat{\phi}^n \hat{\pi}^m + \text{permutations}(\hat{\phi}, \hat{\pi}). \quad (2.53)$$

The Heisenberg equations of motions for an operator  $\hat{A}$  read

$$\frac{d}{dt}\hat{A}_i(x) = i[\hat{H}, \hat{A}_i(x)] + \frac{\partial A}{\partial t} \quad (2.54)$$

and hence also determine the time evolution of the field and momentum operators, respectively,

$$\frac{d}{dt}\hat{\phi}_i(x) = i[\hat{H}, \hat{\phi}_i(x)], \quad (2.55a)$$

$$\frac{d}{dt}\hat{\pi}_i(x) = i[\hat{H}, \hat{\pi}_i(x)], \quad (2.55b)$$

where we supposed that  $\hat{\phi}$  and  $\hat{\pi}$  have no explicit time dependence.<sup>3</sup>

We will now try to relate the commutators appearing in (2.55) to functional derivatives of the Hamilton operator (2.53). One can easily show by mathematical induction, that

$$i[\hat{\pi}_j^n(y), \hat{\phi}_i(x)] = n\hat{\pi}_j^{n-1}(y)\delta_{ij}\delta(x-y) = \frac{\delta\hat{\pi}_j^n(y)}{\delta\hat{\pi}_i(x)}, \quad (2.56)$$

which can be extended with some algebra to

$$i[\hat{\pi}_j^k(x)\hat{\phi}_j^l(x)\hat{\pi}_j^m(x), \hat{\phi}_i(y)] = \frac{\delta}{\delta\hat{\pi}_i(y)}\hat{\pi}_j^k(x)\hat{\phi}_j^l(x)\hat{\pi}_j^m(x). \quad (2.57)$$

Iterating this (cf. Appendix D.2) finally yields

$$i[\hat{H}, \hat{\phi}_i(x)] = \frac{\delta\hat{H}}{\delta\hat{\phi}_i(x)}. \quad (2.58)$$

The same analysis can be done for  $[\cdot, \hat{\pi}]$  yielding an additional minus sign due to one extra commutation,

$$i[\hat{H}, \hat{\pi}_i(x)] = -\frac{\delta\hat{H}}{\delta\hat{\phi}_i(x)}. \quad (2.59)$$

Putting all together, we end up with

$$\begin{aligned} \frac{d}{dt}\hat{\phi}_i(x) &= i[\hat{H}, \hat{\phi}_i(x)] = \frac{\delta\hat{H}}{\delta\hat{\pi}_i(x)}, \\ \frac{d}{dt}\hat{\pi}_i(x) &= i[\hat{H}, \hat{\pi}_i(x)] = -\frac{\delta\hat{H}}{\delta\hat{\phi}_i(x)}. \end{aligned}$$

---

<sup>3</sup>This is a convenient assumption, since otherwise also the Hamiltonian (2.53) would be explicitly time dependent resulting in a violation of energy conservation.

This means that – on an operator level – the Heisenberg equations of motion for the field and momentum operators become the “classical” Hamiltonian equations of motion (2.22).

A more rigorous motivation of the classical approximation based on the *path integral formulation* of quantum field theory will be discussed in the following section.

## 2.4 Classical aspects of quantum field theory out of equilibrium

The time evolution of a given initial state in modern quantum field theory can be described by two fundamentally related concepts: The first one being the *Hamilton operator formalism*, which is perhaps slightly more intuitive, since it is familiar from quantum mechanics, and the second one, the so-called *Schwinger-Keldysh formalism* [29, 30], which is based on a real-time path integral formulation and discussed in Section 2.4.1.

The central quantity in a general quantum theory, defined by a Hamiltonian operator  $\hat{H}$ , is the *density operator*  $\hat{\rho}$ . It includes all information about physical observables  $\mathcal{O}$ , whose expectation values are defined by

$$\langle \mathcal{O} \rangle = \text{Tr} [\hat{\rho} \mathcal{O}]. \quad (2.60)$$

In the Schrödinger picture, the time evolution of  $\hat{\rho}$  is given by the *von Neumann equation*,

$$\partial_t \hat{\rho} = -i[\hat{H}, \hat{\rho}]. \quad (2.61)$$

It is the quantum analogue of the *Liouville equation* in classical-statistical mechanics,

$$\partial_t \rho = \{H, \rho\}_{\text{PB}}, \quad (2.62)$$

where in this case  $\rho$  is the phase space distribution function and  $H$  the system’s (classical) Hamiltonian. A definition of the Poisson bracket  $\{\cdot, \cdot\}_{\text{PB}}$  can be found in Appendix A.3.

Different than in the case of quantum mechanics, we have (infinitely) many degrees of freedom in quantum field theory and thus (2.61) becomes unsuitable. A more appropriate way to study (non-equilibrium) quantum field theory can be achieved through formalisms based on path integrals, such as the Schwinger-Keldysh formalism, which we deal with in following subsection.

### 2.4.1 Schwinger-Keldysh formalism

Starting point is the initial value problem of the von Neumann equation (2.61), which we want to rephrase within the scope of the path integral formalism. In a quantum field theory the generalization of the partition function, the so-called *generating functional*, contains all quantum field-theoretical information and thus entirely determines the described system. For a given initial density matrix  $\rho_0$  in the presence of two sources,  $J$

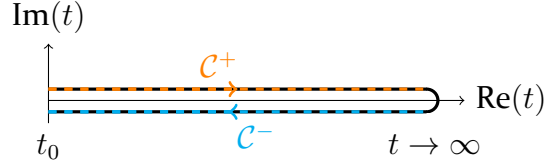


**Figure 2.1:** Closed real-time contour  $\mathcal{C} = \mathcal{C}^+ + \mathcal{C}^-$  (also referred to as *Schwinger-Keldysh contour*). The slight shifts away from the real axis are exclusively done for the purpose of visualization.

and  $R$ , a non-equilibrium generating functional for the Schwinger-Keldysh formulation of real-time path integrals can be expressed as [5, 31–34]

$$\begin{aligned}
 Z[J, R, \rho_0] &= \underbrace{\int dA^{(1)} dA^{(2)} \langle A^{(1)} | \rho_0 | A^{(2)} \rangle}_{\text{initial conditions}} \\
 &\times \underbrace{\int_{A^{(1)}}^{A^{(2)}} \mathcal{D}'A \exp \left[ i \left( S^{\mathcal{C}}[A] + \int_{x, \mathcal{C}} J(x) \cdot A(x) + \frac{1}{2} \int_{x, \mathcal{C}} \int_{y, \mathcal{C}} A(x) R(x, y) A(y) \right) \right]}_{\text{(nonequilibrium) dynamics}}.
 \end{aligned} \tag{2.63}$$

To give a clearer overview, we omitted color and Lorentz indices, i.e. the dot product as well as the matrix product are both performed in Lorentz space and in color space, yielding  $J \cdot A \equiv J_a^\mu A_\mu^a$  and  $ARA \equiv A_\mu^a R_{ab}^{\mu\nu} A_\nu^b$ . We also defined  $\int_{x, \mathcal{C}} \equiv \int_{\mathcal{C}} dx^0 \int d^d x$ , where  $\mathcal{C}$  is the closed real-time contour depicted in Figure 2.1. The prime on the functional measure of the gauge fields  $\mathcal{D}'A$  indicates, firstly, an extent along this contour and, secondly, that the integration over the fields at  $t_0$  are excluded. The Lagrangian density defining the contour action  $S^{\mathcal{C}} \equiv \int_{x, \mathcal{C}} \mathcal{L}$  is for instance in the case of pure Yang-Mills theory given by (2.32) or (2.47).

The path integral equivalent of the expectation value definition in (2.60) for a given generating functional  $Z$  reads

$$\langle \mathcal{O} \rangle = \frac{1}{Z} Z\{\mathcal{O}\} \Big|_{J, R=0}, \tag{2.64}$$

where  $Z\{\mathcal{O}\}$  is, e.g., defined via (2.63), with an insertion of the operator  $\mathcal{O}$  in front of the exponential, i.e.  $Z\{\mathcal{O}\} \equiv (\dots) \int \mathcal{D}'A \mathcal{O} \exp(\dots)$ .

In analogy to equilibrium or vacuum quantum field theory, the non-equilibrium generating functional for connected correlation functions, also known as the *Schwinger functional*, is defined by

$$W = -i \log Z. \tag{2.65}$$

The functional derivatives with respect to the linear source term  $J$  then equals the field expectation value,

$$\frac{\delta W}{\delta J_\mu^a(x)} \Big|_{J, R=0} = -\frac{i}{Z} \frac{\delta Z}{\delta J_\mu^a(x)} \Big|_{J, R=0} = \frac{1}{Z} Z\{A_\mu^a(x)\} \Big|_{J, R=0} \equiv \langle A_\mu^a(x) \rangle. \tag{2.66}$$

Equivalently, we can compute the functional derivative with respect to the bilinear source term  $R$ , yielding

$$\left. \frac{\delta W}{\delta R_{\mu\nu}^{ab}(x, y)} \right|_{J, R=0} = \frac{1}{2} \langle \mathcal{T}_C A_\mu^a(x) A_\nu^b(y) \rangle, \quad (2.67)$$

where  $\mathcal{T}_C$  signifies the time ordering along the Schwinger-Keldysh contour.

We can now define the *connected two-point function*,

$$G_{\mu\nu}^{ab}(x, y) := \langle \mathcal{T}_C A_\mu^a(x) A_\nu^b(y) \rangle - \langle A_\mu^a(x) \rangle \langle A_\nu^b(y) \rangle, \quad (2.68)$$

which can of course also be expressed in terms of the functional derivatives of  $W$  via (2.66) and (2.67). It can be decomposed into its symmetric and anti-symmetric parts, defining the *statistical propagator*,

$$F_{\mu\nu}^{ab}(x, y) := \frac{1}{2} \langle \{A_\mu^a(x), A_\nu^b(y)\} \rangle - \langle A_\mu^a(x) \rangle \langle A_\nu^b(y) \rangle \equiv \frac{1}{2} [G_{\mu\nu}^{ab}(x, y) + G_{\nu\mu}^{ba}(y, x)], \quad (2.69)$$

and the *spectral function*,

$$\rho_{\mu\nu}^{ab}(x, y) := i \langle [A_\mu^a(x), A_\nu^b(y)] \rangle \equiv i \text{sign}_C(x^0 - y^0) [G_{\mu\nu}^{ab}(x, y) - G_{\nu\mu}^{ba}(y, x)], \quad (2.70)$$

respectively. The index at the sign function introduced in the last equation has to be understood again in such a way that all times on the lower branch  $\mathcal{C}^-$  are considered later than those on the upper one  $\mathcal{C}^+$ .

Both  $F$  and  $\rho$  have important physical interpretations: The statistical propagator contains information about occupation numbers while the spectral function comprises the spectrum of the theory. In other words,  $F$  and  $\rho$  provide information about what states are available and how frequent these states are occupied [31]. Hence, it is convenient to express the connected two-point function in the following way:

$$G_{\mu\nu}^{ab}(x, y) = F_{\mu\nu}^{ab}(x, y) - \frac{i}{2} \text{sign}_C(x^0 - y^0) \rho_{\mu\nu}^{ab}(x, y). \quad (2.71)$$

In the following subsection we will show the similarity of the Schwinger-Keldysh formalism and a classical-statistical description. In particular, we will end up with a criterion for the applicability of the classical approximation.

## 2.4.2 Classicity condition

We start with the generating functional (2.63), where we express the contour action  $S^C$  in terms of new field variables,  $A^+$  and  $A^-$ , which are exclusively defined on the time branch  $\mathcal{C}^+$  and  $\mathcal{C}^-$ , respectively,

$$S^C[A^+, A^-] = S[A^+] - S[A^-] =: S[A_{\text{cl}} + \tilde{A}/2] - S[A_{\text{cl}} - \tilde{A}/2], \quad (2.72)$$

where  $S[\cdot]$  is defined as the integral of the Lagrangian  $L = \int d^3x \mathcal{L}$  along the ordinary time axis. Furthermore, we defined the average,  $A_{\text{cl}} := \frac{1}{2}(A^+ + A^-)$ , and the difference,  $\tilde{A} := A^+ - A^-$ , of the branch fields  $A^\pm$ .

Expressing the classical action  $S[A_{\text{cl}} \pm \tilde{A}/2]$  in terms of a functional Taylor expansion around  $A_{\text{cl}}$  yields

$$S[A_{\text{cl}} \pm \tilde{A}/2] = \sum_{n=0}^N \frac{(\pm 1)^n}{n!} \int d^4x_1 \dots d^4x_n \frac{\delta^{(n)} S[A]}{\delta A_{\mu_1}^{a_1}(x_1) \dots A_{\mu_n}^{a_n}(x_n)} \Big|_{A=A_{\text{cl}}} \frac{\tilde{A}_{\mu_1}^{a_1}(x_1) \dots \tilde{A}_{\mu_n}^{a_n}(x_n)}{2^n}. \quad (2.73)$$

Hence, (2.72) only contains odd powers of  $\tilde{A}$  and since usually  $N \leq 3$ , the contour action becomes

$$\begin{aligned} S^c[A_{\text{cl}}, \tilde{A}] &= \underbrace{\int d^4x_1 \frac{\delta S[A]}{\delta A_{\mu_1}^{a_1}(x_1)} \Big|_{A=A_{\text{cl}}} \tilde{A}_{\mu_1}^{a_1}(x_1)}_{\text{classical part}} \\ &+ \underbrace{\frac{1}{24} \int d^4x_1 d^4x_2 d^4x_3 \frac{\delta^{(3)} S[A]}{\delta A_{\mu_1}^{a_1}(x_1) A_{\mu_2}^{a_2}(x_2) A_{\mu_3}^{a_3}(x_3)} \Big|_{A=A_{\text{cl}}} \tilde{A}_{\mu_1}^{a_1}(x_1) \tilde{A}_{\mu_2}^{a_2}(x_2) \tilde{A}_{\mu_3}^{a_3}(x_3)}_{\text{quantum dynamics}}. \end{aligned} \quad (2.74)$$

Since  $\tilde{A}$  only enters linearly in the first term it can be integrated out and we obtain in the absence of sources [35–37]:

$$\int \mathcal{D}\tilde{A} \exp \left[ i \int d^4x \frac{\delta S[A]}{\delta A_\mu^a} \Big|_{A=A_{\text{cl}}} \tilde{A}_\mu^a(x) \right] = \delta \left[ \frac{\delta S[A]}{\delta A_\mu^a} \Big|_{A=A_{\text{cl}}} \right]. \quad (2.75)$$

The delta distribution introduced in the last step entails the least action principle leading to the classical equations of motion for the  $A_{\text{cl}}$  fields [38] and thus explains the declaration in (2.74).

In order to end up with a physically useful criterion that states in which regime the classical description is accurate, we have to look at the connected two-point correlation functions, which are given by [37–39]:

$$\langle \mathcal{T}_c A_{\text{cl},\mu}^a(x) A_{\text{cl},\nu}^b(y) \rangle = F_{\mu\nu}^{ab}(x, y) + \langle A_{\text{cl},\mu}^a(x) \rangle \langle A_{\text{cl},\nu}^b(y) \rangle \quad (2.76a)$$

$$\langle \mathcal{T}_c A_{\text{cl},\mu}^a(x) \tilde{A}_\nu^b(y) \rangle = -G_{\mu\nu}^{(A),ab}(x, y) \quad (2.76b)$$

$$\langle \mathcal{T}_c \tilde{A}_\mu^a(x) A_{\text{cl},\nu}^b(y) \rangle = -G_{\mu\nu}^{(R),ab}(x, y) \quad (2.76c)$$

$$\langle \mathcal{T}_c \tilde{A}_\mu^a(x) \tilde{A}_\nu^b(y) \rangle = 0 \quad (2.76d)$$

We introduced the advanced  $G^{(A)}$  and retarded  $G^{(R)}$  correlators, which are related to the spectral function,<sup>4</sup>

$$\rho_{\mu\nu}^{ab}(x, y) = G_{\mu\nu}^{(R),ab}(x, y) - G_{\mu\nu}^{(A),ab}(x, y). \quad (2.77)$$

<sup>4</sup>A formal definition of the correlation functions  $G^{(A)}$  and  $G^{(R)}$  is not relevant for our purposes and hence we refer the interested reader to the literature instead (cf., e.g., [31, 33, 34, 37–39]).



The crucial point here is the fact that the quantum-like correlation functions containing the auxiliary field  $\tilde{A}$  are proportional to the spectral function  $\rho$ , while the classical correlator is related to the statistical propagator  $F$ .

This observation has been elaborated further in [39, 40], ultimately resulting in the definition of the so-called *classicality condition*,

$$|F_{\mu\nu}^{ab}(x, y)F_{\alpha\beta}^{cd}(z, w)| \gg \frac{3}{4} |\rho_{\mu\nu}^{ab}(x, y)\rho_{\alpha\beta}^{cd}(z, w)|, \quad (2.78)$$

which is not based on any equilibrium assumptions and therefore a valid criterion for the non-equilibrium dynamics we are interested in. However, it naturally holds in equilibrium as well, where a more intuitive illustration in terms of an occupation number density  $n(\vec{p}, t)$  is possible. E.g., for a free field theory<sup>5</sup>, (2.78) translates to

$$\left[ n(\vec{p}, t) + \frac{1}{2} \right]^2 \gg \frac{3}{4}, \quad (2.79)$$

which means that the system behaves classical as long as the number of field quanta in the different modes is sufficiently large. This statement can also be derived for non-equilibrium descriptions whenever an appropriate occupation number (density) can be defined [37]. Hence, it is the key motivation for our classical-statistical description.

---

<sup>5</sup>Following for instance [31], where a time average of  $F^{(\text{free})}(x^0, y^0, \vec{p}) = \frac{1}{\omega(\vec{p})} [n(\vec{p}) + \frac{1}{2}] \cos [\omega(\vec{p})(x^0 - y^0)]$  and  $\rho^{(\text{free})}(x^0, y^0, \vec{p}) = \frac{1}{\omega(\vec{p})} \sin [\omega(\vec{p})(x^0 - y^0)]$  is used, with some mode frequency  $\omega(\vec{p})$ , which is – due to cancellation – irrelevant for the derivation of the classicality condition.



# Chapter 3

## Semiclassical lattice gauge theory

---

### Contents

3.1	Euclidean path integrals . . . . .	21
3.2	Fermions on a Minkowski lattice . . . . .	22
3.3	Stochastic fermion implementation . . . . .	27
3.4	Gluonic lattice Hamiltonian density . . . . .	31
3.5	Lattice equations of motion . . . . .	34
3.6	Gauss's law . . . . .	38
3.7	Real-time static potential . . . . .	42
3.8	Computation of classical-statistical observables . . . . .	44

---

### 3.1 Euclidean path integrals

In Section 2.4.1 we introduced the path integral formalism and its importance regarding the computation of expectation values of physical observables. However, analytically solving infinite dimensional path integrals is generally not possible. One way to circumvent this issue is a reformulation of the path integrals in *Euclidean space* yielding the opportunity for a numerical evaluation by means of so-called *Monte-Carlo methods*. In the following, we will summarize the basic concepts of the Euclidean path integral formulation and will end up with a description in terms of lattice gauge theory.

In thermal equilibrium, the expectation value of an observable  $\mathcal{O}$  for a given action  $S$  reads (cf. (2.64))

$$\langle \mathcal{O} \rangle = \frac{\int \mathcal{D}A \mathcal{D}\psi \mathcal{D}\bar{\psi} \mathcal{O} e^{iS[A, \psi, \bar{\psi}]}}{\int \mathcal{D}A \mathcal{D}\psi \mathcal{D}\bar{\psi} e^{iS[A, \psi, \bar{\psi}]}} \equiv \frac{Z\{\mathcal{O}\}}{Z}, \quad (3.1)$$

with the generating functional  $Z$ .

Although a discretization of (3.1) is yielding an ordinary multidimensional integral, the convergence of a numerical computation cannot be guaranteed due to the highly oscillating integrand. A possible way to bypass this problem is to employ a so-called *Wick rotation* and perform an analytic continuation of the corresponding quantities. In particular, one applies a Wick rotation to the time coordinate,

$$t \equiv x^0 \rightarrow -ix^4 \equiv t_E, \quad (3.2)$$

with the Euclidean metric

$$g_E^{\mu\nu} = \delta^{\mu\nu} \quad (3.3)$$

yielding for the 4-vector product

$$x^2 = (x^0)^2 - \vec{x}^2 \rightarrow -(x^4)^2 - \vec{x}^2 = -x_E^2. \quad (3.4)$$

Note that  $t_E$  is only a mathematical parameter and can no longer be interpreted as the physical time.

The Wick-rotated version of the generating functional defined in (3.1) becomes<sup>1</sup>

$$Z_E = \int \mathcal{D}A \mathcal{D}\psi \mathcal{D}\bar{\psi} e^{-S_E[A, \psi, \bar{\psi}]}. \quad (3.5)$$

The essential difference compared to (3.1), is the real and positive weight  $e^{-S_E}$  in the Euclidean version. It exponentially suppresses field configurations with respect to the minima of the Euclidean action  $S_E$ . After a discretization of the four-dimensional Euclidean spacetime, it hence allows for a numerical evaluation with importance sampling methods via stochastic integration techniques referred to as *Monte-Carlo algorithms*. These studies have achieved major successes, especially in describing static observables such as, e.g., hadron masses.

However, due to the Wick rotation we are not able to compute the time evolution of observables or isotropization times, but which is the goal of our study. From now on, we will therefore use the *Minkowski lattice formulation* instead. The first step will be the introduction of fermions, which is the topic of the subsequent section.

## 3.2 Fermions on a Minkowski lattice

Discretizing the fermionic Lagrangian density (2.4) in a straightforward way, i.e. using the symmetric discretized derivative (cf. Appendix B.1),

$$\partial_\mu \psi(x) = \frac{1}{2a} [\psi(x + \hat{\mu}) - \psi(x - \hat{\mu})], \quad (3.6)$$

---

<sup>1</sup>The Euclidean action and further information can be found in Appendix B.3.

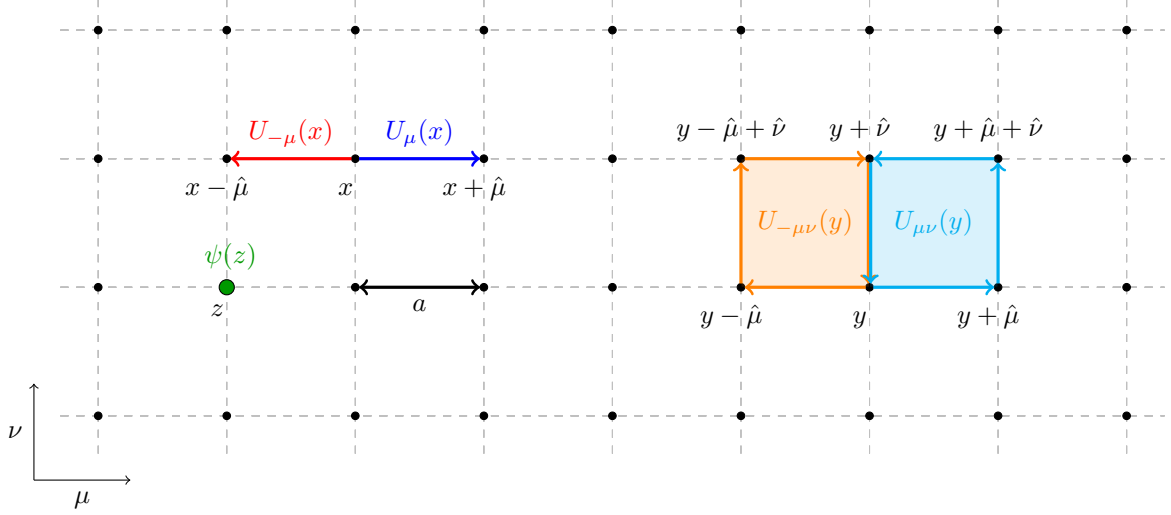


**Figure 3.1:** Illustration of the lattice gauge fields  $U_{\pm\mu}$ , the two plaquettes  $U_{\mu\nu}$  and  $U_{-\mu\nu}$ , as well as the fermionic field  $\psi$  for the lattice spacing  $a$ .

yields

$$\mathcal{L}_F^0 = \sum_f \bar{\psi}_f \left( i\gamma^\mu \frac{\psi_f(x + \hat{\mu}) - \psi_f(x - \hat{\mu})}{2a} - m_f \psi_f(x) \right). \quad (3.7)$$

However, different than it is the case for the continuum version (2.4), this naive choice of a Lagrangian density is for finite lattice spacings  $a$  not invariant under local  $SU(N_c)$  gauge transformations, since

$$\bar{\psi}(x)\psi(x \pm \hat{\mu}) \rightarrow \bar{\psi}'(x)\psi'(x \pm \hat{\mu}) = \bar{\psi}(x) \underbrace{\Omega^\dagger(x)\Omega(x \pm \hat{\mu})}_{\neq 1} \psi(x \pm \hat{\mu}), \quad (3.8)$$

with  $\Omega \in SU(N_c)$ .

We therefore have to render our Lagrangian density (3.7) gauge invariant by introducing (*lattice*) *gauge fields*  $U_{\pm\mu}(x)$ , which should also be elements of  $SU(N_c)$ , transform as

$$U_{\pm\mu}(x) \rightarrow U'_{\pm\mu}(x) = \Omega(x)U_{\pm\mu}(x)\Omega^\dagger(x \pm \hat{\mu}), \quad (3.9)$$

and which should disappear in the naive continuum limit,  $a \rightarrow 0$ .

We can then easily construct gauge invariant objects such as, in particular,

$$\bar{\psi}(x)U_{\pm\mu}(x)\psi(x \pm \hat{\mu}). \quad (3.10)$$

The gauge fields  $U_{\pm\mu}(x)$  connect the two lattice points  $x$  and  $x \pm \hat{\mu}$  (cf. left-hand side of Figure 3.1), which is why they are often referred to as (*gauge*) *link variables*.

Recalling the transformation property of the continuum gauge fields  $A_\mu(x)$ ,

$$A_\mu(x) \rightarrow A'_\mu(x) = \Omega(x)A_\mu(x)\Omega^\dagger(x) + ig(\partial_\mu\Omega(x))\Omega^\dagger(x) \quad (3.11)$$

we obtain that the so-called *gauge transporter*,

$$G(x, y) = P \exp \left[ ig \int_{\mathcal{C}_{xy}} dz_\mu A_\mu(z) \right], \quad (3.12)$$

with the curve  $\mathcal{C}_{xy}$  connecting the two spacetime points  $x$  and  $y$ , transforms in the exact same way as the link variables  $U_\mu(x)$ ,

$$G(x, y) \rightarrow G'(x, y) = \Omega(x)G(x, y)\Omega^\dagger(y). \quad (3.13)$$

Hence, if we consider  $x$  and  $x + \hat{\mu}$  as the end points of the curve in (3.12), the identification

$$U_\mu(x) = \exp[igaA_\mu(x)] \quad (3.14)$$

leads to a linear approximation of the continuum gauge transporter. For this reason, the link variables are also often referred to as (*lattice*) *gauge transporters*. Note that the definition for negative  $\mu$ -directions is obtain via<sup>2</sup>

$$U_{-\mu}(x) \equiv [U_\mu(x - \hat{\mu})]^\dagger = \exp[-igaA_\mu(x - \hat{\mu})], \quad (3.15)$$

where we used  $A_\mu^\dagger = A_\mu$ . In order to satisfy  $U_\mu \in \text{SU}(N_c)$ , the gauge fields  $A_\mu$  have to be elements of the associated Lie algebra  $\text{su}(N_c)$ , i.e.  $A_\mu(x) \equiv A_\mu^a(x)T^a$ , as introduced in Section 2.1.

With this knowledge, we are now able to define a *covariant symmetric derivative* on the lattice,

$$\mathcal{D}_\mu \psi(x) := \frac{1}{2a} [U_\mu(x)\psi(x + \hat{\mu}) - U_{-\mu}(x)\psi(x - \hat{\mu})], \quad (3.16)$$

leading us to a gauge invariant Lagrangian density, which is usually referred to as the *naive fermion Lagrangian density*,

$$\mathcal{L}_F^{\text{naive}} = \sum_f \bar{\psi}_f(x) \left( i\gamma^\mu \mathcal{D}_\mu \psi_f(x) - m_f \psi_f(x) \right). \quad (3.17)$$

This choice has the correct continuum limit (cf. (B.5)) and is invariant under local  $\text{SU}(N_c)$  gauge transformations (2.7), nevertheless, it is still labeled “naive”. The reason why this is the case has its origin in the famous *doubling problem*, which we will carry out in the following.

According to (2.4) and (3.17), the naive lattice Dirac operator takes the following form

$$D(x, y) = i\gamma^\mu \frac{U_\mu(x)\delta_{x+\hat{\mu},y} - U_{-\mu}(x)\delta_{x-\hat{\mu},y}}{2a} - m\delta_{xy}, \quad (3.18)$$

<sup>2</sup>We will mostly use the abbreviating notation  $U_\mu^\dagger(x - \hat{\mu}) \equiv [U_\mu(x - \hat{\mu})]^\dagger$ , which should not lead to any confusion since we never treat spacetime arguments as (matrix) indices.

with (3.17) becoming

$$\mathcal{L}_F^{\text{naive}} = \sum_f \bar{\psi}_f(x) D(x, y) \psi_f(y). \quad (3.19)$$

One consequence of Wick's theorem [41] – amongst others – is that the physically meaningful  $n$ -point functions are directly related to the fermion propagator. Furthermore, the latter is up to a prefactor equivalent to the inverse of the Dirac operator and hence it is convenient to take closer look at its lattice representation.

As it is frequently the case, operator inversions are more comfortable in Fourier space, which also applies for the present issue. Performing a Fourier transformation of (3.18) yields  $\tilde{D}(p, q) = \delta(p - q)\tilde{D}(p)$ , where we defined the Dirac operator in momentum space,

$$\tilde{D}(p) = -\frac{1}{a}\gamma^\mu \sin(ap_\mu) - m. \quad (3.20)$$

For simplicity and since the discussion of the doubling problem remains unimpaired, we considered trivial gauge fields, i.e.  $U_\mu = 1$ . In the massless case, the inverse can easily be obtained with the help of (A.14) and we finally end up with the lattice version of the inverse Dirac operator in momentum space,

$$\tilde{D}^{-1}(p)\Big|_{m=0} = -\frac{a\gamma^\mu \sin(ap_\mu)}{\sin(ap^\mu) \sin(ap_\mu)}. \quad (3.21)$$

Obviously, it has the correct naive continuum limit,

$$\tilde{D}^{-1}(p)\Big|_{m=0} \xrightarrow{a \rightarrow 0} -\frac{\gamma^\mu p_\mu}{p^2}, \quad (3.22)$$

and the inverse of the Dirac operator in position space is then obtained by inverting the Fourier transformation.

However, recalling the definition area of the lattice momenta,  $p_\mu \in (-\frac{\pi}{a}, \frac{\pi}{a}]$ , and comparing the lattice expression (3.21) with its continuum limit (3.22), we identify – due to the sine function – additional poles on the lattice located at the edges of the Brillouin zone. These unphysical poles,  $(\frac{\pi}{a}, 0, \dots, 0), \dots, (\frac{\pi}{a}, \dots, \frac{\pi}{a})$ , are called *doublers*, of which there are  $\sum_{i=1}^d \binom{d}{i}$  in  $d$  dimensions, and hence 15 in our four-dimensional Minkowski spacetime.

One way to circumvent the doubling issue is to add a so-called *Wilson term* to the Dirac operator. It is defined in momentum space as

$$-\frac{1}{a} \sum_{\mu} [1 - \cos(ap_\mu)] \quad (3.23)$$

and obviously vanishes at the physical pole  $p_\mu = 0$ . Furthermore, for each component of the momentum being  $\frac{\pi}{a}$  it becomes  $\frac{2}{a}$ , which is acting as an additional mass term for the unphysical doublers. Hence, in the naive continuum limit,  $a \rightarrow 0$ , the doublers become infinitely heavy and decouple from the theory.

A Fourier transformation of (3.23) leads to the Wilson term that we have to add to the naive Lagrangian density (3.17),

$$\frac{a}{2} \bar{\psi} \square_L \psi, \quad (3.24)$$

where  $\square_L$  is the covariant lattice version of the d'Alembert operator and defined as

$$\square_L \psi(x) := \frac{1}{a^2} \sum_{\mu} \left[ U_{\mu}(x) \psi(x + \hat{\mu}) - 2\psi(x) + U_{-\mu}(x) \psi(x - \hat{\mu}) \right]. \quad (3.25)$$

We end up with the fermionic part of the QCD Lagrangian density for *Wilson fermions*,

$$\begin{aligned} \mathcal{L}_F^L &= \sum_f \bar{\psi}_f \left( i\gamma^{\mu} \mathcal{D}_{\mu} \psi_f - m_f \psi_f + r \frac{a}{2} \square_L \psi_f \right) \\ &\equiv \frac{1}{a^4} \sum_f \bar{\Psi}_f \left( i\gamma^{\mu} \bar{\mathcal{D}}_{\mu} \Psi_f - \bar{m}_f \Psi_f + \frac{r}{2} \bar{\square}_L \Psi_f \right). \end{aligned} \quad (3.26)$$

We introduced the so-called *Wilson parameter*  $r$ , which allows us to study the system depending on the presence of the doublers, i.e., it allows us to switch the doublers on ( $r = 0$ ) and off ( $r = 1$ ). Moreover, in the last line we introduced rescaled dimensionless fermionic fields and masses as well as dimensionless versions of the derivatives defined in (3.16) and (3.25),

$$\psi \rightarrow \Psi := a^{3/2} \psi, \quad (3.27a)$$

$$m_f \rightarrow \bar{m}_f := a m_f, \quad (3.27b)$$

$$\mathcal{D}_{\mu} \rightarrow \bar{\mathcal{D}}_{\mu} := a \mathcal{D}_{\mu}, \quad (3.27c)$$

$$\square_L \rightarrow \bar{\square}_L := a^2 \square_L. \quad (3.27d)$$

With (3.26) we now have constructed a fermionic QCD Lagrangian density on the lattice, which is invariant under local  $SU(N_c)$  gauge transformations (2.7), has the correct continuum limit (2.4) and is free of doublers. Together with (2.20) and (2.28) we obtain the Hamiltonian density for the fermionic part of QCD,

$$\begin{aligned} \mathcal{H}_F^L &= \sum_f \bar{\psi}_f \left( m_f \psi_f - i\gamma^i \mathcal{D}_i \psi_f - r \frac{a}{2} \square_L \psi_f \right) \\ &\equiv \frac{1}{a^4} \sum_f \bar{\Psi}_f \left( \bar{m}_f \Psi_f - i\gamma^i \bar{\mathcal{D}}_i \Psi_f - \frac{r}{2} \bar{\square}_L \Psi_f \right), \end{aligned} \quad (3.28)$$

where we made use of the temporal gauge (2.25).

Recalling the symmetry analysis made in Section 2.1.2, the additional Wilson term breaks chiral symmetry (2.18) explicitly on the lattice, even in the massless case. Since our focus is not on chiral symmetry (breaking) effects, Wilson fermions are still a suitable choice for our analysis. Furthermore, the *Nielsen–Ninomiya theorem* [42–44] states, that it is impossible to construct a Dirac operator  $D$  having the following properties simultaneously [45]:



1.  $\tilde{D}(p)$  is a periodic, analytic function of  $p_\mu$ .  $\leftrightarrow$   $D$  is local
2.  $\tilde{D}(p) \propto \gamma^\mu p_\mu$  for  $a|p_\mu| \ll 1$ .  $\leftrightarrow$  correct continuum limit
3.  $\tilde{D}(p)$  is invertible everywhere except for  $p_\mu = 0$ .  $\leftrightarrow$  no doublers
4.  $\{\gamma^5, D\} = 0$ .  $\leftrightarrow$  chiral symmetry

There are other lattice discretizations of fermions, e.g., the so-called *staggered formulation* [46], which incorporates chiral symmetry. In this approach doublers are still present but their number is reduced (from 16 to 4 in four dimensions) and the remaining ones are treated as *tastes* of the continuum fermions. These tastes can then be removed by a rooting procedure, which is though – at the time of writing – still a controversial method.

Nevertheless, replacing the fourth condition of the Nielsen–Ninomiya theorem by the so-called *Ginsparg-Wilson equation* [47],

$$\{\gamma^5, D\} = aD\gamma^5D, \quad (3.29)$$

allows for lattice descriptions of fermions, which violate chiral symmetry for finite  $a$  but restore it in the continuum limit. Several fermion formulations fulfilling the milder chirality constraint (3.29) have been developed, such as *fixed point* [48], *domain wall* [49–51] or *overlap* [52, 53] fermions. The major drawback of these formulations, however, is the large amount of computational costs, which is a further justification for our choice of Wilson fermions.

### 3.3 Stochastic fermion implementation

The classicality condition (2.79) introduced in Section 2.4 breaks down for fermionic degrees of freedom due to the Pauli exclusion principle. Hence, the fermions in our implementation have to be treated quantum mechanically.

To this end, we perform a *canonical quantization* of the fermionic field and follow [54] apart from the convention of the Fourier transform, which we choose to be symmetric (cf. Appendix B.2). Hence, a Fourier decomposition in terms of creation and annihilation operators yields

$$\psi(x) = \int \frac{d^3p}{(2\pi)^{\frac{3}{2}}} \frac{1}{\sqrt{2p_0}} \sum_s \left( a_s(\vec{p}) u_s(p) e^{-ipx} + b_s^\dagger(\vec{p}) v_s(p) e^{ipx} \right), \quad (3.30)$$

$$\bar{\psi}(x) = \int \frac{d^3p}{(2\pi)^{\frac{3}{2}}} \frac{1}{\sqrt{2p_0}} \sum_s \left( a_s^\dagger(\vec{p}) \bar{u}_s(p) e^{ipx} + b_s(\vec{p}) \bar{v}_s(p) e^{-ipx} \right), \quad (3.31)$$

where the Dirac spinors  $u$  and  $v$  are solutions of the free ( $A_i = 0$ ) Dirac equation for positive and negative energies, respectively. In our case, they are defined as solutions of

the free lattice Dirac equation ( $U_i = 1$ ) at initial time. In momentum space it reads

$$\left[ \frac{1}{\bar{a}_t} \sin(\bar{a}_t \bar{p}_0) - \gamma^0 \left( m + r \sum_i [1 - \cos(\bar{p}_i)] \right) \right] w(\vec{p}) = 0, \quad (3.32)$$

with  $w \in (u, v)$ . We defined the dimensionless mass  $\bar{m} = a_\sigma m$  as well as the dimensionless 4-momentum  $\bar{p}_\mu := a_\sigma p_\mu$ . The lattice Dirac equation becomes equivalent to its continuum expression,

$$(\gamma^\mu s_\mu - \mu) w(\vec{p}) = 0, \quad (3.33)$$

by defining

$$s_0 := \frac{1}{\bar{a}_t} \sin(\bar{a}_t \bar{p}_0), \quad (3.34a)$$

$$s_i := \sin(\bar{p}_i), \quad (3.34b)$$

$$\mu := m + r \sum_i [1 - \cos(\bar{p}_i)]. \quad (3.34c)$$

For equal momenta, the Dirac spinors are normalized by<sup>3</sup>

$$\bar{u}_r u_s = 2\mu \delta_{rs}, \quad u_r^\dagger u_s = 2s_0 \delta_{rs}, \quad (3.35)$$

$$\bar{v}_r v_s = -2\mu \delta_{rs}, \quad v_r^\dagger v_s = 2s_0 \delta_{rs}, \quad (3.36)$$

which is in accordance with the continuum normalization (c.f., e.g., [54]) by identifying  $s_\mu$  as the lattice 4-momentum, with corresponding mass term  $\mu$ , obeying the lattice equivalent of the energy-momentum relation,

$$s_0(\vec{p}) = \sqrt{\sum_i s_i^2(\vec{p}) + \mu^2(\vec{p})}. \quad (3.37)$$

So far, the implementation is straightforward, but difficulties arise at the stage of implementing the creation and annihilation operators, which have to obey

$$\{a_r(\vec{p}), a_s^\dagger(\vec{q})\} = \{b_r(\vec{p}), b_s^\dagger(\vec{q})\} = (2\pi)^{\frac{3}{2}} \delta_{rs} \delta(\vec{p} - \vec{q}), \quad (3.38)$$

with all other anticommutators vanishing.

A possible solution is the description in terms of so-called *low-cost fermions* [12], which are based on a stochastic approach towards the anticommutation relations (3.38). To this end, *gendered* (male and female) fermions are introduced, which only differ in the sign between the positive and negative energy solutions,

$$\psi_{M/F}(x) = \frac{1}{\sqrt{2}} \int \frac{d^3 p}{(2\pi)^{\frac{3}{2}}} \frac{1}{\sqrt{2p_0}} \sum_s \left( \xi_s(\vec{p}) u_s(\vec{p}) e^{-ipx} \pm \eta_s(\vec{p}) v_s(\vec{p}) e^{+ipx} \right), \quad (3.39a)$$

$$\bar{\psi}_{M/F}(x) = \frac{1}{\sqrt{2}} \int \frac{d^3 p}{(2\pi)^{\frac{3}{2}}} \frac{1}{\sqrt{2p_0}} \sum_s \left( \xi_s^*(\vec{p}) \bar{u}_s(\vec{p}) e^{+ipx} \pm \eta_s^*(\vec{p}) \bar{v}_s(\vec{p}) e^{-ipx} \right), \quad (3.39b)$$

<sup>3</sup>The explicit expressions for the Dirac spinors  $u$  and  $v$  can be found in Appendix D.3.1.

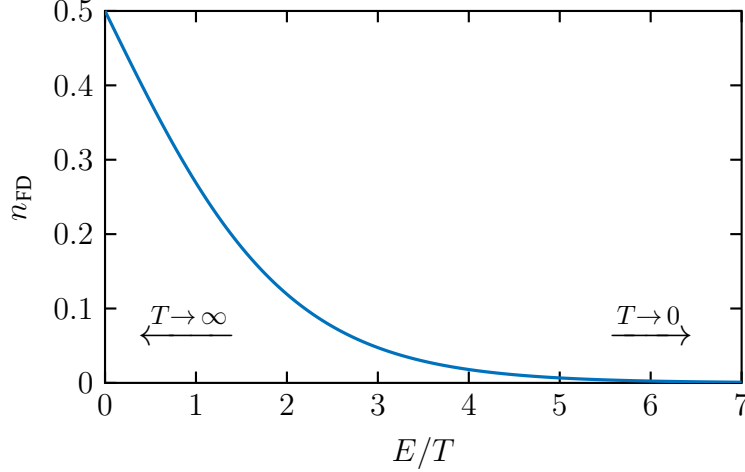


**Figure 3.2:** The Fermi-Dirac distribution (3.41) for different energy-temperature ratios  $E/T$ .

where creation and annihilation operators have been replaced by random complex numbers obeying the following distribution<sup>4</sup>

$$\langle \xi_r(\vec{p}) \xi_s^*(\vec{q}) \rangle = (2\pi)^{\frac{3}{2}} \delta_{rs} \delta(\vec{p} - \vec{q}) \left(1 - 2n_{\text{FD}}(\vec{p})\right), \quad (3.40a)$$

$$\langle \eta_r(\vec{p}) \eta_s^*(\vec{q}) \rangle = (2\pi)^{\frac{3}{2}} \delta_{rs} \delta(\vec{p} - \vec{q}) \left(1 - 2n_{\text{FD}}(\vec{p})\right). \quad (3.40b)$$

Note that we again used the symmetric convention for the Fourier transform, which differs from the one in [12] and, additionally, we use a distinct normalization of the Dirac spinors  $u$  and  $v$ .

In (3.40) we introduced the *Fermi-Dirac distribution*  $n_{\text{FD}}$ , which reads for vanishing chemical potential

$$n_{\text{FD}}(E(\vec{p}), T) = \frac{1}{\exp\left(\frac{E(\vec{p})}{T}\right) + 1}. \quad (3.41)$$

From Figure 3.2 we obtain that the width of the amplitude in the distribution (3.40) ranges from 0 to 1, where the first border corresponds to the limit  $T \rightarrow \infty$ , and the second to a vacuum initialization ( $T=0$ ).

The physical correlation function is then replaced by an ensemble average  $\langle \cdot, \cdot \rangle_{\text{ens}}$  over  $N_{\text{ens}}$  independently drawn ensembles  $(\xi, \eta)$ ,<sup>5</sup>

$$\langle \bar{\psi}(x) \psi(y) \rangle = -\langle \bar{\psi}_{\text{M/F}}(x) \psi_{\text{F/M}}(y) \rangle_{\text{ens}}. \quad (3.42)$$

Having initialized  $N_{\text{ens}}$  fermionic male and female fields, we can easily reduce the stochastic noise by averaging over the two possible correlator expressions, that are analytically

<sup>4</sup>The initialization of the complex random numbers  $\xi$  and  $\eta$  is realized by drawing standard Gaussian distributed amplitudes multiplied by a width corresponding to (3.40), which are then multiplied by  $e^{i\theta}$ , where the random (real) phases  $\theta$  are uniformly distributed over  $[0, 2\pi]$ .

<sup>5</sup>The corresponding derivation can be found in Appendix D.3.2

equivalent and use instead of (3.42) the following expression,

$$\langle \bar{\psi}(x)\psi(y) \rangle = -\frac{1}{2} \left( \langle \bar{\psi}_M(x)\psi_F(y) \rangle_{\text{ens}} + \langle \bar{\psi}_F(x)\psi_M(y) \rangle_{\text{ens}} \right). \quad (3.43)$$

We perform a cross-check by comparing the energy density of a free Fermi gas, which we can both compute in our stochastic fermion implementation and also analytically via [55]

$$\begin{aligned} \epsilon_\psi(T) &= \frac{g_\psi}{(2\pi)^3} \int_{-\infty}^{\infty} d^3p E(\vec{p}) n_{\text{FD}}(E(\vec{p}), T) \\ &\stackrel{a_\sigma \rightarrow 0}{=} \frac{g_\psi}{(2\pi)^3} \int_{-\frac{\pi}{a_\sigma}}^{\frac{\pi}{a_\sigma}} d^3p a_\sigma^{-1} s_0(\vec{p}) n_{\text{FD}}\left(\frac{s_0(\vec{p})}{a_\sigma}, T\right) \\ &= \frac{1}{a_\sigma^4} \frac{g_\psi}{(2\pi)^3} \int_{-\pi}^{\pi} d^3p s_0\left(\frac{\vec{p}}{a_\sigma}\right) n_{\text{FD}}\left(s_0\left(\frac{\vec{p}}{a_\sigma}\right), a_\sigma T\right), \end{aligned} \quad (3.44)$$

with the degeneracy factor  $g_\psi = 2 \times 2 \times 3 = 12$ , including two polarizations, three colors and an additional factor of two for fermions and antifermions. We restricted the momentum integration to the first Brillouin zone, replaced the energy  $E \equiv p_0$  by the dimensionless lattice expression (3.34a) and performed a change of variables to get from the second to the third line.

The definition of the energy density based on the stochastic fermions follows from the Hamiltonian density (3.28) for a single flavor, where we use (3.43) to replace the respective correlators by ensemble averages of the gendered fermions,

$$\begin{aligned} \epsilon_\psi &= -\frac{1}{2a_\sigma^4} \left( \bar{m} \langle \bar{\Psi}_M \Psi_F \rangle_{\text{ens}} - i \langle \bar{\Psi}_M \gamma^i \bar{D}_i \Psi_F \rangle_{\text{ens}} - \frac{r}{2} \langle \bar{\Psi}_M \bar{\square}_L \Psi_F \rangle_{\text{ens}} \right. \\ &\quad \left. + \bar{m} \langle \bar{\Psi}_F \Psi_M \rangle_{\text{ens}} - i \langle \bar{\Psi}_F \gamma^i \bar{D}_i \Psi_M \rangle_{\text{ens}} - \frac{r}{2} \langle \bar{\Psi}_F \bar{\square}_L \Psi_M \rangle_{\text{ens}} \right). \end{aligned} \quad (3.45)$$

We dropped all arguments for the sake of clarity and since it should be easy to restore them. Note that the temperature only enters through the initialization of the complex random numbers (3.40), which depends on the Fermi-Dirac distribution (3.41). We also want to stress that the continuous Fourier transformations in (3.39) and (3.40) have to be substituted by the corresponding lattice versions (cf. Appendix B.2).

The comparison of (3.44) and (3.45) is given in Figure 3.3, where we see a perfect agreement and can thus assume a correct implementation of the stochastic fermions.

Removing the unphysical doublers, corresponding to  $r = 1$  in Figure 3.3, reduces the number of particles and should thus lead to a lower energy density. However, for  $\frac{T}{m} \gtrsim 17$  this is obviously not the case anymore. The reason for this has its origin in the fact that the doubler term acts like an additional mass term (cf. Section 3.2).

Looking at the integrand in (3.44),  $E(\vec{p})n_{\text{FD}}(E, T)$ , we see that for small temperatures the additional exponential damping due to the doubler term in the Fermi-Dirac distribution dominates the additional energy coming from the additional mass term in the

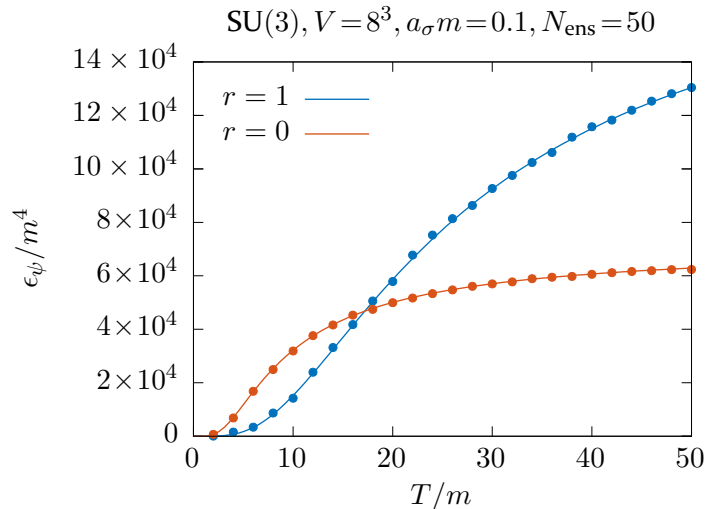


**Figure 3.3:** Temperature dependence of the fermionic energy density scaled by the mass with and without the doubler term. The lines represent the analytic result (3.44) and the dots the respective outcome of our simulation based on stochastic fermions (3.45) for a single run.

nominator. On the other hand, for large temperatures, independent of the doubler term,  $n_{\text{FD}} \rightarrow \frac{1}{2} = \text{const.}$ , which means that only the energy  $E(\vec{p})$  becomes relevant. The latter is larger if the doubler term is present due to the additional mass and hence this also applies to the constant which  $\epsilon_\psi$  approaches.

### 3.4 Gluonic lattice Hamiltonian density

After having established a suitable fermion implementation in the preceding two sections, we will now construct the gluonic part of our lattice description. The key element of this theory is the so-called *plaquette*, which is the shortest, non-trivial closed loop on the lattice. It is depicted on the right-hand side of Figure 3.1 and defined as

$$\begin{aligned} U_{\mu\nu}(x) &:= U_\mu(x)U_\nu(x + \hat{\mu})U_{-\mu}(x + \hat{\nu} + \hat{\nu})U_{-\nu}(x + \hat{\nu}) \\ &\equiv U_\mu(x)U_\nu(x + \hat{\mu})U_\mu^\dagger(x + \hat{\nu})U_\nu^\dagger(x). \end{aligned} \quad (3.46)$$

Using  $A_\mu(x + \hat{\nu}) = A_\mu(x) + a_\nu \partial_\nu A_\mu(x) + \mathcal{O}(a^2)$  together with the Baker-Campbell-Hausdorff formula for matrix exponentials one obtains

$$U_{\mu\nu}(x) = \exp \left[ i g a_\mu a_\nu F_{\mu\nu}(x) + \mathcal{O}(a^3) \right], \quad (3.47)$$

with the field strength tensor (2.8), which demonstrated the physical importance of the plaquette. Note that we introduced lattice spacings with indices allowing for an anisotropic lattice description. This is a necessary step as we will see in the following sections, where we construct the gluonic lattice Hamiltonian both in ordinary Minkowski space,

namely the static box scenario, and in the comoving formulation corresponding to an expanding system.

### 3.4.1 The static box scenario

Before we construct our lattice Hamiltonian density in the static box formulation, we will introduce rescaled fields in order to ease the implementation on a computer. To do so, we first have to determine the (energy) dimensions of the relevant variables,

$$\begin{aligned} [a_\sigma] &= [L] = -1, & [a_t] &= [L] = -1, \\ [A_i] &= \left[ \frac{1}{L} \right] = 1, & [E_i] &= \left[ \frac{1}{L^2} \right] = 2, \\ [t] &= [L] = -1. \end{aligned} \tag{3.48}$$

In our static box calculations we only consider lattices, that are isotropic in space, i.e.,  $a_x = a_y = a_z \equiv a_\sigma$ . The time discretization length  $a_t$ , in turn, will be much smaller (due to reasons that will be discussed in Section 5.4) and hence is labeled differently.

According to (3.48), we rescale the fields and also the time variables in the following convenient way:

$$A_i \rightarrow \bar{A}_i := g a_\sigma A_i, \tag{3.49a}$$

$$E_i \rightarrow \bar{E}_i := g a_\sigma^2 E_i, \tag{3.49b}$$

$$a_t \rightarrow \bar{a}_t := \frac{a_t}{a_\sigma}, \tag{3.49c}$$

$$t \rightarrow \bar{t} := \frac{t}{a_\sigma}. \tag{3.49d}$$

Regarding the definition of the gluonic field strength tensor (2.8), we can – together with (3.48) – read off its dimension,

$$[F_{\mu\nu}] = \left[ \frac{1}{L^2} \right] = 2, \tag{3.50}$$

and define its rescaled version,

$$F_{\mu\nu} \rightarrow \bar{F}_{\mu\nu} := g a_\mu a_\nu F_{\mu\nu}. \tag{3.51}$$

We can then rewrite the gluonic Lagrangian density (2.32) in terms of the rescaled quantities,

$$\mathcal{L}_G^{\text{rescaled}} = \frac{1}{g^2 a_\sigma^4} \text{Tr} \left[ \frac{1}{\bar{a}_t^2} \bar{F}_{0i}^2 - \sum_{i < j} \bar{F}_{ij}^2 \right]. \tag{3.52}$$

By using the relation

$$\begin{aligned}
 \text{Re Tr}(1 - U_{\mu\nu}) &= \text{Re Tr} \left\{ 1 - \exp[iga_{\mu}a_{\nu}F_{\mu\nu} + \mathcal{O}(a^3)] \right\} \\
 &= \text{Re Tr} \left\{ -i[ga_{\mu}a_{\nu}F_{\mu\nu} + \mathcal{O}(a^3)] + \frac{1}{2}g^2a_{\mu}^2a_{\nu}^2F_{\mu\nu}^2 + \mathcal{O}(a^6) \right\} \\
 &= \text{Tr} \left\{ \frac{1}{2}g^2a_{\mu}^2a_{\nu}^2F_{\mu\nu}^2 + \mathcal{O}(a^6) \right\} \\
 &= \text{Tr} \left\{ \frac{1}{2}\bar{F}_{\mu\nu}^2 + \mathcal{O}(a^6) \right\}, \tag{3.53}
 \end{aligned}$$

we are finally able to write down the lattice Lagrangian density,

$$\mathcal{L}_G^L = \frac{2}{g^2a_{\sigma}^4} \text{Re Tr} \left[ \frac{1}{\bar{a}_t^2} \sum_i (1 - U_{0i}) - \sum_{i<j} (1 - U_{ij}) \right]. \tag{3.54}$$

Using the rescaled chromo-electric field (3.49b) and the rescaled field strength tensor (3.51) yields the rescaled version of the Hamiltonian density (2.39),

$$\mathcal{H}_G^{\text{rescaled}} = \frac{1}{g^2a_{\sigma}^4} \text{Tr} \left[ \sum_i \bar{E}_i^2 + \sum_{i<j} \bar{F}_{ij}^2 \right]. \tag{3.55}$$

Ultimately, using again (3.53), we obtain our lattice Hamiltonian density,

$$\mathcal{H}_G^L = \frac{1}{g^2a_{\sigma}^4} \text{Re Tr} \left[ \sum_i \bar{E}_i^2 + 2 \sum_{i<j} (1 - U_{ij}) \right]. \tag{3.56}$$

### 3.4.2 Formulation in an expanding system

In complete analogy to Section 3.4.1, we will now construct the lattice Hamiltonian density in comoving coordinates. The (energy) dimensions in this formulation, which we will refer to as the expanding system, read

$$\begin{aligned}
 [a_{\perp}] &= [L] = -1, & [a_{\tau}] &= [L] = -1, \\
 [\tau] &= [L] = -1, & [\eta] &= [1] = 0, \\
 [A_i] &= \left[ \frac{1}{L} \right] = 1, & [A_{\eta}] &= [1] = 0, \\
 [E_i] &= \left[ \frac{1}{L} \right] = 1, & [E_{\eta}] &= \left[ \frac{1}{L^2} \right] = 2.
 \end{aligned} \tag{3.57}$$

These relations can easily be checked by a dimensional analysis of (2.43), (3.14) and (2.49), respectively. Accordingly and in correspondence with the rescaling in the static box (3.49), we rescale the field variables and the proper time in the following way:

$$a_{\tau} \rightarrow \bar{a}_{\tau} := \frac{a_{\tau}}{a_{\perp}}, \tag{3.58a}$$

$$\tau \rightarrow \bar{\tau} := \frac{\tau}{a_{\perp}} = \frac{n_{\tau}a_{\tau}}{a_{\perp}} \equiv n_{\tau}\bar{a}_{\tau}, \tag{3.58b}$$

$$A_i \rightarrow \bar{A}_i := ga_{\perp}A_i, \quad A_{\eta} \rightarrow \bar{A}_{\eta} := gA_{\eta}, \tag{3.58c}$$

$$E_i \rightarrow \bar{E}_i := ga_{\perp}E_i, \quad E_{\eta} \rightarrow \bar{E}_{\eta} := ga_{\perp}^2E_{\eta}. \tag{3.58d}$$

Regarding the definition of the field strength tensor (2.8), we obtain different dimensions in its components,

$$[F_{\tau j}] = [F_{ij}] = \left[ \frac{1}{L^2} \right] = 2, \quad [F_{\tau\eta}] = [F_{i\eta}] = \left[ \frac{1}{L} \right] = 1, \quad (3.59)$$

which, however, allows for the same rescaled definition as in the static box (3.51) due to the different dimensions of the lattice spacings. The Lagrangian density (2.47) thus becomes

$$\begin{aligned} \mathcal{L}_G^{\text{rescaled}} &= \text{Tr} \left[ a_{\perp} \bar{\tau} \frac{\bar{F}_{\tau i}^2}{(g a_{\tau} a_{\perp})^2} + \frac{1}{a_{\perp} \bar{\tau}} \frac{\bar{F}_{\tau\eta}^2}{(g a_{\tau} a_{\eta})^2} - a_{\perp} \bar{\tau} \frac{\bar{F}_{12}^2}{(g a_{\perp})^2} - \frac{1}{a_{\perp} \bar{\tau}} \frac{\bar{F}_{i\eta}^2}{(g a_{\eta} a_{\perp})^2} \right] \\ &= \frac{1}{g^2 a_{\perp}^3} \text{Tr} \left[ \frac{\bar{\tau} \bar{F}_{\tau i}^2}{\bar{a}_{\tau}^2} + \frac{\bar{F}_{\tau\eta}^2}{\bar{a}_{\tau}^2 a_{\eta}^2 \bar{\tau}} - \bar{\tau} \bar{F}_{12}^2 - \frac{\bar{F}_{i\eta}^2}{a_{\eta}^2 \bar{\tau}} \right]. \end{aligned} \quad (3.60)$$

By once again expressing the rescaled, dimensionless field strength tensor in terms of plaquettes, i.e. by using (3.53), we end up with the gluonic lattice Lagrangian density in comoving coordinates,

$$\mathcal{L}_G^L = \frac{2}{g^2 a_{\perp}^3} \text{Re Tr} \left[ \frac{\bar{\tau}}{\bar{a}_{\tau}^2} \sum_i (1 - U_{\tau i}) + \frac{1}{\bar{a}_{\tau}^2 a_{\eta}^2 \bar{\tau}} (1 - U_{\tau\eta}) - \bar{\tau} (1 - U_{12}) - \frac{1}{a_{\eta}^2 \bar{\tau}} \sum_i (1 - U_{i\eta}) \right]. \quad (3.61)$$

The rescaled version of the Hamiltonian density (2.50) then reads

$$\mathcal{H}_G^{\text{rescaled}} = \frac{1}{g^2 a_{\perp}^3} \text{Tr} \left[ \frac{\bar{E}_i^2}{\bar{\tau}} + \bar{\tau} \bar{E}_{\eta}^2 + \bar{\tau} \bar{F}_{12}^2 + \frac{1}{a_{\eta}^2} \frac{\bar{F}_{i\eta}^2}{\bar{\tau}} \right], \quad (3.62)$$

finally yielding the lattice version of the gluonic Hamiltonian density for the expanding system,

$$\mathcal{H}_G^L = \frac{1}{g^2 a_{\perp}^3} \text{Re Tr} \left[ \frac{\bar{E}_i^2}{\bar{\tau}} + \bar{\tau} \bar{E}_{\eta}^2 + 2\bar{\tau} (1 - U_{12}) + \frac{2}{a_{\eta}^2 \bar{\tau}} \sum_i (1 - U_{i\eta}) \right]. \quad (3.63)$$

## 3.5 Lattice equations of motion

### 3.5.1 Static box

#### Chromo-electric fields

As analogously done in the continuum, we obtain the time evolution of the conjugate momenta, namely the chromo-electric fields (2.34), from the Hamilton's equations of motion (2.22). The functional derivative defined in (2.23) reduces in our case to an ordinary field derivative since the lattice Hamiltonian density (3.56) is independent of spacial derivatives of  $A$ ,

$$\partial_t E_i^a = - \frac{\delta \mathcal{H}^L}{\delta A_i^a} \equiv - \frac{\partial \mathcal{H}^L}{\partial A_i^a}. \quad (3.64)$$



The full lattice Hamiltonian is given by the gluonic part  $\mathcal{H}_G^L$  defined in (3.56) and the fermionic part  $\mathcal{H}_F^L$  defined in (3.28),

$$\mathcal{H}^L = \mathcal{H}_G^L + \mathcal{H}_F^L. \quad (3.65)$$

In terms of the rescaled, dimensionless quantities defined in (3.49), we end up with the equations of motion for chromo-electric field components,

$$\begin{aligned} \partial_{\hat{t}} \bar{E}_i^a(x) &= -g^2 a_\sigma^4 \frac{\partial \mathcal{H}^L}{\partial \bar{A}_i^a(x)} \\ &= 2 \sum_{j \neq i} \text{Im Tr} \left\{ T^a [U_{ji}(x) + U_{-ji}(x)] \right\} \\ &\quad + i \frac{g^2}{2} \left\{ i \left[ \bar{\Psi}(x) \gamma^i T^a U_i(x) \Psi(x + \hat{i}) + \bar{\Psi}(x + \hat{i}) \gamma^i U_{-i}(x + \hat{i}) T^a \Psi(x) \right] \right. \\ &\quad \left. + r \left[ \bar{\Psi}(x) \quad T^a U_i(x) \Psi(x + \hat{i}) - \bar{\Psi}(x + \hat{i}) \quad U_{-i}(x + \hat{i}) T^a \Psi(x) \right] \right\}, \end{aligned} \quad (3.66)$$

where a detailed derivation can be found in Appendix C.1.1.

### Gauge link variables

In temporal gauge (2.25), the plaquettes including the time direction reduce to

$$U_{0i}(x) = U_i(x + \hat{t}) U_i^\dagger(x). \quad (3.67)$$

On the other hand, we can express these plaquettes via (3.47) and insert the definition of the field strength tensor (2.8) yielding

$$U_{0i}(x) = \exp [i g a_t a_\sigma F_{0i}(x) + \mathcal{O}(a^3)] = \exp [i g a_t a_\sigma \partial_t A_i(x) + \mathcal{O}(a^3)]. \quad (3.68)$$

By equating these two expressions, we obtain

$$U_i(x + \hat{t}) = \exp [i g a_t a_\sigma \partial_t A_i(x)] U_i(x), \quad (3.69)$$

where we neglected the  $\mathcal{O}(a^3)$  terms in the exponential function and multiplied both sides by  $U_i(x)$ . With the conjugate momenta (2.34) we finally get

$$U_i(x + \hat{t}) = \exp [i g a_t a_\sigma E_i(x)] U_i(x) = \exp [i \bar{a}_t \bar{E}_i(x)] U_i(x). \quad (3.70)$$

These are the equations of motion for the components of the gauge fields.

### Fermionic fields

From the continuum expression of the Hamiltonian equations of motion for the fermionic degrees of freedom (2.28) we can easily obtain the time evolution of the dimensionless

fields (3.27a),<sup>6</sup>

$$\begin{aligned}
 \partial_{\hat{t}}\Psi(x) &= -\mathbf{i}\frac{\partial\mathcal{H}^L}{\partial\Psi^\dagger(x)} \\
 &= -\mathbf{i}\bar{m}\gamma^0\Psi(x) - \frac{1}{2}\gamma^0\gamma^i[U_i(x)\Psi(x+\hat{i}) - U_{-i}(x)\Psi(x-\hat{i})] \\
 &\quad + \mathbf{i}\frac{r}{2}\gamma^0\sum_i[U_i(x)\Psi(x+\hat{i}) - 2\Psi(x) + U_{-i}(x)\Psi(x-\hat{i})]. \tag{3.71}
 \end{aligned}$$

### 3.5.2 Expanding system

#### Chromo-electric fields

As it was also the case in the static box, our lattice Hamiltonian density in comoving coordinates (3.63) is again independent of spacial derivatives of  $A$  yielding

$$\partial_\tau E_i^a = -\frac{\delta\mathcal{H}^L}{\delta A_i^a} \equiv -\frac{\partial\mathcal{H}^L}{\partial A_i^a}, \tag{3.72a}$$

$$\partial_\tau E_\eta^a = -\frac{\delta\mathcal{H}^L}{\delta A_\eta^a} \equiv -\frac{\partial\mathcal{H}^L}{\partial A_\eta^a}. \tag{3.72b}$$

Since we do not include fermions in the expanding system, we have  $\mathcal{H}^L \equiv \mathcal{H}_G^L$ . A reformulation via the rescaled, dimensionless quantities (3.58) yields<sup>7</sup>

$$\begin{aligned}
 \partial_{\bar{\tau}}\bar{E}_i^a(x) &= -g^2a_\perp^3\frac{\partial\mathcal{H}_G^L}{\partial\bar{A}_i^a(x)} \\
 &= 2\text{Im Tr}\left\{T^a\left(\bar{\tau}\sum_{j\neq i}[U_{ji}(x) + U_{-ji}(x)] + \frac{1}{a_\eta^2\bar{\tau}}[U_{\eta i}(x) + U_{-\eta i}(x)]\right)\right\}, \tag{3.73a}
 \end{aligned}$$

$$\begin{aligned}
 \partial_{\bar{\tau}}\bar{E}_\eta^a(x) &= -g^2a_\perp^3\frac{\partial\mathcal{H}}{\partial\bar{A}_\eta^a(x)} \\
 &= \frac{2}{a_\eta\bar{\tau}}\sum_j\text{Im Tr}\left\{T^a[U_{j\eta}(x) + U_{-j\eta}(x)]\right\}. \tag{3.73b}
 \end{aligned}$$

#### Gauge link variables

In complete analogy to the steps performed in Section 3.5.1, we find

$$U_\mu(x+\hat{\tau}) = \exp[\mathbf{i}ga_\tau a_\mu\partial_\tau A_\mu(x)]U_\mu(x), \tag{3.74}$$

by dropping all terms of  $\mathcal{O}(a^3)$  in the exponential function. With the conjugate momenta defined in (2.49) we get the equations of motion for the gauge fields in the expanding formulation,

$$U_i(x+\hat{\tau}) = \exp\left[\mathbf{i}\frac{ga_\tau a_\perp}{\tau}E_i(x)\right]U_i(x) = \exp\left[\mathbf{i}\frac{\bar{a}_\tau}{\bar{\tau}}\bar{E}_i(x)\right]U_i(x), \tag{3.75a}$$

$$U_\eta(x+\hat{\tau}) = \exp[\mathbf{i}ga_\tau a_\eta\tau E_\eta(x)]U_\eta(x) = \exp[\mathbf{i}\bar{a}_\tau a_\eta\bar{\tau}\bar{E}_\eta(x)]U_\eta(x). \tag{3.75b}$$

<sup>6</sup>A detailed derivation can be found in Appendix C.1.2.

<sup>7</sup>We once again refer to the appendix for details, in this case to Appendix C.2.1.

### 3.5.3 Summary of the field's time evolution on the lattice

We solve the partial differential equations by the so-called *finite difference method*. In our case this means, that the partial derivatives in (3.66) and (3.73) are replaced by forward discretized derivatives (B.1), which allows for an iterative computation of the field's time evolution within our lattice setup. In order to partly compensate for the loss of accuracy owed to the stochastic description, we utilize the symmetric discretized derivative (B.3) for the evolution of the fermions (3.71).

In the following, we give a summary of the lattice implementation of the equations of motion for both the formulation in Minkowski coordinates (static box) and the comoving framework (expanding system).

#### Static box

$$U_i(x + \hat{t}) = \exp [i\bar{a}_t \bar{E}_i(x)] U_i(x) \quad (3.76a)$$

$$\begin{aligned} \bar{E}_i^a(x + \hat{t}) = & \bar{E}_i^a(x) + 2\bar{a}_t \sum_{j \neq i} \text{Im Tr} \left\{ T^a [U_{ji}(x) + U_{-ji}(x)] \right\} \\ & + i \frac{g^2}{2} \left\langle i \left[ \bar{\Psi}(x) \gamma^i T^a U_i(x) \Psi(x + \hat{i}) + \bar{\Psi}(x + \hat{i}) \gamma^i U_{-i}(x + \hat{i}) T^a \Psi(x) \right] \right. \\ & \left. + r \left[ \bar{\Psi}(x) \quad T^a U_i(x) \Psi(x + \hat{i}) - \bar{\Psi}(x + \hat{i}) \quad U_{-i}(x + \hat{i}) T^a \Psi(x) \right] \right\rangle \end{aligned} \quad (3.76b)$$

$$\begin{aligned} \Psi(x + \hat{t}) = & \Psi(x - \hat{t}) - 2i\bar{a}_t \bar{m} \gamma^0 \Psi(x) \\ & - \bar{a}_t \gamma^0 \gamma^i [U_i(x) \Psi(x + \hat{i}) - U_{-i}(x) \Psi(x - \hat{i})] \\ & + i r \bar{a}_t \gamma^0 \sum_i [U_i(x) \Psi(x + \hat{i}) - 2\Psi(x) + U_{-i}(x) \Psi(x - \hat{i})] \end{aligned} \quad (3.76c)$$

#### Expanding system

$$U_i(x + \hat{\tau}) = \exp \left[ i \frac{\bar{a}_\tau}{\bar{\tau}} \bar{E}_i(x) \right] U_i(x) \quad (3.77a)$$

$$U_\eta(x + \hat{\tau}) = \exp [i\bar{a}_\tau a_\eta \bar{\tau} \bar{E}_\eta(x)] U_\eta(x) \quad (3.77b)$$

$$\begin{aligned} \bar{E}_i^a(x + \hat{\tau}) = & \bar{E}_i^a(x) + 2\bar{a}_\tau \text{Im Tr} \left\{ T^a \left( \bar{\tau} \sum_{j \neq i} [U_{ji}(x) + U_{-ji}(x)] \right. \right. \\ & \left. \left. + \frac{1}{a_\eta^2 \bar{\tau}} [U_{\eta i}(x) + U_{-\eta i}(x)] \right) \right\} \end{aligned} \quad (3.77c)$$

$$\bar{E}_\eta^a(x + \hat{\tau}) = \bar{E}_\eta^a(x) + \frac{2\bar{a}_\tau}{a_\eta \bar{\tau}} \sum_j \text{Im Tr} \left\{ T^a [U_{j\eta}(x) + U_{-j\eta}(x)] \right\} \quad (3.77d)$$

Note, that the average in (3.76b) has to be performed within the scope of our stochastic fermion description, i.e., we have to utilize (3.43) yielding an extra minus sign for the fermionic part. In Appendix C.1.1 we give the corresponding explicit expression.

As a cross-check, one can simultaneously take the limits  $\bar{\tau} \rightarrow 1$  ( $\Leftrightarrow \tau \rightarrow a_\perp$ ) and  $a_\eta \rightarrow 1$  in the expanding formulation (3.77) and will obtain the gluonic part of the equations of motion in the static box (3.76).

We note that the proper time explicitly appears in the evolution equations of comoving description. For the implementation on a computer it is crucial to remember that all these variables have to be replaced by  $\bar{\tau} \equiv n_\tau \bar{a}_\tau$ , where  $n_\tau$  is the iteration step in the time evolution.

### 3.6 Gauss's law

Although we perform our calculations in temporal gauge (2.25), we can apply the Euler-Lagrange equations with respect to  $A_0$  before fixing the gauge. This results in a constraint, referred to as *Gauss's law*, which the fields have to fulfill at every step of the system's time evolution.

Physically meaningful initial conditions are chosen to fulfill Gauss's law. In addition, since it is conserved by the equations of motion in the continuum limit, it is a non-dynamical constraint. Nevertheless, due to numerical discrepancies, we can get small deviations during our lattice simulation which have to be monitored.

Applying the Euler-Lagrange equations (D.1) for the fields  $\bar{A}_t$  to our gluonic lattice Lagrangian density in the static box (3.54) yields<sup>8</sup>

$$0 = -\frac{2}{ga_\sigma^3 \bar{a}_t} \sum_i \text{Re Tr} \left\{ iT^a [U_t(x)U_i(x + \hat{0})U_{-t}(x + \hat{0} + \hat{i})U_{-i}(x + \hat{i}) \right. \\ \left. - U_{-i}(x)U_t(x - \hat{i})U_i(x - \hat{i} + \hat{0})U_{-t}(x + \hat{0})] \right\} \Big|_{A_t=0}. \quad (3.78)$$

There are now two possibilities:

1. We rebuild plaquettes and apply temporal gauge only at the stage of the lattice implementation, yielding

$$0 = -\frac{2}{ga_\sigma^3 \bar{a}_t} \sum_i \text{Im Tr} \left\{ T^a [U_{it}(x) + U_{-it}(x)] \right\} \Big|_{A_t=0}. \quad (3.79)$$

or

2. We directly apply temporal gauge to (3.78), leading to an approximate version<sup>9</sup> of Gauss's law,

$$0 \approx \frac{2}{ga_\sigma^3} \sum_i \text{Re Tr} \left\{ T^a [\bar{E}_i(x) - U_{-i}(x)\bar{E}_i(x - \hat{i})U_i(x - \hat{i})] \right\}. \quad (3.80)$$

<sup>8</sup>Corresponding detailed derivations can be found in Appendix C.1.3.

<sup>9</sup>The approximation is due to the identification of a discretized (forward) time derivative leading to the introduction of the chromo-electric fields and is thus of order  $\mathcal{O}(a_t)$ . In the continuum this is obviously an exact equation.

We want to stress that both of these constraints have to be fulfilled for each color component  $a$  and at any spacetime point  $x$ .

The advantage of (3.80) over (3.79) is that we can check Gauss's law separately at each time step. This means, we do not have to store or iterate additional gauge link variables. On the other hand, (3.79) is the more accurate check, since we did not use an approximation as we did in (3.80). We will check the different implementations and drop the more costly but accurate version (3.79), if the deviation is negligible.

In order to monitor the deviations of (3.79) or (3.80) we define the deviation color matrices

$$C_U(x) := -\frac{2}{\bar{a}_t} T^a \sum_i \text{Im Tr} \left\{ T^a [U_{i0}(x) + U_{-i0}(x)] \right\} \Big|_{\bar{A}_0=0} \quad (3.81)$$

and

$$C_E(x) := 2 T^a \sum_i \text{Re Tr} \left\{ T^a [\bar{E}_i(x) - U_{-i}(x) \bar{E}_i(x - \hat{i}) U_i(x - \hat{i})] \right\}, \quad (3.82)$$

where we swallowed the factor  $g a_\sigma^3$  to get dimensionless quantities in accordance with (3.49). A real-valued observable can then be defined as [56]

$$C_{U|E}(t) := \sqrt{\frac{1}{V} \sum_{\vec{x}} \text{Tr} [C_{U|E}^\dagger(x) C_{U|E}(x)]}, \quad (3.83)$$

where  $V = N_\perp^2 N_z$  is the lattice volume.

It is, however, also convenient to define the deviation of Gauss's law via the root mean square of (3.79),

$$C_U^{\text{RMS}}(t) := \frac{2}{\bar{a}_t} \sqrt{\frac{1}{N_g V} \sum_{\vec{x}, a} \left( \sum_i \text{Im Tr} \left\{ T^a [U_{i0}(x) + U_{-i0}(x)] \right\} \right)^2} \Big|_{\bar{A}_0=0}, \quad (3.84)$$

or (3.79), respectively,

$$C_E^{\text{RMS}}(t) := 2 \sqrt{\frac{1}{N_g V} \sum_{\vec{x}, a} \left( \sum_i \text{Re Tr} \left\{ T^a [\bar{E}_i(x) - U_{-i}(x) \bar{E}_i(x - \hat{i}) U_i(x - \hat{i})] \right\} \right)^2}, \quad (3.85)$$

where we average over the  $N_g$  generators and the volume  $V$ .

The computation of (3.84) and (3.85) is more efficient than the detour through the matrix construction (3.81) or (3.82) and calculation of its Frobenius norm (3.83). We will therefore mostly stick to the definition via the root mean squares.

On closer inspection, however, the definitions of the violation of Gauss's law via the Frobenius norm and the root mean square are equivalent up to a constant factor. To show this, we rewrite the matrix defined in (3.81) as  $C(x) \equiv c_a(x) T^a$ , with  $c_a \in \mathbb{R}$ , and

find by starting with the Frobenius norm of (3.83)

$$\begin{aligned}
 \sqrt{\frac{1}{V} \sum_{\vec{x}} \text{Tr} \left[ (c_a(x) T^a)^\dagger (c_b(x) T^b) \right]} &= \sqrt{\frac{1}{V} \sum_{\vec{x}} c_a(x) c_b(x) \text{Tr} \left[ T^a T^b \right]} \\
 &= \sqrt{\frac{1}{V} \sum_{\vec{x}} c_a(x) c_b(x) \frac{1}{2} \text{Tr} \left[ \{T^a T^b\} \right]} \quad (3.86) \\
 &= \frac{1}{\sqrt{2}} \sqrt{\frac{1}{V} \sum_{\vec{x}, a} c_a^2(x)},
 \end{aligned}$$

where we used the cyclicity of the trace, the anticommutation relation (2.2a) and the fact that the generators  $T^a$  are elements of the Lie group  $\text{su}(N_c)$ , i.e., that they are hermitian and traceless.

Up a factor  $\sqrt{\frac{N_g}{2}}$ , the last line of (3.86) is exactly the definition of the Gauss violation via the root mean square (3.84).

### 3.6.1 Restoring algorithm

As discussed above, Gauss's law can get slightly violated during our simulations due to numerical fluctuations. To restore (3.79) or (3.80), respectively, we use an algorithm adapted from [56], where the chromo-electric fields are iterated as

$$E_i(x) \rightarrow E_i(x) + \gamma \left[ U_i(x) C_{U|E}(x + \hat{i}) U_{-i}(x + \hat{i}) - C_{U|E}(x) \right], \quad (3.87)$$

with a real constant  $\gamma$ , which can be determined from a Fourier analysis of the Gauss violation matrix  $C_{U|E}$ .

Figure 3.4 demonstrates the correct operation of the restoring algorithm (3.87) and also shows the mentioned equivalence of the two definitions (3.81) and (3.84). In the zoomed plot, we can easily read off the factor that distinguishes the two curves, which is indeed  $\sqrt{\frac{N_g}{2}} = 2$ .

### 3.6.2 Gauss's law in the expanding formulation

Just like we did in the static box scenario, we can also obtain Gauss's law in the expanding formulation by applying the Euler-Lagrange equations with respect to  $A_\tau$  before fixing the gauge.

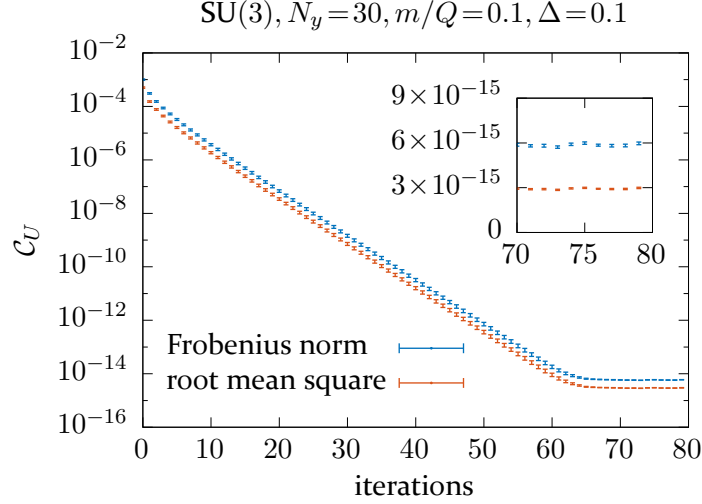


**Figure 3.4:** Violation of Gauss's law (3.79) on a  $4^3$  lattice via the Frobenius norm (3.81) and the root mean square (3.84) depending on the number of iterations following the restoring algorithm (3.87). We chose  $\gamma = 0.12$  as suggested in [56]. The parameters given in the title are unimportant for the moment and will become clear at a later stage.

Applying (D.1) to the Lagrangian density (3.61), we find (cf. Appendix C.2.2)

$$\begin{aligned}
 0 = & -\frac{2}{ga_{\perp}^2 \bar{a}_{\tau}} \operatorname{Re} \operatorname{Tr} \left\{ iT^a \left( \bar{\tau} \sum_i \left[ U_{\tau}(x) U_i(x + \hat{\tau}) U_{\tau}^{\dagger}(x + \hat{i}) U_i^{\dagger}(x) \right. \right. \right. \\
 & \quad \left. \left. \left. - U_i^{\dagger}(x - \hat{i}) U_{\tau}(x - \hat{i}) U_i(x - \hat{i} + \hat{\tau}) U_{\tau}^{\dagger}(x) \right] \right. \right. \\
 & \quad \left. \left. + \frac{1}{a_{\eta}^2 \bar{\tau}} \left[ U_{\tau}(x) U_{\eta}(x + \hat{\tau}) U_{\tau}^{\dagger}(x + \hat{\eta}) U_{\eta}^{\dagger}(x) \right. \right. \right. \\
 & \quad \left. \left. \left. - U_{\eta}^{\dagger}(x - \hat{\eta}) U_{\tau}(x - \hat{\eta}) U_{\eta}(x - \hat{\eta} + \hat{\tau}) U_{\tau}^{\dagger}(x) \right] \right) \right\} \Big|_{A_{\tau}=0}. \quad (3.88)
 \end{aligned}$$

Now we once again have to choose at which point we apply the temporal gauge (2.25) (cf. discussion in the static box framework below (3.78)). We either get

$$\begin{aligned}
 0 = & -\frac{2}{ga_{\perp}^2 \bar{a}_{\tau}} \operatorname{Im} \operatorname{Tr} \left\{ T^a \left( \bar{\tau} \sum_i \left[ U_{i\tau}(x) + U_{-i\tau}(x) \right. \right. \right. \\
 & \quad \left. \left. \left. + \frac{1}{a_{\eta}^2 \bar{\tau}} \left[ U_{\eta\tau}(x) + U_{-\eta\tau}(x) \right] \right) \right\} \Big|_{A_{\tau}=0} \quad (3.89)
 \end{aligned}$$

or

$$\begin{aligned}
 0 \approx & \frac{2}{ga_{\perp}^2} \operatorname{Re} \operatorname{Tr} \left\{ T^a \left( \sum_i \left[ \bar{E}_i(x) - U_{-i}(x) \bar{E}_i(x - \hat{i}) U_i(x - \hat{i}) \right. \right. \right. \\
 & \quad \left. \left. \left. + \frac{1}{a_{\eta}^2} \left[ \bar{E}_{\eta}(x) - U_{-\eta}(x) \bar{E}_{\eta}(x - \hat{\eta}) U_{\eta}(x - \hat{\eta}) \right] \right) \right\}. \quad (3.90)
 \end{aligned}$$

Following the same line of argumentation as in the static box case, we define the dimensionless deviation color matrices

$$C_U(x) := -\frac{2}{\bar{a}_\tau} T^a \operatorname{Im} \operatorname{Tr} \left\{ T^a \left( \bar{\tau} \sum_i [U_{i\tau}(x) + U_{-i\tau}(x)] + \frac{1}{\bar{a}_\eta^2 \bar{\tau}} [U_{\eta\tau}(x) + U_{-\eta\tau}(x)] \right) \right\} \Big|_{A_\tau=0} \quad (3.91)$$

and

$$C_E(x) := 2 \operatorname{Re} \operatorname{Tr} \left\{ T^a \left( \sum_i [\bar{E}_i(x) - U_{-i}(x) \bar{E}_i(x - \hat{i}) U_i(x - \hat{i})] + \frac{1}{\bar{a}_\eta^2} [\bar{E}_\eta(x) - U_{-\eta}(x) \bar{E}_\eta(x - \hat{\eta}) U_\eta(x - \hat{\eta})] \right) \right\}. \quad (3.92)$$

The real-valued observable obtained via the Frobenius norm is then defined in the exact same way as in (3.83).

Consequently, we define the equivalents of (3.84) and (3.85) in the comoving formulation as

$$C_U^{\text{RMS}}(t) := \frac{2}{\bar{a}_\tau} \sqrt{\frac{1}{N_g V} \sum_{a, \vec{x}} \left( \operatorname{Im} \operatorname{Tr} \left\{ T^a \left( \bar{\tau} \sum_i [U_{i\tau}(x) + U_{-i\tau}(x)] + \frac{1}{\bar{a}_\eta^2 \bar{\tau}} [U_{\eta\tau}(x) + U_{-\eta\tau}(x)] \right) \right\} \right)^2} \Big|_{\bar{A}_\tau=0} \quad (3.93)$$

and

$$C_E^{\text{RMS}}(t) := 2 \sqrt{\frac{1}{N_g V} \sum_{a, \vec{x}} \left( \operatorname{Re} \operatorname{Tr} \left\{ T^a \left( \sum_i [\bar{E}_i(x) - U_{-i}(x) \bar{E}_i(x - \hat{i}) U_i(x - \hat{i})] + \frac{1}{\bar{a}_\eta^2} [\bar{E}_\eta(x) - U_{-\eta}(x) \bar{E}_\eta(x - \hat{\eta}) U_\eta(x - \hat{\eta})] \right) \right\} \right)^2} \quad (3.94)$$

respectively.

### 3.7 Real-time static potential

In order to verify the correct implementation of the pure gauge part of our lattice equations of motion in the static box (3.76), we perform test simulations in thermal equilibrium and compare our results of the time evolution of appropriate observables. We use configurations produced with code parts written by C. Schäfer and refer to his PhD thesis [57] for details of the corresponding computation, since equilibrium physics and especially the thermalization process via the so-called *Heatbath algorithm* are of minor interest for this work.



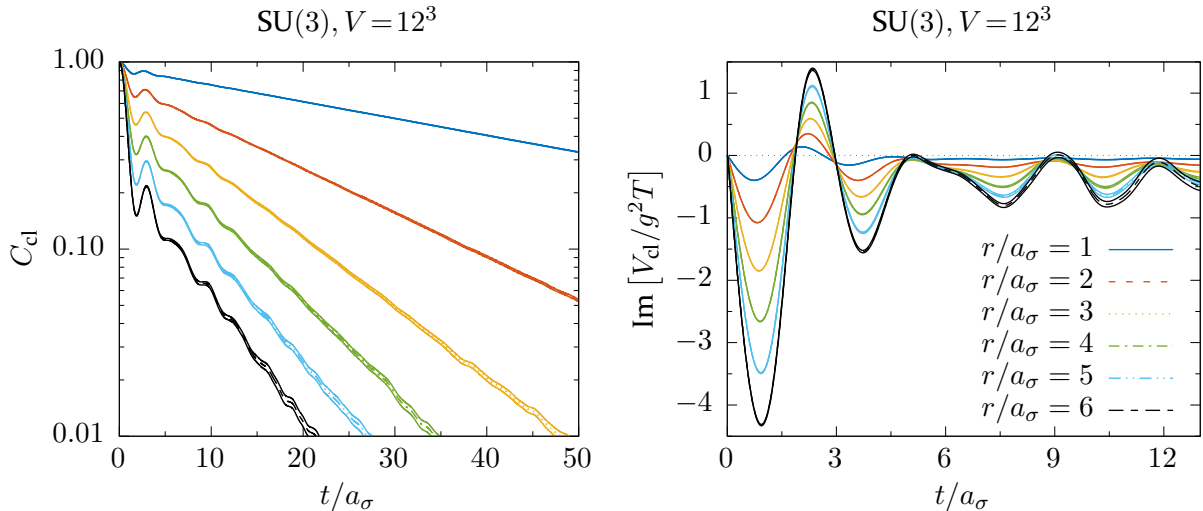


**Figure 3.5:** The classical Wilson loop (left) and the imaginary part of the real-time static potential (right) for 100 configurations and lattice parameters taken from [59].

A suitable observable within our classical framework is the imaginary part of the *real-time static potential*, which has been extensively investigated in [58] and [59]. It is defined via the so-called *Wilson loop*, which is given on the lattice by [60]

$$L(x) := \text{Tr} \prod_{(x,\mu) \in \mathcal{C}} U_\mu(x), \quad (3.95)$$

where  $\mathcal{C}$  represents a closed loop of gauge links. For the computation of the static potential, we will only consider rectangle Wilson loops, which are always extended both in spacial and in time direction. In addition, temporal gauge (2.25) is applied and hence the time expansion becomes trivial.

The classical part of the real-time static potential can then be obtained from (cf. [59])

$$V_{\text{cl}}(t, r) = \text{i} \frac{\partial_t C_{\text{cl}}(t, r)}{C_{\text{cl}}(t, r)}, \quad (3.96)$$

where we introduced the average over Wilson loops with equal spacial extent,

$$C_{\text{cl}}(t, r) := \frac{1}{N_c} \left\langle L(t, \vec{r}) \right\rangle_{|\vec{r}|=r}. \quad (3.97)$$

In Figure 3.5 we show the results for the classical Wilson loop (3.97) and the imaginary part of the real-time static potential (3.96). With regard to possible differences in the thermalization process and the corresponding Gauss's law restoration (cf. Section 3.6.1), we see a very close match between the results presented in [59] and ours. Note, that we included two more spacial expansions,  $r/a_\sigma = 5$  and  $r/a_\sigma = 6$ .

We can thus assume a correct code implementation of the lattice equations of motion (3.76) in the absence of fermions. The equivalent implementation in the comoving framework will be cross-checked in Chapter 7.

### 3.8 Computation of classical-statistical observables

Expectation values of observables in statistical mechanics are calculated via the functional integral over all possible field configurations at initial time [55]

$$\langle \mathcal{O} \rangle = \int \mathcal{D}A_0 \mathcal{D}E_0 \rho_0[A_0, E_0] \mathcal{O}[A_{\text{cl}}, E_{\text{cl}}], \quad (3.98)$$

where  $\rho_0[A_0, E_0]$  is the initial *phase space density* (cf. also Section 2.4). Since we are interested in a classical description, the observables entering the integral have to be functionals of classical fields, which is indicated by their respective indices.

As we will see in Chapter 4, the initial fields  $A_0$  and  $E_0$  are based on randomly initialized variables. The expectation values can hence be evaluated by the ensemble average over  $N_{\text{conf}}$  initial configurations  $(A_0, E_0)$ ,

$$\langle \mathcal{O} \rangle \approx \frac{1}{N_{\text{conf}}} \sum_{(A_0, E_0)} \mathcal{O}[A_{\text{cl}}, E_{\text{cl}}]. \quad (3.99)$$

Thereby we introduce a statistical error, which we determine by the so-called *jackknife (resampling) method* [61]. According to this, the statistical error of an observable  $x$  is defined by the square root of the jackknife estimate of the variance,

$$\sigma(x) = \sqrt{\frac{N_{\text{conf}} - 1}{N_{\text{conf}}} \sum_{i=1}^{N_{\text{conf}}} (\langle x \rangle - \langle x \rangle_i)^2}, \quad (3.100)$$

where the respective averages are defined as

$$\langle x \rangle = \frac{1}{N_{\text{conf}}} \sum_{i=1}^{N_{\text{conf}}} \langle x \rangle_i \quad (3.101)$$

and

$$\langle x \rangle_i = \frac{1}{N_{\text{conf}} - 1} \sum_{j \neq i}^{N_{\text{conf}}} x_j, \quad i, j \in \{1, \dots, N_{\text{conf}}\}. \quad (3.102)$$

Since the initial configurations are drawn completely independently in our case, the jackknife estimate (3.100) does not suffer from autocorrelations and hence no binning is needed.

# Chapter 4

## The color glass condensate

---

### Contents

4.1	Introduction to the CGC framework and the MV model . . . . .	45
4.2	Initial conditions for the gauge link variables . . . . .	48
4.3	Initial conditions for the chromo-electric fields . . . . .	54

---

### 4.1 Introduction to the CGC framework and the MV model

The *color glass condensate* (CGC) is a type of matter, which consists of densely packed gluons at very high energy densities. The corresponding effective field theory was developed in the deep inelastic high energy limit at fixed squared momentum transfer  $Q^2$ , which can be summarized by [62]

$$x = \frac{Q^2}{2M\nu} \approx \frac{Q^2}{s} \rightarrow 0, \quad (4.1)$$

where  $x$  is the *Bjorken variable*, with the (nucleon) mass  $M$ , the energy loss  $\nu$  and the squared center of mass energy  $s$ . In this limit, which is sometimes referred to as the *Regge-Gribov limit* [63], the parton distribution function  $f$  is dominated for sufficiently large momentum transfers by the gluonic contributions which is demonstrated by Figure 4.1. This allows for a classical description as we discussed in Section 2.4.

In the CGC framework the dynamics of the system are captured by the weight functional  $W[\rho]$ . Its dependence on the Bjorken variable  $x$  is described by a non-linear renormalization group equation, which is referred to as the *JIMWLK equation*<sup>1</sup> [65–71]. In addition, this equation separates the dynamics of the plasma and the nuclear partons, where the former is considered at mid-rapidity ( $\eta \ll \eta_{\text{beam}}$ ) and the latter at the high-rapidity regime ( $\eta \lesssim \eta_{\text{beam}}$ ).

---

<sup>1</sup>JIMWLK includes the names Jalilian-Marian, Iancu, McLerran, Weigert, Leonidov and Kovner.

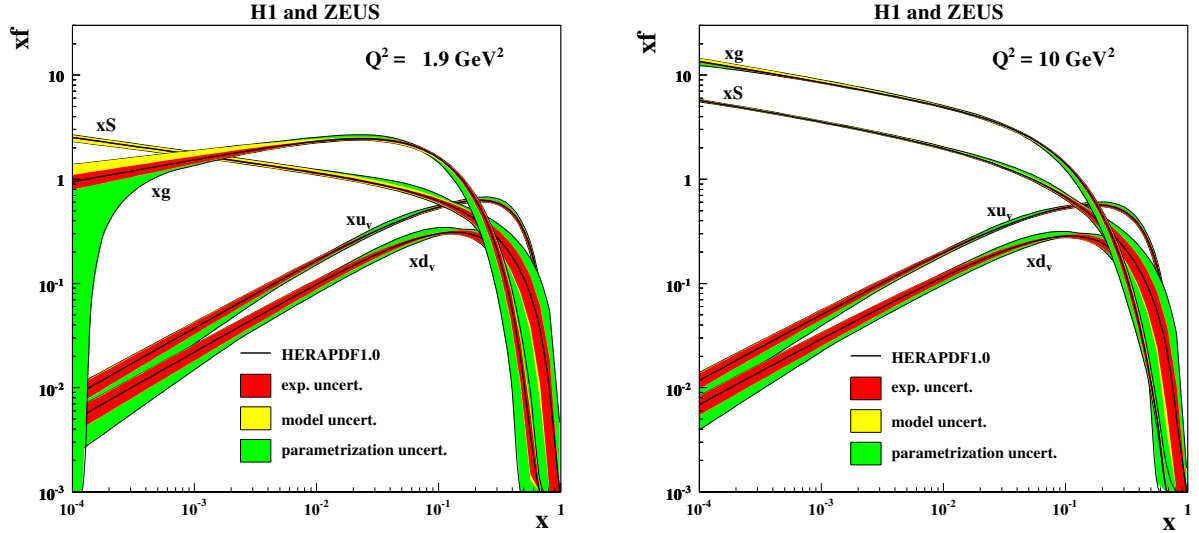


**Figure 4.1:** The parton distribution function at deep inelastic  $e^-p$  scattering experiments for valence quarks  $u_v$  and  $d_v$ , combined sea quarks  $S$  and gluons  $g$ , versus the Bjorken variable  $x$  for two different squared momentum transfers  $Q^2$ . The figure is taken from [64].

There are two effective degrees of freedom in this description: The first one being the color charge densities  $\rho$ , which are frozen due to time dilation and hence form a static current  $J^\mu$ , and the second one being the dynamical gauge fields  $A^\mu$ , which are coupled to this static current via the classical Yang-Mills equations,

$$D_\mu F^{\mu\nu} = J^\nu. \quad (4.2)$$

In the so-called *McLerran-Venugopalan (MV) model* [9–11] the non-Abelian current is given by

$$J^{\mu,a}(x) = \delta^{\mu+} \rho_1^a(x_\perp, x^-) + \delta^{\mu-} \rho_2^a(x_\perp, x^+), \quad (4.3)$$

where we defined  $\rho_1$  and  $\rho_2$  as the color charge densities of the two colliding nuclei and introduced the light-cone coordinates,

$$x^\pm = \frac{t \pm z}{\sqrt{2}}, \quad (4.4)$$

as well as the Kronecker delta  $\delta^{\mu\pm}$ , which forces the current to reside at the positive and negative light-cone, respectively.

In the originally proposed MV model a single infinitely thin sheet of color charge was suggested, i.e.,  $\rho^a(x_\perp, x^\pm) \rightarrow \delta(x^\pm) \rho^a(x_\perp)$ . However, this assumption has proven insufficient [72, 73]. A promising approach is to independently construct  $N_y$  of these sheets allowing for the computation of so-called *Wilson lines* in longitudinal direction, which maintains gauge-covariance in that very direction [72]. A corresponding illustration is given in Figure 4.2.

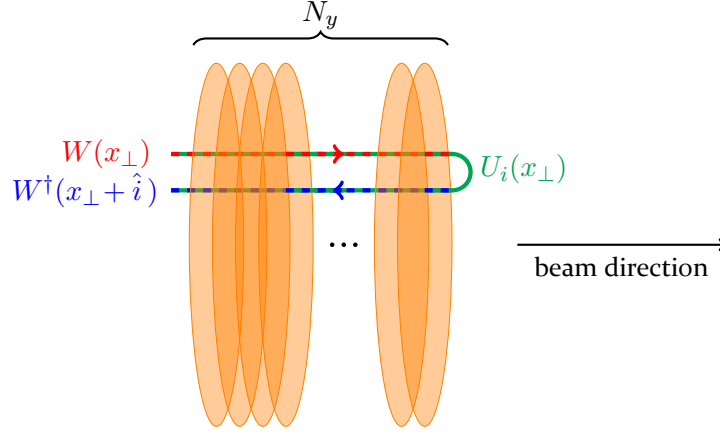


**Figure 4.2:** The  $N_y$  infinitesimal sheets in longitudinal direction describing one of the two colliding nuclei, with the Wilson line  $W$  and the initial gauge field component  $U_i$ .

Note, that the number of sheets  $N_y$  must not be confused with the number of lattice points in  $y$ -direction. For the latter we solely use  $N_\perp$ , since the two transverse lattice extents are always identical in our description. Even though the expansion is in rapidity-direction, i.e.  $\eta$ -direction, we have to distinguish it from the lattice extent in that direction, which is called  $N_\eta$ . Hence, since the rapidity is also sometimes indicated by  $y$ , we stick to the commonly used designation  $N_y$ .

The distribution of the color charge densities in the transverse plane is assumed to be Gaussian with variance  $g^4\mu^2$ , where  $\mu^2$  is the color charge squared per unit area [28]. The value  $g^2\mu$ , sometimes referred to as the *MV parameter*, is closely related to the so-called *saturation scale*  $Q_s$ , which we will introduce in the following. A detailed study of the connection between  $g^2\mu$  and  $Q_s$  as well as the influence of different system parameters on their relation is given in [73]. For now we can assume

$$Q := g^2\mu \approx Q_s. \quad (4.5)$$

As mentioned before, in the CGC framework we have a very high occupation of the gluonic degrees of freedom yielding a rapid growth of the gluon density. On the other hand, the size of a hadron can be considered roughly constant, since it only grows very slowly by increasing the energy of the system [74]. The density of gluons with a fixed size is hence limited due to repulsive interactions. However, it is possible to pack more gluons of a smaller size into the hadron (cf. Figure 4.3). The inverse of the saturation scale  $Q_s$  then defines the size of the smallest gluons that are densely packed.

A more precise definition is given in [73], where the saturation scale  $Q_s$  is defined as the absolute value of the transverse momentum that maximizes the Fourier transformed longitudinal Wilson line weighted by the square of the corresponding momentum.

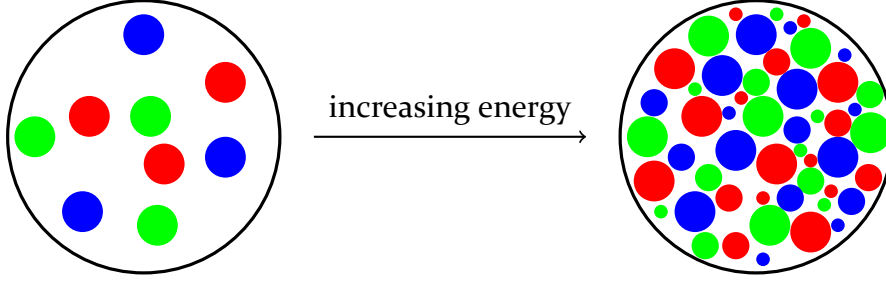


**Figure 4.3:** The rise in the gluon density due to the increasing energy.

## 4.2 Initial conditions for the gauge link variables

We will mostly follow [75], where a lattice description of the originally proposed MV model is provided. However, as discussed in the last section, we extend this model by longitudinal randomness à la [72] yielding the initial conditions presented in [73]. As also done in the latter work, we introduce an IR cutoff  $m$  in order to incorporate the color neutrality phenomenon studied in [76], in other words, it provides a finite scale at which objects – in our case nucleons – are color neutral.

The only scale entering the initial conditions is the MV parameter  $Q$ . As introduced in the preceding section, it has energy dimension 1 and, as a consequence, the color charge density  $\rho$  has the energy dimension 2 (cf., e.g., eq. (4) of [75]). Hence, we define dimensionless lattice versions of these two quantities,

$$\bar{\rho} := a_{\perp}^2 \rho, \quad \bar{Q} := a_{\perp} Q. \quad (4.6)$$

We are now able to write down the initial conditions for the gauge fields  $U^k$ , where  $k \in \{1, 2\}$  designates the respective nucleus.

The longitudinal component is set unity,

$$U_{z|\eta}^k = 1, \quad (4.7)$$

while the construction of the transverse components  $U_i^k$ , with  $i \in \{x, y\}$  (here and in the following), is more involved. The initialization process can be subdivided into the following steps:

- (i) Initialize the dimensionless color charge densities  $\bar{\rho}_1$  and  $\bar{\rho}_2$  on the two-dimensional subspace, where the longitudinal component ( $z|\eta$ ) is 0, according to

$$\begin{aligned} \langle \bar{\rho}_v^{k,a}(x_{\perp}) \bar{\rho}_w^{l,b}(y_{\perp}) \rangle &= a_{\perp}^4 \frac{g^4 \mu^2}{N_y} \delta_{vw} \delta^{kl} \delta^{ab} \delta(x_{\perp} - y_{\perp}) \\ &\equiv \frac{\bar{Q}^2}{N_y} \delta_{vw} \delta^{kl} \delta^{ab} \delta(x_{\perp} - y_{\perp}), \end{aligned} \quad (4.8)$$

with  $N_y$  being the number of infinitesimal sheets in longitudinal direction (cf. Figure 4.2).

(ii) Solve Poisson's equation<sup>2</sup> to get the dimensionless color potentials  $\Lambda$ ,

$$[\Delta_L + m^2]\Lambda_v^{k,a}(x_\perp) = -\bar{\rho}_v^{k,a}(x_\perp), \quad \Lambda_v^k \equiv T^a \Lambda_v^{k,a}. \quad (4.9)$$

(iii) Repeat the previous steps and construct  $N_y$  independent auxiliary fields

$$V_v^k(x_\perp) = \exp [i\Lambda_v^k(x_\perp)], \quad v = 1, \dots, N_y, \quad (4.10)$$

and then construct the Wilson lines in longitudinal direction,

$$W^k(x_\perp) = \prod_{v=1}^{N_y} V_v^k(x_\perp). \quad (4.11)$$

(iv) Use the Wilson lines to build the initial gauge field components of the colliding nuclei in a gauge invariant manner,

$$U_i^k(x_\perp) = W^k(x_\perp)W^{k\dagger}(x_\perp + \hat{i}). \quad (4.12)$$

We can easily confirm that the constructed fields  $U_i^k$  are, as required, elements of the special unitary group of degree  $N_c$  by the following line of implications:

$$\begin{aligned} \rho_v^{k,a} \in \mathbb{R} &\Rightarrow \Lambda_v^{k,a} \in \mathbb{R} \Rightarrow \Lambda_v^k \in \mathfrak{su}(N_c) \\ &\Rightarrow V_v^k \in \mathbf{SU}(N_c) \Rightarrow W^k \in \mathbf{SU}(N_c) \Rightarrow U_i^k \in \mathbf{SU}(N_c). \end{aligned} \quad (4.13)$$

On the lattice, the distribution of the color charge densities (4.8) is realized by initializing standard Gaussian distributed random numbers, which are then multiplied by the appropriate weight,

$$\bar{\rho} = \frac{\bar{Q}}{\sqrt{N_y}} X, \quad X \sim \mathcal{N}(0, 1). \quad (4.14)$$

This random initialization is performed independently for each of the two nuclei, each of the  $N_g$  color components, each of the  $N_y$  longitudinal sheets and each of the  $N_\perp^2$  transverse lattice points.

After the initialization of the gauge fields  $U^k$  which describes the two individual nuclei, we are finally able to construct the collective initial gauge field  $U$  by solving the following set of equations [75]

$$\text{Tr} \left\{ T^a \left[ (U^{(1)} + U^{(2)})(1 + U^\dagger) - \mathbf{h. c.} \right] \right\} = 0, \quad a \in \{1, \dots, N_g\}. \quad (4.15)$$

For the sake of simplicity and easier reading, we omitted the index  $i \in \{x, y\}$  as well as the argument  $x_\perp$ . These are  $N_g$  equations for  $N_g$  parameters, since  $U = \exp(i\alpha_b T^b)$ , with  $b \in \{1, \dots, N_g\}$ .

<sup>2</sup>In Section 4.2.1 the procedure of solving Poisson's equation on the lattice is extensively described.

At the moment, the initial conditions are defined on a single transverse slice. In the boost-invariant case, where no longitudinal fluctuations are considered, it is hence sufficient to perform 2D simulations. However, if we consider the 3D scenario, the field  $U$  obtained from (4.15), as well as  $U^{(1)}$  and  $U^{(2)}$  which – as we will see in the next section – are needed for the initialization of the chromo-electric field  $E$ , are copied from the initial transverse  $x$ - $y$ -plane (where  $z|\eta = 0$ ) to all the remaining transverse slices.<sup>3</sup>

As mentioned in the introduction we will consider  $N_c = 2$  and  $N_c = 3$  colors and in the first case there exists a closed expression for the collective gauge fields, which we will elaborate in the following.

Let us define the matrix  $M := (U^{(1)} + U^{(2)})(1 + U^\dagger)$ . This matrix is in the case of  $N_c = 2$  colors again an element of  $SU(2)$  multiplied by a real constant, which can easily be shown via the following group representation:

$$SU(2) = \left\{ \begin{pmatrix} \alpha & -\beta^* \\ \beta & \alpha^* \end{pmatrix} : \alpha, \beta \in \mathbb{C}, |\alpha|^2 + |\beta|^2 = 1 \right\}. \quad (4.16)$$

Now we use the fact, that every matrix can be split up into a hermitian and an anti-hermitian part, i.e.  $M = \frac{1}{2}(M + M^\dagger) + \frac{1}{2}(M - M^\dagger) \equiv M_h + M_{ah}$ . Obviously, the hermitian part solves (4.15) trivially, whereas the anti-hermitian one does not. Moreover, if we assume the latter to be traceless, we find

$$\begin{aligned} 0 &= \text{Tr} \left[ T^a (M_{ah} - M_{ah}^\dagger) \right] = 2 \text{Tr} [T^a M_{ah}] \stackrel{(*)}{=} -2i \text{Tr} \left[ T^a \sum_b \alpha_b T^b \right] \\ &= -2i \sum_b \alpha_b \text{Tr} [T^a T^b] = -i\alpha_a \quad \Rightarrow \quad M_{ah} = 0. \end{aligned} \quad (4.17)$$

In (\*) we used the assumption that  $\text{Tr}(M_{ah}) = 0$  which means that  $iM_{ah} \in \mathfrak{su}(2)$ , since  $iM_{ah}$  is hermitian by construction, and in the last step we utilized the normalization relation of the generators (2.1).

Since the anti-hermitian part of an  $SU(2)$  matrix is always traceless we have shown that  $M$  is hermitian. It can also be obtained from (4.16), that the hermitian part is proportional to the identity and hence we find that (4.15) is equivalent to

$$M \equiv (U^{(1)} + U^{(2)})(1 + U^\dagger) = c \iff U^\dagger = c(U^{(1)} + U^{(2)})^{-1} - 1, \quad (4.18)$$

where  $c \in \mathbb{R}$  and  $(\cdot)^{-1}$  indicates the matrix inversion. Using the fact that  $U \in SU(2)$ ,

<sup>3</sup>As a consequence, all initial plaquettes  $U_{\mu\nu}$  with  $\mu = z|\eta$  or  $\nu = z|\eta$  are equal to one, since  $U_{z|\eta} = 1$ ,  $U_i(x_\perp) = U_i(x_\perp + \hat{z})$  and  $UU^\dagger = 1$ .



which in particular means that  $U$  is unitary, leads to<sup>4</sup>

$$\begin{aligned}
 1 &= [c(U^{(1)\dagger} + U^{(2)\dagger})^{-1} - 1] [c(U^{(1)} + U^{(2)})^{-1} - 1] \\
 \Leftrightarrow 0 &= c(U^{(1)\dagger} + U^{(2)\dagger})^{-1}(U^{(1)} + U^{(2)})^{-1} - (U^{(1)} + U^{(2)})^{-1} - (U^{(1)\dagger} + U^{(2)\dagger})^{-1} \\
 \Leftrightarrow c &= (U^{(1)\dagger} + U^{(2)\dagger}) + (U^{(1)} + U^{(2)}). \tag{4.19}
 \end{aligned}$$

Since the fields representing the colliding nuclei,  $U^{(1)}$  and  $U^{(2)}$ , are also elements of  $SU(2)$ , their traces are real, yielding  $\text{Tr}(U^{(1,2)}) = \text{Tr}(U^{(1,2)\dagger})$  and thus

$$c \text{Tr}(1) = 2 \text{Tr}(U^{(1)} + U^{(2)}) \Rightarrow c = \text{Tr}(U^{(1)} + U^{(2)}). \tag{4.20}$$

Finally, by inserting (4.20) into (4.18) we obtain that – in the case of  $SU(2)$  – the conditional equation (4.15) reduces to

$$U = \text{Tr}(U^{(1)} + U^{(2)})(U^{(1)\dagger} + U^{(2)\dagger})^{-1} - 1 = (U^{(1)} + U^{(2)})(U^{(1)\dagger} + U^{(2)\dagger})^{-1}, \tag{4.21}$$

where we used (4.19) together with (4.20) to get the second equality.

In the case of  $N_c = 3$  colors there is no closed expression such as (4.21) and thus (4.15) has to be solved numerically. The corresponding algorithm is summarized in the flowchart depicted in Figure 4.4.

---

<sup>4</sup>To get to the last equation we multiplied by  $(U^{(1)\dagger} + U^{(2)\dagger})$  and  $(U^{(1)} + U^{(2)})$  from the left and right side, respectively.

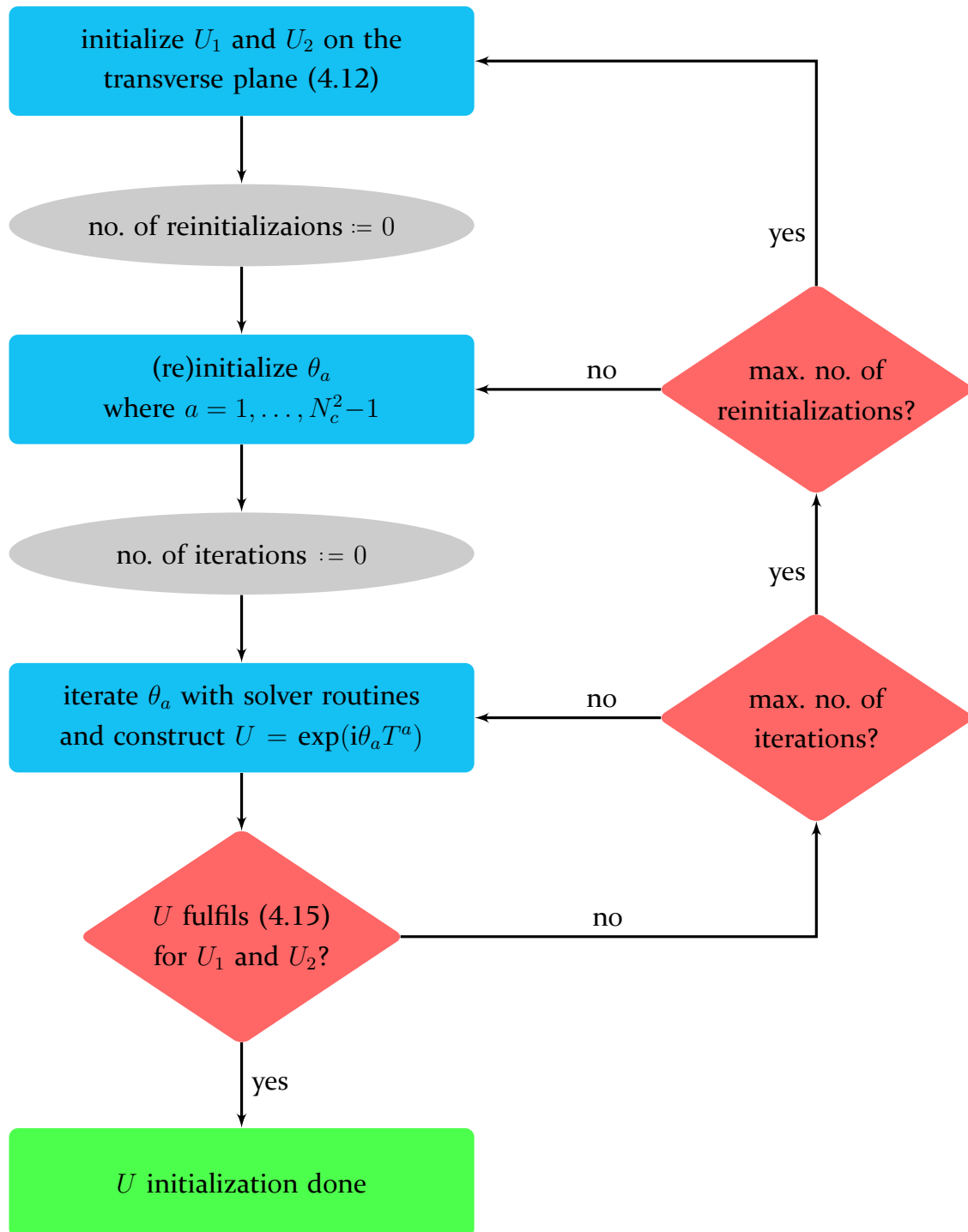


**Figure 4.4:** Flowchart of the initialization process of the collective gauge field  $U$  used in the case of  $N_c = 3$  colors.

### 4.2.1 Solving Poisson's equation on the lattice

This subsection aims on the solution of (4.9) on the lattice in order to get the color potentials  $\Lambda_m^a$ . As discussed in the preceding section, we have a two-dimensional problem yielding

$$\frac{1}{a_\sigma^2} \sum_{i=x,y} \left[ \Lambda(x_\perp + \hat{i}) - 2\Lambda(x_\perp) + \Lambda(x_\perp - \hat{i}) + m^2 \Lambda(x_\perp) \right] = -\rho(x_\perp), \quad (4.22)$$

where we wrote out the lattice Laplacian  $\Delta_L$ .

We now perform a Fourier transformation, which has two advantages: Firstly, the equation is analytically solvable and secondly, we can introduce an additional ultraviolet (UV) momentum cutoff. Following Appendix B.2.3, this yields

$$\Lambda(x, y) = \frac{1}{\sqrt{N_1 N_2}} \sum_{p_1, p_2} \tilde{\Lambda}(p_1, p_2) e^{i(p_1 x + p_2 y)}, \quad (4.23)$$

where the Fourier transformed color potentials are given by

$$\tilde{\Lambda}(p_1, p_2) = \frac{\tilde{\rho}(p_1, p_2)}{4 - e^{ip_1} - e^{-ip_1} - e^{ip_2} - e^{-ip_2} + m^2}. \quad (4.24)$$

Looking carefully at (4.24), one realizes that in the case of no IR cutoff ( $m = 0$ ) the zero mode  $(p_1, p_2) = (0, 0)$  represents a singularity. However, this singularity becomes negligible in the continuum limit,  $N_1, N_2 \rightarrow \infty$ , for two reasons:

- $\tilde{\rho}(0, 0) = \frac{1}{\sqrt{N_1 N_2}} \sum_{x,y} \rho(x, y) \rightarrow 0$  due to the (symmetric) Gaussian distribution of the color sources  $\rho(x, y)$ .
- The sum merges into an integral and hence, the contribution of the point  $(0, 0)$  has Lebesgue measure zero and can be excluded.

There are now two possible ways to handle this issue for finite values of  $N_\perp$ :

1. We exclude the point  $\tilde{\Lambda}(0, 0)$  and accept small discrepancies in the solution of (4.9) for  $\Lambda(x, y)$ . In fact, the deviation is  $\frac{1}{N_1 N_2} \sum_{x,y} \rho(x, y) = \frac{\tilde{\rho}(0,0)}{\sqrt{N_1 N_2}}$ , which vanishes very fast by increasing the size of the transverse plane, since, as mentioned, even the numerator approaches 0.

or

2. We make our distribution artificially symmetric by subtracting  $\frac{1}{N_1 N_2} \sum_{x,y} \rho(x, y)$  from the initialized  $\rho$  field at every point on the transverse plane. As a consequence  $\rho$  is now “perfectly Gaussian” and (4.9) is fulfilled up to numerical precision.

In our computations we adopt the second approach since the initial idea was to have a Gaussian distributed  $\rho$  without any shift. In addition, this choice yields color neutrality of the colliding nuclei for every single sample.

### 4.3 Initial conditions for the chromo-electric fields

The initialization of the chromo-electric fields depends on the one of the gauge fields and thus has to be performed afterwards. In the boost-invariant case, only the longitudinal components of the chromo-electric fields have a non-zero initialization [28, 75, 77],

$$\begin{aligned} \bar{E}_{z|\eta}(x) = & -\frac{i}{4} \sum_{i=1,2} \left\{ \left[ U_i(x) - 1 \right] \left[ U_i^{(2)\dagger}(x) - U_i^{(1)\dagger}(x) \right] - \text{h. c.} \right. \\ & \left. + \left[ U_i^\dagger(x - \hat{i}) - 1 \right] \left[ U_i^{(2)}(x - \hat{i}) - U_i^{(1)}(x - \hat{i}) \right] - \text{h. c.} \right\}, \end{aligned} \quad (4.25)$$

$$\bar{E}_{z|\eta}^a(x) = 2 \text{Tr} \left[ T^a \bar{E}_{z|\eta}(x) \right]. \quad (4.26)$$

(4.26) can serve as a test to see whether  $\bar{E}_{z|\eta} \in \text{su}(N_c)$  or not. For  $N_c = 2$ , (4.26) is fulfilled by construction, whereas for  $N_c = 3$  the situation is different. To see this, we simplify (4.25) to  $B = i(A - A^\dagger)$  and recall that

$$M = M^\dagger \text{ and } \text{Tr} M = 0 \Leftrightarrow M \in \text{su}(N_c). \quad (4.27)$$

One can easily see, that  $B = B^\dagger$ , however,  $\text{Tr} B = 2i \text{Im}[\text{Tr} A]$ . Following the line of argumentation below (4.15), we know that  $A \equiv a A_{\text{SU}(2)}$ , with  $a \in \mathbb{R}$  and  $A_{\text{SU}(2)} \in \text{SU}(2)$ . Since the trace of an  $\text{SU}(2)$  matrix is real,  $\text{Tr} B = 0$  and hence  $\bar{E}_{z|\eta} \in \text{su}(2)$ .

In the case of  $N_c = 3$  colors this is generally not the case, which is why we use (4.26) to project the fields  $\bar{E}_{z|\eta}$  back to  $\text{su}(3)$ . Note, that this means we are setting  $\text{Tr} \bar{E}_{z|\eta} = 0$  in a convenient way.

To sum up, the initial conditions for the chromo-electric fields read:

$$\bar{E}_\perp(x) = 0 \quad (4.28)$$

$$\begin{aligned} \bar{E}_{z|\eta}^a(x) = & -\frac{i}{2} \sum_{i=1,2} \text{Tr} \left\{ T^a \left( \left[ U_i(x) - 1 \right] \left[ U_i^{(2)\dagger}(x) - U_i^{(1)\dagger}(x) \right] \right. \right. \\ & \left. \left. + \left[ U_i^\dagger(x - \hat{i}) - 1 \right] \left[ U_i^{(2)}(x - \hat{i}) - U_i^{(1)}(x - \hat{i}) \right] \right) - \text{h. c.} \right\} \end{aligned} \quad (4.29)$$

The global sign in (4.29) is convention and irrelevant for our observables since it appears in the equations of motion of both the gauge fields and the electric fields. Hence, it is the same like a mirroring of the spacial coordinates. We verified this statement also numerically.

#### 4.3.1 Rapidity fluctuations

Instead of the idealized  $\delta$ -function in (4.8), a more realistic scenario would include color sources with a finite width. To this end, we follow [28] and add  $\eta$ -dependent fluctuations  $\delta E$  to the initial conditions introduced in Section 4.2. Besides the restrictions through

Gauss's law (cf. Section 3.6), the fluctuations can be chosen arbitrarily and thus we set them to fulfill Gauss's law trivially, which means in the continuum,

$$D_i \delta E_i + D_\eta \delta E_\eta = 0. \quad (4.30)$$

Hence, the following definitions are appropriate,

$$\begin{aligned} \delta E_i(x_\perp, \eta) &:= D_\eta F_i(x_\perp, \eta), \\ \delta E_\eta(x_\perp, \eta) &:= -D_i F_i(x_\perp, \eta), \end{aligned} \quad (4.31)$$

where  $F_i(x_\perp, \eta)$  is a twice continuously differentiable function. By recalling the energy dimensions in comoving coordinates of the covariant derivatives and the chromo-electric fields, we can determine the dimension of  $F_i$ ,

$$\begin{aligned} [\delta E_i] = [E_i] = 1, \quad [\delta E_\eta] = [E_\eta] = 2, \\ [D_i] = \left[ \frac{1}{L} \right] = 1, \quad [D_\eta] = [1] = 0, \\ \Rightarrow [F_i] = 1. \end{aligned} \quad (4.32)$$

Thus, with the definition

$$\bar{F}_i := g a_\perp F_i \quad (4.33)$$

we can rewrite (4.31) in terms of dimensionless quantities,

$$\delta \bar{E}_i(x_\perp, \eta) = D_\eta \bar{F}_i(x_\perp, \eta), \quad (4.34a)$$

$$\delta \bar{E}_\eta(x_\perp, \eta) = -\bar{D}_i \bar{F}_i(x_\perp, \eta). \quad (4.34b)$$

On the lattice, we have to insert the lattice equivalent of the continuous covariant derivatives, which we do by backward difference quotients (cf. (3.16) and Appendix B.1), yielding

$$\delta \bar{E}_i(x) = \frac{1}{a_\eta} [\bar{F}_i(x) - \bar{F}_i(x - \hat{\eta})], \quad (4.35a)$$

$$\delta \bar{E}_\eta(x) = -\sum_i [\bar{F}_i(x) - U_i^\dagger(x - \hat{i}) \bar{F}_i(x - \hat{i}) U_i(x - \hat{i})]. \quad (4.35b)$$

We applied the CGC initial conditions for the longitudinal gauge fields (4.7), which transforms the covariant derivative  $D_\eta$  in (4.35a) into an ordinary partial derivative  $\partial_\eta$ .

For the definition of  $\bar{F}_i$  we use a product approach to separate the transverse from the rapidity dependency. Since we are primarily interested in the instability behavior of the system, we perturb our initial setup only by a single  $\eta$ -mode, while the dependence of the transverse coordinate  $x_\perp$  is determined by the random based generated elements  $\xi_i(x_\perp)$ . We thus define

$$\bar{F}_i(x_\perp, \eta) := f(\eta) \xi_i(x_\perp) := \Delta \cos\left(\frac{2\pi\eta}{L_\eta}\right) \xi_i(x_\perp), \quad (4.36)$$

where  $\Delta$  is the real-valued amplitude of the initial fluctuations.

Since  $E$  is an element of the Lie algebra,  $\delta\bar{E}_i$  as well as  $\delta\bar{E}_\eta$  also have to be elements of the Lie algebra and hence the same holds for  $\xi_i$ , i.e.  $\xi_i = \xi_i^a T^a \in \mathfrak{su}(N_c)$ , where the real-valued constants  $\xi_i^a$  are in our case generated as Gaussian random numbers,

$$\xi_i^a(x_\perp) = X(x_\perp), \quad X \sim \mathcal{N}(0, 1). \quad (4.37)$$

### 4.3.2 Translation to the static box

The equivalent of (4.31) in our static box framework is

$$\delta E_\perp(x) = D_z F_\perp(x), \quad (4.38a)$$

$$\delta E_z(x) = -D_\perp F_\perp(x), \quad (4.38b)$$

which fulfills Gauss's law in ordinary Minkowski coordinates trivially. We can easily read off the corresponding energy dimensions,

$$\begin{aligned} [\delta E_i] = [E_i] = 2, \quad [D_i] = \left[ \frac{1}{L} \right] = 1, \\ \Rightarrow [F_\perp] = 1. \end{aligned} \quad (4.39)$$

Following the same steps as in the case of the expanding system, we get the lattice version of (4.38) for the rescaled fields (4.33),

$$\delta\bar{E}_\perp(x) = [\bar{F}_\perp(x) - \bar{F}_\perp(x - \hat{\eta})], \quad (4.40a)$$

$$\delta\bar{E}_z(x) = - \sum_{i \neq z} [\bar{F}_i(x) - U_i^\dagger(x - \hat{i}) \bar{F}_i(x - \hat{i}) U_i(x - \hat{i})], \quad (4.40b)$$

with

$$\bar{F}_\perp(x_\perp, z) := f(z) \xi_\perp(x_\perp) := \Delta \cos\left(\frac{2\pi z}{L_z}\right) \xi_\perp(x_\perp) \quad (4.41)$$

and  $\xi_\perp = \xi_\perp^a T^a$  randomly drawn according to (4.37). Since we are using an isotropic framework in the static box case, i.e.  $a_z = a_\perp \Leftrightarrow \bar{a}_z = 1$ , there is no prefactor in (4.40a).

# Chapter 5

## Technical aspects

---

### Contents

5.1	Lattice parameters . . . . .	57
5.2	Introducing a physical scale . . . . .	59
5.3	UV cutoff . . . . .	61
5.4	Courant-Friedrichs-Lewy condition . . . . .	62

---

### 5.1 Lattice parameters

Our lattice simulations are performed on a 2D or 3D spacial grid, depending on whether longitudinal fluctuations are taken into account or not. In order to ease the numerical implementation, we apply – as commonly done – *periodic boundary conditions* in the spacial coordinates. All fields are then evolved in time by the equations of motions given in (3.76) or (3.77), respectively.

Furthermore, there is a variety of parameters involved in the lattice computations, which we will define and try to enlighten by the following list:

#### General lattice parameters

- *transverse lattice spacing*  $a_{\perp}$ : determines the smallest length scale and is used to construct dimensionless quantities of all dimensioned observables
- *longitudinal lattice spacing*  $a_{z|\eta}$ : equal to the transverse lattice spacing in the static box, i.e.  $a_z = a_{\perp} \equiv a_{\sigma}$ , but set independently in the expanding system due to its different dimension (cf. Section 2.2.2)
- *temporal “lattice” spacing*  $a_{t|\tau}$ : defines the time discretization used to iteratively solve the lattice equations of motion (3.76)/(3.77)

- *transverse lattice extent*  $N_{\perp}$
- *longitudinal lattice extent*  $N_{z|\eta}$
- *time evolution steps*  $N_{t|\tau}$ : defines together with  $a_{t|\tau}$  the total length of the system's time evolution
- *number of configurations*  $N_{\text{conf}}$ : defines the number of performed measurements used to build the ensemble average (3.99)
- *Gauss's law parameters*:
  - *max. Gauss violation*: determines the tolerated deviation of Gauss's law (cf. Section 3.6)
  - *max. Gauss iteration*: defines the maximum number of iterations within the restoring algorithm (cf. Section 3.6.1)
  - *Gauss  $\gamma$* : defines the real-valued constant in (3.87)

### Fermionic parameters

- *coupling constant*  $g$ : defines the strength of the interaction between the fermionic degrees of freedom and the gauge fields
- *Wilson parameter*  $r$ : switches the doubler term on ( $r = 1$ ) or off ( $r = 0$ ), i.e. removes ( $r = 1$ ) the unphysical doublers in (3.28) or not ( $r = 0$ )
- *number of fermions*  $N_{\text{ens}}$ : defines the ensemble size of gendered fermions in (3.42)
- *fermionic mass*  $m_{\psi}$ : determines the mass of the gendered fermions
- *fermionic temperature*  $T_{\text{init}}$ : defines the initial temperature of the gendered fermions via (3.40)

### CGC parameters

- *MV parameter*  $Q$ : sets the overall scale via the combination  $a_{\perp}Q \equiv \bar{Q}$ , which enters the initial conditions through (4.8)
- *IR cutoff*  $m$ : determines the scale at which objects are color neutral (cf. discussion at the beginning of Section 4.2)
- *UV cutoff*  $\Lambda$ : additional to the intrinsic lattice UV cutoff (will be discussed in detail in Section 5.3)
- $N_y$ : number of infinitesimal sheets in longitudinal direction used in (4.8) (cf. also Figure 4.2)
- $\Delta$ : the amplitude of the longitudinal fluctuations defined in (4.41)/(4.36)



- *solver parameters* (only relevant for  $N_c = 3$ ):
    - *solver  $\epsilon$* : defines the tolerated deviation of (4.15)
    - *max. iterations*
    - *max. reinitializations*
- } cf. flowchart in Figure 4.4

While some of these parameters are of pure numerical nature, others can be restricted by physical considerations or even be determined by observations stemming from heavy-ion collisions. We will focus on parts of this in the following section and present a detailed study of the parameter space in Chapter 7.

## 5.2 Introducing a physical scale

Classical Yang-Mills theory in four dimensions is scale invariant and exhibits conformal invariance [78]. However, a physical scale enters through the CGC initial conditions, more precisely through the only dimensioned parameter  $Q$ , which is related to the saturation scale  $Q_s$  (cf. Chapter 4).

Together with the transverse lattice spacing  $a_\perp$ , which is both in the Minkowski and in the comoving formulation dimensional, one can then construct dimensionless combinations that can be matched to physical observables. In the common literature, this is done via the size of the colliding nuclei, which are spread over the whole transverse plane. Hence, for a central collision and equal nuclei, the diameter is equivalent to the transverse lattice size  $L_\perp = N_\perp a_\perp$ .

Assuming that the colliding nuclei correspond to gold (Au) atoms, the nuclear radius can be estimated by [79]

$$R_{\text{Au}} = r_0 A^{1/3} \approx 1.2 \times 197^{1/3} \text{ fm} \approx 7 \text{ fm}, \quad (5.1)$$

with the nucleon number  $A$  and the nuclear radius constant  $r_0$ .

Identifying the size of the transverse lattice plane  $L_\perp^2$  with the transverse extent of the nucleus  $\pi R_{\text{Au}}^2$  and making use of  $Q \approx Q_s$  (cf. (4.5) and the preceding discussion), we find

$$QL_\perp \equiv g^2 \mu a_\perp N_\perp \equiv 120, \quad (5.2)$$

where a value in range of expectations for ultra-relativistic heavy-ion collision at the LHC ( $Q_s \approx 2 \text{ GeV}$  [80]) was chosen. We will stick to this choice and fix  $Q = 2 \text{ GeV}$  as well as  $QL_\perp = 120$  for our simulations throughout this work. Consequently, it makes sense to express all results for our observables as dimensionless ratios of  $Q$ .

Note, that (5.2) also sets the value for the transverse lattice spacing,

$$a_\perp = \frac{L}{N_\perp} = \frac{120}{QN_\perp} \approx \frac{12}{N_\perp} \text{ fm}. \quad (5.3)$$

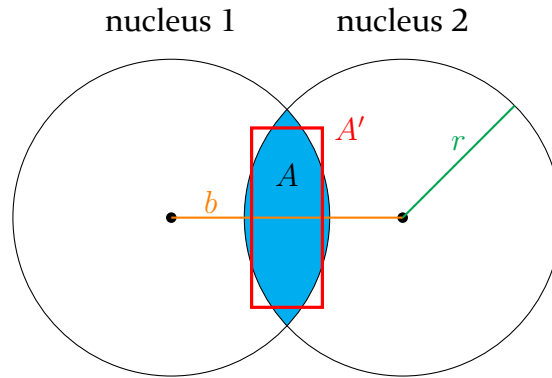


**Figure 5.1:** Illustration of the overlap area  $A$  and the impact parameter  $b$  for two colliding nuclei with the same radius  $r$ . The rectangle describes the approximated lattice area  $A'$ .

As soon as we include longitudinal fluctuations (cf. Section 4.3), the corresponding longitudinal lattice spacing  $a_{z|\eta}$  has to be fixed as well. In the static box we work with an isotropic spatial lattice, yielding  $a_z = a_\perp$ , whereas the 3D simulations in comoving coordinates are performed at  $a_\eta N_\eta = 2.0$  as proposed, e.g., in [81].

### 5.2.1 Towards non-central collisions

Since we are utilizing periodic boundary conditions in the spacial coordinates, the identification of the size of a nucleus with that of the transverse lattice plane seems to be contradictory. In the following, we will develop a possible way to circumvent this issue.

The basic idea is to use the CGC initial conditions only within a small subset of our transverse plane, which then represents the overlap of the two colliding nuclei. At all other points the color charge density is set to zero. This results in the possibility to study *non-central* collisions and introduces a new parameter, the so-called *impact parameter*  $b$ . It defines the closest distance between the center of the two colliding nuclei and thus also fixes the overlap area, which we then approximate on the lattice by a rectangle as depicted in Figure 5.1.

The approximated lattice overlap area is given by

$$A' = L_x^{\text{nucl}} L_y^{\text{nucl}} \equiv a_\perp^2 N_x^{\text{nucl}} N_y^{\text{nucl}}, \quad (5.4)$$

with this respective (lattice) lengths in  $x$ - and  $y$ -direction. A corresponding illustration is given in Figure 5.2.

Obviously, the overall transverse lattice size has to be large enough to avoid boundary effects, i.e.  $N_\perp \gg N_{x,y}^{\text{nucl}}$ . However, as we will see later, very large lattices are needed in order to achieve negligible discretization effects, which entails a tremendous computational effort. This obviously increases even further, if we do not use the scenario which we introduced in the last section, where the nucleus is spread over the whole transverse plane.

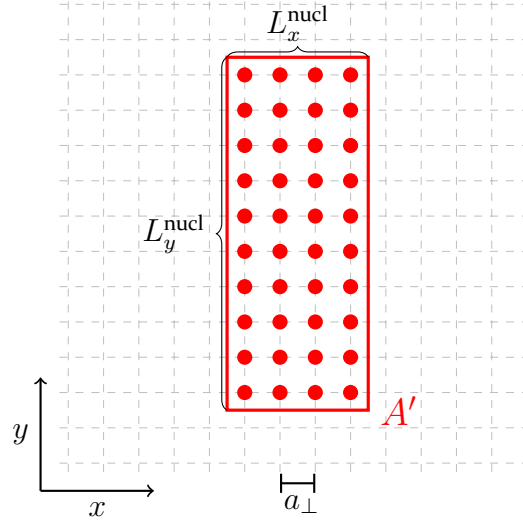


**Figure 5.2:** Implementation of the approximated lattice area  $A'$  into the transverse plane. Here, we have  $A' = 4 a_{\perp} \times 10 a_{\perp}$ .

Hence, if it turns out that the boundary effects are sufficiently small, which is plausible due to the large overall scale of around 12 fm (cf. (5.3)), we will use  $N_x^{\text{nucl}} = N_y^{\text{nucl}} = N_{\perp}$ . The corresponding numerical investigation is given in Chapter 7.

### 5.3 UV cutoff

For a  $d$ -dimensional lattice  $\mathbb{A}$  the reciprocal lattice  $\tilde{\mathbb{A}}$  is defined in momentum space via (cf. e.g. [60])

$$\tilde{\mathbb{A}} = \left\{ p = (p_1, \dots, p_d) \mid p_{\mu} = \frac{2\pi}{a_{\mu} N_{\mu}} (k_{\mu} + \Theta_{\mu}), k_{\mu} = -\frac{N_{\mu}}{2} + 1, \dots, \frac{N_{\mu}}{2} \right\}. \quad (5.5)$$

Employing periodic boundary conditions, we have  $\Theta_{\mu} = 0$ , yielding<sup>1</sup>

$$\tilde{\mathbb{A}} = \left\{ p = (p_1, \dots, p_d) \mid p_{\mu} = \frac{2\pi}{a_{\mu} N_{\mu}} k_{\mu}, k_{\mu} = -\frac{N_{\mu}}{2} + 1, \dots, \frac{N_{\mu}}{2} \right\}. \quad (5.6)$$

Hence, every finite lattice calculation introduces a UV momentum cutoff which is proportional to the inverse of the lattice spacing  $a$ , since the highest possible momentum component on our lattice is given by

$$p_{\mu, \max} = \frac{\pi}{a_{\mu}}. \quad (5.7)$$

Consequently, for our 2D initialization the highest possible transverse lattice momentum is set by

$$|p_{\perp, \max}| \equiv \sqrt{\sum_{i=1,2} p_{i, \max}^2} = \sqrt{2} \frac{\pi}{a_{\perp}}. \quad (5.8)$$

<sup>1</sup>Anti-periodic boundary conditions are realized for  $\Theta_{\mu} = \frac{1}{2}$ .

As already discussed in Chapter 1, we are interested in minimizing the lattice discretization effects by taking the limit  $a \rightarrow 0$ . On the other hand, this limit entails a vanishing UV cutoff, which is needed in order to guarantee a correct description within our classical framework, since UV modes are of quantum nature.

A possible way to circumvent this dilemma is to introduce an *additional UV momentum cutoff*  $\Lambda$ , which will be applied while constructing the color potentials within our CGC initial conditions, i.e. while solving Poisson's equation (4.9).

This bears the advantage that higher momentum modes, which are not correctly described within the scope of our classical formulation, are dropped and do not enter our initial conditions. One could argue that this results in a violation of Poisson's equation and thus in a violation of our initial conditions. However, the UV cutoff procedure can be interpreted as a tuning of the initial color charge distribution and thus the mentioned violation becomes bearable.

Obviously, this additional UV cutoff is only relevant if it is smaller than the lattice cutoff (5.8), yielding  $\Lambda < \sqrt{2} \frac{\pi}{a_{\perp}}$  or equivalently  $\Lambda/Q < \sqrt{2} \pi N_{\perp}/(QL)$ . If this is the case the highest lattice momentum is given by

$$|p_{\perp, \max}| = \Lambda \quad \Rightarrow \quad |k_{\perp, \max}| = \Lambda \frac{L_{\perp}}{2\pi} = \frac{\Lambda}{Q} \frac{QL_{\perp}}{2\pi}. \quad (5.9)$$

Finally, we must define how we introduce the UV cutoff in our lattice framework. In particular there are two possible ways:

1. We cut the lattice according to (5.9) and use a smaller transverse plane in Fourier space, i.e.  $N_k \times N_k$ , with  $N_k = \lfloor k_{\perp, \max} \rfloor$ .
2. We set all modes larger than the cutoff to zero and do not vary the transverse reciprocal lattice size.

The first procedure causes a raise of the system's energy if we lower the momentum cutoff, which is unphysical as throwing away modes should rather lower the energy. The origin of this phenomenon lies in the CGC initial conditions, where the lower modes are highly occupied and therefore carry more energy at initial time. By reducing the size of the Fourier space these IR modes get a higher weight and thus the averaged energy increases.

In contrast, the second approach also simulates a system with a low occupation of UV modes, but paired with the expected dependence on the momentum cutoff, which is why we follow this procedure.

## 5.4 Courant-Friedrichs-Lewy condition

The *Courant-Friedrichs-Lewy condition*, usually simply referred to as *Courant condition*, controls the convergence while solving partial differential equations and yields important

constraints on our simulations. In the following, we will give a short overview of its origin and refer for a detailed discussion to [82].

Starting with an analog of Maxwell's equations in one dimension (which is closely related to our framework), the system's dynamics are governed by

$$\frac{\partial r}{\partial t} = v \frac{\partial s}{\partial x}, \quad (5.10)$$

$$\frac{\partial s}{\partial t} = v \frac{\partial r}{\partial x}. \quad (5.11)$$

The corresponding Courant condition then reads [82]

$$\frac{|v|\Delta t}{\Delta x} \leq 1, \quad (5.12)$$

where  $\Delta t$  and  $\Delta x_i$  are the temporal and spacial step sizes, respectively, and  $|v|$  the absolute value of the maximum propagation velocity in the studied problem. This can be extended to  $N$  dimensions, yielding

$$\sqrt{N} \frac{|v|\Delta t}{\Delta x_i} \leq 1, \quad (5.13)$$

with  $i = 1, \dots, N$ .

For the static box calculations we have  $\Delta t = a_t$ ,  $\Delta x_i = a_\sigma$  and make use of  $|v| \leq 1$ , i.e. (5.13) translates to

$$a_t \ll a_\perp \quad \Leftrightarrow \quad \bar{a}_t \ll 1. \quad (5.14)$$

In our expanding formulation we have on top of this static constraint an additional dynamic Courant condition due to the dimensionless lattice spacing  $a_\eta$  in longitudinal direction. In particular we have  $\Delta t = a_t$ ,  $\Delta x_k = a_\perp$ ,  $\Delta x_\eta = a_\eta$  and  $|v| \propto (a_\eta \bar{\tau})^{-1}$ , with  $k \in \{1, 2\}$ . Thus, (5.13) yields the following two constraints on our simulations in comoving coordinates:

$$a_\tau \ll a_\perp \quad \Leftrightarrow \quad \bar{a}_\tau \ll 1, \quad (5.15a)$$

$$a_\tau \ll a_\eta \tau \quad \Leftrightarrow \quad 1 \ll a_\eta n_\tau. \quad (5.15b)$$

As a check, we can perform the replacement  $\tau \rightarrow a_\perp$  and  $a_\eta \rightarrow 1$  as we also did to double-check the equations of motion and obtain that the static and the dynamic constraints become identical and equivalent to (5.14).



# Chapter 6

## Observables

---

### Contents

6.1	Pressure and energy densities . . . . .	65
6.1.1	Static box . . . . .	66
6.1.2	Expanding system . . . . .	69
6.2	Occupation number . . . . .	71

---

### 6.1 Pressure and energy densities

Since we are interested in the early isotropization process of the plasma, the energy density and the pressure are convenient observables to investigate. They are related to the electromagnetic *energy-momentum tensor*, which is defined as [28]

$$T^{\mu\nu} = -g^{\mu\alpha} g^{\nu\beta} g^{\gamma\delta} F_{\alpha\gamma}^a F_{\beta\delta}^a + \frac{1}{4} g^{\mu\nu} g^{\alpha\gamma} g^{\beta\delta} F_{\alpha\beta}^a F_{\gamma\delta}^a. \quad (6.1)$$

Computing its diagonal entries directly leads us to the system's total energy density and the longitudinal and transverse pressure components. In the following two subsection, we derive the respective lattice expressions both in the Minkowski and in the comoving formulation.

### 6.1.1 Static box

The system's total energy density is determined by the energy-momentum tensor (6.1) and given by its zeroth diagonal element,

$$\begin{aligned}
 \epsilon := T^{00} &= -g^{\gamma\delta} F_{0\gamma}^a F_{0\delta}^a + \frac{1}{4} g^{\alpha\gamma} g^{\beta\delta} F_{\alpha\beta}^a F_{\gamma\delta}^a \\
 &= F_{0i}^{a2} - \frac{1}{2} \left[ F_{0i}^{a2} - \sum_{i<j} F_{ij}^{a2} \right] \\
 &= \frac{1}{2} \left[ E_i^{a2} + \sum_{i<j} F_{ij}^{a2} \right] \\
 &= \text{Tr} \left[ E_i^2 + \sum_{i<j} F_{ij}^2 \right] = \mathcal{H}.
 \end{aligned} \tag{6.2}$$

We used (2.33) to get the second line and temporal gauge (2.25) from the third line on. As expected, we see that the physical energy density is equivalent to the Hamiltonian density (2.39).

To construct the pressure components, we need to calculate the spacial diagonal elements of the energy-momentum tensor (6.1), yielding for the  $x$ -component of the pressure

$$\begin{aligned}
 P_x := T^{11} &= -g^{\gamma\delta} F_{1\gamma}^a F_{1\delta}^a - \frac{1}{4} g^{\alpha\gamma} g^{\beta\delta} F_{\alpha\beta}^a F_{\gamma\delta}^a \\
 &= -F_{10}^{a2} + F_{12}^{a2} + F_{13}^{a2} + \frac{1}{2} \left[ F_{0i}^{a2} - \sum_{i<j} F_{ij}^{a2} \right] \\
 &= \frac{1}{2} \left[ -E_1^{a2} + E_2^{a2} + E_3^{a2} + F_{12}^{a2} + F_{13}^{a2} - F_{23}^{a2} \right] \\
 &= \text{Tr} \left[ -E_1^2 + E_2^2 + E_3^2 + F_{12}^2 + F_{13}^2 - F_{23}^2 \right].
 \end{aligned} \tag{6.3}$$

Equivalently, we find

$$P_y := T^{22} = \text{Tr} \left[ E_1^2 - E_2^2 + E_3^2 + F_{12}^2 - F_{13}^2 + F_{23}^2 \right] \tag{6.4}$$

and

$$P_z := T^{33} = \text{Tr} \left[ E_1^2 + E_2^2 - E_3^2 - F_{12}^2 + F_{13}^2 + F_{23}^2 \right] \tag{6.5}$$

for the remaining pressure components.

Since  $z$  is chosen to be our beam direction, we define the transverse pressure as the average of the two transverse components,

$$P_T := \frac{1}{2} (P_x + P_y) = \text{Tr} \left[ E_3^2 + F_{12}^2 \right]. \tag{6.6}$$



The longitudinal pressure  $P_L$  is hence equivalent to the 3,3-component of the energy momentum tensor,

$$P_L := P_z. \quad (6.7)$$

We can easily verify that

$$T^{00} = T^{11} + T^{22} + T^{33} \quad \Leftrightarrow \quad \epsilon = P_x + P_y + P_z = 2P_T + P_L, \quad (6.8)$$

which in total equilibrium, i.e.  $P_i \equiv P$ , leads to the well-known relation  $\epsilon = 3P$ .

We now have to translate the derived expressions for the continuum observables to our lattice description. We start with the definition of the dimensionless lattice energy density,

$$\begin{aligned} \bar{\epsilon} &:= g^2 a_\sigma^4 \epsilon \\ &= \text{Tr} \left[ \bar{E}_i^2 + \sum_{i < j} \bar{F}_{ij}^2 \right] \\ &= \text{Re Tr} \left[ \bar{E}_i^2 + 2 \sum_{i < j} (1 - U_{ij}) \right]. \end{aligned} \quad (6.9)$$

We can define the longitudinal and transverse part of the energy density and split up each of them into their magnetic and electric components, yielding

$$\begin{aligned} \bar{\epsilon}^B &:= \bar{\epsilon}_L^B + \bar{\epsilon}_T^B, & \bar{\epsilon}^E &:= \bar{\epsilon}_L^E + \bar{\epsilon}_T^E, \\ \bar{\epsilon}_T &:= \bar{\epsilon}_T^B + \bar{\epsilon}_T^E, & \bar{\epsilon}_L &:= \bar{\epsilon}_L^B + \bar{\epsilon}_L^E, \end{aligned} \quad (6.10)$$

where the respective energy density components read

$$\bar{\epsilon}_T^B := 2 \text{Re Tr} [2 - U_{13} - U_{23}], \quad (6.11a)$$

$$\bar{\epsilon}_L^B := 2 \text{Re Tr} [1 - U_{12}], \quad (6.11b)$$

$$\bar{\epsilon}_T^E := \text{Tr} [\bar{E}_1^2 + \bar{E}_2^2], \quad (6.11c)$$

$$\bar{\epsilon}_L^E := \text{Tr} \bar{E}_3^2. \quad (6.11d)$$

Similar to (6.9), we define the dimensionless pressure as  $\bar{P} := g^2 a_\sigma^4 P$ , where the transverse component is given on the lattice by

$$\begin{aligned} \bar{P}_T &:= g^2 a_\sigma^4 P_T \\ &= \text{Tr} \left[ \bar{E}_3^2 + \bar{F}_{12}^2 \right] \\ &= \text{Re Tr} \left[ \bar{E}_3^2 + 2(1 - U_{12}) \right]. \end{aligned} \quad (6.12)$$

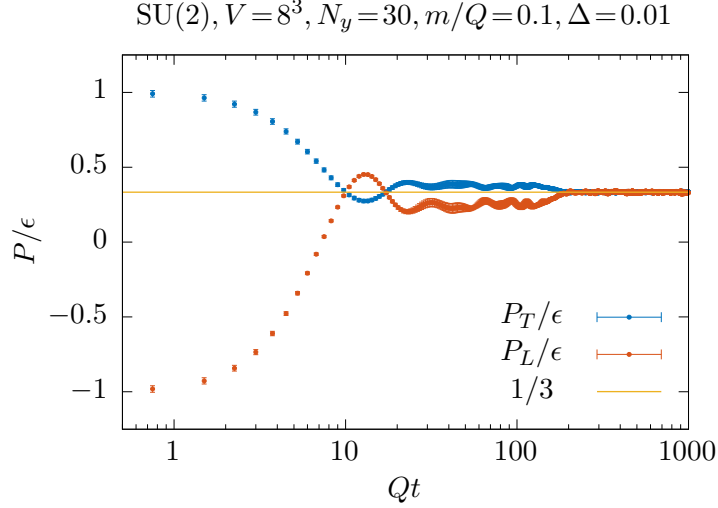


**Figure 6.1:** The transverse (6.12) and longitudinal (6.13) pressures normalized by the energy density (6.9) averaged over 10 configurations. Both pressures approach the value  $\frac{1}{3}$  verifying (6.8) in equilibrium.

In the same manner, the longitudinal component is defined as

$$\begin{aligned}
 \bar{P}_L &:= g^2 a_o^4 P_L \\
 &= \text{Tr} \left\{ \bar{E}_1^2 + \bar{E}_2^2 - \bar{E}_3^2 - \bar{F}_{12}^2 + \bar{F}_{13}^2 + \bar{F}_{23}^2 \right\} \\
 &= \text{Re Tr} \left\{ \bar{E}_1^2 + \bar{E}_2^2 - \bar{E}_3^2 + 2 \left[ -(1 - U_{12}) + (1 - U_{13}) + (1 - U_{23}) \right] \right\} \\
 &= \text{Re Tr} \left\{ \bar{E}_1^2 + \bar{E}_2^2 - \bar{E}_3^2 + 2 \left[ 1 + U_{12} - U_{13} - U_{23} \right] \right\}.
 \end{aligned} \tag{6.13}$$

By making use of (6.10) together with (6.11), we can rewrite the energy density as well as the pressure components as

$$\bar{\epsilon} = \bar{\epsilon}_T + \bar{\epsilon}_L, \tag{6.14}$$

$$\bar{P}_T = \bar{\epsilon}_L, \tag{6.15}$$

$$\bar{P}_L = \bar{\epsilon}_T - \bar{\epsilon}_L, \tag{6.16}$$

which is in accordance with (6.8).

At the moment all observables depend on the spacetime vector  $x = (t, \vec{x})$ . In order to illustrate the time evolution of the system's global observables, we therefore average over the spacial components, i.e.

$$\mathcal{O}(t) \equiv \frac{1}{V} \sum_{\vec{x}} \mathcal{O}(x), \tag{6.17}$$

with  $V$  being the two- or three-dimensional spacial lattice volume.

In Figure 6.1 we verify numerically, that (6.8) indeed transforms into  $\epsilon = 3P$  and hence a correct implementation of the above defined observables can be assumed.

### 6.1.2 Expanding system

Since our expanding formulation is based on comoving coordinates (cf. Section 2.2.2), we have to apply the corresponding metric (2.44) to the definition of the energy-momentum tensor (6.1). This yields for the 0th diagonal entry, which is again identified with the system's total energy density,

$$\begin{aligned}
 \epsilon := T^{\tau\tau} &= -g^{\gamma\delta} F_{\tau\gamma}^a F_{\tau\delta}^a + \frac{1}{4} g^{\alpha\gamma} g^{\beta\delta} F_{\alpha\beta}^a F_{\gamma\delta}^a \\
 &= F_{\tau i}^{a2} + \frac{F_{\tau\eta}^{a2}}{\tau^2} - \frac{1}{2} \left[ F_{\tau i}^{a2} + \frac{F_{\tau\eta}^{a2}}{\tau^2} - F_{12}^{a2} - \frac{F_{i\eta}^{a2}}{\tau^2} \right] \\
 &= \frac{E_i^{a2}}{\tau^2} + E_\eta^{a2} - \frac{1}{2} \left[ \frac{E_i^{a2}}{\tau^2} + E_\eta^{a2} - F_{12}^{a2} - \frac{F_{i\eta}^{a2}}{\tau^2} \right] \\
 &= \frac{1}{2} \left[ \frac{E_i^{a2}}{\tau^2} + E_\eta^{a2} + F_{12}^{a2} + \frac{F_{i\eta}^{a2}}{\tau^2} \right] \\
 &= \text{Tr} \left[ \frac{E_i^2}{\tau^2} + E_\eta^2 + F_{12}^2 + \frac{F_{i\eta}^2}{\tau^2} \right] = \frac{1}{\tau} \mathcal{H},
 \end{aligned} \tag{6.18}$$

where we made use of (2.48) to get the second line and utilized temporal gauge (2.25) in the following line. Here and in the following, we explicitly write out the 0th component as the  $\tau$ -component, as we almost always did before in order to highlight the use of comoving coordinates. Different than in the static box case, the (physical) total energy density  $\epsilon$  does not equal the Hamiltonian density  $\mathcal{H}$ , which is defined in (2.50). However, this is plausible due to the reduced energy dimension of the Hamiltonian density discussed in Section 2.2.2.

Computing the transverse diagonal elements of the energy-momentum tensor, we find

$$\begin{aligned}
 T^{11} &= -g^{\gamma\delta} F_{1\gamma}^a F_{1\delta}^a - \frac{1}{4} g^{\alpha\gamma} g^{\beta\delta} F_{\alpha\beta}^a F_{\gamma\delta}^a \\
 &= -F_{1\tau}^{a2} + F_{12}^{a2} + \frac{F_{1\eta}^{a2}}{\tau^2} + \frac{1}{2} \left[ F_{\tau i}^{a2} + \frac{F_{\tau\eta}^{a2}}{\tau^2} - F_{12}^{a2} - \frac{F_{i\eta}^{a2}}{\tau^2} \right] \\
 &= -\frac{E_1^{a2}}{\tau^2} + F_{12}^{a2} + \frac{F_{1\eta}^{a2}}{\tau^2} + \frac{1}{2} \left[ \frac{E_i^{a2}}{\tau^2} + E_\eta^{a2} - F_{12}^{a2} - \frac{F_{i\eta}^{a2}}{\tau^2} \right] \\
 &= \frac{1}{2} \left[ -\frac{E_1^{a2}}{\tau^2} + \frac{E_2^{a2}}{\tau^2} + E_\eta^{a2} + F_{12}^{a2} + \frac{F_{1\eta}^{a2}}{\tau^2} - \frac{F_{2\eta}^{a2}}{\tau^2} \right] \\
 &= \text{Tr} \left[ -\frac{E_1^2}{\tau^2} + \frac{E_2^2}{\tau^2} + E_\eta^2 + F_{12}^2 + \frac{F_{1\eta}^2}{\tau^2} - \frac{F_{2\eta}^2}{\tau^2} \right]
 \end{aligned} \tag{6.19}$$

and equivalently

$$T^{22} = \text{Tr} \left[ \frac{E_1^2}{\tau^2} - \frac{E_2^2}{\tau^2} + E_\eta^2 + F_{12}^2 - \frac{F_{1\eta}^2}{\tau^2} + \frac{F_{2\eta}^2}{\tau^2} \right]. \tag{6.20}$$

A dimensional analysis yields  $[T^{11}] = [T^{22}] = 4$ , and hence it is physically meaningful to define the transverse pressure as

$$\begin{aligned} P_T &:= \frac{1}{2}(T^{11} + T^{22}) \\ &= \frac{1}{2}(E_\eta^{a2} + F_{12}^{a2}) \\ &= \text{Tr} [E_\eta^2 + F_{12}^2]. \end{aligned} \quad (6.21)$$

Finally, we calculate the expression for the last diagonal entry of the energy-momentum tensor, reading

$$\begin{aligned} T^{33} \equiv T^{\eta\eta} &= -\frac{1}{\tau^4} g^{\gamma\delta} F_{\eta\gamma}^a F_{\eta\delta}^a - \frac{1}{4\tau^2} g^{\alpha\gamma} g^{\beta\delta} F_{\alpha\beta}^a F_{\gamma\delta}^a \\ &= -\frac{1}{\tau^4} [F_{\eta\tau}^{a2} - F_{1\eta}^{a2} - F_{2\eta}^{a2}] + \frac{1}{2\tau^2} [F_{\tau i}^{a2} + \frac{F_{\tau\eta}^{a2}}{\tau^2} - F_{12}^{a2} - \frac{F_{i\eta}^{a2}}{\tau^2}] \\ &= -\frac{1}{\tau^4} [\tau^2 E_\eta^{a2} - F_{i\eta}^{a2}] + \frac{1}{2\tau^2} [\frac{E_i^{a2}}{\tau^2} + E_\eta^{a2} - F_{12}^{a2} - \frac{F_{i\eta}^{a2}}{\tau^2}] \\ &= \frac{1}{2\tau^2} [\frac{E_i^{a2}}{\tau^2} - E_\eta^{a2} - F_{12}^{a2} + \frac{F_{i\eta}^{a2}}{\tau^2}] \\ &= \frac{1}{\tau^2} \text{Tr} [\frac{E_i^2}{\tau^2} - E_\eta^2 - F_{12}^2 + \frac{F_{i\eta}^2}{\tau^2}]. \end{aligned} \quad (6.22)$$

Once again, we determine the energy dimension and obtain  $[T^{\eta\eta}] = 6$ , which leads us to the following convenient definition of the longitudinal pressure,

$$\begin{aligned} P_L &:= \tau^2 T^{\eta\eta} \\ &= \frac{1}{2} [\frac{E_i^{a2}}{\tau^2} - E_\eta^{a2} - F_{12}^{a2} + \frac{F_{i\eta}^{a2}}{\tau^2}] \\ &= \text{Tr} [\frac{E_i^2}{\tau^2} - E_\eta^2 - F_{12}^2 + \frac{F_{i\eta}^2}{\tau^2}]. \end{aligned} \quad (6.23)$$

Using this result together with the ones from (6.18)-(6.23), we find the equivalent expression of (6.8), which reads

$$T^{\tau\tau} = T^{11} + T^{22} + \tau^2 T^{\eta\eta} \quad \Leftrightarrow \quad \epsilon = 2P_T + P_L. \quad (6.24)$$

In complete analogy to Section 6.1.1, we define the dimensionless lattice energy density in comoving coordinates,

$$\begin{aligned} \bar{\epsilon} &:= g^2 a_\perp^4 \epsilon \\ &= \text{Tr} [\frac{\bar{E}_i^2}{\bar{\tau}^2} + \bar{E}_\eta^2 + \bar{F}_{12}^2 + \frac{\bar{F}_{i\eta}^2}{\bar{\tau}^2}] \\ &= \text{Re Tr} [\frac{\bar{E}_i^2}{\bar{\tau}^2} + \bar{E}_\eta^2 + 2(1 - U_{12}) + \frac{2}{a_\eta^2 \bar{\tau}^2} \sum_i (1 - U_{i\eta})], \end{aligned} \quad (6.25)$$

as well as the dimensionless transverse and longitudinal pressure on the lattice,

$$\begin{aligned}
 \bar{P}_T &:= g^2 a_\perp^4 P_T \\
 &= \text{Tr} \left[ \bar{E}_\eta^2 + \bar{F}_{12}^2 \right] \\
 &= \text{Re Tr} \left[ \bar{E}_\eta^2 + 2(1 - U_{12}) \right],
 \end{aligned} \tag{6.26}$$

$$\begin{aligned}
 \bar{P}_L &:= g^2 a_\perp^4 P_L \\
 &= \text{Tr} \left[ \frac{\bar{E}_i^2}{\bar{\tau}^2} - \bar{E}_\eta^2 - \bar{F}_{12}^2 + \frac{\bar{F}_{i\eta}^2}{\bar{\tau}^2} \right] \\
 &= \text{Re Tr} \left[ \frac{\bar{E}_i^2}{\bar{\tau}^2} - \bar{E}_\eta^2 - 2(1 - U_{12}) + \frac{2}{a_\eta^2 \bar{\tau}^2} \sum_i (1 - U_{i\eta}) \right].
 \end{aligned} \tag{6.27}$$

By looking at the large proper time limit, we obtain

$$P_T \xrightarrow{\bar{\tau} \rightarrow \infty} \epsilon \quad \text{and} \quad P_L \xrightarrow{\bar{\tau} \rightarrow \infty} -\epsilon. \tag{6.28}$$

Hence, the absolute values of the pressure components are identical and the opposite sign comprises the fact that we are describing a longitudinally expanding system.

Defining the components of the lattice energy density in an equivalent manner as we did in (6.11), yields

$$\bar{\epsilon}_T^B := \frac{2}{a_\eta^2 \bar{\tau}^2} \sum_i \text{Re Tr} [1 - U_{i\eta}], \tag{6.29a}$$

$$\bar{\epsilon}_L^B := 2 \text{Re Tr} [1 - U_{12}], \tag{6.29b}$$

$$\bar{\epsilon}_T^E := \frac{1}{\bar{\tau}^2} \text{Tr} \bar{E}_i^2, \tag{6.29c}$$

$$\bar{\epsilon}_L^E := \text{Tr} \bar{E}_\eta^2. \tag{6.29d}$$

Now using (6.10) we end up with (6.14)-(6.16), which are hence valid relations both in the Minkowski and in the comoving formulation. As already shown, the latter equation is in accordance with (6.8) and (6.24), respectively.

## 6.2 Occupation number

As motivated in Section 2.4, the validity of the classical approximation relies on a high occupation number and hence the latter is an observable of crucial importance for our work. Furthermore, the IR sector should dominate the total energy of the system, since the classical description breaks down in the UV regime.

In the literature it is customary to compute the Fourier components of the color-electric field and their contribution to the energy. However, color-electric fields (and hence also their Fourier modes) are gauge-dependent, which causes ambiguities in the interpretation of the corresponding momentum distribution. Moreover, the required gauge fixing

procedure introduces a significant computational overhead. We will therefore rather consider the spectral decomposition for a manifestly gauge-invariant quantity, the Fourier transformed total energy density,<sup>1</sup>

$$\tilde{\mathcal{H}}(t, \vec{p}) = \frac{1}{V} \sum_{\vec{x}} e^{-i\vec{p}\vec{x}} \sum_i [\mathcal{H}_i^E(x) + \mathcal{H}_i^B(x)], \quad (6.30)$$

which is related to the population of momentum modes as can be seen by the following considerations.

In [83–85] a free gluon gas is considered and the system's energy  $\mathcal{E}$  (in  $d$  dimensions) is related to the density of gluonic modes  $n_f$  via

$$\mathcal{E} \equiv \int d^d p \epsilon(\vec{p}) = \int d^d p \omega(\vec{p}) n_f(\vec{p}). \quad (6.31)$$

In this case, the eigenfrequency  $\omega$  approaches the free massless dispersion relation  $\omega(p) \approx p$  for  $p \gtrsim 0.1 Q$  and remains constant for lower momenta [83], yielding

$$\omega(p) = \begin{cases} 0.1 Q & , p < 0.1 Q \\ p & , p \geq 0.1 Q \end{cases} \Rightarrow n_f(p) = \begin{cases} \frac{\epsilon(p)}{0.1 Q} & , p < 0.1 Q \\ \frac{\epsilon(p)}{p} & , p \geq 0.1 Q \end{cases}. \quad (6.32)$$

Accordingly, we define the occupation number density  $n(p) \approx n_f(p)$  via the average of (6.30) over momenta with equal absolute value<sup>2</sup> normalized by the respective absolute value of the momentum,

$$n(p) := \frac{N(p)}{\mathcal{V}} := \frac{1}{p} \langle |\tilde{\epsilon}(\vec{p})| \rangle_p, \quad (6.33)$$

where  $\mathcal{V}$  is the physical volume and  $\tilde{\epsilon}(p)$  is given by the Fourier transform of (6.2) or (6.18), respectively. The dimensionless occupation number  $N$  can easily be computed on the lattice,

$$g^2 N(p) = \frac{V}{\bar{p}} \langle |\tilde{\epsilon}(\vec{p})| \rangle_{\bar{p}}, \quad (6.34)$$

with the rescaled momentum  $\bar{p} = a_{\perp} p$ , the spacial lattice volume  $V$  and the Fourier transformed lattice energy density  $\tilde{\epsilon}(\vec{p})$ , which is constructed via (6.9) in the static box scenario and (6.25) in the case of the expanding system.

Note that our definition for the occupation number and its density are only valid for  $p \geq 0.1 Q$  due to the constant behavior below that value. However, since we will consider momenta up to  $14 Q$ , this is a negligible area. In addition one has to keep in mind that we assumed  $n(p) \approx n_f(p)$ .

<sup>1</sup>Note that for dimensional reasons we use the anti-symmetric Fourier transform here.

<sup>2</sup>This means we average over all vectors with the same length, i.e., all combinations of  $p_i, i=1, \dots, d$ , that result in the same absolute value  $p \equiv |\vec{p}| = \sqrt{\sum_i p_i^2}$ . This is indicated by the notation  $\langle \cdot \rangle_p$ .

# Chapter 7

## Pure Yang-Mills simulations

---

### Contents

7.1	SU(2) versus SU(3) . . . . .	74
7.2	Lattice artifacts . . . . .	75
7.3	Investigating the CGC parameter space . . . . .	77
7.4	Occupation numbers . . . . .	82
7.5	Towards isotropization . . . . .	84
7.6	Chromo-Weibel instability . . . . .	88

---

In this chapter we present the main part of our numerical lattice investigation concerning the different observables introduced in the preceding chapter. We present a systematic study of the dependence on the large parameter space we discussed in Section 5.1, which enters through the CGC initial condition as well as through the classical lattice approximation. Furthermore, we compare a treatment of the realistic SU(3) gauge group with the more economical SU(2) as well as the evolution in a static box with the one in an expanding medium.

Unless stated differently, we will use  $QL = 120$  throughout this work, as motivated in Section 5.2. In addition, our results are almost always based on an ensemble size of 10 configurations, and here, too, changes will be annotated.

We want to emphasize, that the initial conditions in the boost invariant scenario, i.e. the one without longitudinal fluctuations, are identical in both frameworks (cf. Chapter 4). To this end, we will present corresponding results for the energy density solely in the expanding formulation, since the counterparts in the static box scenario can easily be derived therefrom. Due to energy conservation in the latter case, they are just constant lines starting from the initial value of the energy density in the expanding formulation.

We also want to mention, that our numerical implementation is based on the well-tested and versatile QDP++ framework [86], which allows for data-parallel programming

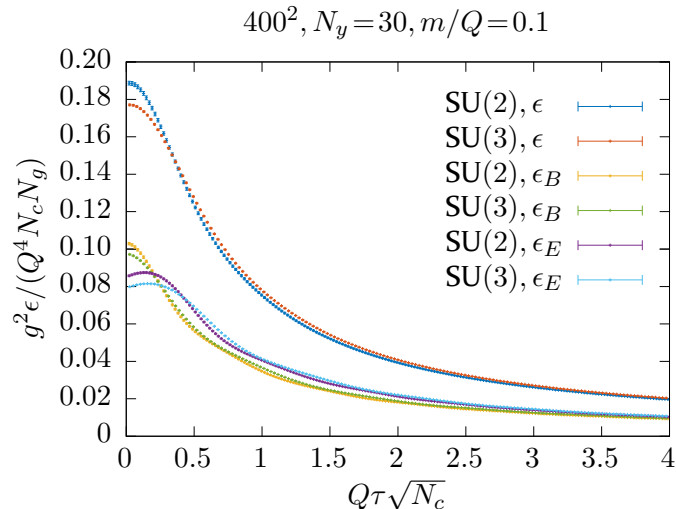


**Figure 7.1:** Total energy density and its chromo-magnetic and chromo-electric components for SU(2) and SU(3).

on high performance clusters. For the numerical solution of (4.15) we utilize multidimensional root finding methods of the GSL library [87].

## 7.1 SU(2) versus SU(3)

Performing the calculations for the realistic SU(3) rather than SU(2) gauge theory introduces roughly an additional factor of 4 in terms of computation time, depending on the studied observables. We want to test whether this gains deeper insights into the underlying physics and hence, if the longer computation time is justified.

However, comparing physical results between the groups is non-trivial, since not only our observables depend on the number of colors  $N_c$ , but also the ratio  $Q_s/Q$  by which our lattice results are linked to physical values. In particular, we have  $Q_s \propto \sqrt{N_c}Q$  for the  $N_c$ -dependence of the saturation scale [73] and  $g^2\epsilon(t|\tau=0) \propto N_c N_g$  for the initial energy density [72]. A physically meaningful, dimensionless combination with the leading  $N_c$ -behavior scaled out is thus  $g^2\epsilon/(Q^4 N_c N_g)$  plotted versus  $\sqrt{N_c}Q\tau$ .

In Figure 7.1, where we applied this rescaling<sup>1</sup>, we clearly see that there is no significant difference in the observables we are studying.<sup>2</sup> In addition, the  $N_c$ -dependence appears to be much weaker than the sensitivity to the parameters of the CGC initial conditions, which will be discussed in Section 7.3. We checked this observation for several parameter settings with the same outcome and will therefore focus mostly on the SU(2) gauge group

<sup>1</sup>In the following, we will keep the scaling factor for the energy density, but we will drop the  $\sqrt{N_c}$  normalization factor in front of  $Q\tau$  in order to ease the comparison with other works, where this is almost always neglected, too.

<sup>2</sup>As a reminder: The pressure components are fully determined by the components of the energy density via (6.15) and (6.16).



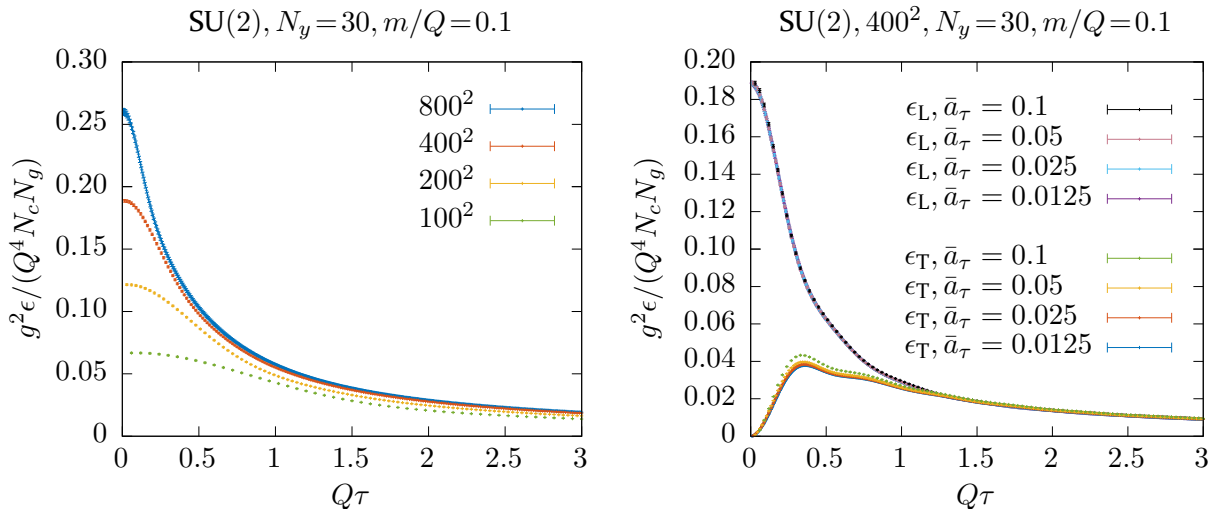


**Figure 7.2:** Left: Total energy density for different transverse lattice extents  $N_\perp^2$ . Right: Transverse and longitudinal components of the energy density for different time discretizations  $\bar{a}_\tau$ .

in the following, in order to reduce numerical costs.

We want to stress that we do not apply any additional UV cutoff, unless it is written in the plot title. The IR and UV cutoffs entailed by our lattice discretization is of course always present. Regarding the  $N_c$ -dependence we found that the lower the additional UV cutoff, the lower the discrepancy between SU(2) and SU(3), which is why we present the results without an additional lattice UV cutoff in Figure 7.1.

## 7.2 Lattice artifacts

Every lattice simulation introduces so-called *lattice artifacts*, which are originating from the discretization of spacetime. On the one hand, there are obviously *discretization effects* as a consequence of the finite lattice spacing  $a_\mu$ . On the other hand, there are also *boundary effects* due to the finite volume of the lattice and, particularly in our case, due to the periodic boundary conditions, which we discussed in Section 5.2.1.

It is hence necessary to study these lattice artifacts in order to be able to define a parameter set, where they are bearable and, at best, negligible yielding a meaningful description of the actual physics. This section is dedicated to exactly this investigation.

We want to stress that instead of the normally used 10 configurations we only use an ensemble of 4 configurations for the largest transverse lattice extent,  $N_\perp = 800^2$ , due to the substantially higher computation times. However, even for this choice the statistical errors are still manageable.

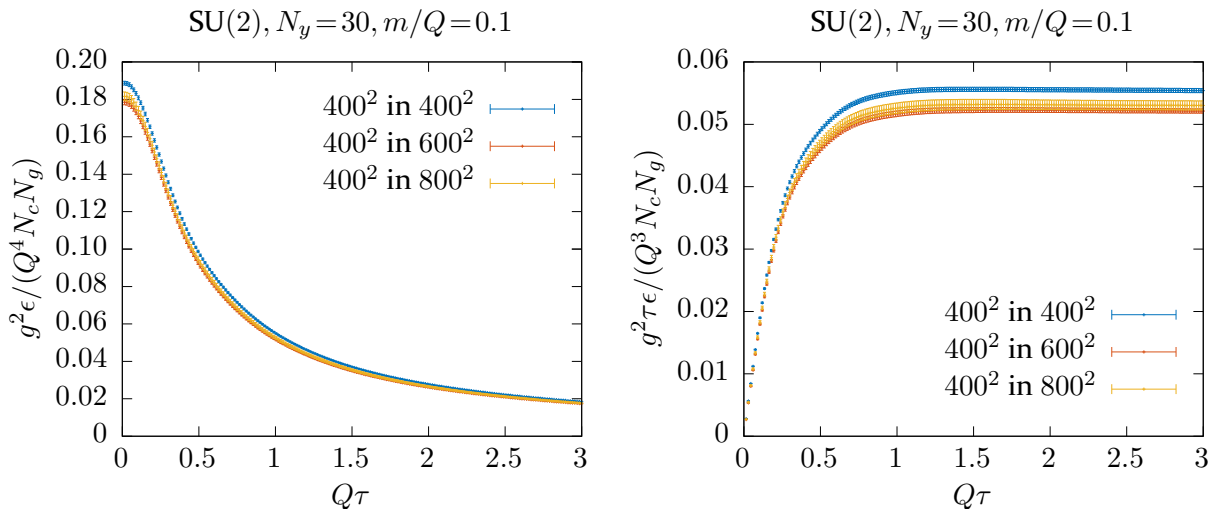


**Figure 7.3:** Total energy density (left) and total energy density times the proper time (right) for a nucleus represented by  $400^2$  lattice points embedded in different lattice sizes.

### 7.2.1 Discretization effects

Ideally, the unphysical lattice spacings  $a_\mu$  should have no effect on our results. As can be seen in Figure 7.2 (left), this is not the case in the classical CGC description, even though the discretization effects become negligible for  $Q\tau \gtrsim 0.3$  and a transverse lattice size of  $N_\perp \geq 400$ . It is crucial to notice, that in the non-expanding case, where the initial energy density stays constant, this is not the case and we have to deal with significant discretization effects. However, the additional UV cutoff (cf. Section 5.3 and Section 7.3) will turn out to be a possibility to tackle this issue.

For the investigation of the different CGC initial condition parameters we will choose a  $400^2$  lattice, since it is a reasonable compromise between accuracy and computation time.

We also have to be sure that there are no discretization effects stemming from the numerical time integration. To this end we vary the dimensionless temporal lattice spacing  $\bar{a}_\tau$ , with corresponding results for the transverse and longitudinal energy density shown in Figure 7.2 (right). We used  $\bar{a}_{t|\tau} = 0.05 \Leftrightarrow a_{t|\tau} = 0.05 a_{\sigma|\perp}$  for all the results presented in this work, since this choice leads to negligible systematic errors coming from our time discretization.

### 7.2.2 Boundary effects

Since we are employing periodic boundary conditions, the identification of the whole transverse plane as the two centrally colliding nuclei is at first glance counterintuitive. We will therefore apply the method introduced in Section 5.2.1 allowing for a description where the nuclei are not spread over the whole transverse plane but rather are embedded in it as depicted in Figure 5.2.

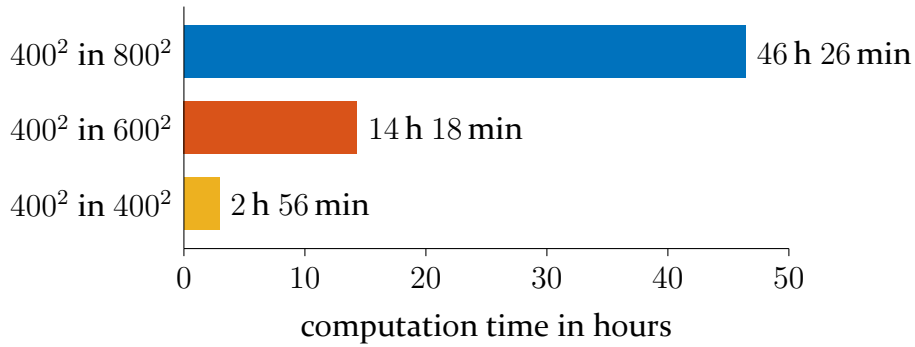


**Figure 7.4:** Computation time for one initial configuration for colliding nuclei represented by  $400^2$  lattice points embedded in three different transverse lattices. All computations were performed on one dual-socket Intel Xeon Ivy Bridge E5-2670v2 node with 20 CPU cores at the LOEWE-CSC cluster.

In the last subsection, we found that a transverse plane with  $400^2$  lattice points is a reasonable choice. We will now use the exactly same initial conditions for the system of two nuclei described by these  $400^2$  lattice points, but this time also embed it into larger planes in order to study possible effects coming from the periodic boundary conditions and the finite lattice volume, respectively.

In Figure 7.3 we show the total energy density  $\epsilon$  (times the proper time  $\tau$ ) for three different scenarios: First, the nucleus is spread over the whole  $400^2$  lattice points on the transverse lattice plane as is usually done in the MV model, second, the nucleus is represented by  $400^2$  lattice points within a  $600^2$  lattice and third, the same nucleus is embedded in an  $800^2$  lattice.

We observe an effect at the 5%-level which is in the ballpark of the discrepancy between SU(2) and SU(3) observed in Section 7.1. However, as we already stated for the  $N_c$ -dependence, this effect is much weaker than the sensitivity to the CGC parameters, as we will see in Section 7.3. Furthermore, the larger transverse lattice extents result in tremendously larger computational costs (cf. Figure 7.4). To this end, we will stick to the originally proposed scenario, where the nuclei cover the whole transverse plane.

A possible explanation for the rather moderate boundary effects is that the total diameter of the plane representing the nuclei is for our choice of parameters around 12 fm, cf. (5.3). Apparently, this distance is large enough to suppress the inaccuracies introduced by the periodic boundary conditions.

### 7.3 Investigating the CGC parameter space

As introduced in Section 5.1, the classical Yang-Mills system depends on various parameters introduced through the CGC initial conditions. For the classical description of the

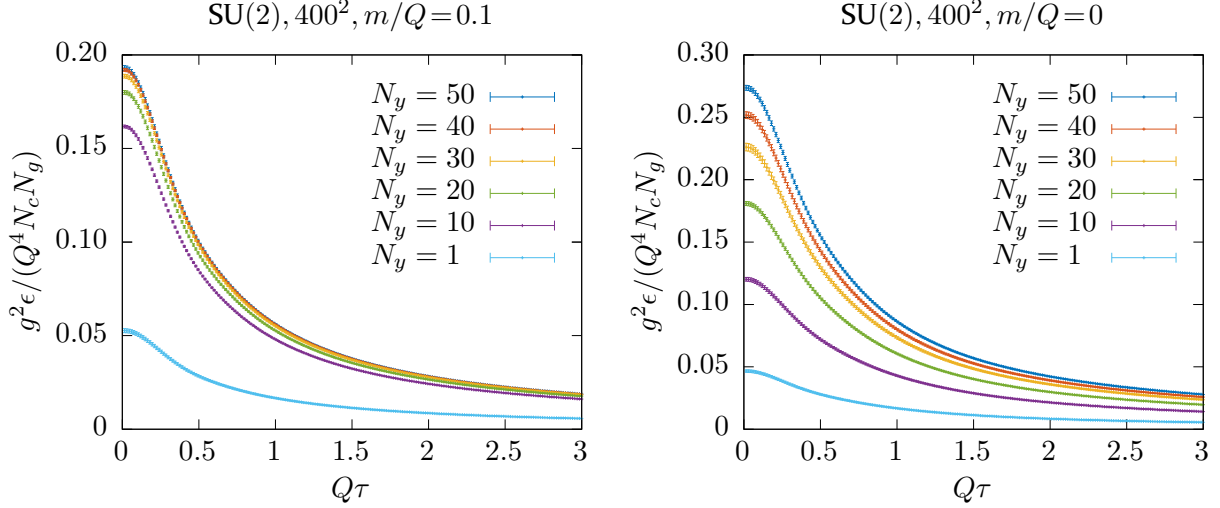


**Figure 7.5:** Total energy density for different numbers of longitudinal sheets  $N_y$  with (left) and without (right) an additional IR cutoff.

CGC-model to be self-consistent, the parameters representing different scales of the problem have to satisfy

$$\frac{1}{L_{\perp}} \lesssim m \ll Q \ll \Lambda \lesssim \frac{1}{a_{\perp}}, \quad (7.1)$$

where  $a_{\perp}$  is the transverse lattice spacing,  $\frac{1}{a_{\perp}}$  the order of the resulting lattice UV cutoff,  $L_{\perp} = N_{\perp} a_{\perp}$  the length of the quadratic transverse plane,  $m$  the IR cutoff, and  $\Lambda$  the additional UV cutoff introduced while solving Poisson's equation (4.9). The dimensionless version of (7.1) reads

$$\frac{1}{QL_{\perp}} \lesssim \frac{m}{Q} \ll 1 \ll \frac{\Lambda}{Q} \lesssim \frac{N_{\perp}}{QL_{\perp}}. \quad (7.2)$$

In particular, this means for our common choice of  $QL_{\perp} = 120$  that we have to fulfill  $N_{\perp} \gg 120$ , which supports the outcome of Section 7.2.

The original MV model, which considers no additional IR or UV cutoff, corresponds to the special case, where  $m$  equals its lower bound and  $\Lambda$  is identical to the lattice cutoff.

In the following subsections, we will study how the system's energy density depends on the two cutoff parameters  $m$  and  $Q$ . We will also present a method to reduce the number of free parameters by keeping the system's physical energy density fixed. Furthermore, we will study the influence of the number of infinitesimal longitudinal sheets (cf. Figure 4.2) and determine its smallest number to sufficiently approximate  $N_y \rightarrow \infty$ .

### 7.3.1 Number of longitudinal sheets

As shown in [72], the initially proposed initial conditions of the MV model lack randomness within the longitudinal dimension. Fukushima proposed to use  $N_y$  sheets describing the colliding nuclei rather than only a single one, as we already discussed in Section 4.1.

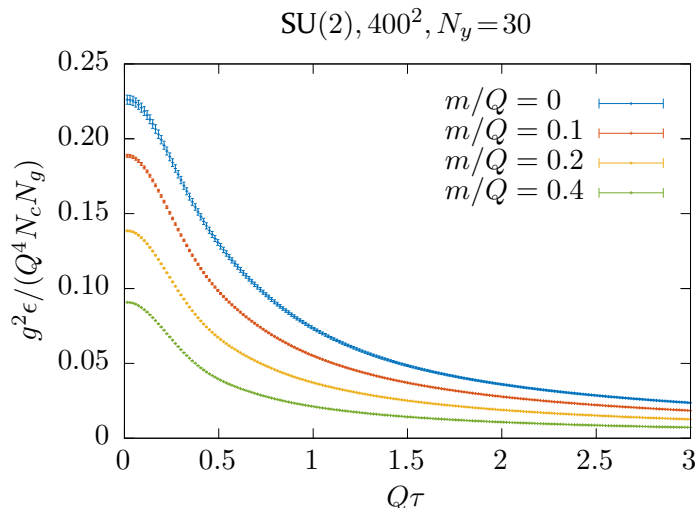


**Figure 7.6:** Total energy density for different IR cutoff parameters  $m$ .

The artificial parameter  $N_y$  originates from our numerical implementation and thus vanishes in the continuum extrapolation, where  $N_y \rightarrow \infty$ . Figure 7.5 shows that the total energy density depends strongly on  $N_y$  for small values  $\lesssim 30$  and then saturates. This saturation gets amplified if we add an additional IR cutoff, since we obviously have a faster saturation for  $m/Q=0.1$  than for  $m/Q=0$ . This has also been observed in [73] and is intuitive since the IR cutoff introduces an additional screening of the color sources and hence reduces the correlation length in rapidity direction.

Since the computation time grows linearly with the number of longitudinal sheets,  $N_y=30$  is a reasonable, which we thus set for almost all simulations.

### 7.3.2 Infrared cutoff

The next parameter of our CGC initial conditions we will have a closer look at is the IR cutoff  $m$ . It enters the initial conditions while solving Poisson's equation (4.9) and is equivalent to the logarithmic infrared cutoff introduced in the solution of its analytical equivalent [73].

Physically the parameter  $m$  indicates the inverse length scale at which objects in our framework are color neutral [76]. Regarding the two colliding nuclei, we can identify these objects as nucleons and hence,

$$m = 0.1 Q \approx 200 \text{ MeV} \approx 1 \text{ fm}^{-1} \approx R_p^{-1}, \quad (7.3)$$

with  $R_p$  being the proton radius, is a sensible choice.

The choice of  $m/Q$  seems to have a huge effect on the initial energy density which can easily be seen in Figure 7.6. However, this can be explained by the fact that the relation of the MV parameter  $Q$  and the saturation scale  $Q_s$  is non-trivial. In particular, as studied in [73], the parameter  $m$  has influence on the ratio  $Q/Q_s$ : At  $N_y = 30$  the

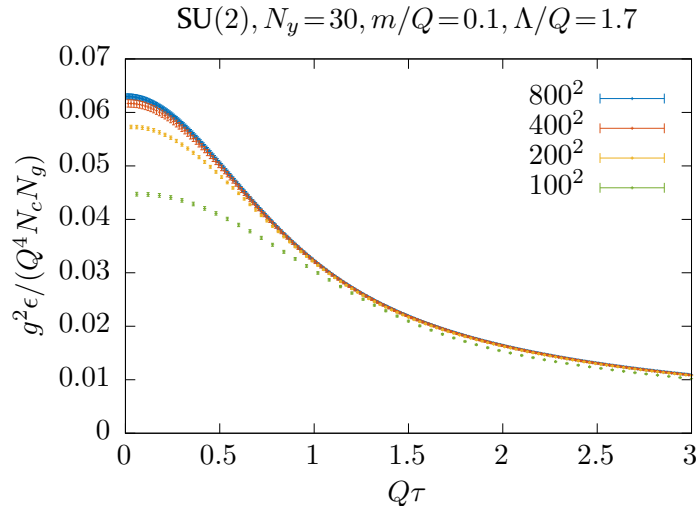


**Figure 7.7:** Total energy density for different transverse lattice extents  $N_{\perp}^2$  with an additional UV cutoff of  $1.7 Q$ , which was suggested in [88].

physical saturation scale  $Q_s$  is around  $0.85 Q$  for  $m/Q = 0.1$  and around  $1.03 Q$  for  $m/Q = 0$ . Since the energy density is normalized by  $Q^4$ , this leads to a factor of  $\approx 2.16$ , if we would consider the physically relevant dimensionless quantity  $\epsilon/Q_s^4$ .

In addition, the required number of infinitesimal sheets  $N_y$ , which is needed to reasonably approximate  $N_y \rightarrow \infty$ , varies with  $m$ , which we already obtained in Figure 7.5. Consequently, this is a further explanation for the seemingly large effect of  $m$  on the initial energy density.

To this end, we almost always stick to the choice  $m/Q = 0.1$ , which we physically motivated in (7.3). However, we will in some cases for comparison present results based on  $m = 0$ , since this was the initially proposed choice of the MV model.

### 7.3.3 Ultraviolet cutoff

We saw in Section 7.2.1 that classical lattice simulations with CGC initial conditions suffer from significant discretization effects, especially in the non-expanding case. In addition, taking the limit  $a_{\perp} \rightarrow 0$  is problematic since more and more UV modes enter the system, which are not correctly described within our classical approximation.

As discussed in Section 5.3, the introduction of an additional UV cutoff  $\Lambda$  is a possible way to handle this conflict. It is applied while constructing the color potentials via Poisson's equation (4.9). This allows us to take the limit  $a_{\perp} \rightarrow 0$ , without violating the classical approximation. However, this procedure introduces a new parameter, for which there is – at the time of writing – no physically motivated value as it was the case for the IR cutoff  $m$ , cf. (7.3).

With the choice  $\Lambda/Q = 1.7$ , which was suggested in [88], we see a faster saturation for  $a_{\perp} \rightarrow 0$ , as can be obtained from Figure 7.2 (left) and Figure 7.7. Obviously, the total

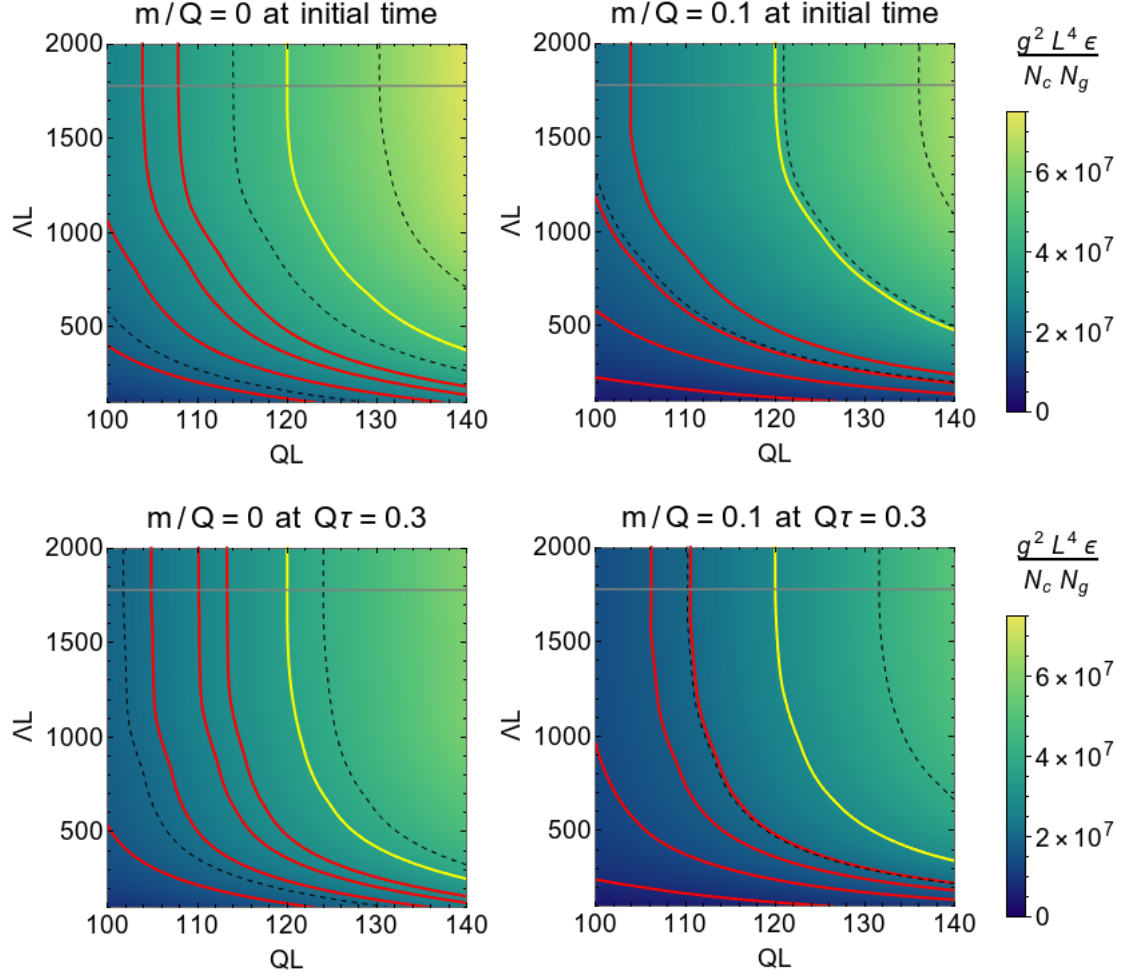


**Figure 7.8:** SU(2) total energy density on a  $400^2$  lattice with  $N_y = 30$  for different scale settings  $QL$  and different UV cutoffs  $\Lambda L$  without IR cut-off (left) and  $m/Q = 0.1$  (right) at initial time (top) and at  $Q\tau = 0.3$  (bottom). The dashed lines represent constant energy density levels, which are even multiples of  $10^7$  and the gray horizontal line represents the lattice UV cutoff above which the additional UV cutoff does no longer affect the system. The red and yellow solid lines are examples for constant energy densities at the common choice of  $QL = 120$ : Red lines indicate the UV cutoffs  $\Lambda \in \{Q, 2Q, 3Q, 4Q\}$  and the yellow line refers to the constant energy density contour without an additional UV cutoff, which is the choice of the majority of previous studies.

energy density computed with an additional UV cutoff is reduced due to the missing higher modes. In this case by a factor of  $\approx 3$  for  $N_\perp = 400$ .

This seems to be similar to the observation we made on the IR cutoff  $m$ , which also entails a strong influence on the system's total energy density, but with an important difference: The ratio  $Q/Q_s$  is practically independent of the UV cutoff  $\Lambda$ , as Fries, Kapusta

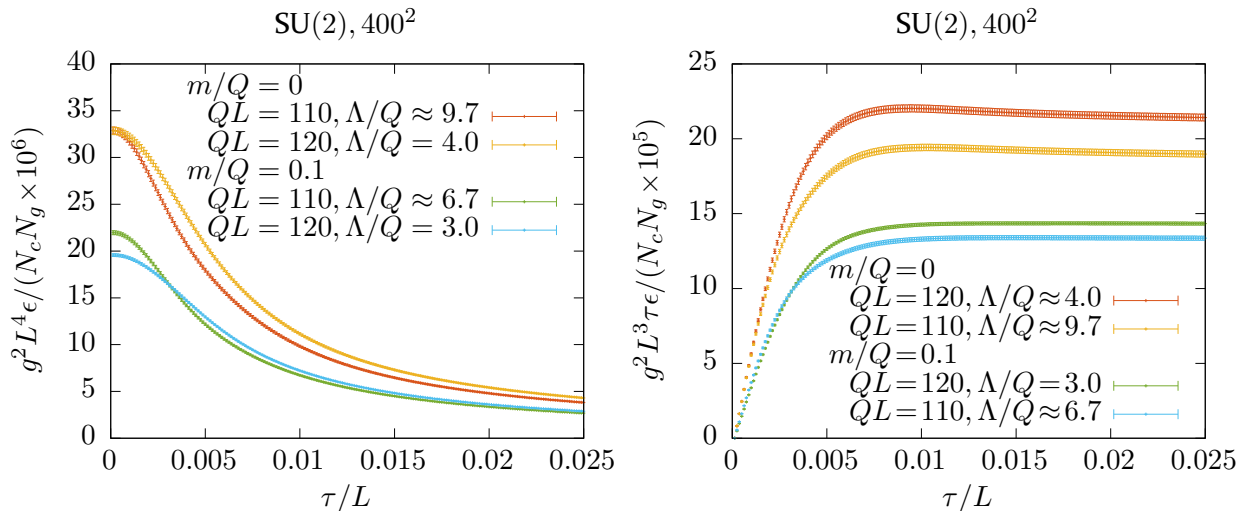


**Figure 7.9:** Total energy density (left) and total energy density times proper time (right) for different values of the UV cutoff parameter  $\Lambda$  corresponding to a fixed physical energy density at initial time using  $m/Q = 0$  and at  $Q\tau = 0.3$  using  $m/Q = 0.1$ .

and Li show in [89].<sup>3</sup>

Consequently, we can tune our total scale  $QL$  to be able to perform computations at constant physical energy  $L^4\epsilon$  for different UV cutoffs  $\Lambda L$ . The outcome of this investigation are the contour plots shown in Figure 7.8. We show the contour plot at  $Q\tau = 0.3$  as well, since this is the region where even without an additional UV cutoff the discretization effects are negligible for  $N_\perp = 400$  in the expanding case, cf. Figure 7.2 (left).

We are now able to perform simulations at constant physical energy density and study the influence of the additional UV cutoff. A corresponding example for the time evolution of the total energy density for different combinations of  $Q$  and  $\Lambda$  is given in Figure 7.9. We present results without an IR cutoff, where we fixed the initial energy density using the top left contour plot in Figure 7.8. Additionally, we show results with an IR cutoff of  $m/Q = 0.1$ , where we fixed the energy density at  $Q\tau = 0.3$ , the time at which discretization effects should have vanished for our choice of parameters, using the right bottom contour plot in Figure 7.8.

## 7.4 Occupation numbers

It is a well-known fact that during the simulation in a static box higher modes get more and more populated compared to the expanding system where the opposite behavior is exhibited [80,88,90,91]. We confirm this by an investigation of the occupation number of

<sup>3</sup>Strictly speaking, they show that the saturation scale  $Q_s$  is virtually independent of the UV cutoff  $\Lambda$ , but thereby, all other parameters were kept fixed, which implies the independence of  $\Lambda$  and the ratio  $Q/Q_s$ .



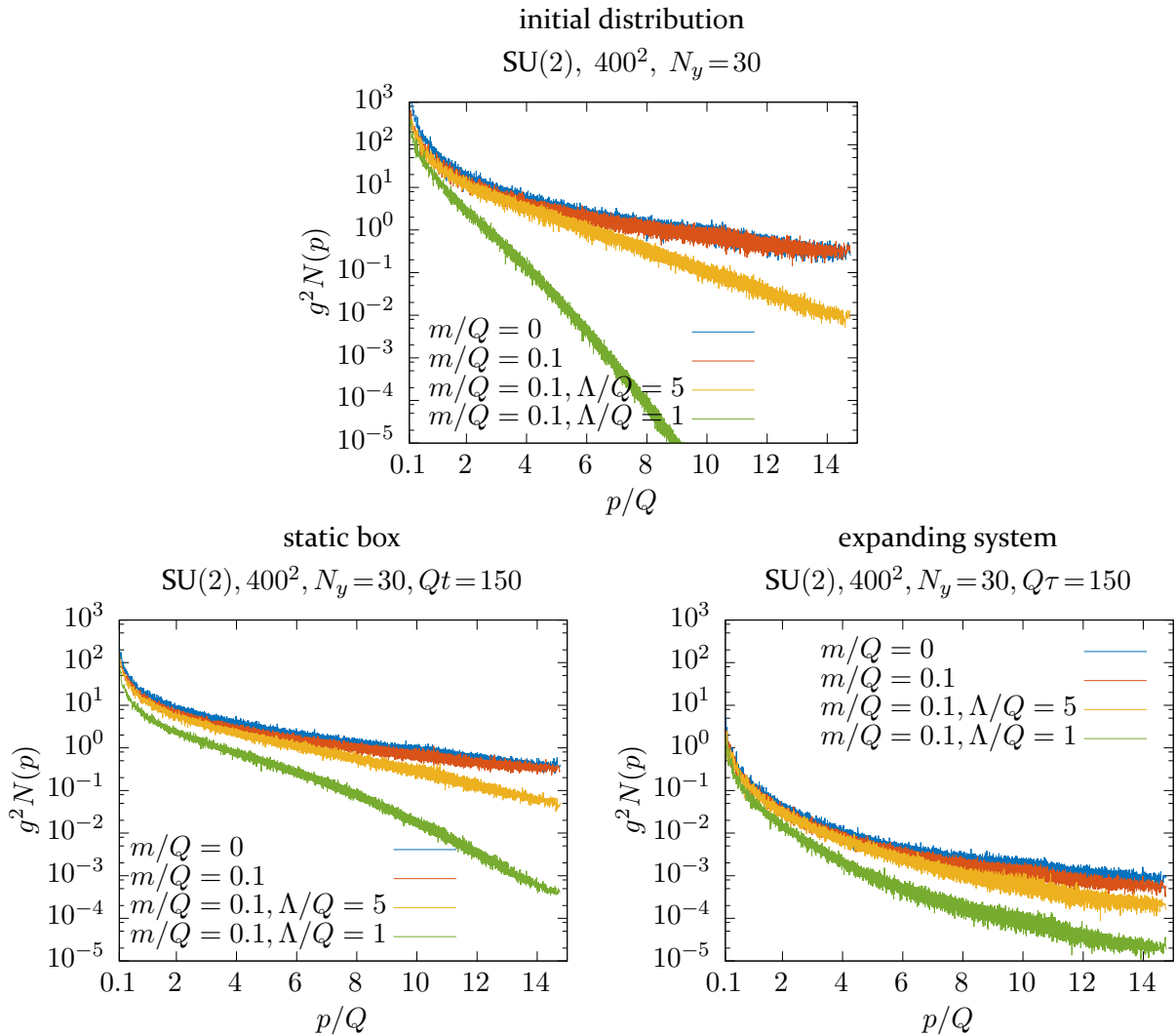


**Figure 7.10:** Occupation number as a function of the momentum  $p/Q$  for different IR and UV cutoffs at initial time (top) and after the same number of time evolutions in the static box scenario (bottom left) and in the expanding formulation (bottom right).

the field quanta depending on their momentum, where the occupation number is defined via the energy density distribution in Fourier space, cf. (6.34).

Figure 7.10 (top) shows the mode occupation for different cutoff values at initial time. In order to study the full range of the influence of the additional UV cutoff, we deliberately chose  $\Lambda = Q$ , which is its smallest sensible value according to (7.1). One clearly sees that the additional UV cutoffs cause a strong suppression of higher modes. Another observation is that the distribution is rather independent of the IR cutoff value.

Note that the horizontal axis starts at  $p=0.1 Q$ , which is the lower border of the regime where the free massless dispersion relation is obtained in [83], cf. also (6.32). The highest momentum, which can be described by our lattice setup is given for the here used

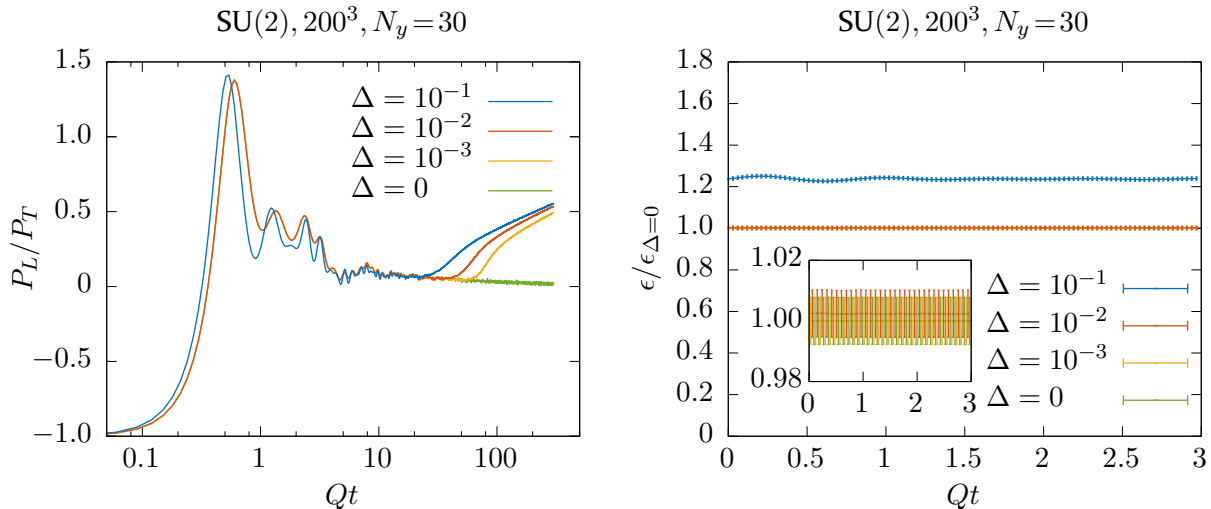


**Figure 7.11:** Pressure ratio (left) and total energy density normalized by its value at  $\Delta=0$  (right) for different fluctuation amplitudes  $\Delta$  using the exact same transverse initialization.

parameter set by

$$p_{\max} \equiv \frac{\sqrt{2\pi}N_{\perp}}{QL}Q \approx 14.81 Q, \quad (7.4)$$

where we used (5.8). As a check, this is in accordance with value where the curves end in Figure 7.10.

The different evolutions of the exact same initial configuration in the two frameworks is depicted in Figure 7.10 (bottom). While without an additional UV cutoff the distributions of the modes nearly reach a plateau in the static box, the occupation of the higher modes in the expanding system stays low. In addition to the possibility of taking the limit  $a_{\perp} \rightarrow 0$ , this is a clear demonstration of the importance of the additional UV cutoff in the static box scenario, since we need high occupancies and a domination of the low-momentum regime in order to verify our classical description.

## 7.5 Towards isotropization

It is a well-known fact, that a system within the CGC framework will never isotropize at lowest order and thus utilizing the “standard” MV model, which is a lowest order description of CGC, is not sufficient to study isotropization [81]. However, the concept of adding longitudinal fluctuations, which we introduced in Section 4.3, is a promising approach. Corresponding investigations of the originally proposed MV model plus these fluctuations are given, e.g., in [28, 81, 88].

One of the findings in these references is that the longitudinal expansion drives the system away from isotropy and consequently no full isotropization can be reached in the

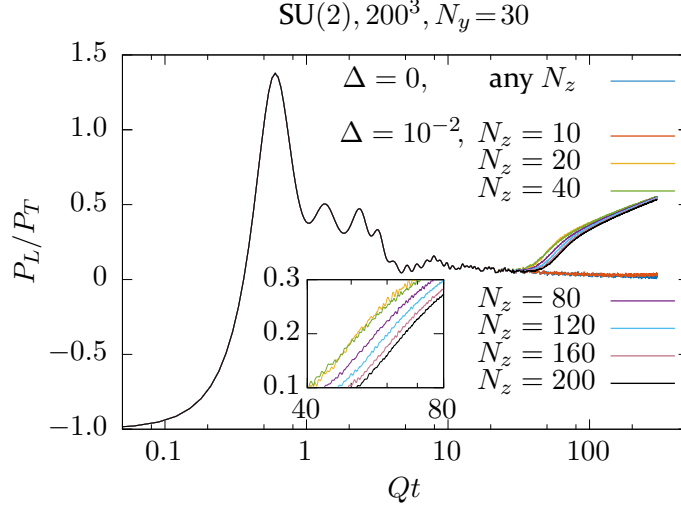


**Figure 7.12:** Pressure ratio for different longitudinal lattice extents  $N_z$  using the exact same transverse initialization. Note that the zoom inlay also has a logarithmic horizontal axis.

comoving formulation.<sup>4</sup> To this end, we focus on the static box scenario and investigate the evolution of the ratio of the pressure components  $P_L/P_T$  in order to quantify the system's isotropy. Obviously, we have to extend our two-dimensional analysis by an additional longitudinal direction  $N_z$  requiring 3D lattice simulations.

### 7.5.1 The effect of the fluctuation amplitude

Adding fluctuations to the initial chromo-electric fields (4.40) yields  $\bar{E}_{\text{init}} \rightarrow \bar{E}_{\text{init}} + \delta\bar{E}$  and thus a non-vanishing initial energy density in the transverse components with the following proportionality,<sup>5</sup>

$$\bar{E}_{\perp,\text{init}} = \delta\bar{E}_{\perp} \propto \Delta \Rightarrow \bar{\epsilon}_{\perp,\text{init}}^E \propto \bar{E}_{\perp,\text{init}}^2 \propto \Delta^2. \quad (7.5)$$

Hence, adding longitudinal fluctuations to the system entails a growth of the initial energy density and, consequently, we have to monitor the total energy density while varying the fluctuation amplitude  $\Delta$ . The corresponding lattice results for the pressure ratio as well as for the energy density is shown in Figure 7.11.

After the peak at around  $Qt \approx 0.6$  it follows a damped oscillating behavior towards  $P_L/P_T = 0$ , which originates from turbulent pattern formation and diffusion [88] and precludes a hydrodynamical description. Then, the pressure ratio rises (for  $\Delta > 0$ ) and the system evolves towards isotropization. Obviously, increasing  $\Delta$  reduces the isotropization time, but a too large seed affects the early behavior of the system, which manifests

<sup>4</sup>A figure substantiating this statement is given in Appendix D.4.

<sup>5</sup>In Appendix D.4 we show the corresponding proportionality in the comoving formulation, which involves additional numerical obstacles and is thus another reason why we stick to static box scenario.

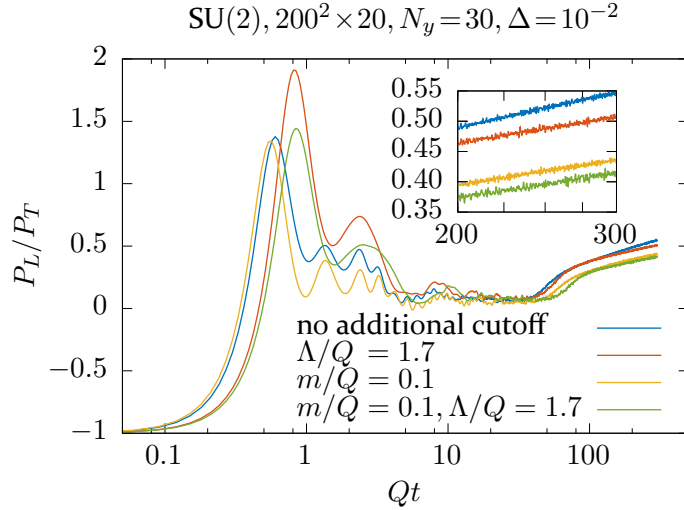


**Figure 7.13:** Pressure ratio for different IR and UV cutoffs for a single run. Note that the zoom inlay also has a logarithmic horizontal axis.

itself through a strong change in the pressure ratio and a significant increase in the energy density.

For  $\Delta \lesssim 10^{-2}$  there is no visible effect on the pressure ratio at early times ( $Qt \lesssim 20$ ) and also the energy stays constant within numerical fluctuations. That is why we will choose this value in the majority of the following investigation concerning the system's isotropization.

### 7.5.2 Variation of the longitudinal box size

Till now, we have not focused on the system's dependence on the longitudinal extent of our static box. Since we are using an isotropic description, i.e.  $a_{\perp} = a_z = a_{\sigma}$ , changing the number of longitudinal lattice points  $N_z$  is equivalent to extending the physical size of the box in that direction. Obviously, the computation time growth linearly with  $N_z$ , since it is the number of transverse slices we have to iterate on the lattice. In Figure 7.12 we see a strong dependence on  $N_z$ , which seems to decrease for larger values and should vanish in the limit  $N_z \rightarrow \infty$ . Interestingly, for a very small value of  $N_z = 10$ , the system behaves comparable to the unperturbed  $\Delta = 0$  case.

However, both varying  $N_z$  and varying  $\Delta$  lead to a similar curve progression at late times, which appears to be logarithmic in  $Qt$ . Extrapolating the values of the  $200^3$  simulation with  $\Delta = 10^{-2}$ , which is the parameter combination we will mostly stick to in the following, leads to a hydrodynamization time<sup>6</sup> of  $t \approx 800/Q \approx 80$  fm. This value is considerably too high, but fits earlier static box observations, e.g., in [88].

<sup>6</sup>The hydrodynamization time is the time where hydrodynamic models are said to be applicable and is commonly defined via the pressure ratio,  $P_L/P_T = 0.7$ .

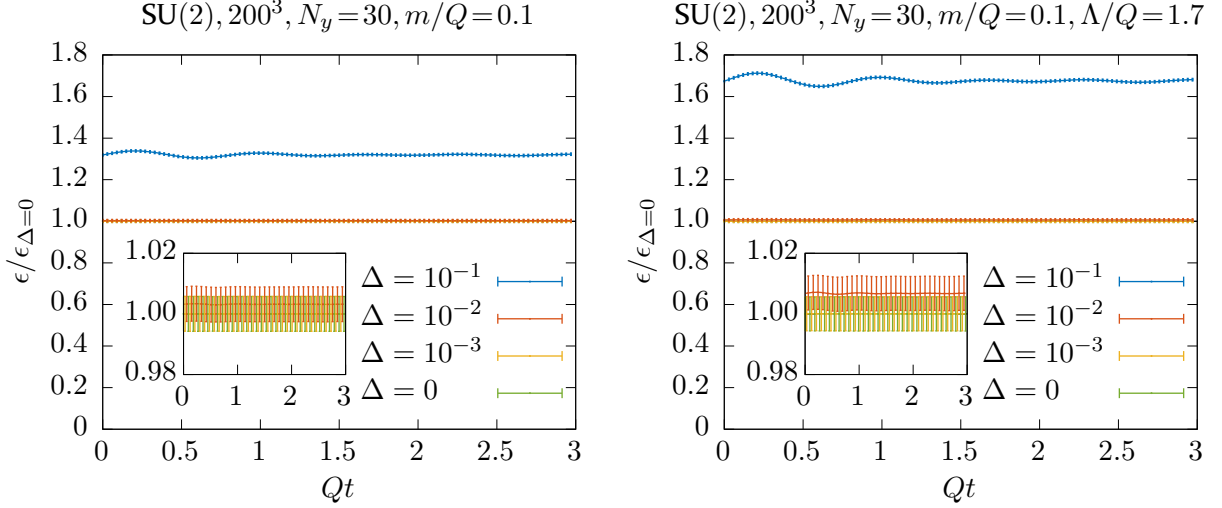


**Figure 7.14:** Energy density with (left) and without (right) additional UV cutoff normalized by their values at  $\Delta = 0$  for different fluctuation amplitudes  $\Delta$ . All curves are based on the exact same transverse initialization.

### 7.5.3 Cutoff dependence of the isotropization times

The pressure ratio is highly sensitive both to the IR and to the UV cutoff as can be obtained from Figure 7.13. The process of isotropization gets clearly slowed down by the IR cutoff  $m$ , while the UV cutoff  $\Lambda$  has a rather moderate influence on it. Furthermore, especially the UV cutoff changes the qualitative curve shape at early times significantly.

Both cutoffs also increase the sensitivity to the fluctuation amplitude  $\Delta$  with regard to the relative growth of the energy density. The respective impact of the IR (left) and UV (right) cutoff on the system's total energy density is shown in Figure 7.14.

A comparison with the cutoff-free result of Figure 7.11 (right), yields that both cutoffs slightly reduce the statistical fluctuations, while the relative rise in the energy density gets reinforced, particularly by the additional UV cutoff. This is due to the fact that the total energy density of the system is reduced by the cutoffs and thus the additional energy density coming from the fluctuation term, which is cutoff independent, gets relatively enhanced. The respective relative growth in the energy density is summarized in Table 7.1, where we clearly see the proportionality of the energy density originating from the fluctuations,  $\epsilon_{\text{fluc}} \propto \Delta^2$ . The absolute increase is independent of the additional cutoffs and reads for the parameters chosen throughout this subsection

$$\frac{g^2 \epsilon_{\text{fluc}}}{Q^4 N_c N_g} \approx 3.9 \Delta^2. \quad (7.6)$$

	$\frac{g^2\epsilon}{Q^4 N_c N_g}$	relative increase		
	$\Delta=0$	$\Delta=10^{-1}$	$\Delta=10^{-2}$	$\Delta=10^{-3}$
no additional cutoff	0.163	23.9 %	0.239 %	0.00239 %
$m/Q=0.1$	0.122	32.2 %	0.321 %	0.00322 %
$m/Q=0.1$ and $\Lambda/Q=1.7$	0.057	68.1 %	0.682 %	0.00683 %

**Table 7.1:** The total energy density and its relative increase due to the fluctuations for different cutoff setups, cf. Figure 7.11 (right) and Figure 7.14. The statistical errors are all below the 1 %-level.

### 7.5.4 Isotropization studies at constant energy density

In Section 7.5.1 we have shown, that the fluctuation seed  $\Delta$  cannot be taken to higher values than  $\approx 10^{-2}$  without affecting the system’s energy density significantly. In Section 7.3.3 we presented investigations at constant energy density, where the energy decrease due to the additional UV cutoff  $\Lambda$  was compensated by changing the overall scale  $QL$ . We will now present a similar study by relating  $\Delta$  and  $\Lambda$ .

By tuning  $\Lambda$  and  $\Delta$  appropriately, we are able to keep the system’s total energy density fixed. Thereby no further parameter has to be varied and hence the physical setup stays unaffected. Hence, changing  $\Lambda$  and  $\Delta$  while keeping the energy density fixed, allows for an investigation of the system depending on the relative amount of initial energy density described by the classical CGC initial conditions and hence allows us to set, in a sense, the “border” that separates the classical IR regime from the quantum UV sector within our description. To this end, we plot the energy density  $\epsilon/Q^4$  in the  $\Delta$ - $(\Lambda/Q)$  plane in Figure 7.15.

## 7.6 Chromo-Weibel instability

In the last subsection we saw that the system isotropizes if we add quantum fluctuations to the classical MV initial conditions. In particular, instabilities such as the so-called *chromo-Weibel instability* have been proposed as a collective phenomenon that may thermalize a weakly coupled non-Abelian plasma and is thus a subject of intense research [92–99].

The chromo-Weibel instability is in the linear limit similar to the *Weibel instability* in electrodynamic plasmas [13, 100]. However, non-abelian plasmas exhibit non-linear interactions which lead to a development of an instability characterized by a turbulent cascade of energy modes [17, 101, 102]. The increase of the pressure ratio towards isotropization, which we obtained in Section 7.5.1, may be attributed to the chromo-Weibel instability as we show now.

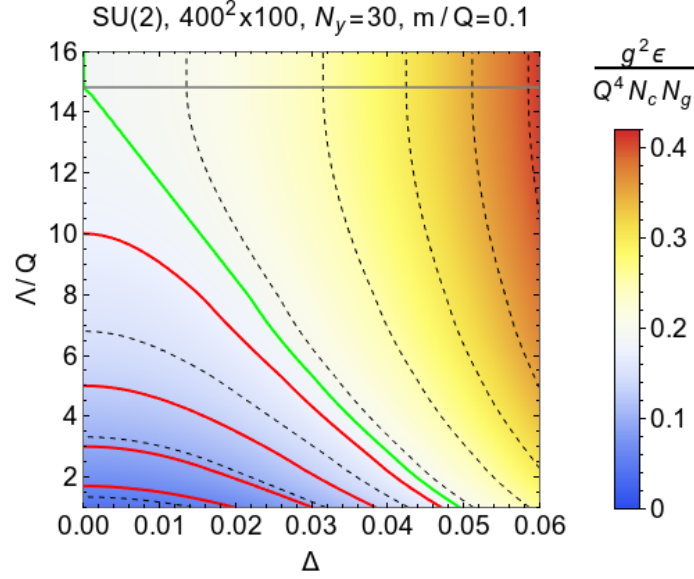


**Figure 7.15:** Total energy density for different fluctuation seeds  $\Delta$  and different UV cutoffs  $\Lambda/Q$  at initial time. The dashed lines represent constant energy density levels, which are integer multiples of 0.05. The solid lines correspond to constant energy densities obtained for  $\Delta = 0$ , where the red lines indicate  $\Lambda$  values of  $1.7Q$ ,  $3Q$ ,  $5Q$  and  $10Q$ , while the green line shows the respective constant energy density contour where no additional UV cutoff was applied. The gray horizontal line represents the lattice UV cutoff above which the additional UV cutoff does no longer affect the system.

First, our anisotropic initial conditions imply a fluctuating current, a necessary ingredient for the occurrence of a Weibel instability. Second, a Weibel instability causes a rapid population of harder modes during evolution in time, which is clearly realized in our system as we showed in Section 7.4.

However, the most striking illustration of the occurrence of a chromo-Weibel instability is obtained by looking at the chromo-electric and chromo-magnetic energy densities in position space, where filaments caused by the instability are clearly visible. Figure 7.16 shows the amplitude of the transverse chromo-magnetic energy density in the  $yz$ -plane while averaging over the remaining  $x$ -direction.<sup>7</sup> Each box is a snapshot at a certain time step given in the plot title, where the position of the time value corresponds to the respective plot row.

The horizontal pattern at  $Qt = 0.3$  (first row of Figure 7.16) for  $\Delta = 10^{-2}$  and  $\Delta = 10^{-3}$  represents the initial fluctuations which are independent of the longitudinal direction  $z$ . At the next time step ( $Qt = 90$ , second row) the chromo-Weibel instability is visible by the filaments that become clearer for higher fluctuation seeds. At late times of the

<sup>7</sup>In Figures 7.16 and 7.17, we can of course replace  $x$  by  $y$  and vice versa, since the two transverse directions are indistinguishable.

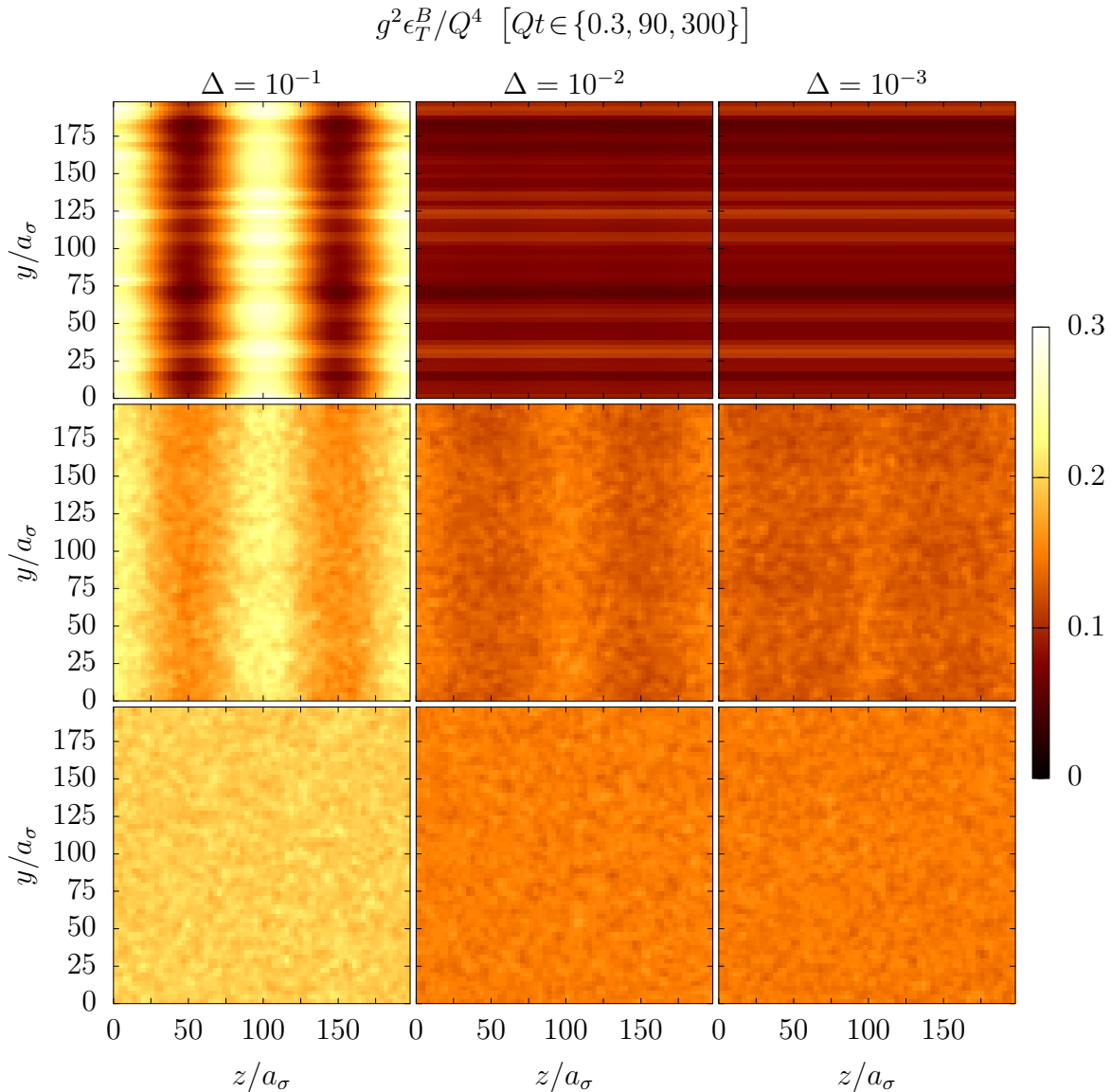


**Figure 7.16:** Snapshots of the transverse component of the chromo-magnetic energy density, cf. (6.10) and (6.11), in the  $yz$ -plane at different times (top down:  $Qt \in \{0.3, 90, 300\}$ ) and different fluctuation amplitudes (left to right:  $\Delta \in \{10^{-1}, 10^{-2}, 10^{-3}\}$ ).

simulation ( $Qt = 300$ , third row) saturation kicks in and the filaments dissolve again.

As a check, Figure 7.17 shows that indeed no filament structure arises in the transverse plane, as expected. This holds both for the chromo-magnetic and for the chromo-electric energy densities as well as for all of their components. The averaged values of the energy densities are random with large deviations at early stages which get smoother during the time evolution.

Qualitatively the snapshots do not change, if we replace the chromo-magnetic energy density  $\epsilon^B$  by the chromo-electric energy density  $\epsilon^E$ , with one exception: For a fluctuation amplitude of  $\Delta = 10^{-1}$ , we see a direct filamentation in the transverse-longitudinal plane



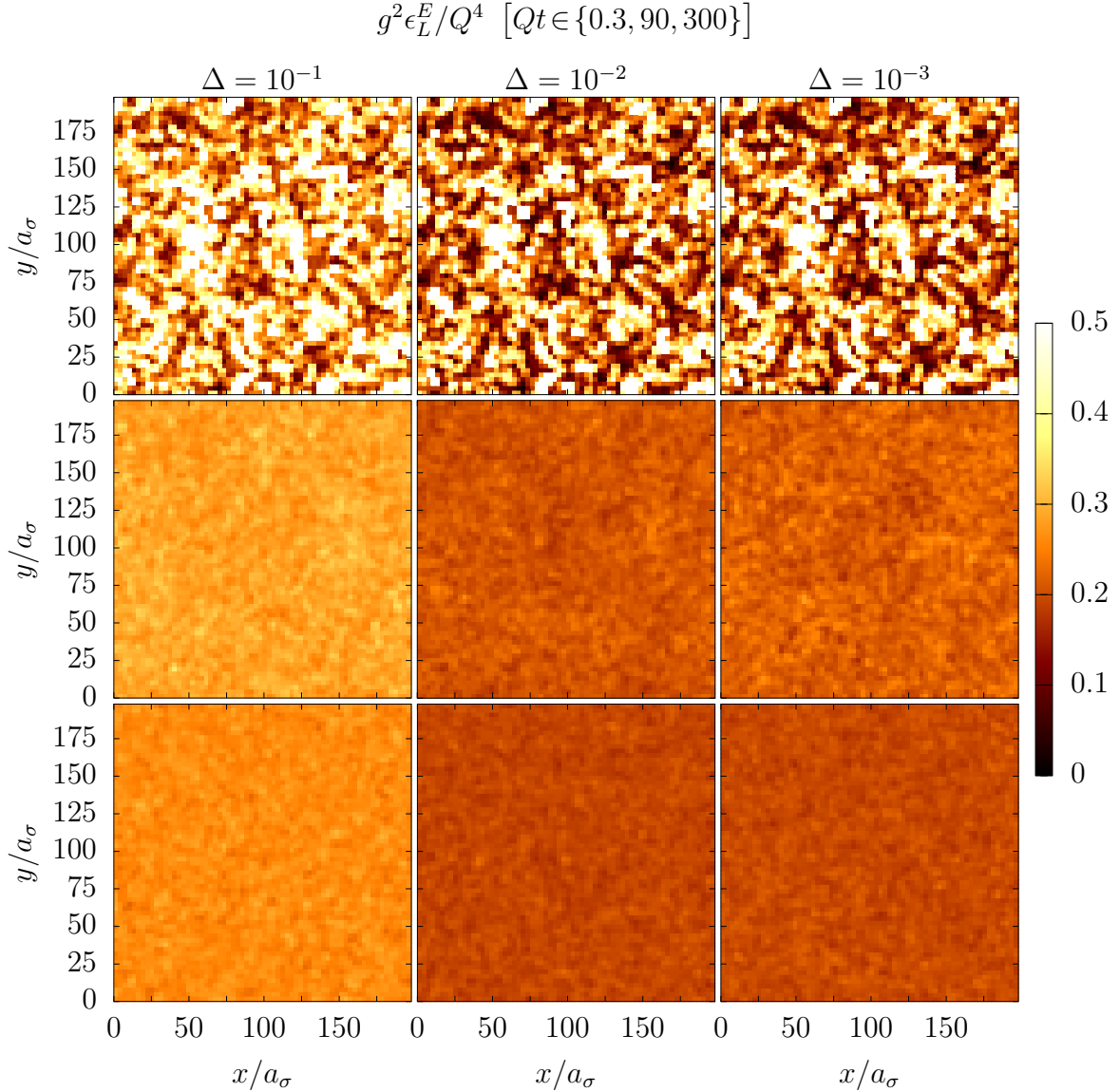


**Figure 7.17:** Snapshots of the longitudinal component of the chromo-electric energy density, cf. (6.10) and (6.11), in the  $xy$ -plane at different times (top down:  $Qt \in \{0.3, 90, 300\}$ ) and different fluctuation amplitudes (left to right:  $\Delta \in \{10^{-1}, 10^{-2}, 10^{-3}\}$ ).

for  $\epsilon_T^B$  and  $\epsilon_L^E$  while this is not the case for  $\epsilon_L^B$  and  $\epsilon_T^E$ , where we only see a dynamic<sup>8</sup> filamentation. The corresponding missing figures can be found in Appendix D.5.

In Figure 7.11 we saw a significant change in the early stages of the simulation (left) and a substantial increase of the system's energy density (right) for a fluctuation seed of  $\Delta = 10^{-1}$ , as discussed in the beginning of this section. Figures 7.16 and 7.17 confirm this observation, which is evident from the fact that for  $\Delta = 10^{-1}$  we already see clear filaments at  $Qt = 0.3$  (cf. Figure 7.16) and also that the colors of the left column of both Figure 7.16 and Figure 7.17 are much brighter than the two others, which implies a higher

<sup>8</sup>The term “dynamic” means in this case “occurring during the time evolution”.

overall energy density of the system.

In the comoving framework we could not find any dynamic filamentation. Nevertheless, for fluctuation amplitudes of the order of  $10^{-1}$  we obviously do see filaments right from the beginning, since the initial configuration is equivalent to the one we have shown for the static box scenario. However, as already stated in Section 7.5.1, even this high fluctuation amplitude is not sufficient to reach isotropization due to the expansion of the system.

# Chapter 8

## Fermionic impact on the CGC system

---

### Contents

8.1	Total energy density . . . . .	94
8.2	Isotropization times . . . . .	95

---

In this chapter we will present first results of simulations of the classical MV initial conditions in the presence of fermions. In particular, this semiclassical study is dedicated to the investigation of the fermionic impact on global observables such as the total energy density (6.9) and the ratio of longitudinal (6.13) and transverse (6.12) pressure. The latter study is especially related to the question, whether the isotropization times we obtained in the pure gauge case (cf. Section 7.5) get affected by the presence of the fermionic degrees of freedom.

As discussed in Chapters 1 and 3, simulations including fermions require significantly larger computational resources, even in the case of our stochastic low-cost implementation (cf. Section 3.3). Therefore, we are forced to use smaller lattices and will choose a cubic<sup>1</sup> one with  $60^3$  lattice points. Furthermore, we use massless fermions and also exclude the doubler term, which introduces additional computational costs due to the entailed field multiplications in the equations of motion (3.76) and the computation of the fermionic energy density (3.45).

For this choice and using an ensemble of  $N_{\text{ens}} = 20$  gendered fermions, which yields numerically robust results, the computation time grows by a factor of  $\approx 30$  compared to the pure gauge case, which should justify the performed simplifications.

---

<sup>1</sup>Since we want to study the System including fluctuations, we need the third spacial dimension. For the pure gauge simulations, we mostly used cubic lattices in order to exclude finite volume effects in longitudinal direction, which is why we do so here as well.

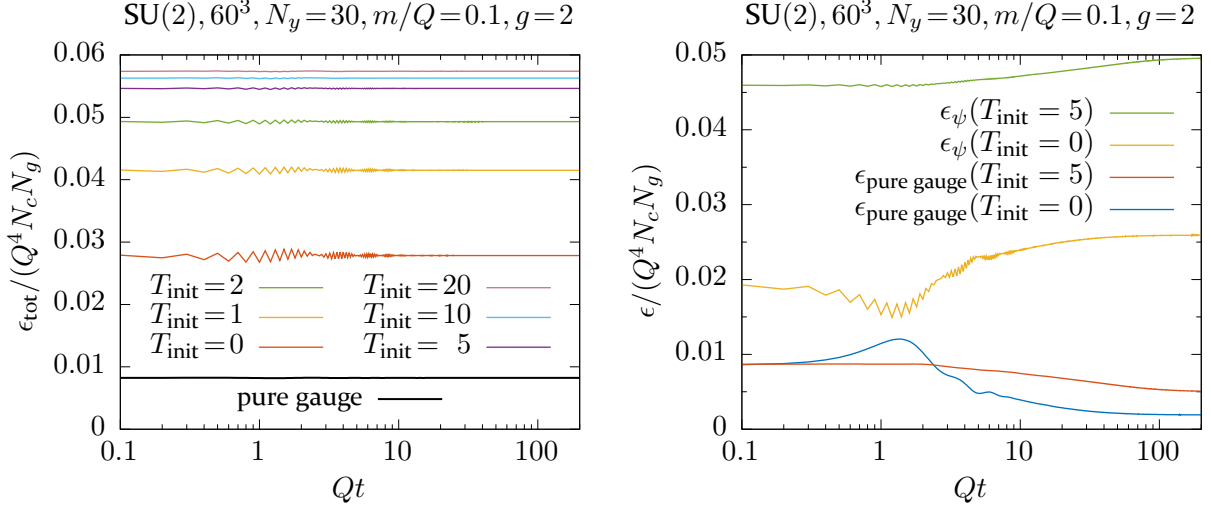


**Figure 8.1:** Left: The sum of the gluonic (pure gauge) and fermionic energy density  $\epsilon_{\text{tot}}$  for different initial fermionic pseudo-Temperatures  $T_{\text{init}}$  compared to the respective pure gauge result. Right: The single gluonic and fermionic contributions for two of these pseudo-temperatures.

## 8.1 Total energy density

The first observable we investigate is the total energy density of the system. Of course adding fermions entails an increase of the system's energy due to the additional amount of elements contributing to it.

In Figure 3.3 we showed that the initial fermionic energy density is highly sensitive to the temperature. However, setting a reasonable value for the latter is non-trivial since a temperature is only defined in a thermalized system whereas the initial stage of a heavy-ion collision which we are investigating is far away from equilibrium. On the other hand, a vacuum initialization also seems to be questionable due to the high energy densities and pressures present in the pure gauge sector.

To this end, we vary the Temperature of the fermionic degrees of freedom and treat it as a *pseudo-temperature*, which defines the initial fermionic energy density.

Different than it was the case in the pure gauge simulations, we now have to separate the two scales building up the MV parameter  $Q \equiv g^2 \mu$ . This is due to the fact that  $g$  has now the import role of the coupling of the fermions to the gauge sector. In accordance with our previous simulations, we will use

$$QL_{\perp} \equiv g^2 \mu a_{\perp} N_{\perp} = 120 \quad (8.1)$$

for all following investigations.

As it is the commonly proposed value of the coupling constant [81, 84, 88], we will use  $g = 2$  as a starting value of our semiclassical studies. In Section 8.2 we will, however, also present results for different couplings in order to study the respective ramifications.

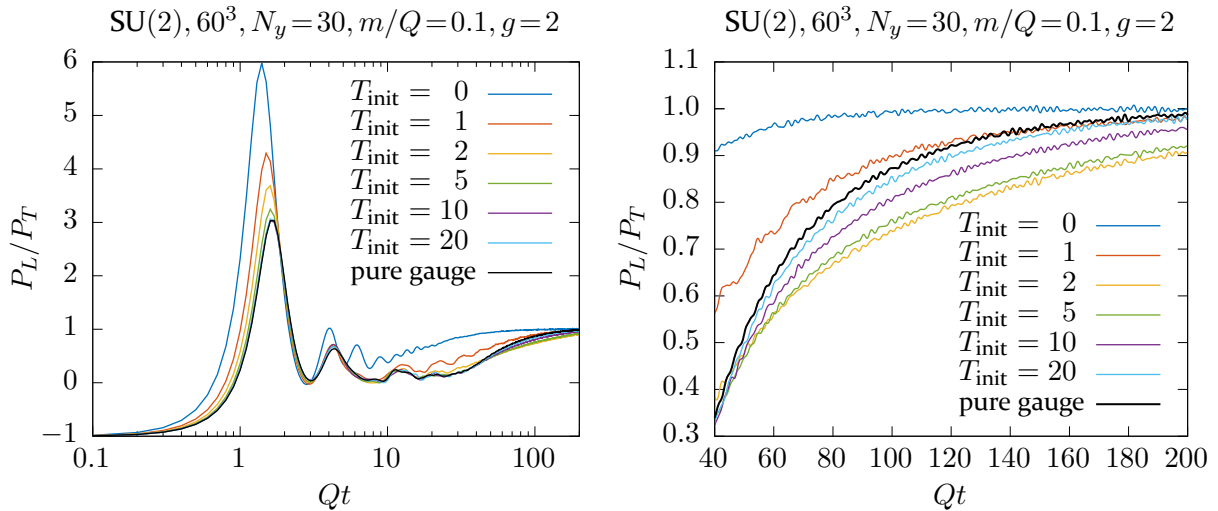


**Figure 8.2:** The pressure ratio for different initial fermionic pseudo-temperatures  $T_{\text{init}}$  compared to the pure gauge case. Note the missing log scale in the right plot.

Figure 8.1 (left) shows the total energy density  $\epsilon_{\text{tot}} \equiv \epsilon_{\psi} + \epsilon_{\text{pure gauge}}$ , where  $\epsilon_{\psi}$  is the fermionic energy density (3.45) and  $\epsilon_{\text{pure gauge}}$  the energy density of the pure gauge sector defined as  $\epsilon$  in (6.9). Besides the expected rise in the total energy density for higher pseudo-temperatures, which originates from the temperature dependence of  $\epsilon_{\psi}$  (cf. Figure 3.3), we see a fluctuating pattern at early times, which gets milder for  $T_{\text{init}} \rightarrow \infty$ .

In Figure 8.1 (right) the pure gauge and the respective pure fermionic parts of the total energy density  $\epsilon_{\text{tot}}$  are presented for a fermionic vacuum initialization ( $T_{\text{init}} = 0$ ) and one with a rather high pseudo-temperature ( $T_{\text{init}} = 5$ ). During the first time evolution steps, we clearly see an exchange of energy first from the fermionic to the gluonic sector and then, for  $Qt \approx 1.5$ , vice versa. This behavior is attenuated in the case of higher pseudo-temperatures. However, in both cases the energy densities saturate and become constant at  $Qt \approx 100$  for  $T_{\text{init}} = 0$  and  $Qt \approx 160$  for  $T_{\text{init}} = 5$ .

Hence, it is obvious that there is a noticeable effect of the fermionic degrees of freedom on the pure gauge system, which becomes milder and milder for higher pseudo-temperatures. In the next section we will see whether and, if so, how the isotropization process changes when we include fermions. To this end, we will also vary the coupling constant  $g$ .

## 8.2 Isotropization times

In order to investigate the isotropization process of system we monitor the time evolution of the longitudinal to transverse pressure ratio as we already did in the pure gauge case, cf. Section 7.5. Apart from the initial fermionic pseudo-temperature  $T_{\text{init}}$ , we will in this section also vary the coupling constant  $g$ , which determines strength of the gluonic and

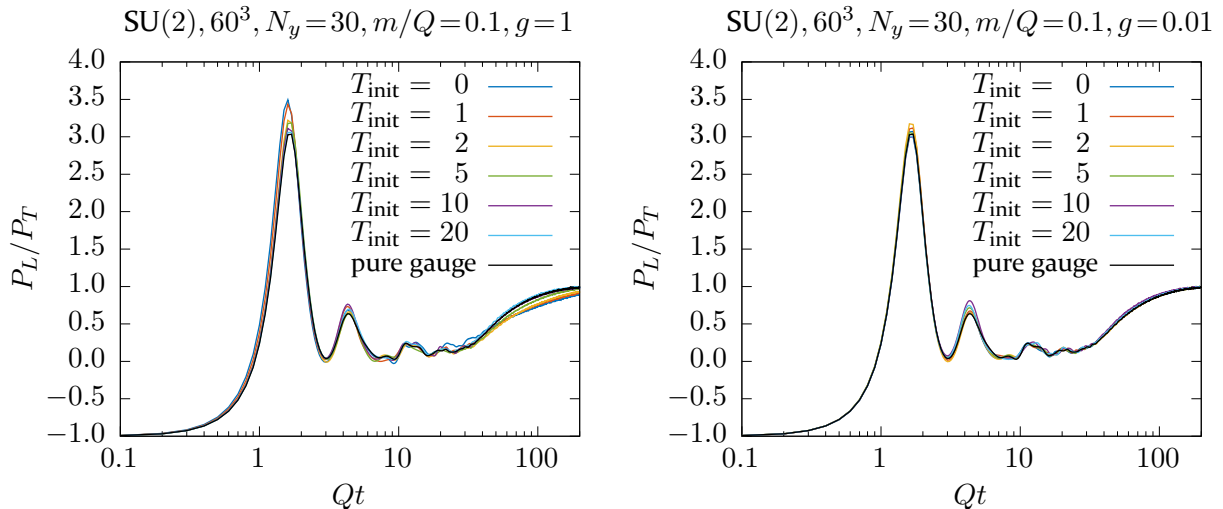


**Figure 8.3:** The pressure ratio for different initial fermionic pseudo-temperatures  $T_{\text{init}}$  compared to the pure gauge case choosing two different couplings,  $g = 1$  (left) and  $g = 0.01$  (right), respectively.

fermionic interactions. Thereby we will keep our overall scale (8.1) constant.

To begin with, we present results for the pressure ratio for various initial fermionic pseudo-temperatures  $T_{\text{init}}$  for the choice of  $g = 2$ , cf. Figure 8.2. For this relatively high value of the coupling constant we see a significant change in the isotropization process. The initial oscillating pattern of the pressure ratio gets amplified, particularly the first peak at  $Qt \approx 1.5$ . This effect gets diminished for higher values of the initial pseudo-temperature  $T_{\text{init}}$ . Moreover, we clearly see a considerably faster isotropization for the vacuum initialization. For  $T_{\text{init}} = 1$  the isotropization time is still shorter while for pseudo-temperatures above that value it appears to be longer with a maximum at  $T_{\text{init}} = 2$ . For  $T_{\text{init}} \rightarrow \infty$  we then approach the pure gauge result, which is in accordance with the findings from Section 8.1, where we observed that the exchange of the gluonic and fermionic sector vanishes in that limit.

We now want to study the influence of the strength of the coupling. We chose two smaller values for the coupling constant,  $g = 1$  and  $g = 0.01$ , and show the corresponding results for the pressure ratios in Figure 8.3.<sup>2</sup> By decreasing the coupling, a clear trend towards the pure gauge result is visible. This is a plausible observation, since for very small couplings the pure gauge system evolves almost independently of the fermionic sector.

Nevertheless, we cannot confirm the claim that the fermionic degrees of freedom do not contribute to the isotropization process. At least for sufficiently large values of the coupling constant and small initialization temperatures we disproved this statement.

<sup>2</sup>A corresponding figure for  $g = 0.6$  can be found in Appendix D.6.

# Chapter 9

## Conclusion

---

### Contents

9.1	Summary and key findings . . . . .	97
9.2	Research perspectives . . . . .	99

---

### 9.1 Summary and key findings

In this work we studied the early stages present immediately after a heavy-ion collision in order to provide insights into the isotropization process of the system. We presented a systematic investigation of the various parameters entering our description through the CGC initial conditions, which are particularly based on the MV model. In the course of this, also the extent of occurring discretization and finite volume effects due to the lattice description as well as systematic errors stemming from the classical approximation were monitored. Moreover, we explored the impact of the fermionic degrees of freedom on the pure gauge setup described by the classical Yang-Mills theory. The key findings as well as the corresponding approaches and methods we were using will be summarized and discussed in the following.

We started out with an introduction of the theoretical basics that form the foundation of this thesis in Chapter 2. It included a compilation of the central aspects of QCD as well as of the Hamiltonian field theory and introduced the two different formulations we utilized, i.e. the static box and the expanding system. It also comprised a motivation of the classical description and a corresponding condition for its validity. Chapter 3 provided a detailed introduction to the employed lattice framework containing the stochastic fermion implementation and the derivation of the lattice equations of motion. Moreover, we presented first numerical cross-checks which confirmed the correct implementation of the fermionic energy density based on the stochastic formulation. Our lattice evolution equations of the pure gauge part were also verified by comparing results of the

real-time static potential with former works. This was followed by an introduction to the CGC effective theory and the MV model in Chapter 4 with whom we constructed the initial conditions for our lattice simulations. Some important technical aspect including definitions of the various lattice and model parameters were discussed in Chapter 5 and the different observables we investigated were summarized in Chapter 6 both in the continuum and on the lattice. The two subsequent chapters then presented the main part of our numerical results.

In Chapter 7 we studied the  $N_c$ -dependence as well as the lattice artifacts and extensively investigated the CGC parameter space. We saw that we have to deal with significant discretization effects in the static box whereas they become negligible in the expanding formulation for  $Q\tau \gtrsim 0.3$  and  $N_\perp \gtrsim 400$ . Furthermore, we found that boundary effects play a rather minor role as well as that the more economical SU(2) gauge group is adequate for our description, since the sensitivity to the initial condition parameters is considerably higher. In particular, we showed that the number of longitudinal sheets  $N_y$  and both additional cutoffs have a major impact on the total energy density of the system. However, for the physically motivated choice of  $m/Q = 0.1$  for the IR cutoff, we obtained that for  $N_y \gtrsim 30$  the dependence on the number of longitudinal sheets is gone and thus the  $N_y \rightarrow \infty$  limit is sufficiently approximated. Even though there is no physically motivated choice for the UV cutoff, we presented a method to reduce the number of free parameters by appropriate contour plots. Moreover, the field occupancies based on a gauge invariant definition were monitored and demonstrated the importance of the additional UV cutoff especially in the static box.

The chapter closed with the investigation of the isotropization time obtained from the longitudinal to transverse pressure ratio. We found that the system cannot isotropize without extending the two-dimensional description to a three-dimensional where we add fluctuations. It became apparent that the finite volume effects in the third spacial direction are very large for small longitudinal extents and become bearable for  $N_z \gtrsim 20$ , whereas the impact of the cutoffs and particularly the fluctuation amplitude  $\Delta$  is tremendous. However, we were once again able to reduce the number of free parameters by relating the additional UV cutoff to the fluctuation seed via a contour plot allowing for studies at constant total energy density. This also incorporates the possibility to vary the amount of the system that is described classically which then determines the part of the initial energy that is induced by the quantum fluctuations.

The last chapter preceding the present one, was devoted to the study of the impact of the fermionic degrees of freedom. We saw a strong dependence of the isotropization process on the initial fermionic pseudo-temperature  $T_{\text{init}}$  as well as on the coupling constant  $g$ . For small values of the former and large one of latter, in particular for  $T_{\text{init}} = 0$  and  $g = 2$ , the isotropization gets highly accelerated. However, increasing the pseudo-temperature or decreasing the coupling reduces this effect and for  $T_{\text{init}} = 20$  or  $g = 0.01$  the results became virtually identical to the corresponding pure gauge result.



## 9.2 Research perspectives

Although we provided an extensive study of the parameter space of the classical MV model, one can still expand this investigation. Especially in the three-dimensional case, i.e. the one including longitudinal fluctuations, one could combine the two-dimensional contour plots of Figure 7.8 and Figure 7.15 to a three-dimensional version in order to further reduce the number of free parameters.

As shown in Section 7.5, the classical CGC system will never isotropize as long as no quantum fluctuations are added. The perturbation of our initial setup by a single  $\eta$ -mode represented by the rather simple fluctuation terms (4.36) and (4.41) was, however, sufficient to cause the system's isotropization. Nevertheless, a more advanced description of the quantum fluctuations will probably yield deeper insights into the mechanisms of thermalization.

A different approach towards a better understanding of the thermalization process would be to employ an appropriate kinetic description. Our results presented in this thesis could then serve as a benchmark for the corresponding kinetic equations in the classical sector.

Obviously, the computation of time evolutions in the quantum regime based on non-perturbative techniques would be a significant breakthrough. A promising real-time approach in this respect is given by the framework of stochastic quantization on the lattice [103–107].

With regard to our fermion implementation, there are clearly further investigations available as well. A reasonable value for the coupling constant  $g$  stemming from first principle considerations as well as sensibly defining an observable which provides information about the number of present fermions together with an inclusion of respective creation and annihilation processes would be a highly interesting extension.

One could also think about implementing more advanced fermion descriptions such as overlap fermions [52, 53]. In particular, they possess perfect lattice chiral symmetry, which allows for studying transport phenomena induced by anomalies such as the chiral magnetic effect [108, 109]. Furthermore, this implementation also offers the possibility of investigating chiral plasma instabilities [110–112].

Moreover, mesons made out of heavy quarks are of particular interest for the study of the medium that is formed in relativistic heavy-ion collisions. Especially the bottomonium, which has a relatively large binding energy in the vacuum make theorists speculate that it can survive in the deconfined phase. Additionally, the formation time of  $\tau \approx 1$  fm [113, 114] will make it sensitive to early-time dynamics. Corresponding production yield rates between the ground state and excited states can provide information about properties such as, e.g., the ratio of the shear viscosity to the entropy density. A natural continuation of this thesis would thus be the study of bottomonia in real-time classical simulations employing the formalism of non-relativistic QCD (NRQCD) [115].



# Appendices



# Appendix **A**

## Conventions and definitions

---

### Contents

A.1	Natural units . . . . .	103
A.2	Comments on notation . . . . .	104
A.3	Poisson bracket . . . . .	104
A.4	Generators and structure constants . . . . .	104
A.5	Gamma matrices . . . . .	105

---

### A.1 Natural units

In natural units the reduces Planck constant  $\hbar$ , the speed of light  $c$  and the Boltzmann constant  $k_B$  are set to one,

$$\hbar = c = k_B = 1. \quad (\text{A.1})$$

As a consequence, we can express all units in terms of the unit of energy,

$$[\text{energy}] = [\text{mass}] = [\text{temperature}] = [\text{length}]^{-1} = [\text{time}]^{-1}. \quad (\text{A.2})$$

We will mostly use  $\text{MeV} = 10^6 \text{ eV} \approx 1.6021766208(98) \times 10^{-13} \text{ J}$  [21] or  $1 \text{ fm} = 10^{-15} \text{ m}$ , since these are convenient energy and length scales in particle physics. They are related by the conversion constant

$$1 \equiv \hbar c = 197.3269788(12) \text{ MeV fm}. \quad (\text{A.3})$$

As a result, the conversion to SI units of mass, temperature and time reads:

$$\text{Mass:} \quad \text{MeV} \approx 1.78266 \times 10^{-30} \text{ kg} \quad (\text{A.4a})$$

$$\text{Temperature:} \quad \text{MeV} \approx 1.16045 \times 10^{10} \text{ K} \quad (\text{A.4b})$$

$$\text{Time:} \quad \text{MeV}^{-1} \approx 6.58212 \times 10^{-22} \text{ s} \quad (\text{A.4c})$$

## A.2 Comments on notation

- Throughout this work we use a large number of lattice and CGC parameters. They are summarized and explained in Section 5.1.
- We apply Einstein's summation convention, i.e., a sum over all identical indices (within one expression) is implied unless explicitly indicated otherwise.
- A variable with a "bar", e.g.  $\bar{\epsilon}$ , denotes a rescaled dimensionless variable. In this case the rescaled dimensionless energy density  $\bar{\epsilon} \equiv g^2 a_{\perp} \epsilon$ , cf. (6.9) or (6.25).

## A.3 Poisson bracket

Given the functions  $f(q_i, p_i, t)$ ,  $g(q_i, p_i, t)$  and  $h(q_i, p_i, t)$ , the Poisson brackets are defined as

$$\{f, g\}_{\text{PB}} = \sum_{i=1}^N \left( \frac{\partial f}{\partial q_i} \frac{\partial g}{\partial p_i} - \frac{\partial f}{\partial p_i} \frac{\partial g}{\partial q_i} \right). \quad (\text{A.5})$$

They have the following properties ( $a, b \in \mathbb{R}$ ),

$$\{f, g\}_{\text{PB}} = -\{g, f\}_{\text{PB}}, \quad (\text{A.6a})$$

$$\{af + bg, h\}_{\text{PB}} = \{af, h\}_{\text{PB}} + \{bg, h\}_{\text{PB}}, \quad (\text{A.6b})$$

$$\{fg, h\}_{\text{PB}} = \{f, h\}_{\text{PB}}g + f\{g, h\}_{\text{PB}}, \quad (\text{A.6c})$$

and fulfill the Jacobi identity,

$$\{f, \{g, h\}_{\text{PB}}\}_{\text{PB}} + \{g, \{h, f\}_{\text{PB}}\}_{\text{PB}} + \{h, \{f, g\}_{\text{PB}}\}_{\text{PB}} = 0. \quad (\text{A.7})$$

## A.4 Generators and structure constants

### A.4.1 SU(2)

The generators of the Lie algebra  $\mathfrak{su}(2)$  are defined via the Pauli matrices,  $T^a = \sigma^a/2$ , which have the following form:

$$\sigma^1 = \begin{pmatrix} 0 & 1 \\ 1 & 0 \end{pmatrix} \quad \sigma^2 = \begin{pmatrix} 0 & -i \\ i & 0 \end{pmatrix} \quad \sigma^3 = \begin{pmatrix} 1 & 0 \\ 0 & -1 \end{pmatrix} \quad (\text{A.8})$$

The antisymmetric structure constants are identical to the Levi-Civita symbol in three dimensions

$$f^{abc} \equiv \epsilon^{abc} = \begin{cases} +1, & \text{if } (a, b, c) \in \{(1, 2, 3), (2, 3, 1), (3, 1, 2)\} \\ -1, & \text{if } (a, b, c) \in \{(1, 3, 2), (2, 1, 3), (3, 2, 1)\} \\ 0, & \text{else} \end{cases} \quad (\text{A.9})$$

and the symmetric structure constants  $d^{abc}$  are all equal to zero.

The antisymmetric structure constants are given by:

$abc$	123	147	156	246	257	345	367	458	678
$f^{abc}$	1	$\frac{1}{2}$	$-\frac{1}{2}$	$\frac{1}{2}$	$\frac{1}{2}$	$\frac{1}{2}$	$-\frac{1}{2}$	$\frac{\sqrt{3}}{2}$	$\frac{\sqrt{3}}{2}$

**Table A.1:** Antisymmetric structure constants of SU(3).

and symmetric structure constants by:

$abc$	118	146	157	228	247	256	338	344
$d^{abc}$	$\frac{1}{\sqrt{3}}$	$\frac{1}{2}$	$\frac{1}{2}$	$\frac{1}{\sqrt{3}}$	$-\frac{1}{2}$	$\frac{1}{2}$	$\frac{1}{\sqrt{3}}$	$\frac{1}{2}$
$abc$	355	366	377	448	558	668	778	888
$d^{abc}$	$\frac{1}{2}$	$-\frac{1}{2}$	$-\frac{1}{2}$	$-\frac{1}{2\sqrt{3}}$	$-\frac{1}{2\sqrt{3}}$	$-\frac{1}{2\sqrt{3}}$	$-\frac{1}{2\sqrt{3}}$	$-\frac{1}{\sqrt{3}}$

**Table A.2:** Symmetric structure constants of SU(3).

#### A.4.2 SU(3)

In the case of SU(3) the generators of the related Lie algebra are similarly specified, i.e.  $T^a = \lambda^a/2$ , where the Gell-Mann matrices  $\lambda^a$  are defined as:

$$\begin{aligned}
\lambda^1 &= \begin{pmatrix} \sigma^1 & 0 \\ 0 & 0 \end{pmatrix} & \lambda^2 &= \begin{pmatrix} \sigma^2 & 0 \\ 0 & 0 \end{pmatrix} & \lambda^3 &= \begin{pmatrix} \sigma^3 & 0 \\ 0 & 0 \end{pmatrix} & \lambda^4 &= \begin{pmatrix} 0 & 0 & 1 \\ 0 & 0 & 0 \\ 1 & 0 & 0 \end{pmatrix} \\
\lambda^5 &= \begin{pmatrix} 0 & 0 & -i \\ 0 & 0 & 0 \\ i & 0 & 0 \end{pmatrix} & \lambda^6 &= \begin{pmatrix} 0 & 0 & 0 \\ 0 & 0 & 1 \\ 0 & 1 & 0 \end{pmatrix} & \lambda^7 &= \begin{pmatrix} 0 & 0 & 0 \\ 0 & 0 & -i \\ 0 & i & 0 \end{pmatrix} & \lambda^8 &= \frac{1}{\sqrt{3}} \begin{pmatrix} 1 & 0 & 0 \\ 0 & 1 & 0 \\ 0 & 0 & -2 \end{pmatrix}
\end{aligned} \tag{A.10}$$

All other structure constants are equal to zero, if they cannot be related by permutation to the  $abc$ -combinations in Table A.1 and Table A.2, respectively. Note that each permutation gives an additional minus sign in the antisymmetric case.

## A.5 Gamma matrices

The gamma matrices in the so-called *Dirac basis* are defined via the Pauli matrices (A.8),

$$\gamma^0 = \begin{pmatrix} 1 & 0 \\ 0 & -1 \end{pmatrix}, \quad \gamma^i = \begin{pmatrix} 0 & \sigma^i \\ -\sigma^i & 0 \end{pmatrix}, \tag{A.11}$$

with the defining property

$$\{\gamma^\mu, \gamma^\nu\} \equiv \gamma^\mu \gamma^\nu + \gamma^\nu \gamma^\mu = 2\eta^{\mu\nu}. \quad (\text{A.12})$$

Note that we use the time favored metric (2.30a). The  $\gamma^5$ -matrix is given by

$$\gamma^5 = i\gamma^0\gamma^1\gamma^2\gamma^3 = \begin{pmatrix} 0 & 1 \\ 1 & 0 \end{pmatrix}, \quad \text{with} \quad \{\gamma^5, \gamma^\mu\} = 0. \quad (\text{A.13})$$

A useful relation for a 4-vector in Minkowski space  $x$ , which directly follows from (A.12), reads

$$(\gamma^\mu x_\mu)^2 = \gamma^\mu \gamma^\nu x_\mu x_\nu = \eta^{\mu\nu} x_\mu x_\nu = x^\mu x_\mu \equiv x^2, \quad (\text{A.14})$$

with Einstein's summation convention as usual.



# Appendix **B**

## Lattice relations

---

### Contents

B.1	Discretized derivatives . . . . .	107
B.2	Fourier transformation . . . . .	108
B.3	Euclidian formulation . . . . .	109
B.4	From lattice output to physical quantities . . . . .	110

---

### B.1 Discretized derivatives

The forward and backward discretized derivatives of a function  $f(x)$ , with  $h \ll 1$ , are given by:

$$f'^f(x) = \frac{f(x+h) - f(x)}{h} + \mathcal{O}(h) \quad (\text{B.1})$$

$$f'^b(x) = \frac{f(x) - f(x-h)}{h} + \mathcal{O}(h) \quad (\text{B.2})$$

The symmetric version and the second discretized derivative reads:

$$f'(x) = \frac{f(x+h) - f(x-h)}{2h} + \mathcal{O}(h^2) \quad (\text{B.3})$$

$$f''(x) = \frac{f(x+h) - 2f(x) + f(x-h)}{h^2} + \mathcal{O}(h^2) \quad (\text{B.4})$$

The last line can easily be proven by a Taylor expansion of  $f(x \pm h)$  around  $x$  and a following comparison of  $f(x+h) - f(x-h)$  and  $f(x+h) + f(x-h)$ .

Note that for the symmetric discretized derivative the approximation error is  $\mathcal{O}(h^2)$ , while for a backward or forward discretization the error is  $\mathcal{O}(h)$ .

To show that the covariant symmetric derivative on the lattice (3.16) has the correct naive continuum limit, we expand the exponentials in the definition of the gauge link variables (3.14) and (3.15), yielding

$$\begin{aligned}
 \mathcal{D}_\mu \psi(x) &= \frac{1}{2a} \left\{ [1 + \text{iga}A_\mu(x + \hat{\mu}) + \mathcal{O}(a^2)]\psi(x + \hat{\mu}) \right. \\
 &\quad \left. - [1 - \text{iga}A_\mu(x - \hat{\mu}) + \mathcal{O}(a^2)]\psi(x - \hat{\mu}) \right\} \\
 &= \frac{\psi(x + \hat{\mu}) - \psi(x - \hat{\mu})}{2a} \\
 &\quad + \text{ig} \frac{A_\mu(x + \hat{\mu})\psi(x + \hat{\mu}) + A_\mu(x - \hat{\mu})\psi(x - \hat{\mu})}{2} + \mathcal{O}(a) \\
 &\xrightarrow{a \rightarrow 0} \partial_\mu \psi(x) + \text{ig}A_\mu(x).
 \end{aligned} \tag{B.5}$$

## B.2 Fourier transformation

### B.2.1 Continuum definition

Throughout this work, we use the symmetric convention for the Fourier transformation. Accordingly, the Fourier transform and its inverse is given in the continuum and  $d$  dimensions by

$$\tilde{f}(p) = \frac{1}{(2\pi)^{\frac{d}{2}}} \int_{\mathbb{R}^d} f(x) e^{-ip \cdot x}, \tag{B.6a}$$

$$f(x) = \frac{1}{(2\pi)^{\frac{d}{2}}} \int_{\mathbb{R}^d} \tilde{f}(p) e^{+ip \cdot x}. \tag{B.6b}$$

### B.2.2 Lattice equivalent

Let us define the function  $f(n)$  on a lattice  $\Lambda = \{n = (n_1, \dots, n_d) \mid n_\mu = 0, 1, \dots, N_\mu - 1\}$ , with  $|\Lambda| = N_1 \cdots N_d = V$ . Its Fourier transform  $\tilde{f}(p)$  is then defined on the reciprocal lattice  $\tilde{\Lambda} = \{p = (p_1, \dots, p_d) \mid p_\mu = \frac{2\pi}{a_\mu N_\mu} k_\mu, k_\mu = -\frac{N_\mu}{2} + 1, \dots, \frac{N_\mu}{2}\}$ , with  $|\tilde{\Lambda}| = |\Lambda|$ , reading

$$\begin{aligned}
 \tilde{f}(p) &= \frac{1}{\sqrt{|\Lambda|}} \sum_{n \in \Lambda} f(n) \exp(-ipna) \\
 &= \frac{1}{\sqrt{V}} \sum_{n_1=0}^{N_1-1} \cdots \sum_{n_d=0}^{N_d-1} f(n_1, \dots, n_d) \exp\left(-i \sum_{\mu=1}^d \frac{2\pi}{N_\mu} k_\mu n_\mu\right),
 \end{aligned} \tag{B.7a}$$

$$\begin{aligned}
 f(n) &= \frac{1}{\sqrt{|\Lambda|}} \sum_{p \in \tilde{\Lambda}} \tilde{f}(p) \exp(+ipna) \\
 &= \frac{1}{\sqrt{V}} \sum_{k_1=-\frac{N_1}{2}+1}^{\frac{N_1}{2}} \cdots \sum_{k_d=-\frac{N_d}{2}+1}^{\frac{N_d}{2}} \tilde{f}(k_1, \dots, k_d) \exp\left(+i \sum_{\mu=1}^d \frac{2\pi}{N_\mu} k_\mu n_\mu\right).
 \end{aligned} \tag{B.7b}$$

### B.2.3 Additions to the solution of Poisson's equation

Applying

$$\Lambda(x \pm 1) = \frac{1}{\sqrt{N}} \sum_p \tilde{\Lambda}(p) e^{ip(x \pm 1)} \quad (\text{B.8})$$

$$\rho(x) = \frac{1}{\sqrt{N}} \sum_p \tilde{\rho}(p) e^{ipx} \quad (\text{B.9})$$

to (4.22) leads in one dimension to:

$$\begin{aligned} \sum_p \tilde{\Lambda}(p) \left[ e^{ip(x+1)} - 2e^{ipx} + e^{ip(x-1)} + m^2 e^{ipx} \right] &= - \sum_p \tilde{\rho}(p) e^{ipx} \\ \Leftrightarrow \sum_p \tilde{\Lambda}(p) \left[ e^{ip} e^{i(p-p')x} - 2e^{i(p-p')x} + e^{-ip} e^{i(p-p')x} + m^2 e^{i(p-p')x} \right] &= - \sum_p \tilde{\rho}(p) e^{i(p-p')x} \\ \Leftrightarrow \tilde{\Lambda}(p) \left[ e^{ip} - 2 + e^{-ip} + m^2 \right] &= -\tilde{\rho}(p) \\ \Leftrightarrow \tilde{\Lambda}(p) &= \frac{\tilde{\rho}(p)}{2 - e^{ip} - e^{-ip} + m^2} \end{aligned} \quad (\text{B.10})$$

This can easily be extended to the two-dimensional case we are interested in,

$$\tilde{\Lambda}(p_1, p_2) = \frac{\tilde{\rho}(p_1, p_2)}{4 - e^{ip_1} - e^{-ip_1} - e^{ip_2} - e^{-ip_2} + m^2}, \quad (\text{B.11})$$

where

$$\tilde{\rho}(p_1, p_2) = \frac{1}{\sqrt{N_1 N_2}} \sum_{x,y} \rho(x, y) e^{i(p_1 x + p_2 y)}. \quad (\text{B.12})$$

## B.3 Euclidian formulation

The Euclidean expression for the action belonging to the fermionic part of the QCD Lagrangian density (2.4) with a single flavor reads

$$S_E = \int d^4x \mathcal{L}_E \equiv \int d^4x d^4y \bar{\psi}(x) D_E(x, y) \psi(y), \quad (\text{B.13})$$

where we introduced the Euclidean Dirac operator

$$D_E(x, y) = \delta(x - y) (\gamma_E^\mu D_\mu + m) \quad (\text{B.14})$$

and a new set of gamma matrices  $\gamma_E^\mu$ , which are related to those defined in Minkowski space (cf. (A.5)) via <sup>1</sup>

$$\left\{ \gamma_E^1, \gamma_E^2, \gamma_E^3, \gamma_E^4 \right\} = \left\{ -i\gamma^1, -i\gamma^2, -i\gamma^3, \gamma^0 \right\}. \quad (\text{B.15})$$

<sup>1</sup>This definition is usually referred to as the *non-relativistic representation*.

Applying the Euler-Lagrange (D.1) for  $\bar{\psi}$  and the Euclidean Lagrangian density defined in (B.13) yields [60]

$$(\gamma_E^\mu D_\mu + m)\psi(x) = 0, \quad (\text{B.16})$$

which is the Euclidean Dirac equation.

## B.4 From lattice output to physical quantities

The dimensionless combinations of physical quantities, which are used throughout this work are related to the bare lattice output (red) in the following way:

$$Q\tau = \frac{\bar{Q}}{a_\perp} a_\perp \bar{\tau} = \bar{Q} \bar{\tau} = \bar{Q} \bar{a}_\tau n_\tau \quad (\text{B.17a})$$

$$\frac{g^2 \epsilon}{Q^4} = \frac{g^2 \epsilon}{\left(\frac{\bar{Q}}{a_\perp}\right)^4} = \frac{g^2 a_\perp^4 \epsilon}{\bar{Q}^4} = \frac{1}{\bar{Q}^4} \bar{\epsilon} \quad (\text{B.17b})$$

$$\frac{g^2 \tau \epsilon}{Q^3} = \frac{g^2 a_\perp \bar{\tau} \epsilon}{\left(\frac{\bar{Q}}{a_\perp}\right)^3} = \frac{\bar{\tau} g^2 a_\perp^4 \epsilon}{\bar{Q}^3} = \frac{\bar{a}_\tau}{\bar{Q}^3} n_\tau \bar{\epsilon} \quad (\text{B.17c})$$

Obviously, we can replace  $\tau$  by  $t$  and  $\epsilon$  by  $P_{L/T}$ .

The occupation number by definition is dimensionless, however, the relation to the lattice output is non-trivial,

$$g^2 N(k) = g^2 n(k) \mathcal{V} = g^2 \frac{\tilde{\epsilon}(k)}{p(k)} a_\perp^3 V = \frac{g^2 a_\perp^4 \tilde{\epsilon}(k)}{a_\perp p(k)} V = \frac{g^2 a_\perp^4 \tilde{\epsilon}(k)}{\left(\frac{2\pi k}{N}\right)} V = \frac{NV}{2\pi k} \tilde{\tilde{\epsilon}}(k). \quad (\text{B.18})$$

# Appendix C

## Lattice equations of motion

### Contents

C.1	Static box	111
C.2	Expanding system	115

### C.1 Static box

#### C.1.1 Chromo-electric fields

We separate the derivation in a gluonic and a fermionic part,

$$\partial_i \bar{E}_i^a(x) = -g^2 a_\sigma^4 \frac{\partial \mathcal{H}^L}{\partial \bar{A}_i^a(x)} = -g^2 a_\sigma^4 \frac{\partial \mathcal{H}_F^L}{\partial \bar{A}_i^a(x)} - g^2 a_\sigma^4 \frac{\partial \mathcal{H}_G^L}{\partial \bar{A}_i^a(x)}. \quad (\text{C.1})$$

We find for the gluonic part <sup>1</sup>

$$\begin{aligned} -g^2 a_\perp^4 \frac{\partial \mathcal{H}_G^L}{\partial \bar{A}_i^a(x)} &= -\frac{\partial}{\partial \bar{A}_i^a(x)} \sum_y \text{Re Tr} \left[ \sum_i \bar{E}_i^2(y) + 2 \sum_{k < j} (1 - U_{kj}(y)) \right] \\ &= 2 \frac{\partial}{\partial \bar{A}_i^a(x)} \sum_{y, k < j} \text{Re Tr} \left\{ U_k(y) U_j(y + \hat{k}) U_k^\dagger(y + \hat{j}) U_j^\dagger(y) \right\} \\ &= 2 \sum_{y, k < j} \text{Re Tr} \left\{ i \left[ T^b U_k(y) U_j(y + \hat{k}) U_k^\dagger(y + \hat{j}) U_j^\dagger(y) \delta_{ab} \delta_{ik} \delta_{xy} \right. \right. \\ &\quad \left. \left. + U_k(y) T^b U_j(y + \hat{k}) U_k^\dagger(y + \hat{j}) U_j^\dagger(y) \delta_{ab} \delta_{ij} \delta_{x, y + \hat{k}} \right. \right. \\ &\quad \left. \left. - U_k(y) U_j(y + \hat{k}) U_k^\dagger(y + \hat{j}) T^b U_j^\dagger(y) \delta_{ab} \delta_{ik} \delta_{x, y + \hat{j}} \right. \right. \\ &\quad \left. \left. - U_k(y) U_j(y + \hat{k}) U_k^\dagger(y + \hat{j}) U_j^\dagger(y) T^b \delta_{ab} \delta_{ij} \delta_{xy} \right] \right\} \end{aligned}$$

<sup>1</sup>The sum over the spacetime points  $y$  is artificially introduced and does not influence the result, since only the fields at  $y = x$  contribute.

$$\begin{aligned}
 &= 2 \sum_{y,k < j} \text{Re Tr} \left\{ iT^a \left[ U_k(y) U_j(y + \hat{k}) U_k^\dagger(y + \hat{j}) U_j^\dagger(y) \delta_{ik} \delta_{xy} \right. \right. \\
 &\quad \left. \left. + U_j(y + \hat{k}) U_k^\dagger(y + \hat{j}) U_j^\dagger(y) U_k(y) \delta_{ij} \delta_{x,y+\hat{k}} \right. \right. \\
 &\quad \left. \left. - U_j^\dagger(y) U_k(y) U_j(y + \hat{k}) U_k^\dagger(y + \hat{j}) \delta_{ik} \delta_{x,y+\hat{j}} \right. \right. \\
 &\quad \left. \left. - U_k(y) U_j(y + \hat{k}) U_k^\dagger(y + \hat{j}) U_j^\dagger(y) \delta_{ij} \delta_{xy} \right] \right\} \\
 &= 2 \sum_{y,k < j} \text{Re Tr} \left\{ iT^a \left[ U_{kj}(y) \delta_{ik} \delta_{xy} \right. \right. \\
 &\quad \left. \left. + U_{j,-k}(y + \hat{k}) \delta_{ij} \delta_{x,y+\hat{k}} \right. \right. \\
 &\quad \left. \left. - U_{-jk}(y + \hat{j}) \delta_{ik} \delta_{x,y+\hat{j}} \right. \right. \\
 &\quad \left. \left. - U_{kj}(y) \delta_{ij} \delta_{xy} \right] \right\} \\
 &= 2 \sum_{k < j} \text{Re Tr} \left\{ iT^a \left[ U_{kj}(x) \delta_{ik} + U_{j,-k}(x) \delta_{ij} - U_{-jk}(x) \delta_{ik} - U_{kj}(x) \delta_{ij} \right] \right\} \\
 &= 2 \text{Re Tr} \left\{ iT^a \left( \sum_{i < j} [U_{ij}(x) - U_{-ji}(x)] - \sum_{k < i} [U_{ki}(x) - U_{i,-k}(x)] \right) \right\} \\
 &\quad \left[ \text{Re}(iz) = -\text{Im}(z) \right] \\
 &= -2 \text{Im Tr} \left\{ T^a \left( \sum_{i < j} [U_{ij}(x) - U_{-ji}(x)] - \sum_{j < i} [U_{ji}(x) - U_{i,-j}(x)] \right) \right\} \\
 &\quad \left[ \text{Im Tr}\{T^a U_{ji}(x)\} = -\text{Im Tr}\{T^a U_{ij}(x)\}, \text{ since } T^{a\dagger} = T^a \text{ and } U_{ij}^\dagger(x) = U_{ji}(x) \right] \\
 &= -2 \text{Im Tr} \left\{ T^a \left( \sum_{i < j} [U_{ij}(x) - U_{-ji}(x)] + \sum_{j < i} [U_{ij}(x) - U_{-ji}(x)] \right) \right\} \\
 &= -2 \sum_{i \neq j} \text{Im Tr} \left\{ T^a [U_{ij}(x) - U_{-ji}(x)] \right\} \\
 &= -2 \sum_{j \neq i} \text{Im Tr} \left\{ T^a [U_{ij}(x) + U_{i,-j}(x)] \right\} \\
 &= 2 \sum_{j \neq i} \text{Im Tr} \left\{ T^a [U_{ji}(x) + U_{-ji}(x)] \right\}, \tag{C.2}
 \end{aligned}$$

where we used the symmetry of the plaquette as well as the cyclicity of the trace to evaluate the derivative of the links.

For the fermionic part, we have to expand the gauge link fields (3.14) in terms of

$$U_{\pm\mu}(x) = 1 \pm ig a A_\mu^a T^a + \mathcal{O}(a^2) \equiv 1 \pm i \bar{A}_\mu^a T^a + \mathcal{O}(a^2). \tag{C.3}$$

$$\begin{aligned}
 -g^2 a_\perp^4 \frac{\partial \mathcal{H}_F^L}{\partial \bar{A}_i^a} &= -g^2 \frac{\partial}{\partial \bar{A}_i^a(x)} \sum_y \left\{ -i \bar{\Psi}(y) \gamma^j \frac{1}{2} [U_j(y) \Psi(y + \hat{j}) - U_j^\dagger(y - \hat{j}) \Psi(y - \hat{j})] \right. \\
 &\quad \left. - \frac{r}{2} \bar{\Psi}(y) \sum_j [U_j(y) \Psi(y + \hat{j}) - 2\Psi(y) + U_j^\dagger(y - \hat{j}) \Psi(y - \hat{j})] \right\} \\
 &= g^2 \sum_y \left\{ i \bar{\Psi}(y) \gamma^j \frac{1}{2} [iT^b U_j(y) \Psi(y + \hat{j}) \delta_{ij} \delta_{ab} \delta_{xy} \right.
 \end{aligned}$$

$$\begin{aligned}
 & + \mathbf{i}U_j^\dagger(y - \hat{j})T^b\Psi(y - \hat{j})\delta_{ij}\delta_{ab}\delta_{x,y-\hat{j}}] \\
 & + \frac{r}{2}\bar{\Psi}(y)\sum_j\left[\mathbf{i}T^bU_j(y)\Psi(y + \hat{j})\delta_{ij}\delta_{ab}\delta_{xy} \right. \\
 & \quad \left. - \mathbf{i}U_j^\dagger(y - \hat{j})T^b\Psi(y - \hat{j})\delta_{ij}\delta_{ab}\delta_{x,y-\hat{j}}\right] \Big\} \\
 & = \mathbf{i}\frac{g^2}{2}\left\{\mathbf{i}\left[\bar{\Psi}(x)\gamma^iT^aU_i(x)\Psi(x + \hat{i}) + \bar{\Psi}(x + \hat{i})\gamma^iU_i^\dagger(x)T^a\Psi(x)\right] \right. \\
 & \quad \left. + r\left[\bar{\Psi}(x) \quad T^aU_i(x)\Psi(x + \hat{i}) - \bar{\Psi}(x + \hat{i}) \quad U_i^\dagger(x)T^a\Psi(x)\right]\right\} \quad (\text{C.4})
 \end{aligned}$$

which is in equivalence with (3.66). For the computation in the framework of our stochastic low-cost fermions, we have to take the ensemble average and utilize (3.43), yielding together with (C.1) and (C.2)

$$\partial_{\hat{i}}\bar{E}_i^a(x) = 2\sum_{j\neq i}\text{Im Tr}\left\{T^a[U_{ji}(x) + U_{-ji}(x)]\right\} \quad (\text{C.5})$$

$$-\mathbf{i}\frac{g^2}{4}\left\langle\mathbf{i}\left[\bar{\Psi}_M(x)\gamma^iT^aU_i(x)\Psi_F(x + \hat{i}) + \bar{\Psi}_M(x + \hat{i})\gamma^iU_{-i}(x + \hat{i})T^a\Psi_F(x) \right. \right. \quad (\text{C.6})$$

$$\left. + \bar{\Psi}_F(x)\gamma^iT^aU_i(x)\Psi_M(x + \hat{i}) + \bar{\Psi}_F(x + \hat{i})\gamma^iU_{-i}(x + \hat{i})T^a\Psi_M(x)\right] \quad (\text{C.7})$$

$$+ r\left[\bar{\Psi}_M(x) \quad T^aU_i(x)\Psi_F(x + \hat{i}) - \bar{\Psi}_M(x + \hat{i}) \quad U_{-i}(x + \hat{i})T^a\Psi_F(x) \quad (\text{C.8})$$

$$\left. + \bar{\Psi}_F(x) \quad T^aU_i(x)\Psi_M(x + \hat{i}) - \bar{\Psi}_F(x + \hat{i}) \quad U_{-i}(x + \hat{i})T^a\Psi_M(x)\right] \Big\rangle_{\text{ens}}. \quad (\text{C.9})$$

### C.1.2 Fermionic degrees of freedom

Using (3.27a) and (3.27c), we get

$$\partial_t\psi = -\mathbf{i}\frac{\partial\mathcal{H}^L}{\partial\psi^\dagger} \Rightarrow \partial_t\Psi = -\mathbf{i}a_\sigma^4\frac{\partial\mathcal{H}^L}{\partial\Psi^\dagger}. \quad (\text{C.10})$$

With the Hamiltonian density (3.28), we obtain

$$\begin{aligned}
 \partial_{\hat{t}}\Psi(x) & = -\mathbf{i}a_\sigma^4\frac{\partial\mathcal{H}^L}{\partial\Psi^\dagger(x)} \\
 & = -\mathbf{i}\frac{\partial}{\partial\Psi^\dagger(x)}\sum_y\left\{\bar{m}\bar{\Psi}(y)\Psi(y) - \mathbf{i}\bar{\Psi}(y)\gamma^i\mathcal{D}^i\Psi(y) - \frac{r}{2}\bar{\Psi}(y)\square_L\Psi(y)\right\} \\
 & = -\mathbf{i}\frac{\partial}{\partial\Psi^\dagger(x)}\sum_y\left\{\bar{m}\Psi^\dagger(y)\gamma^0\Psi(y) - \mathbf{i}\Psi^\dagger(y)\gamma^0\gamma^i\frac{1}{2}[U_i(y)\Psi(y + \hat{i}) - U_{-i}(y)\Psi(y - \hat{i})] \right. \\
 & \quad \left. - \frac{r}{2}\Psi^\dagger(y)\gamma^0[U_i(y)\Psi(y + \hat{i}) - 2\Psi(y) + U_{-i}(y)\Psi(y - \hat{i})]\right\} \\
 & = -\mathbf{i}\bar{m}\gamma^0\Psi(x) - \frac{1}{2}\gamma^0\gamma^i[U_i(x)\Psi(x + \hat{i}) - U_{-i}(x)\Psi(x - \hat{i})] \\
 & \quad + \mathbf{i}\frac{r}{2}\gamma^0\sum_i[U_i(x)\Psi(x + \hat{i}) - 2\Psi(x) + U_{-i}(x)\Psi(x - \hat{i})]. \quad (\text{C.11})
 \end{aligned}$$

### C.1.3 Gauss's law

The Lagrangian densities (3.26) as well as (3.54) are independent of derivatives of the continuum gauge fields  $A_\mu$ . The Euler-Lagrange equations (D.1) hence become

$$\begin{aligned}
 0 &= \left. \frac{\partial \mathcal{L}_G}{\partial A_0^a(x)} \right|_{A_0=0} \\
 &= -\frac{2}{g^2 a_\sigma^4 \bar{a}_t^2} \frac{\partial}{\partial A_0^a(x)} \sum_{y,i} \text{Re Tr} \left\{ U_0(y) U_i(y + \hat{0}) U_0^\dagger(y + \hat{i}) U_i^\dagger(y) \right\} \Big|_{A_0=0} \\
 &= -\frac{2}{g a_\sigma^3 \bar{a}_t} \sum_{y,i} \text{Re Tr} \left\{ i \left[ T^b U_0(y) U_i(y + \hat{0}) U_0^\dagger(y + \hat{i}) U_i^\dagger(y) \delta^{ab} \delta_{xy} \right. \right. \\
 &\quad \left. \left. - U_0(y) U_i(y + \hat{0}) U_0^\dagger(y + \hat{i}) T^b U_i^\dagger(y) \delta^{ab} \delta_{y+\hat{i},x} \right] \right\} \Big|_{A_0=0} \\
 &= -\frac{2}{g a_\sigma^3 \bar{a}_t} \sum_i \text{Re Tr} \left\{ iT^a \left[ U_0(x) U_i(x + \hat{0}) U_0^\dagger(x + \hat{i}) U_i^\dagger(x) \right. \right. \\
 &\quad \left. \left. - U_i^\dagger(x - \hat{i}) U_0(x - \hat{i}) U_i(x - \hat{i} + \hat{0}) U_0^\dagger(x) \right] \right\} \Big|_{A_0=0}. \quad (\text{C.12})
 \end{aligned}$$

Rebuilding plaquettes then yields

$$\begin{aligned}
 \dots &= -\frac{2}{g a_\sigma^3 \bar{a}_t} \sum_i \text{Re Tr} \left\{ iT^a [U_{0i}(x) - U_{-i0}(x)] \right\} \Big|_{\bar{A}_0=0} \\
 &= -\frac{2}{g a_\sigma^3 \bar{a}_t} \sum_i \text{Im Tr} \left\{ T^a [U_{i0}(x) + U_{-i0}(x)] \right\} \Big|_{\bar{A}_0=0}. \quad (\text{C.13})
 \end{aligned}$$

In contrast, a direct application of the temporal gauge leads to

$$\begin{aligned}
 \dots &= -\frac{2}{g a_\sigma^3 \bar{a}_t} \sum_i \text{Re Tr} \left\{ iT^a [U_i(x + \hat{0}) U_i^\dagger(x) - U_i^\dagger(x - \hat{i}) U_i(x - \hat{i} + \hat{0})] \right\} \\
 &= -\frac{2}{g a_\sigma^3} \sum_i \text{Re Tr} \left\{ iT^a \left[ \underbrace{\frac{U_i(x + \hat{0}) - U_i(x)}{\bar{a}_t}}_{\approx \partial_0 U_i(x) = i \bar{E}_i(x) U_i(x)} U_i^\dagger(x) \right. \right. \\
 &\quad \left. \left. - U_i^\dagger(x - \hat{i}) \underbrace{\frac{U_i(x - \hat{i} + \hat{0}) - U_i(x - \hat{i})}{\bar{a}_t}}_{\approx \partial_0 U_i(x - \hat{i}) = i \bar{E}_i(x - \hat{i}) U_i(x - \hat{i})} \right] \right\} \\
 &= \frac{2}{g a_\sigma^3} \sum_i \text{Re Tr} \left\{ T^a [\bar{E}_i(x) - U_i^\dagger(x - \hat{i}) \bar{E}_i(x - \hat{i}) U_i(x - \hat{i})] \right\}. \quad (\text{C.14})
 \end{aligned}$$



## C.2 Expanding system

### C.2.1 Chromo-electric fields

$$\begin{aligned}
 \partial_{\bar{\tau}} \bar{E}_i^a(x) &= -g^2 a_{\perp}^3 \frac{\partial \mathcal{H}_G^L}{\partial \bar{A}_i^a(x)} \\
 &= -g^2 a_{\perp}^3 \frac{\partial}{\partial \bar{A}_i^a(x)} \frac{1}{g^2 a_{\perp}^3} \sum_y \text{Re Tr} \left\{ 2\bar{\tau} [1 - U_{12}(y)] + \frac{2}{a_{\eta}^2 \bar{\tau}} \sum_j [1 - U_{j\eta}(y)] \right\} \\
 &= 2 \sum_y \text{Re Tr} \left\{ \frac{\partial}{\partial \bar{A}_i^a(x)} \left[ \bar{\tau} U_{12}(y) + \frac{1}{a_{\eta}^2 \bar{\tau}} \sum_j U_{j\eta}(y) \right] \right\} \\
 &= 2 \sum_y \text{Re Tr} \left\{ i\bar{\tau} \left[ T^b U_1(y) U_2(y + \hat{1}) U_1^{\dagger}(y + \hat{2}) U_2^{\dagger}(y) \delta_{ab} \delta_{i1} \delta_{xy} \right. \right. \\
 &\quad \left. \left. + U_1(y) T^b U_2(y + \hat{1}) U_1^{\dagger}(y + \hat{2}) U_2^{\dagger}(y) \delta_{ab} \delta_{i2} \delta_{x,y+\hat{1}} \right. \right. \\
 &\quad \left. \left. - U_1(y) U_2(y + \hat{1}) U_1^{\dagger}(y + \hat{2}) T^b U_2^{\dagger}(y) \delta_{ab} \delta_{i1} \delta_{x,y+\hat{2}} \right. \right. \\
 &\quad \left. \left. - U_1(y) U_2(y + \hat{1}) U_1^{\dagger}(y + \hat{2}) U_2^{\dagger}(y) T^b \delta_{ab} \delta_{i2} \delta_{xy} \right] \right. \\
 &\quad \left. + \frac{i}{a_{\eta}^2 \bar{\tau}} \sum_j \left[ U_{\eta}(y) T^b U_j(y + \hat{\eta}) U_{\eta}^{\dagger}(y + \hat{j}) U_j^{\dagger}(y) \delta_{ab} \delta_{ij} \delta_{x,y+\hat{\eta}} \right. \right. \\
 &\quad \left. \left. - U_{\eta}(y) U_j(y + \hat{\eta}) U_{\eta}^{\dagger}(y + \hat{j}) U_j^{\dagger}(y) T^b \delta_{ab} \delta_{ij} \delta_{x,y} \right] \right\} \\
 &= -2 \text{Im Tr} \left\{ \bar{\tau} T^a \left[ U_i(x) U_2(x + \hat{i}) U_i^{\dagger}(x + \hat{2}) U_2^{\dagger}(x) \right. \right. \\
 &\quad \left. \left. + U_i(x) U_1^{\dagger}(x - \hat{1} + \hat{i}) U_i^{\dagger}(x - \hat{1}) U_1(x - \hat{1}) \right. \right. \\
 &\quad \left. \left. - U_2^{\dagger}(x - \hat{2}) U_i(x - \hat{2}) U_2(x - \hat{2} + \hat{i}) U_i^{\dagger}(x) \right. \right. \\
 &\quad \left. \left. - U_1(x) U_i(x + \hat{1}) U_1^{\dagger}(x + \hat{i}) U_i^{\dagger}(x) \right] \right. \\
 &\quad \left. + \frac{1}{a_{\eta}^2 \bar{\tau}} T^a \left[ U_i(x) U_{\eta}^{\dagger}(x - \hat{\eta} + \hat{i}) U_i^{\dagger}(x - \hat{\eta}) U_{\eta}(x - \hat{\eta}) \right. \right. \\
 &\quad \left. \left. - U_{\eta}(x) U_i(x + \hat{\eta}) U_{\eta}^{\dagger}(x + \hat{i}) U_i^{\dagger}(x) \right] \right\} \\
 &= -2 \text{Im Tr} \left\{ \bar{\tau} T^a \left[ U_{i2}(x) + U_{i,-1}(x) - U_{-2i}(x) - U_{1i}(x) \right] \right. \\
 &\quad \left. + \frac{1}{a_{\eta}^2 \bar{\tau}} T^a \left[ U_{i,-\eta}(x) - U_{\eta i}(x) \right] \right\} \\
 &= 2 \text{Im Tr} \left\{ T^a \left( \bar{\tau} \sum_{j \neq i} [U_{ji}(x) + U_{-ji}(x)] + \frac{1}{a_{\eta}^2 \bar{\tau}} [U_{\eta i}(x) + U_{-\eta i}(x)] \right) \right\} \quad (\text{C.15})
 \end{aligned}$$

$$\begin{aligned}
 \partial_{\bar{\tau}} \bar{E}_{\eta}^a(x) &= -g^2 a_{\perp}^3 \frac{\partial \mathcal{H}^L}{\partial \bar{A}_{\eta}^a(x)} \\
 &= -g^2 a_{\perp}^3 \frac{\partial}{\partial \bar{A}_{\eta}^a(x)} \frac{1}{g^2 a_{\perp}^3} \text{Re Tr} \left\{ \frac{2}{a_{\eta}^2 \bar{\tau}} \sum_{y,j} [1 - U_{j\eta}(y)] \right\} \\
 &= \frac{2}{a_{\eta}^2 \bar{\tau}} \sum_{y,j} \text{Re Tr} \left\{ \frac{\partial}{\partial \bar{A}_{\eta}^a(x)} U_{j\eta}(y) \right\}
 \end{aligned}$$

$$\begin{aligned}
 &= \frac{2}{a_\eta^2 \bar{\tau}} \sum_{y,j} \text{Re Tr} \left\{ \text{i} a_\eta \left[ T^b U_\eta(y) U_j(y + \hat{\eta}) U_\eta^\dagger(y + \hat{j}) U_j^\dagger(y) \delta_{ab} \delta_{x,y} \right. \right. \\
 &\quad \left. \left. - U_\eta(y) U_j(y + \hat{\eta}) U_\eta^\dagger(y + \hat{j}) T^b U_j^\dagger(y) \delta_{ab} \delta_{x,y+\hat{j}} \right] \right\} \\
 &= -\frac{2}{a_\eta \bar{\tau}} \sum_j \text{Im Tr} \left\{ T^a \left[ U_\eta(x) U_j(x + \hat{\eta}) U_\eta^\dagger(x + \hat{j}) U_j^\dagger(x) \right. \right. \\
 &\quad \left. \left. - U_j^\dagger(x - \hat{j}) U_\eta(x - \hat{j}) U_j(x - \hat{j} + \hat{\eta}) U_\eta^\dagger(x) \right] \right\} \\
 &= \frac{2}{a_\eta \bar{\tau}} \sum_j \text{Im Tr} \left\{ T^a \left[ U_{j\eta}(x) + U_{-j\eta}(x) \right] \right\} \tag{C.16}
 \end{aligned}$$

### C.2.2 Gauss's law

$$\begin{aligned}
 0 &= \left. \frac{\partial \mathcal{L}_L}{\partial A_\tau^a(x)} \right|_{A_\tau=0} \\
 &= \frac{2}{g^2 a_\perp^3} \frac{\partial}{\partial A_\tau^a(x)} \sum_y \text{Re Tr} \left\{ \frac{\bar{\tau}}{\bar{a}_\tau^2} \sum_i [1 - U_{\tau i}(y)] + \frac{1}{\bar{a}_\tau^2 a_\eta^2 \bar{\tau}} [1 - U_{\tau\eta}(y)] \right\} \Big|_{A_\tau=0} \\
 &= -\frac{2}{g^2 a_\perp^3 \bar{a}_\tau^2} \frac{\partial}{\partial A_\tau^a(x)} \sum_y \text{Re Tr} \left\{ \bar{\tau} \sum_i U_{\tau i}(y) + \frac{1}{a_\eta^2 \bar{\tau}} U_{\tau\eta}(y) \right\} \Big|_{A_\tau=0} \\
 &= -\frac{2}{g^2 a_\perp^3 \bar{a}_\tau^2} \frac{\partial}{\partial A_\tau^a(x)} \sum_y \text{Re Tr} \left\{ \bar{\tau} \sum_i U_\tau(y) U_i(y + \hat{\tau}) U_\tau^\dagger(y + \hat{i}) U_i^\dagger(y) \right. \\
 &\quad \left. + \frac{1}{a_\eta^2 \bar{\tau}} U_\tau(y) U_\eta(y + \hat{\tau}) U_\tau^\dagger(y + \hat{\eta}) U_\eta^\dagger(y) \right\} \Big|_{A_\tau=0} \\
 &= -\frac{2}{g^2 a_\perp^3 \bar{a}_\tau^2} \sum_y \text{Re Tr} \left\{ \text{i} g a_\tau \left( \bar{\tau} \sum_i \left[ T^b U_\tau(y) U_i(y + \hat{\tau}) U_\tau^\dagger(y + \hat{i}) U_i^\dagger(y) \delta_{ab} \delta_{xy} \right. \right. \right. \\
 &\quad \left. \left. - U_\tau(y) U_i(y + \hat{\tau}) U_\tau^\dagger(y + \hat{i}) T^b U_i^\dagger(y) \delta_{ab} \delta_{x,y+\hat{i}} \right] \right. \\
 &\quad \left. + \frac{1}{a_\eta^2 \bar{\tau}} \left[ T^b U_\tau(y) U_\eta(y + \hat{\tau}) U_\tau^\dagger(y + \hat{\eta}) U_\eta^\dagger(y) \delta_{ab} \delta_{xy} \right. \right. \\
 &\quad \left. \left. - U_\tau(y) U_\eta(y + \hat{\tau}) U_\tau^\dagger(y + \hat{\eta}) T^b U_\eta^\dagger(y) \delta_{ab} \delta_{x,y+\hat{i}} \right] \right) \Big|_{A_\tau=0} \\
 &= -\frac{2}{g a_\perp^2 \bar{a}_\tau} \text{Re Tr} \left\{ \text{i} T^a \left( \bar{\tau} \sum_i \left[ U_\tau(x) U_i(x + \hat{\tau}) U_\tau^\dagger(x + \hat{i}) U_i^\dagger(x) \right. \right. \right. \\
 &\quad \left. \left. - U_i^\dagger(x - \hat{i}) U_\tau(x - \hat{i}) U_i(x - \hat{i} + \hat{\tau}) U_\tau^\dagger(x) \right] \right. \\
 &\quad \left. + \frac{1}{a_\eta^2 \bar{\tau}} \left[ U_\tau(x) U_\eta(x + \hat{\tau}) U_\tau^\dagger(x + \hat{\eta}) U_\eta^\dagger(x) \right. \right. \\
 &\quad \left. \left. - U_\eta^\dagger(x - \hat{\eta}) U_\tau(x - \hat{\eta}) U_\eta(x - \hat{\eta} + \hat{\tau}) U_\tau^\dagger(x) \right] \right) \Big|_{A_\tau=0} \tag{C.17}
 \end{aligned}$$

Rebuilding plaquettes then yields

$$\begin{aligned}
 \dots &= \frac{2}{ga_{\perp}^2 \bar{a}_{\tau}} \text{Im Tr} \left\{ T^a \left( \bar{\tau} \sum_i \left[ U_{\tau i}(x) - U_{-i\tau}(x) \right] + \frac{1}{a_{\eta}^2 \bar{\tau}} \left[ U_{\tau\eta}(x) - U_{-\eta\tau}(x) \right] \right) \right\} \Big|_{\bar{A}_{\tau}=0} \\
 &= -\frac{2}{ga_{\perp}^2 \bar{a}_{\tau}} \text{Im Tr} \left\{ T^a \left( \bar{\tau} \sum_i \left[ U_{i\tau}(x) + U_{-i\tau}(x) \right] \right. \right. \\
 &\quad \left. \left. + \frac{1}{a_{\eta}^2 \bar{\tau}} \left[ U_{\eta\tau}(x) + U_{-\eta\tau}(x) \right] \right) \right\} \Big|_{\bar{A}_{\tau}=0} \tag{C.18}
 \end{aligned}$$

In contrast, a direct application of the temporal gauge leads to

$$\begin{aligned}
 \dots &= -\frac{2}{ga_{\perp}^2 \bar{a}_{\tau}} \text{Re Tr} \left\{ iT^a \left( \bar{\tau} \sum_i \left[ U_i(x + \hat{\tau}) U_i^{\dagger}(x) - U_i^{\dagger}(x - \hat{i}) U_i(x - \hat{i} + \hat{\tau}) \right] \right. \right. \\
 &\quad \left. \left. + \frac{1}{a_{\eta}^2 \bar{\tau}} \left[ U_{\eta}(x + \hat{\tau}) U_{\eta}^{\dagger}(x) - U_{\eta}^{\dagger}(x - \hat{\eta}) U_{\eta}(x - \hat{\eta} + \hat{\tau}) \right] \right) \right\} \\
 &= -\frac{2}{ga_{\perp}^2} \text{Re Tr} \left\{ iT^a \left( \bar{\tau} \sum_i \left[ \underbrace{\frac{U_i(x + \hat{\tau}) - U_i(x)}{\bar{a}_{\tau}}}_{\approx \partial_{\bar{\tau}} U_i(x) = \frac{i}{\bar{\tau}} \bar{E}_i(x) U_i(x)} U_i^{\dagger}(x) \right. \right. \right. \\
 &\quad \left. \left. - U_i^{\dagger}(x - \hat{i}) \underbrace{\frac{U_i(x - \hat{i} + \hat{\tau}) - U_i(x - \hat{i})}{\bar{a}_{\tau}}}_{\approx \partial_{\bar{\tau}} U_i(x - \hat{i}) = \frac{i}{\bar{\tau}} \bar{E}_i(x - \hat{i}) U_i(x - \hat{i})} \right] \right) \right. \\
 &\quad \left. + \frac{1}{a_{\eta}^2 \bar{\tau}} \left[ \underbrace{\frac{U_{\eta}(x + \hat{\tau}) - U_{\eta}(x)}{\bar{a}_{\tau}}}_{\approx \partial_{\bar{\tau}} U_{\eta}(x) = i\bar{\tau} \bar{E}_{\eta}(x) U_{\eta}(x)} U_{\eta}^{\dagger}(x) \right. \right. \\
 &\quad \left. \left. - U_{\eta}^{\dagger}(x - \hat{\eta}) \underbrace{\frac{U_{\eta}(x - \hat{\eta} + \hat{\tau}) - U_{\eta}(x - \hat{\eta})}{\bar{a}_{\tau}}}_{\approx \partial_{\bar{\tau}} U_{\eta}(x - \hat{\eta}) = i\bar{\tau} \bar{E}_{\eta}(x - \hat{\eta}) U_{\eta}(x - \hat{\eta})} \right] \right) \right\} \\
 &= \frac{2}{ga_{\perp}^2} \text{Re Tr} \left\{ T^a \left( \sum_i \left[ \bar{E}_i(x) - U_i^{\dagger}(x - \hat{i}) \bar{E}_i(x - \hat{i}) U_i(x - \hat{i}) \right] \right. \right. \\
 &\quad \left. \left. + \frac{1}{a_{\eta}^2} \left[ \bar{E}_{\eta}(x) - U_{\eta}^{\dagger}(x - \hat{\eta}) \bar{E}_{\eta}(x - \hat{\eta}) U_{\eta}(x - \hat{\eta}) \right] \right) \right\}. \tag{C.19}
 \end{aligned}$$



# Appendix **D**

## Miscellaneous

---

### Contents

D.1 Euler-Lagrange equations . . . . .	119
D.2 Operator commutation relations . . . . .	119
D.3 Stochastic low-cost fermions . . . . .	120
D.4 Initial time problem in the 3D expanding system . . . . .	122
D.5 Chromo-Weibel instability: additional figures . . . . .	123
D.6 Pressure ratio including fermions: additional figure . . . . .	127

---

### D.1 Euler-Lagrange equations

The Euler-Lagrange equation for fields  $\phi^a$  and the Lagrangian density  $\mathcal{L}$  read [26]

$$0 = \partial_t \frac{\partial \mathcal{L}}{\partial(\partial_t \phi^a)} + \sum_i \partial_{x_i} \frac{\partial \mathcal{L}}{\partial(\partial_{x_i} \phi^a)} - \frac{\partial \mathcal{L}}{\partial \phi^a}. \quad (\text{D.1})$$

### D.2 Operator commutation relations

Starting with (2.56) we, first of all, notice that if we add a field operator  $\hat{\phi}^m$  in front of or at the end of the left-hand side of the commutator, the equality obviously holds since  $\hat{\phi}^m$  commutes with  $\hat{\phi}$  independent of its argument and indices. Therefore, we directly show

the relation for the next non-trivial case: <sup>1</sup>

$$\begin{aligned}
 \mathbf{i}[\pi^k \phi^l \pi^m, \phi] &= \mathbf{i}([\pi^k \phi^l, \phi] \pi^m + \pi^k \phi^l [\pi^m, \phi]) \\
 &= \mathbf{i}([\pi^k, \phi] \phi^l \pi^m + \pi^k \phi^l [\pi^m, \phi]) \\
 &= k \pi^{k-1} \phi^l \pi^m + m \pi^k \phi^l \pi^{m-1} \\
 &= \frac{\delta}{\delta \pi} (\pi^k \phi^l \pi^m)
 \end{aligned} \tag{D.2}$$

With the same argumentation as before, the next relevant case to proof is:

$$\begin{aligned}
 \mathbf{i}[\pi^k \phi^l \pi^m \phi^n \pi^p, \phi] &= \mathbf{i}([\pi^k \phi^l \pi^m \phi^n, \phi] \pi^p + \pi^k \phi^l \pi^m \phi^n [\pi^p, \phi]) \\
 &= \mathbf{i}([\pi^k \phi^l \pi^m, \phi] \phi^n \pi^p + \pi^k \phi^l \pi^m \phi^n [\pi^p, \phi]) \\
 &= k \pi^{k-1} \phi^l \pi^m \phi^n \pi^p + m \pi^k \phi^l \pi^{m-1} \phi^n \pi^p + p \pi^k \phi^l \pi^m \phi^n \pi^{p-1} \\
 &= \frac{\delta}{\delta \pi} (\pi^k \phi^l \pi^m \phi^n \pi^p)
 \end{aligned} \tag{D.3}$$

Surely by now the pattern should be obvious and we conclude

$$\mathbf{i}[\underbrace{\pi^{n_1} \phi^{n_2} \dots \pi^{n_N}}_{\text{alternating } \pi \text{ and } \phi}, \phi] = \frac{\delta}{\delta \pi} (\underbrace{\pi^{n_1} \phi^{n_2} \dots \pi^{n_N}}_{\text{alternating } \pi \text{ and } \phi}). \tag{D.4}$$

Since the commutator is bilinear and since the derivative commutes with the addition operation, we ultimately end up with (2.58).

## D.3 Stochastic low-cost fermions

### D.3.1 Dirac spinors

The solutions of the free lattice Dirac equation (3.32) fulfilling the normalization (3.35) and given by

$$u_0 = \frac{1}{\sqrt{s_0 + \mu}} \begin{pmatrix} s_0 + \mu \\ 0 \\ s_3 \\ s_1 + \mathbf{i}s_2 \end{pmatrix}, \quad u_1 = \frac{1}{\sqrt{s_0 + \mu}} \begin{pmatrix} 0 \\ s_0 + \mu \\ s_1 - \mathbf{i}s_2 \\ -s_3 \end{pmatrix}, \tag{D.5a}$$

$$v_0 = \frac{1}{\sqrt{s_0 + \mu}} \begin{pmatrix} s_3 \\ s_1 + \mathbf{i}s_2 \\ s_0 + \mu \\ 0 \end{pmatrix}, \quad v_1 = \frac{1}{\sqrt{s_0 + \mu}} \begin{pmatrix} s_1 - \mathbf{i}s_2 \\ -s_3 \\ 0 \\ s_0 + \mu \end{pmatrix}, \tag{D.5b}$$

where we dropped the momentum argument ( $\vec{p}$ ) of all variables.

<sup>1</sup>We dropped all indices and hats and just remember that those of the single  $\hat{\phi}$  on the right-hand side of the operator are different from the others

### D.3.2 Correlator relations

In the following we show the relation between the continuum equal time correlation function  $\langle \bar{\psi}(x)\psi(y) \rangle|_{x_0=y_0}$  and the equivalent expression in terms of gendered fermions.

The continuum result reads

$$\begin{aligned}
 \langle \bar{\psi}(x)\psi(y) \rangle|_{x_0=y_0} &= \int \frac{d^3p}{(2\pi)^{\frac{3}{2}}} \int \frac{d^3q}{(2\pi)^{\frac{3}{2}}} \frac{1}{2p_0} \sum_{r,s} \left( a_r^\dagger(\vec{p}) \bar{u}_r(\vec{p}) e^{i\vec{p}\vec{x}} + b_r(\vec{p}) \bar{v}_r(\vec{p}) e^{-i\vec{p}\vec{x}} \right) \\
 &\quad \times \left( a_s(\vec{q}) u_s(\vec{q}) e^{-i\vec{q}\vec{y}} + b_s^\dagger(\vec{q}) v_s(\vec{q}) e^{i\vec{q}\vec{y}} \right) \\
 &= \int \frac{d^3p}{(2\pi)^{\frac{3}{2}}} \int \frac{d^3q}{(2\pi)^{\frac{3}{2}}} \frac{1}{2p_0} \sum_{r,s} \underbrace{b_r(\vec{p}) b_s^\dagger(\vec{q})}_{=-b_s^\dagger(\vec{q}) b_r(\vec{p}) + \{b_r(\vec{p}), b_s^\dagger(\vec{q})\}} \bar{v}_r(\vec{p}) v_s(\vec{q}) e^{-i\vec{p}\vec{x}} e^{i\vec{q}\vec{y}} \\
 &= \int \frac{d^3p}{(2\pi)^{\frac{3}{2}}} \int \frac{d^3q}{(2\pi)^{\frac{3}{2}}} \frac{1}{2p_0} \sum_{r,s} \underbrace{\{b_r(\vec{p}), b_s^\dagger(\vec{q})\}}_{(2\pi)^{\frac{3}{2}} \delta_{rs} \delta(\vec{p}-\vec{q})} \bar{v}_r(\vec{p}) v_s(\vec{q}) e^{-i\vec{p}\vec{x}} e^{i\vec{q}\vec{y}} \\
 &= \int \frac{d^3p}{(2\pi)^{\frac{3}{2}}} \frac{1}{2p_0} \sum_s \underbrace{\bar{v}_s(\vec{p}) v_s(\vec{p})}_{=-2m} e^{-i\vec{p}(\vec{x}-\vec{y})} \\
 &= - \int \frac{d^3p}{(2\pi)^{\frac{3}{2}}} \frac{2m}{p_0} e^{-i\vec{p}(\vec{x}-\vec{y})}, \tag{D.6}
 \end{aligned}$$

where used the action of annihilation operators on the vacuum,  $a|0\rangle = b|0\rangle = 0$ , the (continuum) normalization of the Dirac spinors, cf. (3.35), and the definition of the anticommutation relations (3.38).

The equivalent expression for gendered fermions takes the following form

$$\begin{aligned}
 \langle \bar{\psi}_{M/F}(x)\psi_{F/M}(y) \rangle|_{x_0=y_0} &= \frac{1}{2} \int \frac{d^3p}{(2\pi)^{\frac{3}{2}}} \int \frac{d^3q}{(2\pi)^{\frac{3}{2}}} \frac{1}{2p_0} \sum_{r,s} \left\{ \left( \xi_r^*(\vec{p}) \bar{u}_r(\vec{p}) e^{i\vec{p}\vec{x}} \pm \eta_r^*(\vec{p}) \bar{v}_r(\vec{p}) e^{-i\vec{p}\vec{x}} \right) \right. \\
 &\quad \left. \times \left( \xi_s(\vec{q}) u_s(\vec{q}) e^{-i\vec{q}\vec{y}} \mp \eta_s(\vec{q}) v_s(\vec{q}) e^{i\vec{q}\vec{y}} \right) \right\} \\
 &= \frac{1}{2} \int \frac{d^3p}{(2\pi)^{\frac{3}{2}}} \int \frac{d^3q}{(2\pi)^{\frac{3}{2}}} \frac{1}{2p_0} \sum_{r,s} \left\{ \underbrace{\xi_r^*(\vec{p}) \xi_s(\vec{q})}_{(2\pi)^{\frac{3}{2}} \delta_{rs} \delta(\vec{p}-\vec{q})} \bar{u}_r(\vec{p}) u_s(\vec{q}) e^{i\vec{p}\vec{x}} e^{-i\vec{q}\vec{y}} \right. \\
 &\quad \left. - \underbrace{\eta_r^*(\vec{p}) \eta_s(\vec{q})}_{(2\pi)^{\frac{3}{2}} \delta_{rs} \delta(\vec{p}-\vec{q})} \bar{v}_r(\vec{p}) v_s(\vec{q}) e^{-i\vec{p}\vec{x}} e^{i\vec{q}\vec{y}} \right\} \\
 &\quad \times \left( \xi_s(\vec{q}) u_s(\vec{q}) e^{-i\vec{q}\vec{y}} \mp \eta_s(\vec{q}) v_s(\vec{q}) e^{i\vec{q}\vec{y}} \right) \Big\} \\
 &= \frac{1}{2} \int \frac{d^3p}{(2\pi)^{\frac{3}{2}}} \frac{1}{2p_0} \sum_s \left\{ \underbrace{\bar{u}_s(\vec{p}) u_s(\vec{p})}_{=2m} e^{i\vec{p}(\vec{x}-\vec{y})} - \underbrace{\bar{v}_s(\vec{p}) v_s(\vec{p})}_{=-2m} e^{-i\vec{p}(\vec{x}-\vec{y})} \right\} \\
 &= \int \frac{d^3p}{(2\pi)^{\frac{3}{2}}} \frac{2m}{p_0} e^{-i\vec{p}(\vec{x}-\vec{y})}, \tag{D.7}
 \end{aligned}$$

where we used that  $\bar{u}v = \bar{v}u = 0$ , the distribution of the random numbers (3.40) and

$$\int_{-a}^a dx e^x = \int_{-a}^a dx e^{-x}. \quad (\text{D.8})$$

Furthermore, one can easily verify that

$$\langle \bar{\psi}_{\text{M/F}}(x) \psi_{\text{M/F}}(y) \rangle \Big|_{x_0=y_0} = 0. \quad (\text{D.9})$$

## D.4 Initial time problem in the 3D expanding system

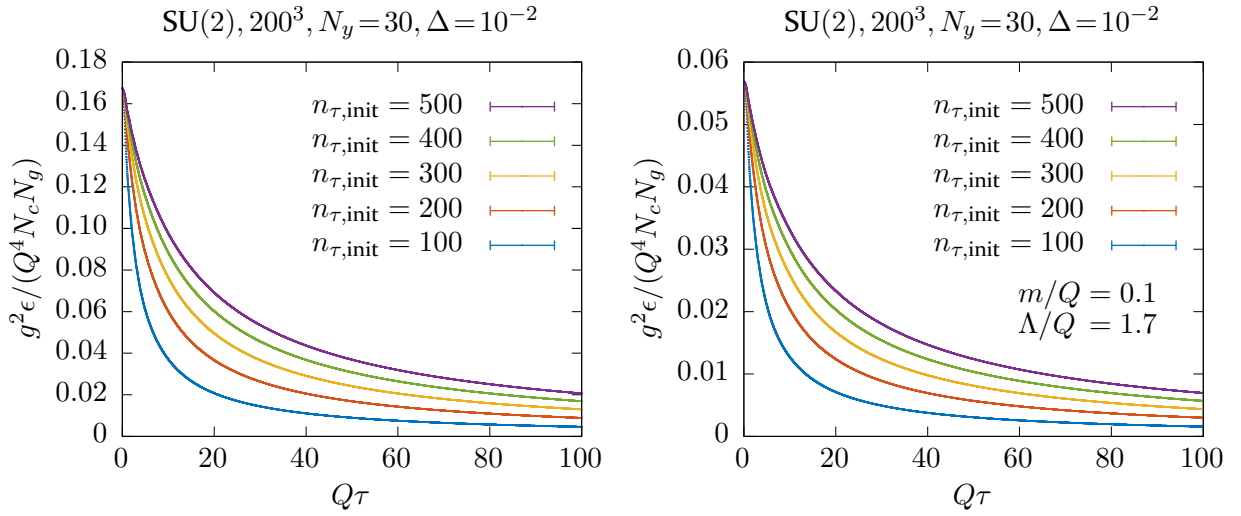


**Figure D.1:** Energy density with and without additional cutoffs in the expanding system for different values of  $n_{\tau,\text{init}}$  using the same transverse initialization.

Due to the  $1/\tau$  factors in the equations of motion in the expanding formulation (3.77), we obviously have to start our simulation at  $\tau = a_\tau$ , though for the three-dimensional case with fluctuations, there is another restriction.

In the comoving formulation, it is crucial to take the additional factors for the initial transverse chromo-electric energy density into account and hence (7.5) becomes

$$\bar{\epsilon}_{T,\text{init}}^E \propto \frac{\delta \bar{E}_\perp^2}{\bar{\tau}_{\text{init}}^2} \propto \frac{\Delta^2}{a_\eta^2 \bar{\tau}_{\text{init}}^2} \equiv \frac{\Delta^2}{a_\eta^2 \bar{a}_\tau^2 n_{\tau,\text{init}}^2}, \quad (\text{D.10})$$

where we introduced the number of time iterations  $n_\tau$ . For the 2D case, we e.g. usually have  $n_{\tau,\text{init}} = 1$ .

However, for our usual parameter choices,  $\Delta = 10^{-2}$ ,  $\bar{a}_\tau = 0.05$ ,  $N_\eta = 200$ ,  $a_\eta N_\eta = 2.0$ ,  $N_\perp = 200$  and  $QL_\perp = 120$ , we find

$$\frac{g^2 \epsilon_{T,\text{init}}^E}{Q^4 N_c N_g} \propto \frac{1}{(Q a_\perp)^4 N_c N_g} \frac{\Delta^2}{a_\eta^2 \bar{a}_\tau^2 n_{\tau,\text{init}}^2} \approx \frac{3000}{N_c N_g n_{\tau,\text{init}}^2}. \quad (\text{D.11})$$



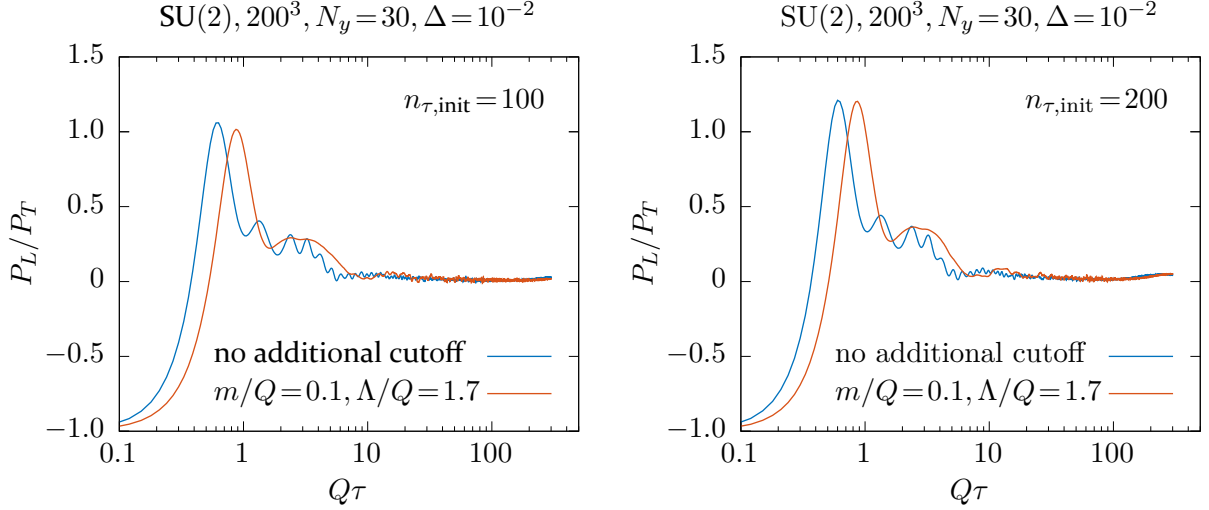


**Figure D.2:** Pressure ratio with and without additional cutoffs in the expanding system for two different values of  $n_{\tau,\text{init}}$ .

Since the left-most term is added to the total initial energy density, which is of order  $10^{-1}$  (cf. e.g. Figure 7.1), we have to verify  $n_{\tau,\text{init}} \gtrsim 50$ , depending on the number of considered colors. This means, the dynamics within the first 50 time iterations is neglected and hence the turbulent behavior at early times is highly suppressed due to the  $1/\tau$  damping in the equations of motion (3.77), which is of course undesired.

Figure D.1 shows the simulation for different  $n_{\tau,\text{init}}$  values without (left) and with (right) additional cutoffs. The higher  $n_{\tau,\text{init}}$  is chosen, the slower the energy density decreases due to the mentioned suppression of the initial turbulences.

To this end, and for the reasons explained in Section 7.5, we consider the static box scenario as long as we want to study the system's isotropization. Nevertheless, for the sake of completeness, we show the pressure ratio for  $n_{\tau,\text{init}} = 200$  without (left) and with (right) additional cutoffs in Figure D.2, where we clearly see no isotropization. The pressure ratio slightly starts to grow, but then saturates again.

## D.5 Chromo-Weibel instability: additional figures

In this section we show some additional plots concerning the filamentation of the energy density in position space, which indicates the presence of chromo-Weibel instabilities. In each of the following snapshots the horizontal axis represents the longitudinal direction, i.e. along beam line, and the vertical axis indicates the transverse direction.

For further explanations on the parameters shown in the figure and how the plots have to be read we refer to Chapter 4 and particularly to Section 7.6.

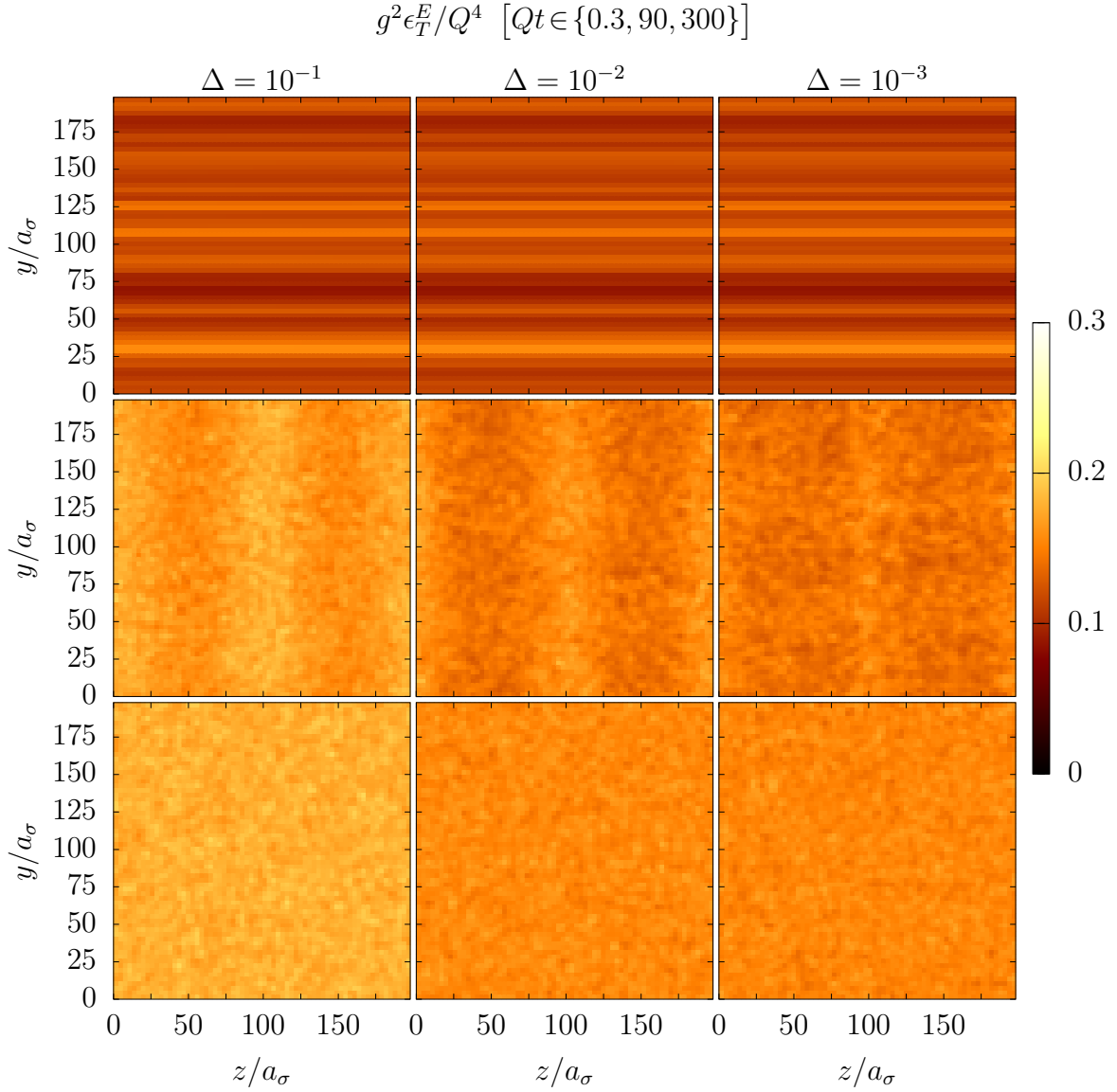


**Figure D.3:** Snapshots of the transverse component of the chromoelectric energy density, cf. (6.10) and (6.11), in the  $yz$ -plane at different times (top down:  $Qt \in \{0.3, 90, 300\}$ ) and different fluctuation amplitudes (left to right:  $\Delta \in \{10^{-1}, 10^{-2}, 10^{-3}\}$ ).

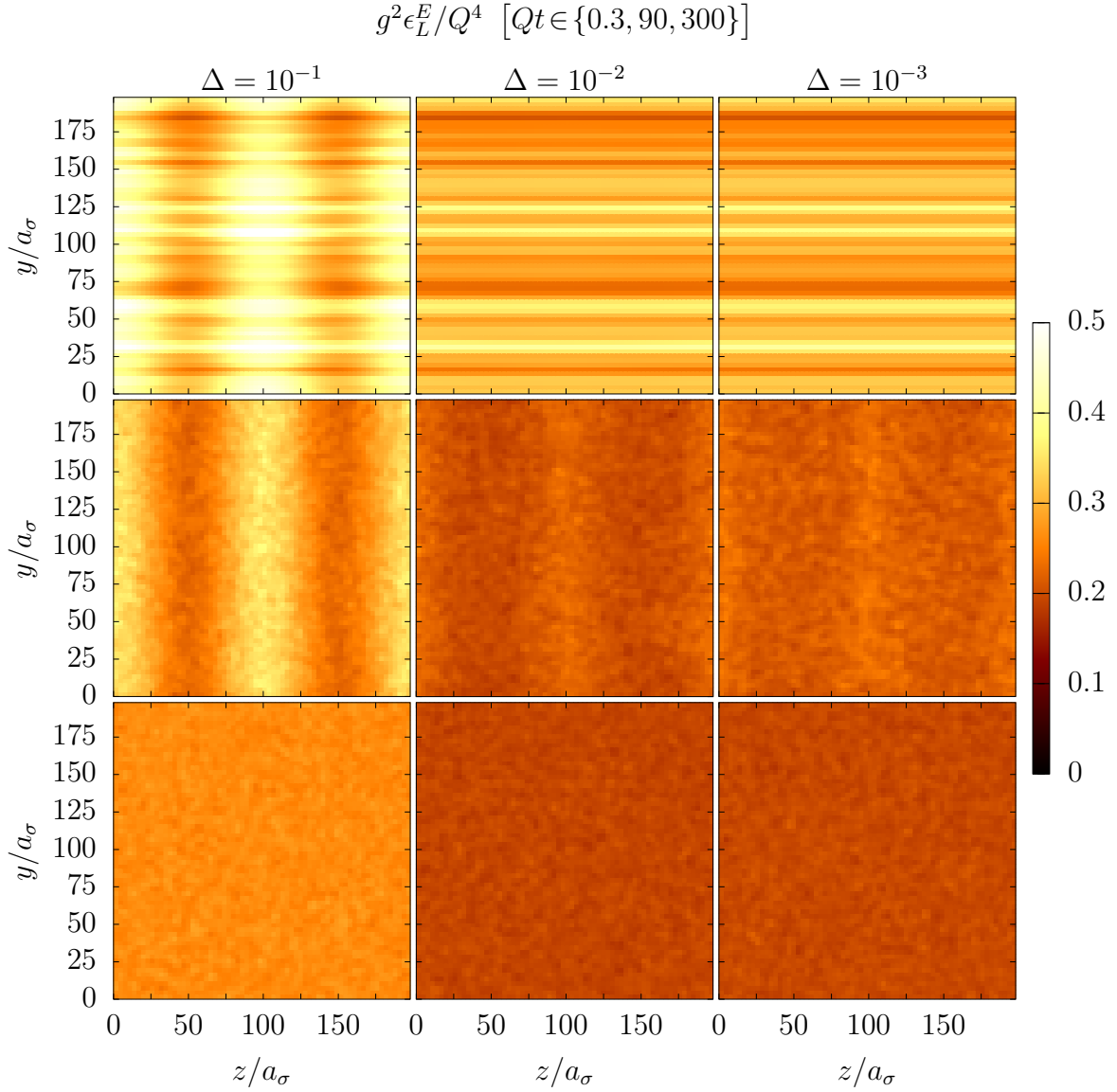


**Figure D.4:** Snapshots of the longitudinal component of the chromo-electric energy density, cf. (6.10) and (6.11), in the  $yz$ -plane at different times (top down:  $Qt \in \{0.3, 90, 300\}$ ) and different fluctuation amplitudes (left to right:  $\Delta \in \{10^{-1}, 10^{-2}, 10^{-3}\}$ ).

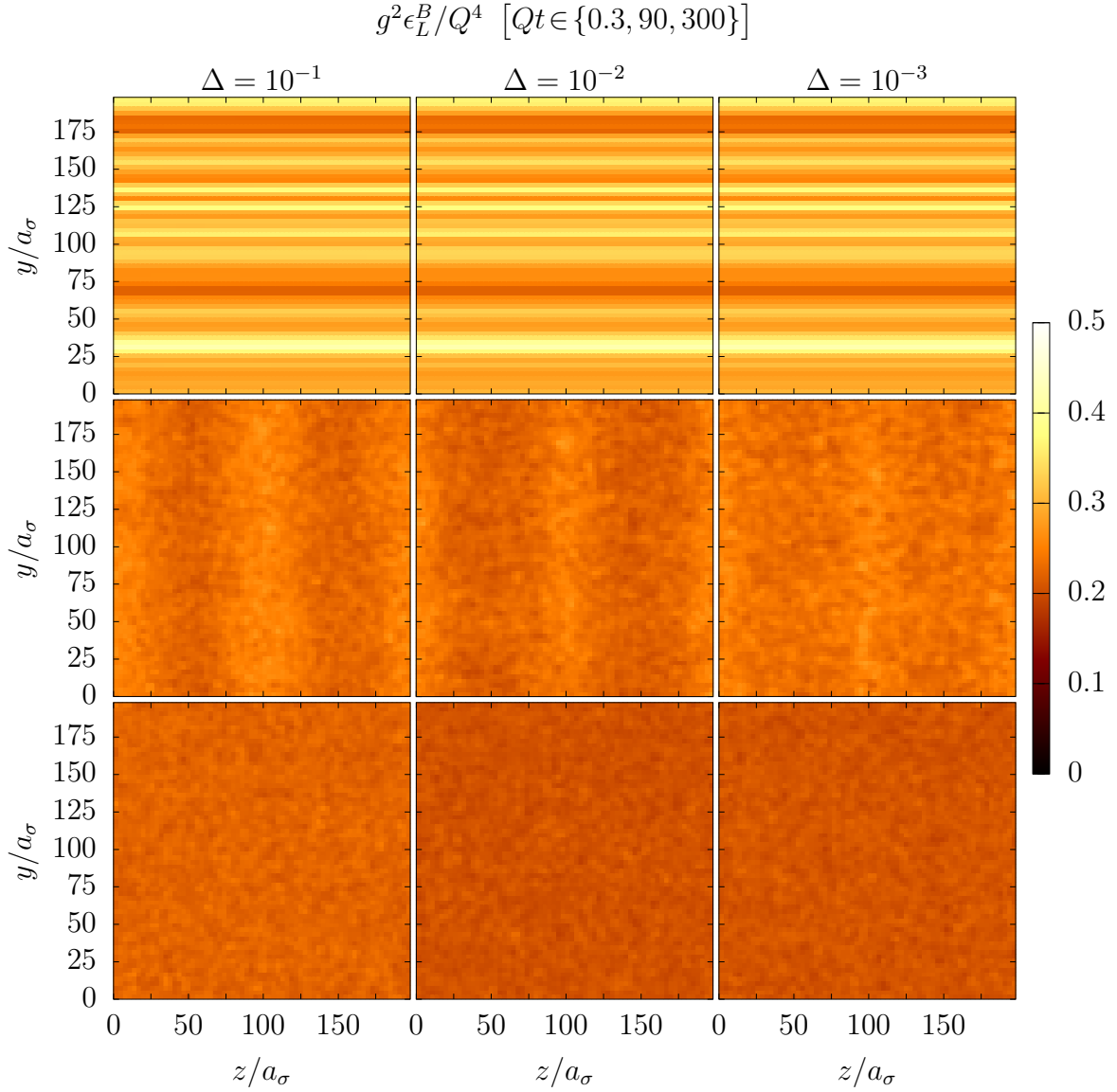


**Figure D.5:** Snapshots of the longitudinal component of the chromomagnetic energy density, cf. (6.10) and (6.11), in the  $yz$ -plane at different times (top down:  $Qt \in \{0.3, 90, 300\}$ ) and different fluctuation amplitudes (left to right:  $\Delta \in \{10^{-1}, 10^{-2}, 10^{-3}\}$ ).

## D.6 Pressure ratio including fermions: additional figure

We show here an additional figure concerning Section 8.2, where we plot the pressure ratio for various initial fermionic pseudo-temperatures  $T_{\text{init}}$  and a rather small coupling of  $g=0.6$ .

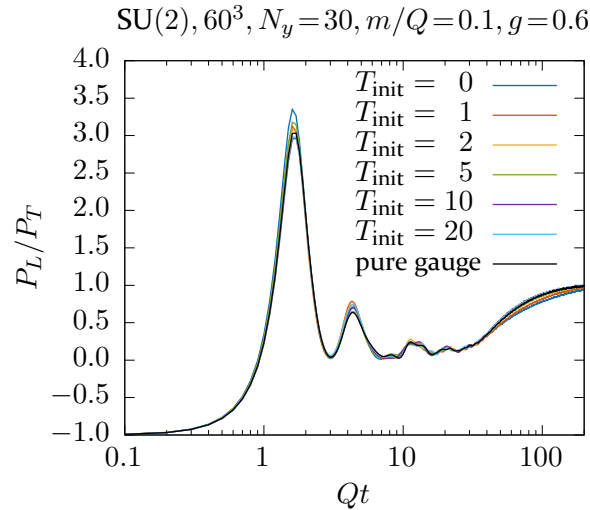


**Figure D.6:** The pressure ratio for different initial fermionic pseudo-temperatures  $T_{\text{init}}$  compared to the pure gauge case choosing  $g=0.6$ .



# Bibliography

---

- [1] J. Ellis, “Physics Beyond the Standard Model,” *Nucl. Phys.* **A827** (2009) 187C–198C, arXiv:0902.0357.
- [2] B. Gripaios, “Lectures on Physics Beyond the Standard Model,” arXiv:1503.02636.
- [3] O. Philipsen, “Lattice calculations at non-zero chemical potential: The QCD phase diagram,” *PoS CONFINEMENT8* (2008) 011.
- [4] J. B. Kogut and L. Susskind, “Hamiltonian Formulation of Wilson’s Lattice Gauge Theories,” *Phys. Rev.* **D11** (1975) 395–408.
- [5] J. Berges, “Introduction to nonequilibrium quantum field theory,” *AIP Conf. Proc.* **739** (2005) 3–62, arXiv:hep-ph/0409233.
- [6] R. Baier, A. H. Mueller, D. Schiff, and D. T. Son, “‘Bottom up’ thermalization in heavy ion collisions,” *Phys. Lett.* **B502** (2001) 51–58, arXiv:hep-ph/0009237.
- [7] D. Gelfand, F. Hebenstreit, and J. Berges, “Early quark production and approach to chemical equilibrium,” *Phys. Rev.* **D93** (2016) 085001, arXiv:1601.03576.
- [8] G. Aarts and J. Smit, “Classical approximation for time dependent quantum field theory: Diagrammatic analysis for hot scalar fields,” *Nucl. Phys.* **B511** (1998) 451–478, arXiv:hep-ph/9707342.
- [9] L. D. McLerran and R. Venugopalan, “Computing quark and gluon distribution functions for very large nuclei,” *Phys. Rev.* **D49** (1994) 2233–2241, arXiv:hep-ph/9309289.
- [10] L. D. McLerran and R. Venugopalan, “Gluon distribution functions for very large nuclei at small transverse momentum,” *Phys. Rev.* **D49** (1994) 3352–3355, arXiv:hep-ph/9311205.
- [11] L. D. McLerran and R. Venugopalan, “Green’s functions in the color field of a large nucleus,” *Phys. Rev.* **D50** (1994) 2225–2233, arXiv:hep-ph/9402335.
- [12] S. Borsanyi and M. Hindmarsh, “Low-cost fermions in classical field simulations,” *Phys. Rev.* **D79** (2009) 065010, arXiv:0809.4711.

- [13] E. S. Weibel, “Spontaneously Growing Transverse Waves in a Plasma Due to an Anisotropic Velocity Distribution,” *Phys. Rev. Lett.* **2** (1959) 83–84.
- [14] S. Mrowczynski, “Plasma instability at the initial stage of ultrarelativistic heavy ion collisions,” *Phys. Lett.* **B314** (1993) 118–121.
- [15] S. Mrowczynski, “Color collective effects at the early stage of ultrarelativistic heavy ion collisions,” *Phys. Rev.* **C49** (1994) 2191–2197.
- [16] S. Mrowczynski, “Color filamentation in ultrarelativistic heavy ion collisions,” *Phys. Lett.* **B393** (1997) 26–30, arXiv:hep-ph/9606442.
- [17] M. Strickland, “The Chromo-Weibel instability,” *Braz. J. Phys.* **37** (2007) 762–765, arXiv:hep-ph/0611349.
- [18] M. Strickland, “Thermalization and the chromo-Weibel instability,” *J. Phys.* **G34** (2007) 429–436, arXiv:hep-ph/0701238.
- [19] M. Attems, O. Philipsen, C. Schäfer, B. Wagenbach, and S. Zafeiropoulos, “A real-time lattice simulation of the thermalization of a gluon plasma: first results,” *Acta Phys. Polon. Supp.* **9** (2016) 603, arXiv:1605.07064.
- [20] O. Philipsen, B. Wagenbach, and S. Zafeiropoulos, “From the color glass condensate to filamentation instabilities: systematics of classical yang-mills theory.” to be published, 2018.
- [21] **Particle Data Group** Collaboration, C. Patrignani *et al.*, “Review of Particle Physics,” *Chin. Phys.* **C40** (2016) 100001.
- [22] S. L. Adler, “Axial vector vertex in spinor electrodynamics,” *Phys. Rev.* **177** (1969) 2426–2438.
- [23] J. S. Bell and R. Jackiw, “A PCAC puzzle:  $\pi^0 \rightarrow \gamma \gamma$  in the sigma model,” *Nuovo Cim.* **A60** (1969) 47–61.
- [24] Y. Nambu, “Quasiparticles and Gauge Invariance in the Theory of Superconductivity,” *Phys. Rev.* **117** (1960) 648–663.
- [25] J. Goldstone, “Field Theories with Superconductor Solutions,” *Nuovo Cim.* **19** (1961) 154–164.
- [26] H. Goldstein, C. Poole, and J. Safko, *Classical Mechanics*. Addison-Wesley, 3rd ed., 2002.
- [27] A. Duncan, *The Conceptual Framework of Quantum Field Theory*. Oxford University Press, 2012.



- 
- [28] P. Romatschke and R. Venugopalan, “The Unstable Glasma,” *Phys. Rev.* **D74** (2006) 045011, arXiv:hep-ph/0605045.
- [29] J. S. Schwinger, “Brownian motion of a quantum oscillator,” *J. Math. Phys.* **2** (1961) 407–432.
- [30] L. V. Keldysh, “Diagram technique for nonequilibrium processes,” *Zh. Eksp. Teor. Fiz.* **47** (1964) 1515–1527. [*Sov. Phys. JETP*20,1018(1965)].
- [31] J. Berges, “Nonequilibrium Quantum Fields: From Cold Atoms to Cosmology,” arXiv:1503.02907.
- [32] E. A. Calzetta and B.-L. B. Hu, *Nonequilibrium Quantum Field Theory*. Cambridge Monographs on Mathematical Physics. Cambridge University Press, 2008.
- [33] A. Kamenev, *Field Theory of Non-Equilibrium Systems*. Cambridge University Press, 2011.
- [34] T. Zöller, *Nonequilibrium Formulation of Abelian Gauge Theories*. PhD thesis, Darmstadt, Tech. U., 2013. <http://tuprints.ulb.tu-darmstadt.de/3373/>.
- [35] P. C. Martin, E. D. Siggia, and H. A. Rose, “Statistical Dynamics of Classical Systems,” *Phys. Rev.* **A8** (1973) 423–437.
- [36] S. Jeon, “The Boltzmann equation in classical and quantum field theory,” *Phys. Rev.* **C72** (2005) 014907, arXiv:hep-ph/0412121.
- [37] J. Berges and T. Gasenzer, “Quantum versus classical statistical dynamics of an ultracold Bose gas,” *Phys. Rev.* **A76** (2007) 033604, arXiv:cond-mat/0703163.
- [38] J. Berges and D. Mesterhazy, “Introduction to the nonequilibrium functional renormalization group,” *Nucl. Phys. Proc. Suppl.* **228** (2012) 37–60, arXiv:1204.1489.
- [39] J. Berges, “Nonequilibrium quantum fields and the classical field theory limit,” *Nucl. Phys.* **A702** (2002) 351–355, arXiv:hep-ph/0201204.
- [40] G. Aarts and J. Berges, “Classical aspects of quantum fields far from equilibrium,” *Phys. Rev. Lett.* **88** (2002) 041603, arXiv:hep-ph/0107129.
- [41] G. C. Wick, “The Evaluation of the Collision Matrix,” *Phys. Rev.* **80** (1950) 268–272.
- [42] H. B. Nielsen and M. Ninomiya, “Absence of Neutrinos on a Lattice. 1. Proof by Homotopy Theory,” *Nucl. Phys.* **B185** (1981) 20.

- [43] H. B. Nielsen and M. Ninomiya, “Absence of Neutrinos on a Lattice. 2. Intuitive Topological Proof,” *Nucl. Phys.* **B193** (1981) 173–194.
- [44] H. B. Nielsen and M. Ninomiya, “No Go Theorem for Regularizing Chiral Fermions,” *Phys. Lett.* **B105** (1981) 219–223.
- [45] D. B. Kaplan, “Chiral Symmetry and Lattice Fermions,” in *Modern perspectives in lattice QCD: Quantum field theory and high performance computing. Proceedings, International School, 93rd Session, Les Houches, France, August 3-28, 2009*, pp. 223–272. 2009. arXiv:0912.2560.  
<http://inspirehep.net/record/839996/files/arXiv:0912.2560.pdf>.
- [46] L. Susskind, “Lattice Fermions,” *Phys. Rev.* **D16** (1977) 3031–3039.
- [47] P. H. Ginsparg and K. G. Wilson, “A Remnant of Chiral Symmetry on the Lattice,” *Phys. Rev.* **D25** (1982) 2649.
- [48] P. Hasenfratz and F. Niedermayer, “Perfect lattice action for asymptotically free theories,” *Nucl. Phys.* **B414** (1994) 785–814, arXiv:hep-lat/9308004.
- [49] D. B. Kaplan, “A Method for simulating chiral fermions on the lattice,” *Phys. Lett.* **B288** (1992) 342–347, arXiv:hep-lat/9206013.
- [50] Y. Shamir, “Chiral fermions from lattice boundaries,” *Nucl. Phys.* **B406** (1993) 90–106, arXiv:hep-lat/9303005.
- [51] Y. Shamir, “Constraints on the existence of chiral fermions in interacting lattice theories,” *Phys. Rev. Lett.* **71** (1993) 2691–2694, arXiv:hep-lat/9306023.
- [52] H. Neuberger, “Exactly massless quarks on the lattice,” *Phys. Lett.* **B417** (1998) 141–144, arXiv:hep-lat/9707022.
- [53] H. Neuberger, “More about exactly massless quarks on the lattice,” *Phys. Lett.* **B427** (1998) 353–355, arXiv:hep-lat/9801031.
- [54] M. E. Peskin and D. V. Schroeder, *An Introduction to quantum field theory*. Addison-Wesley, Reading, USA, 1995.  
<http://www.slac.stanford.edu/~mpeskin/QFT.html>.
- [55] K. Huang, *Statistical mechanics*. Wiley New York, 2nd ed. ed., 1987.
- [56] G. D. Moore, “Motion of Chern-Simons number at high temperatures under a chemical potential,” *Nucl. Phys.* **B480** (1996) 657–688, arXiv:hep-ph/9603384.
- [57] C. Schäfer, *Real Time Observables for the Quark-Gluon Plasma from the Lattice*. PhD thesis, Goethe-Universität Frankfurt am Main, 2014. <http://publikationen.ub.uni-frankfurt.de/frontdoor/index/index/docId/35026>.

- 
- [58] M. Laine, O. Philipsen, P. Romatschke, and M. Tassler, “Real-time static potential in hot QCD,” *JHEP* **03** (2007) 054, arXiv:hep-ph/0611300.
- [59] M. Laine, O. Philipsen, and M. Tassler, “Thermal imaginary part of a real-time static potential from classical lattice gauge theory simulations,” *JHEP* **09** (2007) 066, arXiv:0707.2458.
- [60] C. Gattringer and C. B. Lang, “Quantum chromodynamics on the lattice,” *Lect. Notes Phys.* **788** (2010) 1–343.
- [61] B. Efron and C. Stein, “The jackknife estimate of variance,” *The Annals of Statistics* **9** (1981) 586–596. <http://www.jstor.org/stable/2240822>.
- [62] R. Venugopalan, “The Color glass condensate: An Overview,” *Eur. Phys. J.* **C43** (2005) 337–344, arXiv:hep-ph/0502190.
- [63] F. Gelis, E. Iancu, J. Jalilian-Marian, and R. Venugopalan, “The Color Glass Condensate,” *Ann. Rev. Nucl. Part. Sci.* **60** (2010) 463–489, arXiv:1002.0333.
- [64] **ZEUS, H1** Collaboration, F. D. Aaron *et al.*, “Combined Measurement and QCD Analysis of the Inclusive  $e^+p$  Scattering Cross Sections at HERA,” *JHEP* **01** (2010) 109, arXiv:0911.0884.
- [65] J. Jalilian-Marian, A. Kovner, A. Leonidov, and H. Weigert, “The BFKL equation from the Wilson renormalization group,” *Nucl. Phys.* **B504** (1997) 415–431, arXiv:hep-ph/9701284.
- [66] J. Jalilian-Marian, A. Kovner, L. D. McLerran, and H. Weigert, “The Intrinsic glue distribution at very small  $x$ ,” *Phys. Rev.* **D55** (1997) 5414–5428, arXiv:hep-ph/9606337.
- [67] J. Jalilian-Marian, A. Kovner, A. Leonidov, and H. Weigert, “The Wilson renormalization group for low  $x$  physics: Towards the high density regime,” *Phys. Rev.* **D59** (1998) 014014, arXiv:hep-ph/9706377.
- [68] A. Kovner, J. G. Milhano, and H. Weigert, “Relating different approaches to nonlinear QCD evolution at finite gluon density,” *Phys. Rev.* **D62** (2000) 114005, arXiv:hep-ph/0004014.
- [69] E. Iancu, A. Leonidov, and L. D. McLerran, “Nonlinear gluon evolution in the color glass condensate. 1.,” *Nucl. Phys.* **A692** (2001) 583–645, arXiv:hep-ph/0011241.
- [70] E. Iancu, A. Leonidov, and L. D. McLerran, “The Renormalization group equation for the color glass condensate,” *Phys. Lett.* **B510** (2001) 133–144, arXiv:hep-ph/0102009.

- [71] E. Ferreiro, E. Iancu, A. Leonidov, and L. McLerran, “Nonlinear gluon evolution in the color glass condensate. 2.,” *Nucl. Phys.* **A703** (2002) 489–538, arXiv:hep-ph/0109115.
- [72] K. Fukushima, “Randomness in infinitesimal extent in the McLerran-Venugopalan model,” *Phys. Rev.* **D77** (2008) 074005, arXiv:0711.2364.
- [73] T. Lappi, “Wilson line correlator in the MV model: Relating the glasma to deep inelastic scattering,” *Eur. Phys. J.* **C55** (2008) 285–292, arXiv:0711.3039.
- [74] L. McLerran, “A Brief Introduction to the Color Glass Condensate and the Glasma,” in *Proceedings, 38th International Symposium on Multiparticle Dynamics (ISMD 2008): Hamburg, Germany, September 15-20, 2008*, pp. 3–18. 2009. arXiv:0812.4989. <https://inspirehep.net/record/806434/files/arXiv:0812.4989.pdf>.
- [75] A. Krasnitz and R. Venugopalan, “Non-perturbative computation of gluon mini-jet production in nuclear collisions at very high-energies,” *Nucl. Phys.* **B557** (1999) 237, arXiv:hep-ph/9809433.
- [76] E. Iancu, K. Itakura, and L. McLerran, “A Gaussian effective theory for gluon saturation,” *Nucl. Phys.* **A724** (2003) 181–222, arXiv:hep-ph/0212123.
- [77] T. Lappi, *Classical chromodynamics and heavy ion collisions*. PhD thesis, Helsinki U., 2004. arXiv:hep-ph/0505095. <http://urn.fi/URN:ISBN:952-10-2100-4>.
- [78] A. Bagchi, R. Basu, A. Kakkar, and A. Mehra, “Galilean Yang-Mills Theory,” *JHEP* **04** (2016) 051, arXiv:1512.08375.
- [79] W. D. Myers and W. J. Swiatecki, “Average nuclear properties,” *Annals Phys.* **55** (1969) 395.
- [80] H. Fujii, K. Fukushima, and Y. Hidaka, “Initial energy density and gluon distribution from the Glasma in heavy-ion collisions,” *Phys. Rev.* **C79** (2009) 024909, arXiv:0811.0437.
- [81] K. Fukushima and F. Gelis, “The evolving Glasma,” *Nucl. Phys.* **A874** (2012) 108–129, arXiv:1106.1396.
- [82] W. H. Press, S. A. Teukolsky, W. T. Vetterling, and B. P. Flannery, *Numerical Recipes in C (2nd Ed.): The Art of Scientific Computing*. Cambridge University Press, 1992.
- [83] A. Krasnitz and R. Venugopalan, “The Initial gluon multiplicity in heavy ion collisions,” *Phys. Rev. Lett.* **86** (2001) 1717–1720, arXiv:hep-ph/0007108.

- 
- [84] T. Lappi, “Production of gluons in the classical field model for heavy ion collisions,” *Phys. Rev.* **C67** (2003) 054903, arXiv:hep-ph/0303076.
- [85] D. Bodeker and K. Rummukainen, “Non-abelian plasma instabilities for strong anisotropy,” *JHEP* **07** (2007) 022, arXiv:0705.0180.
- [86] **SciDAC Collaboration, LHPC Collaboration, UKQCD Collaboration** Collaboration, R. G. Edwards and B. Joo, “The Chroma software system for lattice QCD,” *Nucl.Phys.Proc.Suppl.* **140** (2005) 832, arXiv:hep-lat/0409003.
- [87] B. Gough, *GNU Scientific Library Reference Manual - Third Edition*. Network Theory Ltd., 3rd ed., 2009.
- [88] K. Fukushima, “Turbulent pattern formation and diffusion in the early-time dynamics in relativistic heavy-ion collisions,” *Phys.Rev.* **C89** (2014) 024907, arXiv:1307.1046.
- [89] R. J. Fries, J. I. Kapusta, and Y. Li, “Near-fields and initial energy density in the color glass condensate model,” arXiv:nucl-th/0604054.
- [90] Y. V. Kovchegov, “Can thermalization in heavy ion collisions be described by qcd diagrams?,” *Nucl. Phys.* **A762** (2005) 298–325.
- [91] T. Lappi, “Energy density of the glasma,” *Phys. Lett.* **B643** (2006) 11–16, arXiv:hep-ph/0606207.
- [92] U. W. Heinz, “QUARK - GLUON TRANSPORT THEORY,” *Nucl.Phys.* **A418** (1984) 603C–612C.
- [93] S. Mrowczynski, “Stream Instabilities of the Quark - Gluon Plasma,” *Phys.Lett.* **B214** (1988) 587.
- [94] Y. Pokrovsky and A. Selikhov, “Filamentation in a Quark - Gluon Plasma,” *JETP Lett.* **47** (1988) 12–14.
- [95] S. Mrowczynski, “Plasma instability at the initial stage of ultrarelativistic heavy ion collisions,” *Phys.Lett.* **B314** (1993) 118–121.
- [96] J.-P. Blaizot and E. Iancu, “The Quark gluon plasma: Collective dynamics and hard thermal loops,” *Phys.Rept.* **359** (2002) 355–528, arXiv:hep-ph/0101103.
- [97] P. Romatschke and M. Strickland, “Collective modes of an anisotropic quark gluon plasma,” *Phys.Rev.* **D68** (2003) 036004, arXiv:hep-ph/0304092.
- [98] P. B. Arnold, J. Lenaghan, and G. D. Moore, “QCD plasma instabilities and bottom up thermalization,” *JHEP* **0308** (2003) 002, arXiv:hep-ph/0307325.

- [99] M. E. Carrington, K. Deja, and S. Mrowczynski, “Plasmons in Anisotropic Quark-Gluon Plasma,” *Phys.Rev.* **C90** (2014) 034913, arXiv:1407.2764.
- [100] B. D. Fried, “Mechanism for Instability of Transverse Plasma Waves,” *Physics of Fluids* **2** (May, 1959) 337–337.
- [101] P. B. Arnold and G. D. Moore, “QCD plasma instabilities: The NonAbelian cascade,” *Phys. Rev.* **D73** (2006) 025006, arXiv:hep-ph/0509206.
- [102] P. B. Arnold and G. D. Moore, “The Turbulent spectrum created by non-Abelian plasma instabilities,” *Phys. Rev.* **D73** (2006) 025013, arXiv:hep-ph/0509226.
- [103] J. Berges, S. Borsanyi, D. Sexty, and I. O. Stamatescu, “Lattice simulations of real-time quantum fields,” *Phys. Rev.* **D75** (2007) 045007, arXiv:hep-lat/0609058.
- [104] J. Berges and D. Sexty, “Real-time gauge theory simulations from stochastic quantization with optimized updating,” *Nucl. Phys.* **B799** (2008) 306–329, arXiv:0708.0779.
- [105] G. Aarts and I.-O. Stamatescu, “Stochastic quantization at finite chemical potential,” *JHEP* **09** (2008) 018, arXiv:0807.1597.
- [106] G. Aarts, “Can stochastic quantization evade the sign problem? The relativistic Bose gas at finite chemical potential,” *Phys. Rev. Lett.* **102** (2009) 131601, arXiv:0810.2089.
- [107] R. Anzaki, K. Fukushima, Y. Hidaka, and T. Oka, “Restricted phase-space approximation in real-time stochastic quantization,” *Annals Phys.* **353** (2015) 107–128, arXiv:1405.3154.
- [108] K. Fukushima, D. E. Kharzeev, and H. J. Warringa, “The Chiral Magnetic Effect,” *Phys. Rev.* **D78** (2008) 074033, arXiv:0808.3382.
- [109] N. Müller, S. Schlichting, and S. Sharma, “Chiral magnetic effect and anomalous transport from real-time lattice simulations,” *Phys. Rev. Lett.* **117** no. 14, (2016) 142301, arXiv:1606.00342.
- [110] Y. Akamatsu and N. Yamamoto, “Chiral Plasma Instabilities,” *Phys. Rev. Lett.* **111** (2013) 052002, arXiv:1302.2125.
- [111] P. V. Buividovich and M. V. Ulybyshev, “Numerical study of chiral plasma instability within the classical statistical field theory approach,” *Phys. Rev.* **D94** no. 2, (2016) 025009, arXiv:1509.02076.

- 
- [112] Y. Akamatsu, A. Rothkopf, and N. Yamamoto, “Non-Abelian chiral instabilities at high temperature on the lattice,” *JHEP* **03** (2016) 210, arXiv:1512.02374.
- [113] F. Karsch and H. Satz, “The Spectral analysis of strongly interacting matter,” *Z. Phys.* **C51** (1991) 209–224.
- [114] J. F. Gunion and R. Vogt, “Determining the existence and nature of the quark - gluon plasma by upsilon suppression at the LHC,” *Nucl. Phys.* **B492** (1997) 301–337, arXiv:hep-ph/9610420.
- [115] G. P. Lepage, L. Magnea, C. Nakhleh, U. Magnea, and K. Hornbostel, “Improved nonrelativistic QCD for heavy quark physics,” *Phys. Rev.* **D46** (1992) 4052–4067, arXiv:hep-lat/9205007.





# CURRICULUM VITAE

## Personal details

---

Name: Björn Fröhlich Wagenbach  
Address: Wiesenstraße 10, 60385 Frankfurt am Main  
Birthday: 12 January 1989  
Birthplace: Bad Soden am Taunus  
Nationality: German

## Education

---

2014–2018 PhD student, Goethe University Frankfurt am Main  
*“Real-time lattice simulations of classical Yang-Mills theory and fermions”*  
2012–2014 Master of Science, Goethe University Frankfurt am Main  
*“Lattice Investigation of Heavy Meson Interactions”*  
2009–2012 Bachelor of Science, Goethe University Frankfurt am Main  
*“Numerische Berechnung des Quark-Antiquark-Potentials zur Bestimmung der kritischen Temperatur in der SU(2) Yang-Mills-Theorie”*  
1999–2008 Main-Taunus-Schule, Gymnasium, Hofheim am Taunus, Germany  
1995–1999 Steinberg-Schule, Primary School, Hofheim am Taunus, Germany

## Teaching

---

SS 2018 Theoretical physics IV: quantum mechanics  
WS 2017 Introduction to programming for physicists  
SS 2017 Advanced quantum mechanics  
WS 2016 Theoretical physics III: classical electrodynamics  
SS 2016 Theoretical physics II: classical mechanics  
WS 2015 Theoretical physics I: mathematical methods of theoretical physics  
SS 2015 Theoretical physics II: classical mechanics  
WS 2014 Theoretical physics V: thermodynamics and statistical physics  
SS 2014 Theoretical physics IV: quantum mechanics  
WS 2013 Theoretical physics I: mathematical methods of theoretical physics  
SS 2013 Physics for minor subject students II  
WS 2012 Physics for minor subject students I  
WS 2011 Mathematics for physicists I

## Presentations and conference talks

---

- 02/2017 Lattice Journal Club, Frankfurt, Germany  
“Real-time lattice simulation of classical Yang-Mills theory”
- 10/2016 Excited QCD Conference, Lisbon, Portugal  
“A real-time lattice simulation of the thermalization of QGP: first results”
- 06/2016 Physics Day – Expert Group 1, Frankfurt, Germany  
“A real-time lattice simulation of the thermalization of QGP”
- 12/2015 Lattice Journal Club, Frankfurt, Germany  
“Domain wall fermions”
- 09/2014 FAIRNESS Conference, Vietri sul Mare, Italy  
“Lattice Investigation of Heavy Meson Interactions”
- 07/2014 Palaver, Frankfurt, Germany  
“Lattice Investigation of Heavy-Heavy-Light-Light Tetraquark Candidates”
- 06/2014 Lattice Seminar, Frankfurt, Germany  
“Lattice Investigation of Heavy-Heavy-Light-Light Tetraquark Candidates”
- 09/2012 Bachelor Seminar, Frankfurt, Germany  
“Numerische Berechnung des Quark-Antiquark-Potentials zur Bestimmung der kritischen Temperatur in der SU(2) Yang-Mills-Theorie”

## Publications

---

- /2018 O. Philipsen, B. Wagenbach, and S. Zafeiropoulos  
“From the color glass condensate to filamentation instabilities: systematics of classical yang-mills theory”  
to be published
- 05/2016 M. Attems, O. Philipsen, C. Schäfer, B. Wagenbach, and S. Zafeiropoulos  
“A real-time lattice simulation of the thermalization of a gluon plasma: first results”  
published in Acta Phys.Polon.Supp. 9 (2016) 603, arXiv:1605.07064
- 08/2015 P. Bicudo, K. Cichy, A. Peters, B. Wagenbach, and M. Wagner  
“Exploring possibly existing  $qq\bar{b}\bar{b}$  tetraquark states with  $qq = ud, ss, cc$ ”  
published in PoS LATTICE2015 (2016) 095, arXiv:1508.00343
- 05/2015 P. Bicudo, K. Cichy, A. Peters, B. Wagenbach, and M. Wagner  
“Evidence for the existence of  $ud\bar{b}\bar{b}$  and the non-existence of  $ss\bar{b}\bar{b}$  and  $cc\bar{b}\bar{b}$  tetraquarks from lattice QCD”  
published in Phys.Rev. D92 (2015) no.1, 014507, arXiv:1505.00613
- 11/2014 P. Bicudo, B. Wagenbach, and M. Wagner  
“Lattice investigation of heavy meson interactions”  
published in J.Phys.Conf.Ser. 599 (2015) no.1, 012006, arXiv:1411.2453

## Other work experience

---

- 2009–2018 Table tennis trainer, youth director and member of the managing board, TV 1860 Hofheim/TuS Kriftel
- 2008–2009 Civilian service at Drehpunkt e.V. as integration assistant, Bodelschwingh-Schule (school for physically and mentally handicapped children), Hofheim a. Ts., Germany

## Skills

---

Languages:	German:	native speaker
	Danish:	native speaker
	English:	fluent
	French:	basic
Computer:	OS:	Linux, macOS, Windows
	Scientific Software:	Mathematica, Matlab
	Programming:	C/C++, Python
	Others:	Latex, Microsoft/Open Office